VIBRATION-BASED STRUCTURAL DAMAGE IDENTIFICATION USING SPARSE RECOVERY AND SPARSE BAYESIAN LEARNING

HOU RONGRONG

PhD

The Hong Kong Polytechnic University

2019

The Hong Kong Polytechnic University
Department of Civil and Environmental Engineering

VIBRATION-BASED STRUCTURAL DAMAGE IDENTIFICATION USING SPARSE RECOVERY AND SPARSE BAYESIAN LEARNING

HOU Rongrong

A thesis submitted in partial fulfilment of the requirements for the degree of **Doctor of Philosophy**

January 2019

CARTIFICATE OF ORIGINALITY

I hereby declare that this thesis is my own work and that, to the best of my knowledge and belief, it reproduces no material previously published or written, nor material that has been accepted for the award of any other degree or diploma, except where due acknowledgement has been made in the text.

_____ (Signed)

HOU Rongrong (Name of student)

To My Family

ABSTRACT

Numerous vibration-based structural damage detection methods have been developed over the past decades. The basic idea of these methods is that structural damage may induce changes in vibration characteristics, such as frequencies, mode shapes, and their variants. Finite element model updating is a widely used technique to identify damage location and quantify damage extent.

Most of these studies have achieved limited success in small civil structures or scaled models in laboratory only. There are two major difficulties and challenges, among others, that hinder successful applications of vibration-based damage detection methods to practical civil structures: First, civil structures generally contain a large number of elements or components whereas the number of vibration measurement data is limited in general. To avoid this underdetermined problem in mathematics, super-elements are usually employed in numerical modelling and model updating. However, the use of such elements hinders the direct quantification of local damage with the updating parameter of the entire super-element. Second, the vibration-based damage detection is essentially an inverse problem and typically ill-posed. A small perturbation in the input data (for example, measurement noise) would lead to a significant change in the solution. Most previous model updating techniques employ the Tikhonov regularization (or l_2 regularization), which causes the identified damage distributed to many structural elements. However, this result does not match the practical situation in which damage usually occurs at several locations only especially at the early stage of damage development.

Taking these difficulties into consideration, this PhD study exploits the sparsity of structural damage and aims to develop accurate and reliable structural damage detection methods based on sparse recovery and sparse Bayesian learning. The damage index is defined as the elemental stiffness reduction and thus can be regarded as a sparse vector with several non-zero items at the damaged elements but many zeros at others. Consequently the sparse recovery theory can be applied to obtain the sparse damage index.

An l_1-regularized model updating technique is first developed to identify sparse damage using the first several natural frequencies and mode shapes. In regularization methods, the regularization parameter controls the trade-off between data fidelity and solution size and thus exerts a crucial effect on the solution. Two strategies of selecting the regularization parameter for the l_1-regularized damage detection problem are proposed. Further, an optimal sensor placement technique is proposed using the combinatory genetic algorithm such that the columns of the resulting sensitivity matrix are of the maximum independence.

Next, an iteratively reweighted l_1 regularization algorithm is proposed for structural damage detection. The regularization parameter in one step is revised according to the identification results in the previous iteration, making the technique resemble the l_0 regularization technique and outperform the l_1 regularization for sparse recovery.

The last contribution of the study is to develop a sparse Bayesian learning method, in which the sparsity of structural damage is exploited as the prior information from the Bayesian perspective. Since structural modal parameters have a nonlinear relation with structural damage, the evidence function cannot be obtained explicitly. An expectation–maximization based technique is developed to obtain the structural damage index and hyper-parameters iteratively.

The proposed structural damage detection methods are applied to several numerical and laboratory structures. The results demonstrate that the proposed methods are able to locate and quantify the sparse damage accurately, even when the number of measurement data is much less than the number of structural elements. The other advantage of the proposed damage detection methods is that the structure of interest can be modelled using a relatively large number of elements. This enables the local damage be appropriately modelled and directly quantified, which is unable to achieve through the conventional l_2 regularization methods.

PUBLICATIONS

Journal Papers

Hou RR, Xia Y*, Zhou XQ. Structural damage detection based on l_1 regularization using natural frequencies and mode shapes. *Structural Control and Health Monitoring* 2018; 25(3), e2107.

Hou RR, Xia Y*, Bao YQ, Zhou XQ. Selection of regularization parameter for l_1-regularized damage detection. *Journal of Sound and Vibration* 2018; 423(9):141–160.

Hou RR, Xia Y*, Xia Q, Zhou XQ. Genetic algorithm based optimal sensor placement for L_1-regularized damage detection. *Structural Control and Health Monitoring* 2019; 26(1), e2274.

Zhou XQ, **Hou RR***, Wu YH. Structural damage detection based on iteratively reweighted l_1 regularization algorithm. *Advances in Structural Engineering* 2018; DOI: 10.1177/1369433218817138.

Hu YD, **Hou RR**, Xia Q*. Temperature-induced displacement of supertall structures: A case study. *Advances in Structural Engineering* 2018; DOI: 10.1177/1369433218795288.

Hou RR, Xia Y*, Zhou XQ, Huang Y. Sparse Bayesian learning for structural damage detection using expectation–maximization technique. *Structural Control and Health Monitoring*, accepted.

Conference Papers

Hou RR, Xia Y. Optimal sensor placement by genetic algorithm for l_1-regularized damage detection. *The 15th International Symposium on Structural Engineering (ISSE-15)*, 25–27 October 2018, Hangzhou, China.

Hou RR, Xia Y. Sparse regularization for structural damage identification. *The 8th International Conference on Structural Health Monitoring of Intelligent Infrastructure (SHMII)*, 5–8 December 2017, Brisbane, Australia.

Hou RR, Xia Y. Vibration-based damage identification using sparse recovery technique. *The 13th International Workshop on Advanced Smart Materials and Smart Structures Technology (ANCRiSST)*, 22–23 July 2017, Tokyo, Japan.

ACKNOWLEDGEMENTS

First and foremost, I would like to express my sincere gratitude to my supervisor, Professor Yong Xia, for providing me the opportunity to pursue my Ph.D. study. His enlightening guidance, continuous encouragement, invaluable suggestions, patient training, and perfectionism in academic research, have benefited me during my past three years. Moreover, his meticulous attitudes, kindness, sincerity, and integrity, left a deep impression on me. It is a great honor to study under his supervision.

I would also like to express my special thanks to my former supervisor, Professor Yue-Quan Bao, when I pursued my master degree at the Harbin Institute of Technology, for his insightful guidance and generous support. Without his encouragement and recommendation, I would have never started my doctoral study.

I am grateful to the Department of Civil and Environmental Engineering of The Hong Kong Polytechinic University for the financial support, and for the provided research environment and facilities.

Thanks must also go to many past and current group members of Professor Xia's research group, Drs. Sun Weng, Jia-Zhan Su, Hai-Quan Jing, Peng Zhang, Wei-Li Luo, Ping-He Ni, Qi Xia, Yi-Ding Hu, Fu-Nian Li, Yi Zhou, as well as Mses. Ling-Fang Li, Xiao-You Wang, and Messrs. Wang-Lin Wu, Jia-Lin Li, and Wei Tian for their valuable suggestions and warm assistances. Special thanks go to Dr. Yong Huang from the Harbin Institute of Technology, who provided many valuable comments and guidance on my research work. I am grateful to all technicians in Laboratory QT005 and Mr. Sheng Zhan for their kind assistance in the experimental work.

I am also grateful to my friends at and beyond The Hong Kong Polytechnic University who have helped me both in my research and my daily life: Dr Jin-Long Xu, Jian-Fu Lin, You-Wu Wang, as well as Mses Ying-Yu Hua, Jin-Jie Liu, Na Yang, Jia-Wen Xie,

and Messrs. He-He Ren, Wen-Yong Yuan, Jin-Yang Li, Qin-Lin Cai, Pan Zhang, Hong Zheng, Yu-Han Wu and many others.

Special gratitude is due to my family, for all of their love, understanding, and encouragement during the past years, and to whom this thesis is dedicated.

CONTENTS

LIST OF FIGURES

LIST OF TABLES

LIST OF SYMBOLS

Symbols

E	Young's modulus
A	Cross-sectional area
k	Stiffness
$\phi_{j,i}$, $\boldsymbol{\phi}_i$, $\boldsymbol{\Phi}$	*i*th mode shape at *j*th point, *i*th mode shape vector, mode shape matrix
$\boldsymbol{\phi}_i^{A0}$	*i*th calculated mode shape before adjustment
ϕ_j''	Mode shape curvature at *j*th point
h	Distance between two measurement points
I	Bending moment of inertia
U_i	*i*th modal strain energy
$\boldsymbol{K}$, $\boldsymbol{K}^i$	Stiffness matrix, *i*th element stiffness matrix
$\Delta\boldsymbol{K}$	Stiffness changes after damage
$\boldsymbol{F}$	Flexibility matrix
$\boldsymbol{M}$	Mass matrix
ω_i, $\boldsymbol{f}$	*i*th natural frequency, natural frequency vector
λ_i, $\boldsymbol{\lambda}$, $\boldsymbol{\Omega}$	*i*th eigenvalue, eigenvalue vector, eigenvalue matrix
$\boldsymbol{V}_i$	*i*th residual force vector
$\boldsymbol{r}$	Residual error
$\boldsymbol{R}$, $\boldsymbol{R}^0$	Modal parameters, initial analytical modal parameters
$\mathbf{S}$	Sensitivity matrix
$\mathbf{S}_{\boldsymbol{\lambda}}$	Sensitivity matrix of the eigenvalues
$\mathbf{S}_{\boldsymbol{\phi}}$	Sensitivity matrix of the eigenvectors (mode shapes)
β	Regularization parameter
$\boldsymbol{y}$	Measurements
$\boldsymbol{X}$	Linear operator
$\boldsymbol{\varepsilon}$	Measurement noise

$\boldsymbol{I}$	Identity matrix
α_i, $\tilde{\alpha}_i$	Element stiffness parameter in the undamaged and damaged states
$\boldsymbol{\theta}$	stiffness reduction factor
m, N_m	Number of measured modes
n	Number of elements
np, N_p	Number of measurement points
δ	Noise level
$\boldsymbol{D}$	Relative discrepancy
δ_S	*S*-restricted isometry constant
μ	Mutual coherence
l	Candidate locations
p_{c}	Crossover probability
p_{m}	Mutation probability
w_i	Weight corresponding to the damage parameter θ_i
$\mathcal{M}$	Structural model class
$\boldsymbol{\mathcal{D}}$	Measured modal data
c	Normalizing constant
ν_r	Measurement errors of natural frequencies
$\boldsymbol{e}_r$	Measurement errors of mode shapes
η	Hyper-parameter reflects the precision of the identified eigenvalues
γ	Hyper-parameter reflects the precision of the identified mode shapes
ρ_i	Hyper-parameter reflects the precision of the associated damage parameter θ_i
$\mathcal{H}$	Hessian matrix
N_s	Number of sets of modal data
τ	Identification error

Abbreviations

NDT	non-destructive testing
CS	compressive sensing
SHM	structural health monitoring
SBL	sparse Bayesian learning
HHT	Hilbert–Huang transform
FE	finite element
MSE	modal strain energy
MAC	modal assurance criterion
COMAC	coordinate modal assurance criterion
DOF	degree of freedom
OSP	optimal sensor placement
MSC	mode shape curvature
GSM	gapped smoothing method
ULS	uniform load surface
RFV	residual force vector
FRF	frequency response function
GA	genetic algorithm
NN	neural network
EMD	empirical mode decomposition
MCMC	Markov chain Monte Carlo
ANN	artificial neural network
ICA	independent component analysis
SVM	support vector machine
SLV	scanning laser vibrometer
PZT	lead zirconate titanate
PVDF	polyvinylidene-fluoride
LASSO	Least Absolute Shrinkage and Selection Operator
ARD	automatic relevance determination
PDF	probability density function
MAP	maximum a posteriori
DS	damage scenario

RFP	rational fraction polynomial
SRF	stiffness reduction factor
MSF	modal scale factor
DP	discrepancy principle
GCV	generalized cross validation
QO	quasi-optimality
RIP	restricted isometry property
IRLR	iteratively reweighted l_1 regularization
EM	expectation–maximization
IRLS	iteratively reweighted least squares
FOCUSS	FOCal Underdetermined System Solve

CHAPTER 1

INTRODUCTION

1.1 Background

Civil structures are inevitably subjected to deterioration and natural and manmade hazards, such as typhoons, earthquakes, fires, floods, erosion, collisions, and explosions. These hazards may cause structural damage or even collapse. The failure of structures could be catastrophic, not only in terms of losses in life and economy, but also because of the subsequent social and psychological impacts. Therefore, structural damage detection in the early state is very important as it could enable the identification of abnormal states of the structure and appropriate actions could be taken to avoid sudden failures. Moreover, based on damage detection and structural condition assessment, cost effective maintenance and retrofit decisions could be made in order to reduce the maintenance costs and increase reliability of the structure in the life-cycle. For these reasons, structural damage detection has become a worldwide research topic and received considerable attention in the past decades.

1.2 Vibration-based Damage Detection

Structural damage detection methods mainly consist of two categories, namely, non-destructive testing (NDT) methods and vibration-based methods. The former are either visual or local experimental methods, which are typically expensive and time consuming. Moreover, NDT methods require the damage location to be known *a prior*. Therefore, these methods have difficulty in detecting damage located inside the structure and are prohibitive for large-scale civil structures when the damage location is unknown.

Vibration-based methods are based on changes in structural vibration characteristics, which are the global properties of a structure. Finite element (FE) model updating is a widely used technique for structural damage detection that uses vibration properties such as frequencies, mode shapes, mode shape curvature (MSC), modal strain energy (MSE), frequency response function (FRF), and so forth. With the development of sensing technology and signal processing techniques, the vibration properties of a structure can be measured more conveniently and accurately. Vibration-based methods have been successfully applied in mechanical and aerospace engineering. However, their applications in civil structures remain limited. There are several factors that hinder successful applications of these methods to practical civil structures:

(1) Civil structures generally have large geometric size and thus contain a large number of components. However, the number of available vibration measurements is limited. The number of potential damage locations is typically greater than that of available measurements resulting in an underdetermined problem. To avoid this underdetermined problem, previous studies adopt super-elements in both numerical modeling and model updating. Due to the large size of the super-elements, the local small damage cannot be directly quantified using the updating parameter of the elements. An equivalent stiffness reduction of the elements is typically used. This simplification leads to a small reduction in the updating parameter, which is difficult to detect reliably;

(2) The identification of structural damage based on measured modal parameters is essentially an inverse problem in mathematics and is typically ill-posed because the sensitivity matrix usually has a large condition number. Therefore, measurement noise would lead to inaccurate damage identification. Tikhonov regularization, also known as l_2 regularization, is a most commonly used technique to stabilize the inverse problem and has been widely used in model updating. However, this method tends to produce over-smooth solutions because the quadratic regularizer cannot recover the sharp features of the solution. Consequently, damage identification results are usually distributed to many structural elements; that is, many elements may be identified as having non-zero values of damage. The result does not match the real situation in which damage usually occurs only in a few elements;

(3) Civil structures are under a certain operational environment. Varying environmental factors, particularly temperature, may cause significant changes in the identified modal parameters. Previous studies have found that the changes of structural modal parameters due to changing environmental conditions could be larger than those caused by structural damage. Consequently, structural damage cannot be reliably identified. Moreover, civil structures under the operational environment are subject to significant measurement noise.

Subject to these difficulties, there has been a demand for more effective and accurate techniques to localize and quantify structural damage using only a few available measurements.

1.3 Sparsity of Structural Damage

Structural damage often occurs at several locations only especially at the early stage, which is sparse compared with the large total number of elements in the entire structure. Therefore, structural damage identification is essentially a sparse recovery problem. Recently, the sparse recovery theory, particularly compressive sensing (CS), has attracted considerable interest due to its practical utility in a wide range of applications. According to the sparse recovery theory, when the number of measurement is smaller than the size of the entire vector, the unknown sparse vector can still be accurately recovered using appropriate algorithms.

In the past decades, a number of methods have been proposed for sparse signal recovery. A typical method of solving such an ill-posed and underdetermined problem is the penalized least-squares via an l_1 regularization or its variants, which can be regarded as deterministic regularization-based approach. Moreover, the sparse recovery problem can also be formulated from a Bayesian perspective by specifying a sparsity inducing prior. The methods within the Bayesian framework exhibit certain distinct advantages over the regularization-based methods.

Although the sparse recovery theory has received widely applications in a number of areas, it is mainly employed for solving linear problems but seldom in nonlinear problems such as vibration-based damage detection.

1.4 Research Objectives

This study is to develop more accurate and reliable structural damage detection methods use a few number of measurements by exploiting the sparsity of the structural damage. This goal will be achieved from the two following perspectives:

(1) Develop sparse damage detection methods for practical civil structures based on the regularization-based approach:
   - Develop an l_1-regularized model updating technique with the use of a few natural frequencies and mode shapes;
   - Propose regularization parameter selection strategies for the l_1-regularized damage detection problem;
   - Develop an optimal sensor placement (OSP) technique to improve the reliability of the sparse damage detection;
   - Develop an iteratively reweighted l_1 regularization (IRLR) algorithm which is equivalent to the l_0 regularization technique;

(2) Develop a sparse Bayesian learning (SBL) method using an iterative expectation–maximization (EM) technique.

1.5 Thesis Organization

This thesis comprises eight chapters as illustrated in Figure 1.1. Chapter 2 presents a literature review of damage detection methods and two relevant topics, i.e., sparse recovery technique and SBL. In addition, the limitations of the existing vibration-based damage detection methods are reviewed and the challenging issues are addressed. Two numerical examples and three experimental structures are described in Chapter 3 for applications in later chapters.

In Chapter 4, an l_1 regularization-based model updating technique is developed through exploiting the sparse property of structural damage. Moreover, two strategies for

selecting the regularization parameter in the l_1-regularized damage detection problem are developed.

In l_1-regularized damage detection, the sensitivity matrix actually acts as the sensing matrix, and it is directly related to the mode shapes used or sensor locations. Therefore in Chapter 5, an OSP technique is proposed based on the genetic algorithm (GA) such that the resulting sensitivity matrix is of the maximum independence.

An IRLR algorithm is proposed in Chapter 6 to improve the accuracy of the l_1-regularized damage detection method. This technique resembles the l_0 regularization, of which the corresponding nonconvex optimization problem is solved through an iterative procedure.

In Chapter 7, the sparsity of structural damage is exploited from the Bayesian perspective. An SBL method is developed based on the EM technique and two sampling techniques are employed.

Chapter 9 concludes the thesis and discusses possible future research.

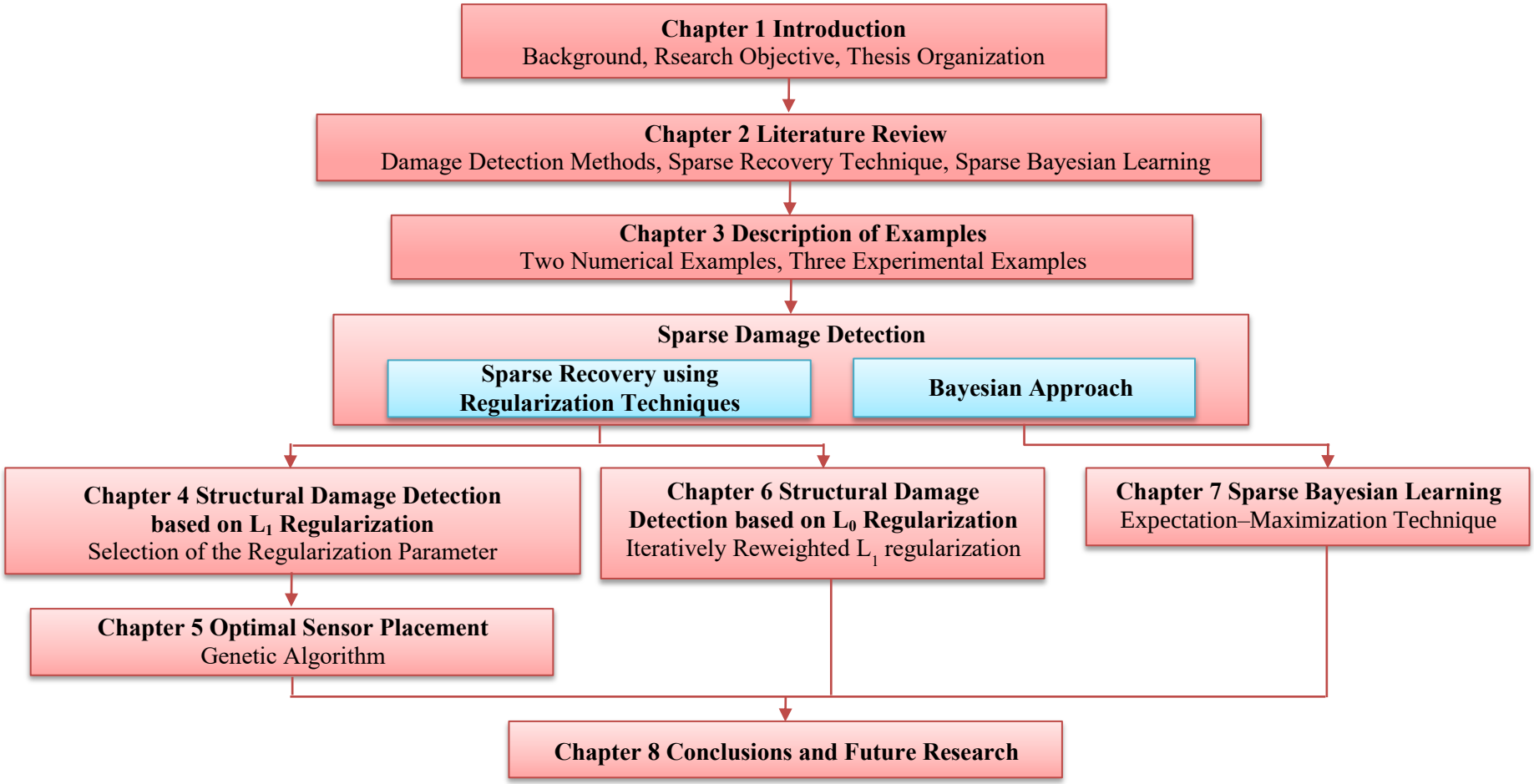

Figure 1.1 Organization of Thesis

CHAPTER 2

LITERATURE REVIEW

2.1 Introduction

As introduced in Chapter 1, this study aims to develop accurate and reliable structural damage detection methods through exploiting the sparsity of structural damage. This chapter presents a review of the relevant topics.

Damage is defined as changes introduced into a system that adversely affects its current or future performance (Sohn *et al*., 2003). This definition means that damage is only meaningful through comparison of two different states, one of which is supposed to represent the initial or undamaged state and the other is the damaged one. There are typically four levels of damage detection: determination of the existence of damage; determination of the geometric location of damage; quantification of the severity of damage; and finally prediction of the remaining service life of the structure (Rytter, 1993).

Structural damage detection methods can be divided into two categories: NDT methods and vibration-based methods. NDT methods, such as acoustic/ultrasonic methods, magnetic field methods, and radiographys, require that the damage location to be known *a priori* and they can only detect damage within the vicinity of the sensors. Subjected to these limitations, NDT methods have difficulty in detecting damage located inside the structure. When the damage location is unknown, these methods are not applicable to large-scale and complicated structures since extremely long inspection time is required due to the large geometry size. Therefore, NDT methods are generally regarded as local damage detection methods and restricted to the structural component level. They cannot assess the global performance and deterioration of the structure. Vibration-based methods are based on changes in structural dynamic characteristics, which provide both

global and local information of the structure. Therefore, they are not subjected to the above mentioned problems of local methods. Due to its efficiency in practice and simplicity of implementation, the vibration-based damage detection methods have attracted considerable attention over the past decades. In this chapter, only the vibration-based damage detection methods will be reviewed.

Structural damage usually appears in a few sections or members only, which is sparse compared with the total elements of the entire structure. Damage identification, which aims to induce the sparse damaged elements, is a sparse recovery problem. Recently, sparse signal recovery has received widely attention in a number of areas, including statistics, applied mathematics, and electirical engineering. According to the sparse recovery theory, the sparse vector of which only a few entries are non-zero can be recovered using a small number of measurement data only. However, this theory has seldom been utilized in previous damage detection until recently due to the booming of CS. The sparse recovery technique and its applications in structural health monitoring (SHM) and structural damage detection will be reviewed.

Within the Bayesian framework, the SBL is effective in encouraging sparsity in the inferred predictors and has been rapidly developed recently in the context of regression and classification (Tipping, 2001). Through specifying a sparsity inducing prior over the inferred parameters, the desired sparse solution can be obtained using appropriate estimation techniques. Compared with the frequentist methods, SBL has some superior performances for sparse signal recovery. In recent years, SBL has received increasing attention and been introduced to SHM and structural damage detection. The relevant studies will also be reviewed in this chapter.

2.2 Damage Detection Methods

Vibration-based damage detection methods have been first developed and applied in aerospace and mechanical engineering. Until the early 1980s, the civil engineering community began to apply the vibration-based damage detection methods to bridge structures. The basic idea of vibration-based damage detection methods is that structural vibration characteristics are functions of the physical properties of the structure, i.e.,

mass, damping, and stiffness. Once damage occurs, the physical properties of the structure will change and the vibration characteristics will change accordingly. Therefore, the changes in vibration characteristics can be utilized to locate and quantify structural damage (Doebling *et al*., 1996). The existing damage detection methods usually assume that there will be a detectable change in stiffness with the mass remaining unchanged (Sampaio *et al*., 1999). Damping is usually disregarded, although it has been employed by a small number of researchers for damage detection (Brownjohn, 1979).

Over the past decades, the vibration-based damage detection methods have been developed within three domains, i.e., time domain, frequency domain, and time-frequency domain. Time domain methods use time-history responses, e.g. accelerations (Zimmerman and Kaouk, 1994; Yang *et al.*, 2014). The time-frequency domain methods are based on time-frequency analysis tools, such as Wavelet transform and Hilbert–Huang transform (HHT) (Hou *et al*., 2000; Wang and Chen, 2014). The frequency domain methods use modal parameters, e.g. natural frequencies (Salawu, 1997; Kim and Stubbs, 2003), mode shapes (Shi *et al*., 2000b; Xia *et al*., 2008), and MSC (Pandey *et al*., 1991), which can be readily interpreted physically. With the development of modal analysis technology, the majority of vibration-based methods fall into the frequency domain. In order to compare the existing damage detection methods on a common basis, the benchmark problems have been established (Johnson *et al*., 2000, 2004; Casciati, 2010)

According to the algorithm used, damage detection methods can be classified into non-model based (or data-driven methods) and model-based (usually model updating methods). The former are entirely built upon the vibration property measurements without recourse to a prior FE model (Zhong and Oyadiji, 2007; Bayissa *et al.*, 2008). Model updating methods (Friswell and Mottershead, 1995) iteratively adjust the structural parameters of the FE model to minimize the discrepancy between analytical predictions and experimental data. Therefore, both damage location and severity can be identified by examining the change in the structural parameters of the FE model.

The vibration-based damage detection methods will be first introduced according to the damage identification index used.

2.2.1 Natural Frequency-based Methods

Natural frequency is one of the commonly used modal parameters for vibration-based damage detection. Frequency measurements can be quickly conducted and cheaply acquired and they are often more accurate, reliable and simpler to be measured than other vibration properties. In addition, due to the global nature of frequencies, one or two sensors are enough to obtain the first few frequencies and the measurement points could be selected flexibly, which is an important advantage in practical applications.

Adams *et al*. (1978) might be the first researcher using frequencies to locate and quantify structural damage in a 1D component. In their method, only axial modes of vibration were considered and damage was represented by an infinitesimal spring. The damage location was determined utilizing two or more frequencies combined with a theoretical model. EA/k was calculated as an indicator of the severity of damage, where E represents the Young's modulus, A is the cross-sectional area, and k denotes the stiffness of the spring. Hearn and Testa (1991) determined the damage location using the frequency changes based on a perturbation of the motion equation. A simplification was made in their method that damage will influence the primary stiffness only. The damage location was determined by comparing the measured and characteristic frequency change ratios for each member.

Shah *et al*. (2000) found that frequencies were sensitive to the presence of fatigue-induced cracks in concrete specimens. Therefore, shifts in the frequencies could be related to the remaining service life of the structure and then used to predict the fatigue life. Morassi (2001) detected the single crack in a vibrating rod based on the damage-induced shifts in a pair of natural frequencies. However, cracks in different locations may produce identical changes in natural frequencies, especially if the uniform rod is under free-free boundary condition. The effect of this non-uniqueness was found to be reduced by means of a careful choice of the data under certain conditions.

Kim and Stubbs (2003) determined the damage size and location in beam-type structures using frequency data. Utilizing the frequency changes of different modes and modal sensitivities derived from the theoretical model, single damaged element was determined. The damage size was quantified by relating frequency changes to the changes of MSE based on the Euler-Bernoulli model. Moreover, increasing the number of modes used could improve the damage identification accuracy. Zhong *et al*. (2008) developed a new approach based on auxiliary mass spatial probing and spectral center correction method to identify damage of beam-like structures using the accurate natural frequencies.

Although the use of frequency changes for damage detection has been greatly developed, there are still some limitations in these methods. Since the stiffness change is proportional to the square of the frequency change, natural frequencies are not sensitive to structural damage, especially for large-scale structures. Moreover, the ambient and environmental effects may cause significant variations (5%–10%) in nature frequencies, which are difficult to distinguish from the damage-induced frequency changes (Salawu 1997). Cawley (1997) found that the natural frequencies of a cantilever beam were more sensitive to thermal changes than cracks. Some experimental results also showed that the frequency change may be an unreliable indicator when damage was located at low stress region (Salane and Baldwin Jr, 1990). Another critical problem is that the frequency-based damage detection methods usually lead to non-unique damage identification results. In many cases, damage with similar sizes at different locations are likely to cause the same amount of frequency changes, particularly for symmetrical structures. This problem will become more severe for multiple damage situations.

2.2.2 Mode Shape-based Methods

Compared to natural frequencies, mode shapes have some appealing features for damage detection. First, mode shapes could provide both local and spatial information of a structure and thus have higher sensitivity to local damage than natural frequencies (Kim *et al*., 2003). In addition, mode shapes are less sensitive to ambient effects than

natural frequencies are. Therefore, many damage detection methods have been developed based on mode shapes in the past decades.

The modal assurance criterion (MAC) (Allemang and Brown 1982) and the coordinate modal assurance criterion (COMAC) (Lieven and Ewins 1988) are two commonly used statistical indicators of the inconsistence between different mode shapes. Salawu and Williams (1995) studied the mode shapes of a reinforced concrete bridge before and after repairs. The MAC values changed considerably after repairs and gave an indication of the location of repairs. Fr ýba and Pirner (2001) recommended that the COMAC could be used as a damage location indicator in practice. If the COMAC value was less than one, damage may occur on the target structure. The lower the COMAC value was, the more likely damage will occur.

Shi *et al*. (2000b) developed a sensitivity- and statistical-based method to identify structural damage using incomplete mode shapes. The incomplete mode shapes were utilized first to locate the possible damage sites and then the accurate damage location and severity were determined using the measured natural frequencies. The measured data can be used directly to locate damage sites without mode shape expansion or reduction of the FE model. The performance of the proposed method was demonstrated on a numerical planar truss model. The results showed that the proposed method was accurate and robust in damage localization with or without noise effect. Abdo and Hori (2002) proposed that the mode shape corresponding to the rotational degree of freedom (DOF) was a sensitive indicator of damage, especially for multiple damage with different sizes. The proposed method was verified through the numerical analysis of two plates with different boundary conditions. An improved damage detection method based on modal displacement measurements was introduced by Guan and Karbhari (2008). The new sensitive damage index was directly calculated from the modal displacement and modal rotation. The modal rotation was determined from the measured modal displacement using a penalty-based minimization method. Since the calculation of the damage index did not rely on numerical differentiation, the proposed method avoided the problems associated with the differentiation procedures.

Unlike the above introduced methods, some methods only depend on the mode shapes obtained from the damaged structures. These methods can be termed as non-model based methods. Ratcliffe (1997) applied a Laplacian operator on the mode shape data to identify damage. This technique only used the mode shapes obtained from the damaged structure and required no reference to any undamaged model of the structure. If damage was severe, a Laplacian operator was directly applied to the mode shapes. Instead, when the damage was less severe, a post processing was adopted to fit the Laplacian locally using a cubic polynomial. The most appealing feature of the proposed technique was that it could identify a thickness change of a beam as small as 0.5%. Hadjileontiadis *et al*. (2005) proposed a new method for crack identification in beam-like structures based on fractal dimension analysis. The location and size of cracks were determined by sudden changes in the fractal dimension calculated from the modal shapes. This new method directly utilized response data and no analytical model was required for crack identification. Numerical studies showed that the proposed method had good robustness against noise. Later, Hadjileontiadis and Douka (2007) extended this method to plate-type structures. They proved that the concept of the fractal dimension-based crack detector in beams could be extended to the case of 2D-structures and the performance was sustained. The location, length and depth of cracks could be accurately identified using the proposed method despite the presence of noise.

The mode shape-based damage detection methods also have some disadvantages. First, the mode shapes of lower modes are not sensitive to small local damage especially for large-scale structures. When damage is located near the node of a mode, the mode shape may exhibit no change (Maia *et al*., 2003). Second, the process of extracting mode shapes from dynamic measurements is prone to noise amplification and thus produces some unavoidable errors, which makes the obtained mode shapes less accurate than natural frequencies. Moreover, since a series of sensors are required in order to obtain accurate mode shapes, the number of sensors used and the OSP may have a significant influence on the accuracy of damage detection (Shi *et al*., 2000a).

2.2.3 Modal Shape Curvature-based Methods

Since the displacement mode shape is not very sensitive to small local damage, the MSC has been developed as a damage indicator to improve the sensitivity of mode shape data to structural damage. Pandey *et al*. (1991) first reported that changes in the curvature mode shapes can be used to detect structural damage. The MSC was calculated using a central difference approximation as

$$\phi_j'' = \frac{\phi_{j+1,i} - 2\phi_{j,i} + \phi_{j-1,i}}{h^2} \tag{2.1}$$

where $\phi_{j,i}$ was the *i*th mode shape at *j*th point, and *h* was the distance between two measurement points. The absolute changes in the curvature mode shapes were proved to be sensitive to damage. Wahab and De Roeck (1999) proposed that a fine measurement grid was required in order to obtain accurate MSCs and that the lower MSCs were more accurate than the higher ones in general. In this regard, a new damage indicator, which averaged the differences in curvature mode shapes for all modes, was developed and applied to a prestressed concrete bridge.

Some researchers also applied the signal processing method to modal curvature to improve the damage identification accuracy. Ratcliffe and Bagaria (1998) applied the gapped smoothing method (GSM) to the MSC to locate the delamination in a composite beam. A localized cubic polynomial curve was used to fit the MSC and the damage index was defined as the square of the difference between the calculated cubic and the curvature. The proposed method did not depend on any model or data of the undamaged structure. Yoon *et al*. (2005) later applied and generalized the 1D GSM to 2D plate-like structures. Xu *et al*. (2015) investigated the mechanism of using 2D MSC to characterize damage in plates. On the basis of this mechanism, a synergy between wavelet transform and a Teager energy operator was proposed to detect damage in plates.

In many MSC-based methods, modal curvatures were obtained from displacement mode shapes through curve fitting or numerical differentiation. These strategies, such as the

central difference method, are essentially approximations and would introduce significant errors when the distance of the measurement points is too long. However, in practical applications, the spacing of measurement points depends on many factors, e.g. the availability of the equipment, and only a limited number of spatial points can be measured. In addition, noise in the mode shape measurements would propagate during this extraction process, which would have a significant effect on the final results. For beam-type structures satisfying the Euler-Bernoulli beam model, the curvature is proportional to the surface bending strain. Therefore, the MSC can be obtained directly by measuring strains. Yao *et al*. (1992) and Chang *et al*. (1993) pointed out that the strain mode shapes performed better than displacement mode shapes in damage detection.

2.2.4 Modal Strain Energy Methods

MSE is another widely used damage identification indicator derived from the mode shapes. For Bernoulli-Euler beams, the strain energy associated with a particular mode is given by

$$U_i = \frac{1}{2}\int_0^l EI\left(\frac{\partial^2 \boldsymbol{\phi}_i}{\partial x^2}\right)^2 dx \tag{2.2}$$

where I is the bending moment of inertia, $\boldsymbol{\phi}_i$ is the ith displacement mode shape, and x is the coordinate along the length of the beam.

Kim and Stubbs (1995) proposed a damage index based on the ratio of the original MSE to the damaged one and applied it for damage detection in a plate girder. The effect of model uncertainties on the accuracy of damage detection was also studied. Later, the proposed damage indicator and technique were successfully applied to damage identification in a bridge structure (Farrar and Doebling, 1999). The results showed that the proposed method performed better than the MSC-based methods.

Cornwell *et al*. (1999) extended the MSE method for 1D beam-type structures to 2D plate-like structures, which were characterized by 2D curvature. The proposed method

used only the first several mode shapes before and after damage, which were not necessarily mass normalized of the structure. Therefore, it was applicable to actual structures under ambient excitations. However, the performance of this method was poor for multiple damage locations with different severities. Shi *et al*. (2000b) developed an MSE-based damage detection method with the requirement of an analytical model. First, the MSE change ratio was calculated to determine the suspected damage location. An iterative process was then adopted to calculate the damage coefficients, which were used to locate and quantify damage. The numerical and experimental studies showed that the method was able to successfully locate damage even for multiple damage cases, while was sensitive to noise in damage quantification. In later work, Shi *et al*. (2002) extended the technique using the elemental MSE change. Through reducing the modal truncation and FE modelling errors, this algorithm improved the convergence properties as compared with their previous study (Shi *et al*., 2000b).

Peterson *et al*. (2001) utilized changes in MSE to identify local damage and decay in timber beams. Both analytical and experimental results showed that the damage location and severity could be determined accurately even for damage with small magnitudes. Pradeep *et al*. (2014) used the MSE change ratio as an indicator to detect the delamination of sandwich structures. Through numerical and experimental analysis, the MSE change ratio was proved to be an efficient indicator of damage in sandwich structures.

Kim and Stubbs (2002) proposed an improved MSE-based method and compare it with two existing strain energy based methods by eliminating the erratic assumptions and limits in two existing methods. However, since the MSE was calculated from MSCs, the problems associated with the numerical differentiation process still existed. Wang *et al*. (2014) applied two different MSE-based methods to the simulated and measured data of a 3D offshore platform model. Results indicated that the MSE decomposition method outperformed the traditional MSE-based method.

2.2.5 Modal Flexibility-based Methods

With the development of the natural frequency-based and mode shape-based methods for damage identification, some researchers began to develop damage detection methods utilizing both the natural frequencies and mode shapes. The modal stiffness matrix $\boldsymbol{K}$ could be calculated from modal data

$$\boldsymbol{K} = \mathbf{M}\boldsymbol{\Phi}\boldsymbol{\Omega}\boldsymbol{\Phi}^{T}\mathbf{M} = \mathbf{M}\left(\sum_{i=1}^{m} \omega_i^2 \boldsymbol{\phi}_i \boldsymbol{\phi}_i^T\right)\mathbf{M} \tag{2.3}$$

The modal flexibility matrix $\boldsymbol{F}$ is defined as the inverse of the stiffness matrix

$$\boldsymbol{F} = \boldsymbol{K}^{-1} = \boldsymbol{\Phi}\boldsymbol{\Omega}^{-1}\boldsymbol{\Phi}^{T} = \sum_{i=1}^{m} \frac{1}{\omega_i^2} \boldsymbol{\phi}_i \boldsymbol{\phi}_i^T \tag{2.4}$$

where $\boldsymbol{M}$ is the mass matrix, $\boldsymbol{\Phi} = [\boldsymbol{\phi}_1, \boldsymbol{\phi}_2, \cdots, \boldsymbol{\phi}_n]$ is the mode shape matrix, $\boldsymbol{\Omega} = \text{diag}(\omega_i^2)$ is the eigenvalue matrix, ω_i is the *i*th natural frequency, and *m* is the number of modes used.

Mannan and Richardson (1990) directly utilized the changes in the stiffness matrix before and after damage of the structure to locate damage. As illustrated in Equation (2.3), the modal contribution to the stiffness matrix is directly proportional to the square of the modal frequency, which means that higher modal responses should be measured in order to obtain accurate damage identification results. However, in practice, it is difficult to measure higher modes due to experimental limitations (Hearn and Testa, 1991). Therefore, the damage detection methods based on stiffness matrix changes are less practical.

Since the modal flexibility is inversely proportional to the square of the natural frequencies, it is more sensitive to frequency changes of lower modes. Therefore, the modal flexibility has the potential to locate damage accurately without using the higher modes. Pandey and Biswas (1994) utilized the changes in flexibility matrix for damage

detection. The proposed method was based on the experimental data only and no analytical model of the target structure was required. The propagation of damage was detected through the increase in the flexibility change.

Zhang and Aktan (1998) applied the modal flexibility and its derivative, uniform load surface (ULS), to structural identification. Since the ULS is a weighted average of mode shapes, it has less truncation effect and is insensitive to experimental error compared with the mode shapes. Wu and Law (2004) utilized changes in ULS curvature to detect damage of the 2D plate-like structures. They found that the ULS curvature was sensitive to the presence of local damage, even with truncated incomplete noisy measurements. Subsequently, Wu and Law (2005) studied the sensitivity of the ULS curvature with respect to the elemental stiffness parameters to locate and quantify damage for plate-like structures. Zhang *et al*. (2013) proposed a new flexibility-based damage index for structural damage detection, which is a function of the ULS curvature. The proposed method utilized the advanced signal processing procedure to identify structural flexibility, and each mode was weighted unequally according to their contributions for the structural flexibility.

Montazer and Seyedpoor (2014) used the strain changes in structural elements between undamaged and damaged states to locate damage of truss systems. The strain of an element was evaluated using the columnar coefficients of the flexibility matrix estimated via modal analysis. Wickramasinghe *et al*. (2015) applied the modal flexibility method to locate damage in long span large diameter cables. The results showed that the damage index based on lateral vibration modes was able to successfully locate damage in suspended cables with 5% noise effect for a range of cable parameters.

Shih *et al*. (2009) presented a multi-criteria procedure incorporating the modal flexibility and MSE methods for damage detection in flexural members. Neither of the two damage identification algorithms was effective in locating multiple damage and estimating the severities of damage. The proposed multi-criteria system, which combines the two complementary damage identification algorithms, was able to locate multiple damage accurately and cross check the results.

2.2.6 Residual Force Vector Methods

Under the assumption that the mass matrix is unchanged before and after damage, the eigenvalue equation for the *i*th mode of a damaged structure is

$$(\boldsymbol{K}_d - \omega_{di}^2 \boldsymbol{M})\boldsymbol{\phi}_{di} = 0 \tag{2.5}$$

$$\boldsymbol{K}_d = \boldsymbol{K}_u - \Delta\boldsymbol{K} \tag{2.6}$$

where the subscripts "*d*" and "*u*" represent the terms for the damaged and undamaged states, respectively; $\Delta\boldsymbol{K}$ is the stiffness changes after damage. Substituting Equation (2.6) into Equation (2.5), the *i*th residual force vector (RFV) is defined as

$$\boldsymbol{V}_i = \Delta\boldsymbol{K}\boldsymbol{\phi}_{di} = (\boldsymbol{K}_u - \omega_{di}^2 \boldsymbol{M})\boldsymbol{\phi}_{di} \tag{2.7}$$

If the nature frequencies and mode shapes are determined from measured vibration data and an initial analytical model of the target structure is available, the right-hand side of Equation (2.7) is known. Each row of the RFV corresponds to one DOF of the structure. When damage occurs to an element, the entry in the RFV associated with this element would become significantly larger compared to other entries. Therefore, the entry in the RFV with large value could be utilized as an indicator for structural damage location.

Kosmatka and Ricles (1999) presented a damage identification method for flexible structures. The damage location was determined using the RFV and the extent of mass and/or stiffness variations were estimated through a weighted sensitivity analysis. The mode shapes used for determination of the residual forces were measured at every DOF. The proposed method was applied to a ten-bay space truss and the experimental results showed that the location and extent of damage were estimated accurately. Variations in mass and centers of mass locations were determined successfully. Moreover, it was found that the analytical model correlated to the experimental baseline data could improve the prediction accuracy of damage severity. Eraky *et al*. (2015) used the nodal RFV to locate and evaluate damage for plate-like structures. Plates with three configurations were used to validate the efficiency of the proposed technique. The proposed method was proved to be able to locate single and multiple damage locations

in all plate models with high accuracy. Comparison studies showed that this method was more effective for damage detection in single plate model than in continuous and L-shape plates, and performed better in identifying minor damage.

In practice, the mode shapes cannot be measured at all DOFs of the analytical model, especially for large structures. In this regard, some techniques have been developed to deal with the incomplete measurement problem. Castello *et al*. (2002) introduced a continuum damage identification approach built on minimization of the global error, which is derived from the dynamic RFVs. The continuum damage model was established by introducing a scalar variable, which represented the local cohesion state of the material. Due to the incomplete measurement of the mode shapes, a mode shape projection technique was utilized to ensure that the dimension of the experimental mode shapes was compatible with that of the analytical model. The effectiveness and applicability of the proposed algorithm have been demonstrated through an analytical 2D truss structure and a cantilever Euler–Bernouilli beam. Yang and Liu (2007) proposed a RFV-based structural damage identification method using the incomplete measured modal parameters. The damage locations were first determined by the nodal RFV. Three damage quantification techniques, i.e., the residual force based method, the minimum-rank elemental update technique and the natural frequency sensitivity method, were then examined to determine the damage severity. In consideration of the DOF mismatch between the test and analytical models, a mode shape expansion technique was presented based on the best achievable eigenvector concept. Numerical results showed that the natural frequency sensitivity method was the most effective technique, compared with the other two.

2.2.7 Frequency Response Function-based Methods

Since modal identification is a time-consuming process, some researchers directly utilized the measured FRF for damage identification. Compared with modal data, using measured FRFs for damage detection has some appealing advantages. The FRFs retain raw information about the structure and are not contaminated by modal extraction errors. Moreover, a complete set of modal data may not be obtained in practical situations due to the limited number of sensors and inaccessibility of some structural

components. The FRFs can provide much more information about damage in a desired frequency range than modal data, which are extracted from a number of FRFs around the resonances (Lee and Shin 2002). The FRF-based damage detection methods can be regarded as a generalization of the mode shape-based methods to the whole frequency range of the measurements.

Wang *et al*. (1997) determined the location and magnitude of damage based on the nonlinear perturbation equations of FRF data. A weighting technique was introduced for the perturbation equations at different locations and frequencies to minimize the influence of measurement errors. For incomplete measurement of the receptance matrix, an analytical model was utilized to calculate the unmeasured coordinates through an iterative process. The proposed damage detection method has been demonstrated by a planar 3-bay frame structure numerically and experimentally. Crespo *et al*. (1996) determined the size and location of the crack of a cantilever beam using high order FRFs. The cracked beam was considered as an asymmetric bilinear oscillator and its non-linear characteristics were described using high order FRFs based on the Volterra Series. The numerical results showed that the high order FRFs were effective in exhibiting the non-linear behavior of the beam for different positions and depths of the cracks. Fanning and Carden (2004) detected the added mass of a frame structure based on a single FRF and a numerical model of the structure.

Sampaio *et al*. (1999) located and quantified damage using the absolute differences between FRF curvatures, which are insensitive to noise and the exciting position, but sensitive to the selected frequency range. Numerical examples showed that the FRF curvature based method had a better performance over an MSC method and damage index method. Maia *et al*. (2003) compared several FRF-based and mode shape-based damage detection methods and evaluated their performance using numerical and experimental examples. For the FRF-based methods, the detection results degenerated with the increase of the frequency range. An improved technique was thus proposed to overcome this problem by summing the occurrences of the maximum differences of damage indices instead of the differences themselves. The results showed that using higher derivatives of the mode shapes had a better performance and the FRF-based damage index method was the most effective one in damage localization.

Reddy and Swarnamani (2012) used FRF curvature energy to detect and quantify damage for plate-like structures. The damage index was a function of the frequency bandwidth, based on which the optimum frequency range were determined. The results showed that damage with over 10% reduction in the elemental thickness could be identified with confidence and the damage identification accuracy was little affected by the measurement noise and excitation location. Nuno (2013) applied the FRF curvature method to detect damage of an actual steel truss bridge. Four damage cases with different severity levels were introduced to one of the crossbeams. The experimental results indicated that the damage index at the center location of the beam was most sensitive to the presence of damage and the FRF curvature method had the potential to be applied for damage detection of bridge structures.

The above mentioned damage detection methods using the measured modal parameters of the structure, such as natural frequencies and mode shapes, could be classified as damage index methods. In the following subsections, different analysis techniques for damage detection will be reviewed.

2.2.8 Model Updating-based Methods

The model updating methods use measured response data to reproduce an optimal model of the structural property matrices (i.e., mass, stiffness, and damping matrices), so that the analytical predictions of the updated model resemble the experimental data as closely as possible (Friswell and Mottershead 1995). The changes in the structural parameters could be utilized to identify damage location and quantify damage extent. Model updating methods can be classified as time domain methods and frequency domain methods. The former directly use the time domain responses for model updating, while the latter are based on modal characteristics, such as frequencies, mode shapes, and their variants.

2.2.8.1 Direct Model Updating Methods

The direct model updating methods modify the system matrices of the analytical model by perturbing the items of the matrices directly. Zimmerman and Kaouk (1994) developed an algorithm for structural damage detection using minimum rank update theory. Yang and Liu (2009) proposed a flexibility-based damage identification method. The number of damaged elements was determined by minimizing the rank of the perturbed flexibility matrix.

The advantage of the direct model updating methods is that they do not require the parametric analytical model and iteration procedures. However, these methods have several apparent drawbacks. For example, the updated matrices may have no physical meaning. Moreover, the symmetry, sparseness, and positive-definiteness of the updated system matrices are not guaranteed.

2.2.8.2 Iterative Model Updating Methods

The iterative model updating methods update the system matrices through modifying the physical parameters of the FE model, such as axial stiffness (*EA*) and bending rigidity (*EI*). Consequently, a parametric FE model is required. Other than the direct model updating methods concentrating on global system matrices, the physical parameters are updated in elemental or substructural level and then the discrete stiffness and mass matrices of all elements are assembled together. Therefore, the matrix properties of symmetry, sparseness and positive-definiteness are retained after model updating and the structural connectivity is guaranteed. In addition, the updated parameters have meaningful interpretation (Xu and Xia, 2011). Due to these merits, the iterative model updating methods are widely used for structural damage detection.

FE model updating mainly includes three aspects, the updating parameters, the objective function and the optimization algorithm (Weng, 2010, Van Overschee and De Moor, 1996). In selecting the parameters to be updated, two critical issues should be considered, i.e., which parameters are used and the number of the updating parameters. The objective function comprises the discrepancy between the analytical predictions and the practical measurements, which is usually formulated as the following least square problem

$$\widehat{\boldsymbol{\theta}} = \arg\min_{\widehat{\boldsymbol{\theta}}} \|\boldsymbol{r}(\boldsymbol{\theta})\|_2^2 = \arg\min_{\widehat{\boldsymbol{\theta}}} \ \|\boldsymbol{R}^A(\boldsymbol{\theta}) - \boldsymbol{R}^E\|_2^2 \tag{2.8}$$

where $\boldsymbol{\theta}$ is a vector of the updating parameters, $\boldsymbol{r}(\boldsymbol{\theta})$ is the residual error, and $\boldsymbol{R}^A(\boldsymbol{\theta})$ and $\boldsymbol{R}^E$ are the analytical and measured modal parameters, respectively. In the objective function, different types of data can be weighted differently for taking into consideration of their importance and measurement accuracy. The optimization algorithm serves to minimize the objective function. The sensitivity-based model updating and the evolutionary algorithm are two widely used optimization algorithms. This subsection will focus on the sensitivity-based model updating. The evolutionary algorithms, such as neural network (NN) algorithm, will be detailed in Section 2.2.11.

The sensitivity-based model updating adjusts the parameters $\boldsymbol{\theta}$ of the FE model through an iterative process to minimize the objective function in Equation (2.8). Under the assumption that the structure behaves linearly before and after damage, the relationship between $\boldsymbol{\theta}$ and $\Delta\boldsymbol{R}$ can be expressed as (Zhou *et al*., 2015)

$$\boldsymbol{S\theta} = \Delta\boldsymbol{R} = \boldsymbol{R}^A(\boldsymbol{\theta}) - \boldsymbol{R}^0 \tag{2.9}$$

where $\boldsymbol{R}^0$ represents the initial analytical modal parameters, and $\mathbf{S}$ is the sensitivity matrix defined as the derivative of the modal parameters with respect to the updating parameters. For example, the sensitivity matrices of the eigenvalues $\boldsymbol{\lambda}$ and mode shapes $\boldsymbol{\phi}$ can be expressed as

$$\mathbf{S}_{\boldsymbol{\lambda}} = \frac{\partial \boldsymbol{\lambda}}{\partial \boldsymbol{\theta}} \tag{2.10}$$

$$\mathbf{S}_{\boldsymbol{\phi}} = \frac{\partial \boldsymbol{\phi}}{\partial \boldsymbol{\theta}} \tag{2.11}$$

Therefore, $\boldsymbol{R}(\boldsymbol{\theta})$ can be calculated using the following linear equation

$$\boldsymbol{R}^A(\boldsymbol{\theta}) = \boldsymbol{S\theta} + \boldsymbol{R}^0 \tag{2.12}$$

where $\mathbf{S}$ and $\boldsymbol{R}^0$ can be obtained either from the global FE model (Nelson, 1976) or using the substructuring approach (Weng *et al*., 2011, Xia *et al*., 2010). The nonlinear minimization problem in Equation (2.8) is thus transferred into a linear optimization problem at each iteration.

Fritzen *et al*. (1998) proposed a sensitivity-based model updating algorithm to locate and quantify structural damage. Since the sensitivity matrix is ill-conditioned, the QR orthogonal decomposition strategy was used to deal with the resulting ill-posed inverse problem by reduction of the original parameter space to a smaller subspace. Jaishi and Ren (2006) used the modal flexibility residue in the model updating. The effectiveness and robustness of the proposed method have been demonstrated numerically and experimentally. The damage identification pattern was well fit to the actual damage even though all elements of the FE model were used in the updating process.

The sensitivity-based model updating for damage detection is usually ill-posed because the sensitivity matrix usually has a large condition number. Moreover, the optimization problem in Equation (2.8) is underdetermined because the number of available modal parameters is usually less than that of the unknown parameters. In this regard, the Tikhonov regularization (or l_2 regularization) is commonly employed by adding a penalty term as (Ahmadian *et al*., 1998; Weber *et al*., 2009; Li and Law, 2010)

$$\widehat{\boldsymbol{\theta}} = \arg\min_{\boldsymbol{\theta}} \ \|\boldsymbol{R}^A(\boldsymbol{\theta}) - \boldsymbol{R}^E\|_2^2 + \beta \ \|\boldsymbol{\theta}\|_2^2 \tag{2.13}$$

where $\beta \geq 0$ is the regularization parameter. Since the Tikhonov regularization has the closed-form solution and is convenient for implementation, it has received wide applications in structural damage detection. However, the Tikhonov regularization tends to produce over smooth solutions and causes the damage identification results distributed to many structural elements. This is not consistent with the practical situation, in which damage usually occurs in a few sections or members only especially at the early stage. This problem will be addressed in Chapter 4.

2.2.9 Signal-based Methods

Since structural damage is typically a local phenomenon, the dynamic responses of the structure are usually not sensitive to damage. In order to extract sensitive features to structural damage, several signal processing technologies, such as wavelet transform, HHT, and empirical mode decomposition (EMD), have been utilized and developed for structural damage detection.

The wavelet transform is an effective time-frequency analysis method which has received wide applications in signal processing area. The basic idea of this technique is that any signal can be decomposed into a series of local basis functions called "wavelets" (Liew and Wang, 1998). Compared to the traditional Fourier transform, the translated-version and scaled-version of wavelet transform could provide information about the signal in both time and frequency domains. Singularities or discontinuities in a signal which cannot be observed directly may cause considerable changes of the wavelet coefficients. Therefore, the wavelet transform is an effective tool for structural damage detection through close examination of the signal with multiple scales.

Liew and Wang (1998) may be the first applying the wavelet theory to structural damage detection. They utilized the wavelet expressions in the space domain to identify the crack of a simply supported beam. The results showed that the wavelet analysis performed better than the traditional eigenvalue analysis. Hou *et al*. (2000) located damage and simultaneously determined the moment when damage occurred. In their method, the dynamic signal of the structural response was decomposed into details and approximations. Damage was located by spikes in the details of the wavelet decomposition. Lu and Hsu (2002) proposed the discrete wavelet transform for damage detection. The number and location of defects were determined through comparing the wavelet transforms of vibration signals of the original and defected structures in the space domain. Numerical results showed that the wavelet coefficients were very sensitive to the localized defect and the maximum change of the wavelet coefficients normally occurred in the proximity of the defect. Since higher mode shapes carry much information and are more sensitive to damage than lower modes, Rucka (2011) applied continuous wavelet transform to high-order mode shapes and operational deflection

shapes, which were obtained from scanning laser measurement. The influence of the mode order on the effectiveness of damage detection was also investigated.

Although the wavelet transform has been widely used for damage detection, it can only provide a uniform time-frequency resolution. To overcome these problems, the EMD and HHT have been developed and introduced for structural damage detection which are effective in analyzing nonstationary and nonlinear signals. EMD and HHT are able to provide more precise decompositions of the signal in the time-frequency domain than the wavelet analysis (Yan *et al*., 2007).

Yang *et al*. (2004) proposed two methods to analyze the measured data that contained damage events of the structure. The first method, based on the EMD, was capable of detecting the time instants of damage and damage locations. The second method, based on the EMD and Hilbert transform, further determined the natural frequencies and damping ratios of the structure before and after damage. Xu and Chen (2004) presented an experimental investigation on the applicability of the EMD for identifying structural damage caused by a sudden change of the structural stiffness. The instants of damage were accurately detected in terms of damage spikes extracted directly from the measured time histories using EMD. The spatial distribution of the spikes along the building was then employed to determine the damage location. Li *et al*. (2007) combined the EMD and wavelet analysis. Firstly, the EMD technique was used to decompose the structural response signal into several mono-component signals. Each mono-component signal was then analysed via the wavelet transform to detect the exact location and severity of damage. This combination method was capable of identifying the time and extent of damage more precisely than using the wavelet transform method alone. Roveri and Carcaterra (2012) proposed a novel HHT-based method for bridge structures under a moving load. The damage location was revealed by the inspection of the first instantaneous frequency curve.

2.2.10 Statistical-based Methods

Structural damage detection always entails uncertainties, which may consist of modeling errors, methodology errors, and measurement noise. Moreover, operational

and environmental variations also cause significant changes in the identified modal parameters. Many researchers have proposed probabilistic approaches to tackle the uncertainties in structural damage detection. One category is based on the perturbation technique, which assigns a random variable to each uncertainty and then calculates the statistics of the variable. The other widely used category is the Bayesian approach, which explicitly quantifies the posterior probability of the uncertainties according to observations and prior information (Beck and Katafygiotis, 1998; Katafygiotis and Beck, 1998).

Liu (1995) used the perturbation method to investigate the influence of measurement errors on the identification results of a truss. Xia *et al*. (2002) and Xia and Hao (2003) proposed the statistical damage detection method based on modal parameters taking into account the effects of random noise in both the vibration data and FE model. The statistics of stiffness parameters were estimated by the perturbation method and verified by Monte Carlo technique. The probability of damage existence was estimated by comparing the probability distributions of the stiffness parameters in the undamaged and damaged states. Hua *et al*. (2008) improved the perturbation method for the statistical identification of structural parameters. Two recursive systems of equations were derived for estimating the first two moments of random structural parameters from the statistics of the measured modal parameters.

Bayesian inference was first introduced to structural damage identification by Sohn and Law (1997). They identified multiple damage locations using estimated modal parameters. The relative posterior probability was formulated based on the modal output error, which is defined as the difference between the estimated modal parameters and the theoretical ones. The most probable damage locations were determined by comparing the relative probabilities for different damage events. Later, they applied the approach to predict the location of plastic hinge deformation of a reinforced-concrete bridge column (Sohn and Law, 2000).

Vanik *et al*. (2000) proposed a probabilistic damage measure for SHM based on identified modal parameters. A high likelihood of reduction in model stiffness was taken as a proxy for damage. Beck and Au (2001) used a sequence of identified modal

parameter data sets to continually compute the probability of damage for on-line SHM. The variation in time of a probabilistic damage measure was studied which enabled small levels of damage to be detected through monitoring the structure over long times. The applicability of the proposed SHM procedure was illustrated using a shear building structure with simulated data.

Beck and Au (2002) developed an adaptive Markov chain Monte Carlo (MCMC) simulation approach for structural response predictions and performance reliability, which combined the Metropolis-Hastings algorithm with a concept similar to simulated annealing. The effectiveness of the proposed method was demonstrated using simulated dynamic test data, regardless of whether the class of models was identifiable for not.

Jiang and Mahadevan (2008) presented a Bayesian wavelet probabilistic method for structural damage detection. Before damage detection, a Bayesian discrete wavelet packet transform-based denoising approach was employed to perform data cleansing. The fuzzy wavelet NN was used to perform the nonparametric system identification to predict dynamic responses of the structure. In order to assess the difference between the measured data and model prediction, Bayesian hypothesis testing was developed and the Bayes factor was treated as a random variable, of which the probability density function (PDF) was constructed using the Monte Carlo simulation technique.

Mustafa *et al*. (2015) presented a Bayesian probabilistic methodology for structural model updating and damage detection using incomplete measured modal data. The uncertainties associated with the measurement and modelling errors were taken into consideration. An iterative algorithm was used to get the most probable values of the model parameters. Yin *et al*. (2017) combined the FE model reduction technique and Bayesian inference for detecting structural bolted-connection. The method did not need the system mode shapes of the full model and mode matching. An efficient iterative solution strategy was proposed for calculating the most probable model as well as system modal parameters. Lam *et al*. (2018) proposed a Bayesian method based on the MCMC algorithm. Through calculating the probability distribution of damage to various structural components, the damage location and damage extent were

determined, together with the associated uncertainties. Experimental example also demonstrated the ability of the proposed method to handle the unidentifiable problems.

The SBL algorithms for structural damage detection will be reviewed in Section 2.4.

2.2.11 Neural Network-based Methods

Since structural damage detection is normally an inverse and ill-posed problem, optimization algorithms have been employed by many researchers for damage detection. With the development of signal processing and system identification, some intelligence algorithms have been proposed and used to identify structural damage. The intelligence algorithms are effective in dealing with uncertainties and insufficient information, that are typical problems existing in structural damage detection and intractable using traditional optimization algorithms.

NN is a powerful intelligence optimization algorithm inspired from the study of biological neurons. It has received widely applications in many areas, such as artificial intelligence, pattern recognition, and signal processing, because of its superior nonlinear mapping ability. NN is particularly applicable to deal with complicated data for which an explicit algorithm is difficult to be identified (Carden and Fanning, 2004).

Sahin and Shenoi (2003) used artificial neural networks (ANNs) for damage location and severity prediction in beam-like structures. The necessary features as inputs to ANNs were selected through performing sensitivity analyses on changes of the natural frequencies and curvature mode shapes. Bakhary *et al*. (2010) combined a multistage ANN model with the substructure technique to determine the location and severity of damage. The nature frequencies and mode shapes were used as inputs to the ANN. The effectiveness of the proposed approach was validated using a two-span continuous concrete slab and a three-storey frame. Compared with the conventional one-stage ANN technique, the proposed approach reduced the size of the ANN model effectively and thus saved the computational effort substantially.

Lee *et al*. (2005) used the differences or ratios of mode shapes, instead of mode shapes themselves, as the inputs to the NNs to reduce the effect of modelling errors. The inflicted damage in a lab tested bridge model was identified with good accuracy for various damage cases. For a real bridge with multiple girders, the damage locations were identified successfully, although there were small errors existing in the estimated damage severities. Bakhary *et al*. (2007) proposed a statistical ANN approach for damage identification taking into account the uncertainties from the FE modelling error and measurement noise. The Monte Carlo simulation was adopted to verify the accuracy of the statistical approach. Both numerical and experimental results showed that the proposed statistical ANN approach was superior to the normal ANN approach for the identification of structural damage under different severities and noise levels.

2.2.12 Other Methods

In addition to the above introduced typical vibration-based damage detection methods, there are some other techniques that are not classified to the above categories. Sawyer and Rao (2000) presented a fuzzy logic methodology for structural damage detection using static displacements, nature frequencies and mode shapes as inputs. A fuzzy associative memory, including the information of fuzzy associations between structural responses and damage conditions, was established through FE simulations and supervised learning. Then, the fuzzy associative memory as a knowledge base combined with a fuzzy inference algorithm were used to identify possible damage locations and severities based on changes in the structural states. Numerical examples showed that the proposed method had superior performance under noisy or uncertain conditions.

Song *et al.* (2006) integrated independent component analysis (ICA) and support vector machines (SVMs). The independent components were extracted from measured sensor data through ICA, and were then used as input data for an SVM classifier. The prediction output was used to identify different types and levels of structure damage. The proposed method was more accurate than the approach by integrating ICA and ANN.

2.2.13 Comparative Studies

The performances of different damage detection methods have been compared. For example, Farrar and Jauregui (1998) compared five widely used damage detection methods, i.e., damage index method, MSC-based method, ULS method, stiffness method, and flexibility method. Through experimental and numerical studies, the damage index and MSC methods performed better than others.

Ndambi *et al*. (2002) conducted a comparative study of five damage detection methods using two reinforced concrete beams. Increasing levels of crack damage were introduced in different steps to simulate damage spreading and accumulation. It was found that: (1) The eigenfrequencies decreased monotonically with the accumulation of cracks but were not influenced by crack locations; (2) The MAC was less sensitive to crack damage than eigenfrequencies; (3) The COMAC evolution could indicate the existence and location of damage in the tested beams, but was not able to follow the damage severity and spreading; (4) The changes in flexibility matrices were only effective in detecting the presence of the crack damage; (5) The damage index method based on MSE was more precise than other methods for local damage identification.

Alvandi and Cremona (2006) accessed four damage identification techniques (i.e., MSC method, flexibility method, flexibility curvature method, and MSE method) through a simply supported beam model numerically. It was found that the MSE method was least sensitive to noise and more efficient for multiple damage situations. The MSC method was the least efficient one compared with the other three methods. The damaged element located near the supports was difficult to identify using all four methods. Except for the MSE method, other methods also had difficulties in identifying damage near the excitation force.

Zhou *et al*. (2007) compared five vibration-based damage detection methods through a lab experiment and the FE analysis on the deck slab of a simply supported bridge with minor damage. These methods were able to identify and locate minor damage using a small number of sensors and only the fundamental mode shape. Three curvature-based methods, i.e., the MSC method, MSE method, and flexibility curvature method, tended

to identify damage location at the measurement point and display a maximum error in damage localization of approximately half of the measurement spacing. The other two mode shape- and flexibility-based methods performed better with numerical data. However, when experimental data were used, similar results were obtained as the curvature-based methods. When damage was located in a near-support region, the performance of all five methods degraded that the localization resolution decreased by 50%. It was found that increasing the number of measurement points could improve the localization resolution, particularly for the three curvature-based methods.

Qiao *et al*. (2007) evaluated and compared three damage detection techniques, i.e., GSM, generalized fractal dimension method, and MSE method, for composite laminated plates. Two measurement systems, scanning laser vibrometer (SLV) with lead zirconate titanate (PZT) actuators and polyvinylidene-fluoride (PVDF) sensors with PZT actuators, were utilized to measure curvature mode shapes. Experimental and numerical analyses showed that both measurement systems could successfully extract the modal parameters and PZT-SLV system seemed to perform better than PZT-PVDF system in the numerical simulation. The non-contact PZT-SLV system was simple and convenient and able to account for dense measurement; while the PZT-PVDF system directly obtaining the curvature mode shapes was sensitive to damage and capable of real time on-board monitoring. The three damage detection algorithms were capable of identifying the presence, location, and size of the delamination in the composite plate using three consecutive mode curvatures and ULS curvatures. In general, the GSM was superior to the other two algorithms in detecting and isolating the delamination of the composite plate. Since the MSC-based method did not require data from the undamaged state of the structure, it had the potential to be applied to online structural monitoring system.

Das *et al*. (2016) conducted a comparative study on different damage detection methods: modal-based method, local diagnostic method, non-parametric method, and the time series method. Integration of autoregressive moving average model with time series model was more successful in damage identification than the rest. The non-parametric methods, e.g., Bayesian probabilistic method, were not able to detect nonlinear damage in the structure.

2.3 Sparse Recovery Technique

As introduced previously, structural damage possesses sparsity in the spatial domain. Therefore, damage identification is essentially a sparse recovery problem. In practice, the number of vibration measurements is limited and typically less than that of the structural model parameters, resulting in an underdetermined system of equations.

Mathematically, there is a linear model

$$\boldsymbol{y} = \boldsymbol{X}\boldsymbol{\theta} + \boldsymbol{\varepsilon} \tag{2.14}$$

where $\boldsymbol{y} \in R^M$ is the available measurements, $\boldsymbol{\theta} \in R^N$ refers to the unknown vector to be reconstructed, $\boldsymbol{X} \in R^{M \times N}$ $(M < N)$ is a linear operator, and $\boldsymbol{\varepsilon}$ is the error associated with the measurement noise. *A priori* knowledge is available that the unknown vector $\boldsymbol{\theta}$ is sparse. The sparsity of a vector is defined that only a small number of items are non-zero and the rest are zero or very close to zero (Theodoridis, 2012). Therefore, the inverse mapping from $\boldsymbol{y}$ to $\boldsymbol{\theta}$ is a sparse recovery problem. Unlike the classical linear regression problem with $M \geq N$, the problem in Equation (2.14) is underdetermined which has an infinite number of solutions. Moreover, inverse problems are usually ill-posed, which means that at least one of the three conditions is not satisfied in the sense of Hadamard, that is, existence, uniqueness, and stability of a solution (Isakov, 2006). A large number of commonly encountered problems can be cast under this scenario.

In the past decades, numerous methods have been proposed and extensively studied for sparse recovery problem. One category is the greedy search techniques, e.g., Matching Pursuit (Mallat and Zhang, 1993), and Orthogonal Matching Pursuit (Davis *et al*., 1994). At each iteration, these algorithms select the column of $\boldsymbol{X}$ that is most correlated with the current residuals and add this column into the set of selected columns. The residuals are updated taking into account the columns previously selected. The algorithm iterates until a convergence criterion is met and a sub-optimal solution is obtained (Cai and Wang, 2011). The greedy search techniques have not received widely applications due to its computational complexity.

The other widely used category is based on the regularization technique, which has been utilized to address the underdetermined and ill-posed problems in mathematics by adding a regularization term in the objective function. For sparse recovery problem, a proper regularizier should be selected such that the resulting optimization problem is tractable and leads to sparse solutions. The l_1 regularization technique is the most widely used and has been proved to be effective in promoting sparsity in the solution. The technique was first applied in seismology to promote sparsity, where the reflection signal, that indicates changes between subsurface layers, is sparse (Claerbout and Muir, 1973; Taylor *et al*., 1979). Later, Donoho and Stark (1989) and Donoho and Logan (1992) verified the sparsity-promoting ability of the l_1 regularization through rigorous proofs. The l_1 regularization is well known as Least Absolute Shrinkage and Selection Operator (LASSO) in statistics (Tibshirani, 1996), and Basis Pursuit in the signal analysis community (Chen *et al*., 1998).

Recently, the l_1 regularization is starting to gain popularity due to the booming of the CS, which has received widely applications in signal processing, wireless sensing, and communication (Candès, 2006; Donoho, 2006a; Baraniuk, 2011). The basic idea is that, a signal can be recovered or reconstructed from far fewer samples than required by the Shannon–Nyquist sampling theorem, provided that the signal is sparse with respect to a known orthonornmal basis and the sensing matrix satisfies certain incoherence properties (Candès, 2006). The sparse signal is reconstructed through an optimization process, i.e., finding the sparse solution to the underdetermined linear system. A typical means of solving such optimization problem is via the l_1 regularization technique (Donoho, 2006b).

The small number of damage locations can be treated as spatial sparsity as compared with the total elements of the entire structure. Therefore, the identification of the damaged elements is a sparse recovery problem. However, the sparse recovery theory starts to attract interest and be applied in SHM and damage detection until very recently. Wang and Hao (2010) discussed some potential applications of the CS in structural engineering. These potential applications included improvement of sampling, optimization of model updating, and proposition of innovative damage indicators. Bao

et al. (2014) first introduced the CS technology to SHM and conducted a series of applications of CS to SHM. Bao *et al*. (2011) investigated the application of the CS for vibration data compression. In contrast to the traditional data compression methods, CS enabled acquiring the data directly in a compressed form. The data compression ability of the CS was demonstrated using the acceleration data collected from the SHM system of the Shandong Binzhou Yellow River Highway Bridge. Since the data loss is a common problem of wireless sensors, Bao *et al*. (2012) applied the CS to recover the lost data of a wireless sensor network used in the SHM system. The validity and accuracy of the proposed data loss recovery approach was investigated using the field test acceleration data. The results showed that the CS technique was able yo recover the data with high accuracy, provided that the original data was sparsity in some orthonormal basis. Later, Bao *et al*. (2016) identified the distribution of moving heavy vehicle loads for cable-stayed bridges based on the sparse l_1 optimization technique using cable force measurements. They assumed that the vehicle loads on the bridge deck followed a sparse distribution. Moreover, the CS theory has been applied for denoising of structural vibration responses (Yang and Nagarajaiah, 2014a), and modal identification (Yang and Nagarajaiah, 2013; 2015).

More recently, several researchers have applied the sparse recovery technique to structural damage detection. Bao *et al*. (2014) proposed the potential application of CS technology for structure damage detection. Yang and Nagarajaiah (2014b) developed a two-step damage identification method via a combination of blind feature extraction and sparse representation classification. In the classification step, the modal features were expressed as a sparse linear combination of the bases of an over-complete reference feature dictionary. The resulting underdetermined linear system of equations was solved using the l_1 minimization and the sparse representation was thus recovered. Then, the relevant damage class was identified for damage detection. Numerical simulations and experimental study showed that the method was capable of identifying small and severe single or multiple damage with limited sensors. Moreover, the proposed method was robust to random excitation and noise.

Hernandez (2014) expanded the sensitivity-based model updating to localize and quantify isolated structural damage using l_1 minimization. The change in a subset of

eigenvalues of the system was selected as the damage sensitive feature. The proposed method was able to identify damage accurately using only a subset of the spectrum with significantly fewer elements than the potentially damaged elements through two different types of simulated structures. Zhou *et al.* (2015) applied the l_1 regularization approach to detect structural damage using the first few frequency data. The numerical and experimental results showed that the proposed technique could successfully identify moderate damage using only a small number of measurements compared to the entire structural elements, whereas the l_2 regularization cannot. Moreover, parametric studies were conducted to investigate the effects of measurement number, damage severity, number of damage, and noise level on the damage detection results.

Zhang and Xu (2016) conducted a comparative study between Tikhonov regularization and sparse regularization in time-domain model updating for damage identification. A reweighted sparse regularization technique was utilized to not only enhance the sparsity of solution but also provide an alternative method for selection of the regularization parameter. Both numerical and experimental studies showed that the proposed sparse regularization provided more accurate damage identification result than the traditional Tikhonov regularization. Zhang *et al*. (2017) presented a time-domain damage detection algorithm based on extended Kalman filter with the l_1 regularization technique using free vibration responses. A pseudomeasurement technique was utilized to enforce the l_1 constraint in each recursive step of the extended Kalman filter framework. The introduction of l_1 regularization effectively suppressed the interference of measurement noise and improved the identification accuracy. Compared with the traditional extended Kalman filter, the proposed algorithm showed good robustness and excellent accuracy of damage identification with the unknown initial structural state.

Fan *et al*. (2018) proposed a structural damage identification approach based on model updating with electromechanical impedance sensitivity and the sparse regularization technique to identify the location and severity of minor damage. The sensitivities of the resonance frequency shifts in the impedance responses with respect to the stiffness parameters of the host structure were calculated. The l_1 regularization technique, instead of the traditional Tikhonov regularization, was employed for solving this inverse problem. The results showed that the proposed approach was able to determine the

location and severity of the simulated structural damage accurately, even when the measured signal was noisy and the number of frequency shifts was limited.

2.4 Spare Bayesian Learning

In recent years, the sparse recovery problem has been considered and developed from a Bayesian perspective. SBL, as a supervised learning framework, is first proposed by Tipping (2001) in the machine learning community. It has received much attention as a means of deriving sparse solutions to problems like (2.14) in the context of regression and classification (Williams *et al*., 2005; Zhang and Rao, 2011; Lin *et al*., 2013). Later, SBL has been introduced to deal with the problems in CS as an effective alternative to the existing algorithms (Wipf and Rao, 2004; Ji *et al*., 2008). Over the last two years, SBL also began to be applied to earthquake engineering (Mu and Yuen, 2017) and geotechnical engineering (Ching *et al*., 2017; Wang and Zhao, 2017).

In Bayesian framework, the prior distribution can induce sparsity in the inferred parameters, which functions as the regularization term for the regularizaiton techniques. A widely used sparse prior is the Laplace distribution, which is equivalent to the l_1 regularization (Babacan *et al*., 2010). However, since the Laplace prior is not conjugate to the Gaussian likelihood, the resulting posterior probability distribution is usually intractable (Gelman *et al*., 2003). This problem has been addressed in SBL and specifically the relevance vector machine (Tipping, 2001). SBL proposes to use the automatic relevance determination (ARD) prior to incorporate a preference for sparser parameters which allows convenient conjugate-exponential Bayesian inference (Tipping, 2001; Ji *et al*., 2008). Rather than assuming a fixed prior, SBL relies on a parameterized prior. An individual hyper-parameter is assigned to each unknown parameter which controls the precision of the associated parameter. For linear regression problems, these hyper-parameters can be iteratively estimated using type-II maximization likelihood (Tipping, 2001; Bishop, 2006). During the iteration process, most hyper-parameters tend to approach infinity, and the corresponding unknown parameters approach zero, resulting in a sparse regression model. Considering the computational cost of the iterative algorithm, Faul and Tipping (2002) and Tipping and Faul (2003) developed the fast SBL algorithm to achieve highly efficient computation.

This algorithm maximize the evidence function monotonically through a sequential addition and deletion of candidate basis function (i.e., columns of $\boldsymbol{X}$). Besides the well-known sparse priors mentioned above, some priors have also shown to encourage sparsity in the inferred parameters, e.g., the horseshoe prior (Carvalho, 2010), double-exponential with an exponential mixing density (Carlin and Polson, 1991; Hans, 2009), and normal-gamma (Griffin and Brown, 2010).

The SBL has several significant advantages for sparse recovery, compared with the most widely used methods within the non-Bayesian framework, e.g., the l_1 regularization technique and Orthogonal Matching Pursuit. The SBL closely resembles the l_0 regularization which typically results in a more sparse solution with high accuracy than the l_1 regularization. For SBL, the global minimum is achieved at the maximally sparse solution, which is a desirable property of the l_0 regularization (Wipf and Rao, 2004). Moreover, when the sensing matrix does not satisfy the incoherence criteria, the performance of most existing CS algorithms will degrade, while the SBL still retains excellent ability for sparse recovery (Wipf, 2011).

Although Bayesian probabilistic approach has been introduced and applied to structural damage identification for nearly two decades, SBL has seldom been utilized and explored in SHM and structural damage detection. Huang *et al*. (2014) reported that the SBL algorithm suffered from a robustness problem. When the number of measurements was considerably smaller than the number of unknown model parameters, sub-optimal solutions were obtained during the optimization process with large reconstruction errors. In this regard, they developed a stochastic optimization and successive relaxation for optimization of the hyperparameters to enhance the robustness. The signal reconstruction robustness and accuracy in CS increased significantly using the proposed method.

Huang and Beck (2015) and Huang *et al*. (2017a) proposed the hierarchical SBL framework for damage detection. A hierarchical Bayesian model combined with Laplace's asymptotic approximation was used to infer the sparse stiffness reductions on the basis of experimentally identified modal parameters in a way that was consistent with the Bayesian Ockham razor. An iterative procedure, which involved a series of

coupled linear regression problems, was developed to deal with the nonlinear eigenvalue problem.

Huang *et al*. (2017b) used two Gibbs sampling algorithms to efficiently sample the posterior PDF of the uncertain parameters. Compared with the Laplace approximation, the proposed GS methods were able to provide a fuller treatment of the posterior uncertainty. Huang *et al*. (2018) presented a general Bayesian system identification framework based on full Gibbs sampling procedure and SBL. The concept of ARD was incorporated through a likelihood function in their improved SBL method. Moreover, an improved Gibbs sampling procedure for SBL was developed to characterize the full posterior uncertainty rather than just using maximum a posteriori (MAP) values of the hyperparameters.

Multi-task learning is a useful tool for exploiting informative relationships or data redundancy. Huang *et al*. (2018a) presented a multi-task SBL method utilizing multiple groups of measurements. Two hierarchical Bayesian models for multitask SBL were presented and a shared sparseness-inducing ARD prior across multiple tasks was assigned. To obtain higher learning robustness, the precision parameters of the prediction error were also marginalized in the hierarchical models instead of merely finding its MAP value. It has been shown that the proposed multi-task SBL approach improved both learning robustness and uncertainty quantification of the sparse approximation. Huang *et al*. (2018b) proposed a two-stage damage identification method based on the fractal dimension analysis and multi-task SBL. The Higuchi's fractal dimension based and Katz's fractal dimension based damage indices were introduced. The multi-task SBL technique was employed to infer the damage localization vector, which incorporated the sparsity of structural damage as the prior information.

A complete review on the recent development of SBL for structural damage detection and assessment was also provided in Huang *et al*. (2018).

2.5 Challenges in Vibration-based Damage Detection

The vibration-based damage detection methods as well as their pros and cons have been reviewed. The applicability and effectiveness of different available techniques depend on the type of damage and structures to be detected and the test conditions (Chandrashekhar and Ganguli, 2009). There is not a universal methodology which is able to identify any type of damage for various different structures. Additionally, little existing algorithm is capable of predicting the remaining service life of the structure, which is regarded as Level 4 of structural damage detection.

Although the vibration-based damage detection has been investigated extensively over the past decades, there are still some challenging issues to be addressed in this area:

1) Most of the damage detection methods are not sensitive to initial tiny damage in structures. Since structural damage is typically a local phenomenon, it may not significantly influence the low-order modal properties of the structure that are typically available during vibration tests (Farrar *et al*., 2001). In practice, it would be always difficult to excite higher modes of the structure due to the limitation of the input energy (Alvandi and Cremona, 2006).
2) Environmental conditions, such as temperature and humidity, may have a severe effect on structural vibration properties. The changes of modal parameters caused by the environmental variations may mask the changes due to structural damage and then cause false damage identification. Therefore, how to remove the environmental effects should be considered for accurate damage detection. A reliable damage detection method, which is robust to environmental effects, is required.
3) Many existing algorithms depend on the analytical model or baseline data for structural damage detection. However, the analytical model may not be an accurate representation of the target structure, especially for large-scale structures. For example, approximation of boundary conditions, lumping of the distributed parameter system, lacking of the damping representation, and inadequate modeling of joints and couplings may cause considerable errors in the FE model.
4) During the vibration test, the measured data are inevitably contaminated by noise, which may significantly influence the damage detection results (Alvandi and

Cremona, 2006). In addition, some problems associated with the dynamic testing, such as the number and layout of sensors, and consistency and reliability of the testing procedures should be taken into consideration.

5) Civil structures are generally large in size and contain a large number of components, while the number of available vibration measurements is limited. Therefore, the vibration-based damage detection problem is underdetermined in the presence of infinite solutions. Moreover, the identification of structural damage is essentially an inverse problem in mathematics and is typically ill-posed. Due to the nature of the ill-posed problem, a small perturbation in the input data (e.g., the measurement noise) will be amplified and thus leads to a significant change in the solution (Engl *et al*., 1996).

In summary, there is a pressing need to develop more accurate and reliable methods for structural damage detection using only a few vibration measurement data.

CHAPTER 3

NUMERICAL AND EXPERIMENTAL EXAMPLES

3.1 Introduction

This chapter will introduce the numerical and experimental examples together for convenience, which will be employed in the subsequent chapters. The numerical examples, including a planar truss and a cantilever beam, are used to investigate the accuracy and robustness of the proposed damage detection methods. Three experimental structures, i.e., a cantilever beam, a three-storey frame, and a six-bay frame, serve to verify the effectiveness and applicability of the proposed methods for damage detection.

3.2 Numerical Examples

3.2.1 A Planar Truss

A 6-bay planar truss as shown in Figure 3.1 is simply supported and consists of 31 bar elements and 14 pin joints, resulting in 25 DOFs in total. The total length and height of the truss is 9.00 m and 1.50 m, respectively. The diagonal bar is 2.12 m long. The cross section of each bar is a square with the dimension of 0.05 m. The mass density and Young's modulus are 2.77×10^3 kg/m^3 and 7.0×10^{10} N/m^2, respectively.

The damage is simulated by the reduction of Young's modulus of the bar element, or reduction of the axial stiffness while mass remaining unchanged. As shown in Figure 3.1, element No.3 is assumed to be damaged by 50%. It is assumed that the complete mode shapes at all 25 DOFs are available in the undamaged and damaged states. The first six natural frequencies and MAC of the undamaged and damaged structure are listed in Table 3.1. It can be seen that mode No.3 is not sensitive to the simulated

damage. The MAC indicates the similarity between the experimental and numerical mode shapes and is defined as follows

$$MAC(\boldsymbol{\phi}_i, \boldsymbol{\phi}_{di}) = \frac{\left|\boldsymbol{\phi}_i^T \boldsymbol{\phi}_{di}\right|^2}{(\boldsymbol{\phi}_i^T \boldsymbol{\phi}_i)(\boldsymbol{\phi}_{di}^T \boldsymbol{\phi}_{di})} \tag{3.1}$$

where $\boldsymbol{\phi}_{di}$ is the *i*th mode shape of the damaged structure. The value of MAC is bounded between zero and one. An MAC value of one indicates that the two vectors are exactly the same, whereas a value of zero represents that two vectors are orthogonal.

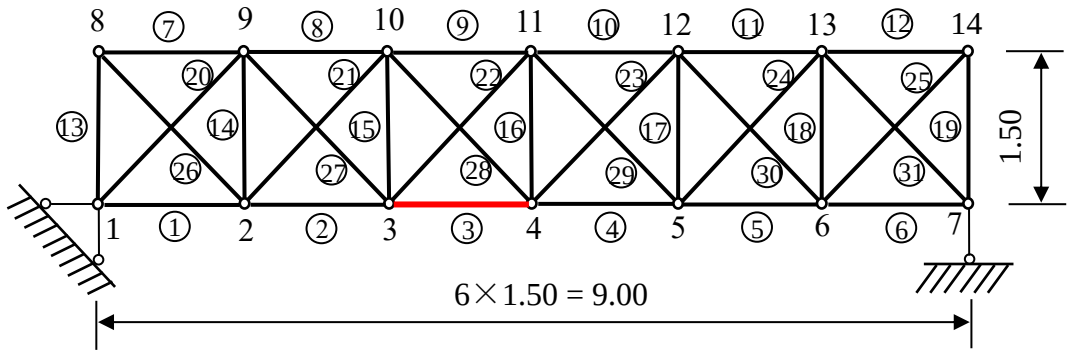

Figure 3.1 Geometric configuration of the truss structure (unit: m)

Table 3.1 Modal data of the truss in the undamaged and damaged states.

Mode	Undamaged	Damaged	
	Freq. (Hz)	Freq. (Hz)	MAC (%)
1	36.92	34.50 (–6.55)	99.79
2	77.11	76.00 (–1.44)	99.80
3	135.59	135.52 (–0.06)	99.98
4	226.36	217.90 (–3.74)	98.58
5	253.52	252.95 (–0.22)	99.42
6	364.15	361.33 (–0.77)	87.06
Average		–2.26	99.51

Note: Values in parentheses are the frequency change ratios (%) between the damaged and undamaged states.

3.2.2 A Cantilever Beam

A cantilever beam (Figure 3.2) is 900 mm long, 50.75 mm wide, and 6.0 mm thick. The mass density and Young's modulus are 7.67×10^3 kg/m^3 and 7.0×10^{10} N/m^2 ,

respectively. The beam is modeled with 45 equal Euler–Bernoulli beam elements, each 20 mm long. Damage is simulated by the reduction of the bending stiffness while mass remains unchanged. As shown in Figure 3.2, the clamped end and mid-span of the beam are assumed to be damaged by 50%, corresponding to element Nos. 1 and 23, respectively. For this numerical example, the natural frequencies only are used for damage detection. The first six natural frequencies of the beam before and after damage are listed in Table 3.2.

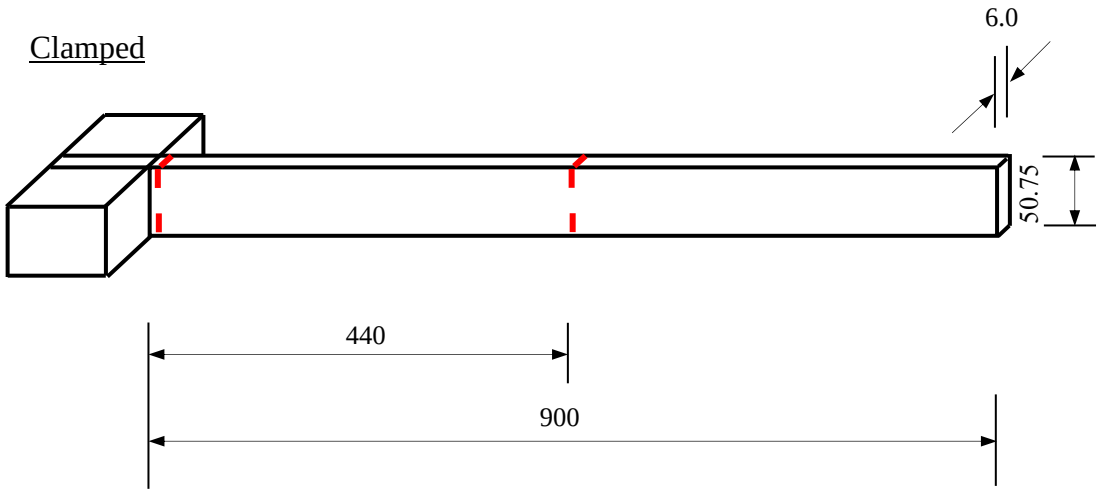

Figure 3.2 Geometric configuration of the beam structure (unit: mm)

Table 3.2 Frequencies of the beam in the undamaged and damaged states.

Mode no.	Undamaged Freq. (Hz)	Damaged Freq. (Hz)	Change ratio (%)
1	6.02	5.75	−4.56
2	37.75	35.67	−5.50
3	105.73	102.44	−3.11
4	207.25	197.69	−4.61
5	342.70	333.96	−2.55
6	512.07	492.45	−3.83
Average of frequency change (%)			−4.03

3.3 Experimental Examples

3.3.1 Experimental Instruments

The Bruel & Kjaer accelerometers were used to measure the acceleration signals during the laboratory tests. It is a type of single axis piezoelectric accelerometer, which has small dimension and excellent anti-interference ability. The applicable frequency range of the accelerometers is from 0.1 Hz to maximum 7 kHz. It is especially applicable for low frequency vibration measurement. The operating temperature range is −74°C~250°C. The accelerometer has a magnetic base which enables itself to be directly mounted on the metallic structures.

The signal amplifier employed in the experiments was Bruel & Kjaer 2962, consisting of four modular channels (Figure 3.3a). Each modular channel is equivalent to a four-stage amplifier including the input amplifier, lowpass filter amplifier, integrator amplifier, and output amplifier. The test oscillator, overload detector, and power supply unit are integrated together in this system.

The EDX-100A data acquisition system made by Kyowa Electronic Instruments was used to record the acceleration data (Figure 3.3b) and the LAN (or USB) port enables online data transfer to PC. EDX-100A consists of 16 channels and has a sampling rate of 10 kHz. The operating temperature range of this recorder is 0 to 50°C and the storage temperature range is −20°C to 60°C.

A hammer was employed in the laboratory tests to produce excitation to the experimental models due to its convenience. The specification of the hammer is listed in Table 3.3 and the rubber tip was used during the test. The overview of the instruments utilized in the experiments is shown in Figure 3.4.

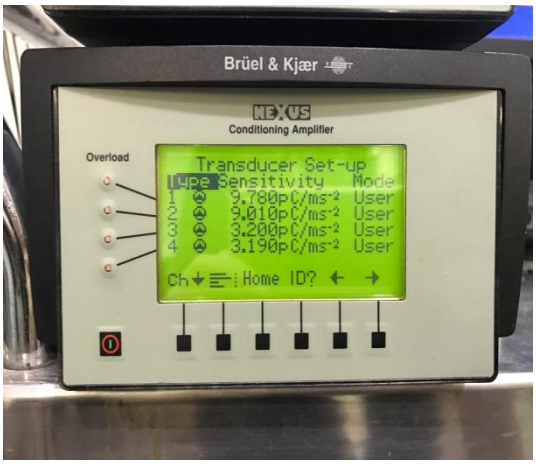

(a) Signal amplifier (Bruel & Kjaer 2962)

(b) Data acquisition board (EDX-100A)

(c) Hammer

Figure 3.3 Experimental instruments

Table 3.3 Specification of the hammer.

Sensitivity (pC/N)	4	
Max. shock force (kN)	60	
Head diameter (mm)	30	
Head mass (g)	300	
Usable frequency range	Steel tip	10 kHz
	Aluminum tip	3 kHz
	Nylon tip	2 kHz
	Rubber tip	500 Hz

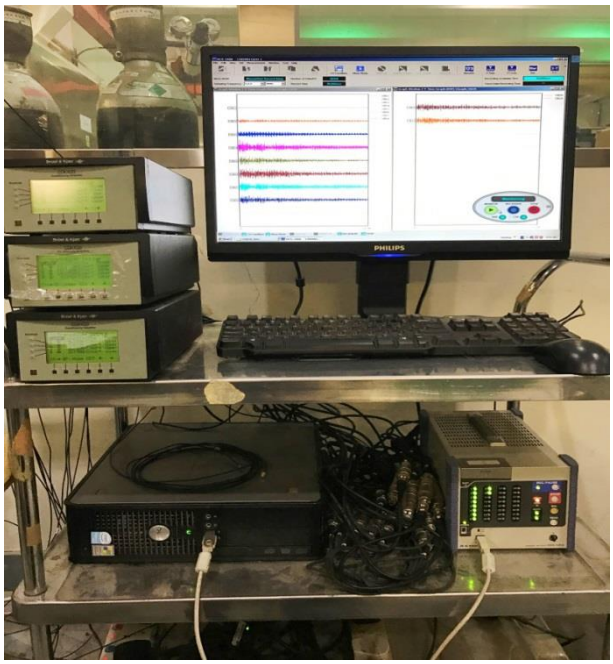

Figure 3.4 Instruments used in the experiment

3.3.2 A Cantilever Beam

The first laboratory example is a steel cantilever beam as shown in Figure 3.5. The total length of the beam is 1000 mm, and the size of the cross section is 49.60 mm ×5.0 mm. The mass density and Young's modulus are estimated as 7.67×10^{3} kg/m^{3} and 2.0×10^{11} N/m^{2}, respectively.

Figure 3.5 Overview of the beam structure

A series of modal testing was conducted on the intact beam. During the laboratory test, 10 accelerometers were mounted on the beam to measure the acceleration responses to the impact force from the instrumented hammer. The measurement points were chosen

every 100 mm (Figure 3.6). The axial deformation of the beam is negligible; thus, only the out-of-plane horizontal vibration was measured.

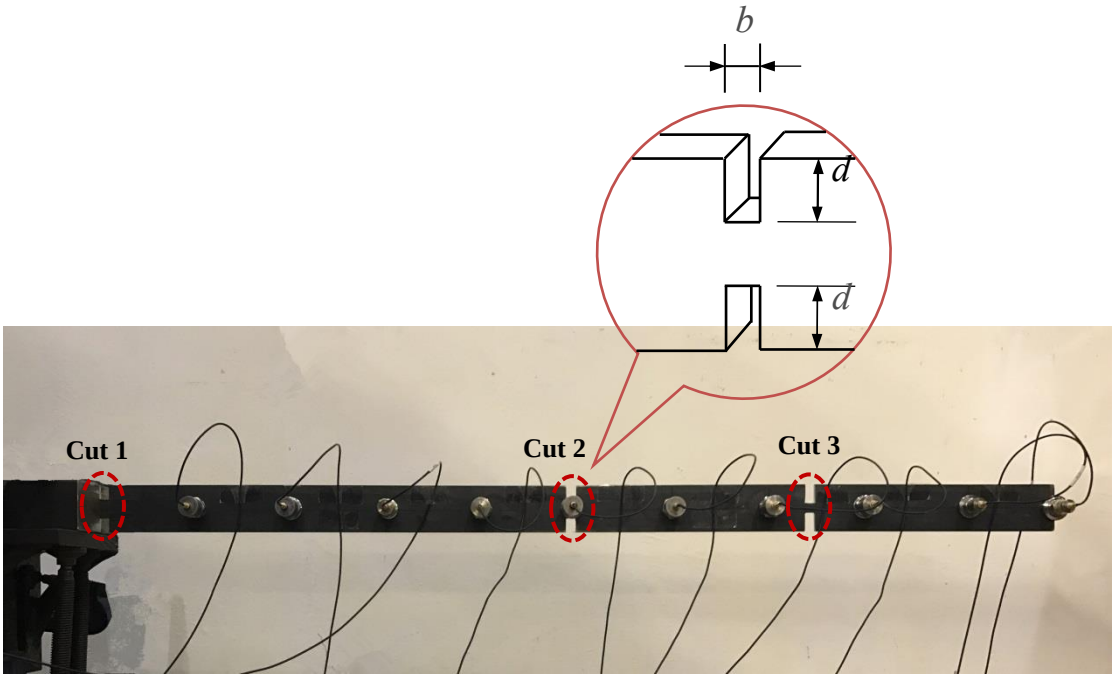

Figure 3.6 Locations of accelerometers and simulated damage

The sampling frequency was 2000 Hz, which is adequate for the tested model (the frequency range of interest is about 0~300 Hz). The structure was impacted ten times for average purpose to improve the modal identification accuracy. Each impact lasted for 60 seconds. After completing the test, modal analyses were performed on the input force and output accelerations with the DIAMOND software (Doebling *et al.*, 1997). For one typical measurement set, the input and output time histories, and the corresponding power spectral density, FRF function, and coherence function are shown in Figure 3.7~3.11. The first six frequencies and mode shapes were extracted using the rational fraction polynomial (RFP) method (Formenti and Richardson, 2002) and are illustrated in Figure 3.12.

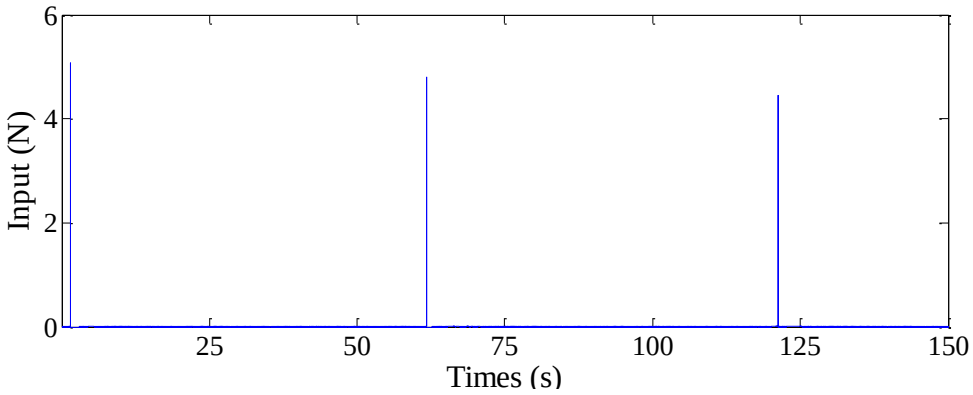

Figure 3.7 Input force time history

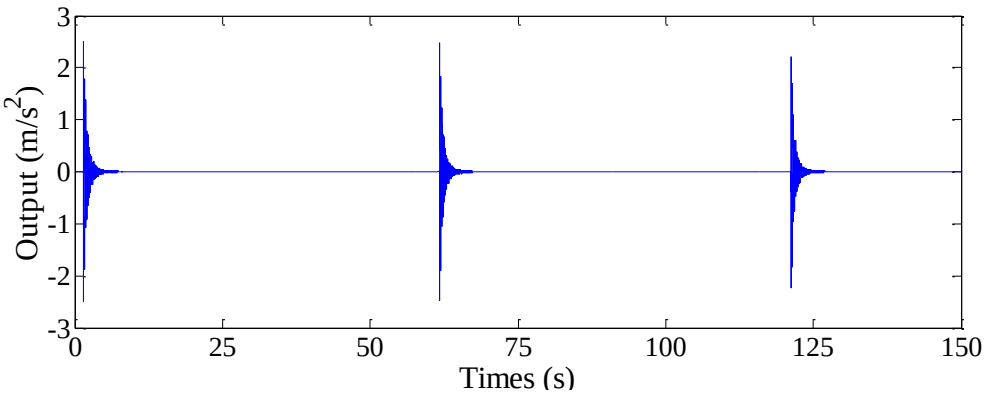

Figure 3.8 Acceleration response time history

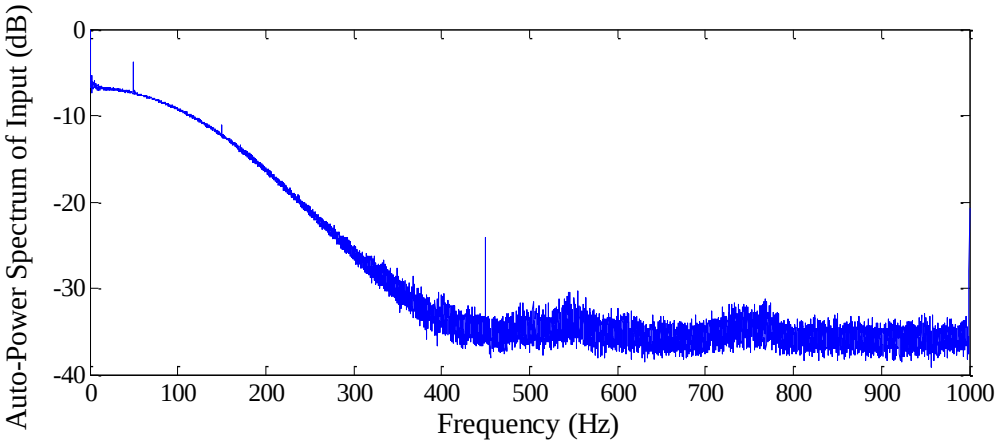

Figure 3.9 Auto-power spectral density of the input force

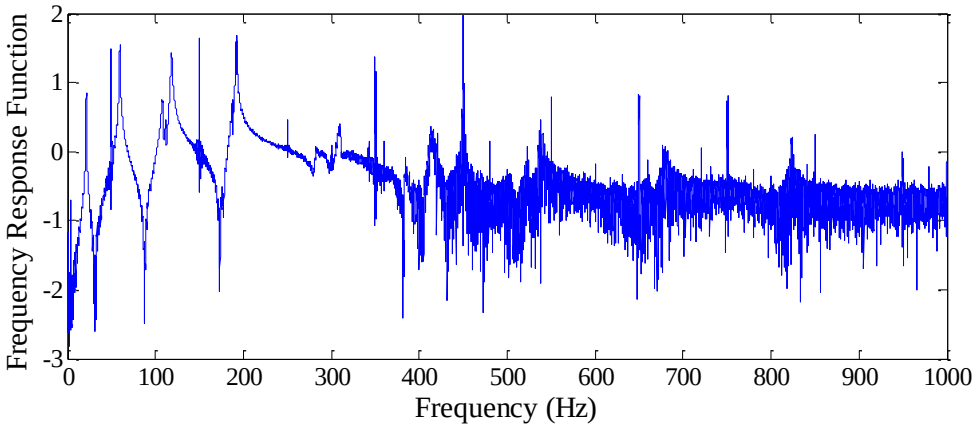

Figure 3.10 Magnitude of FRF

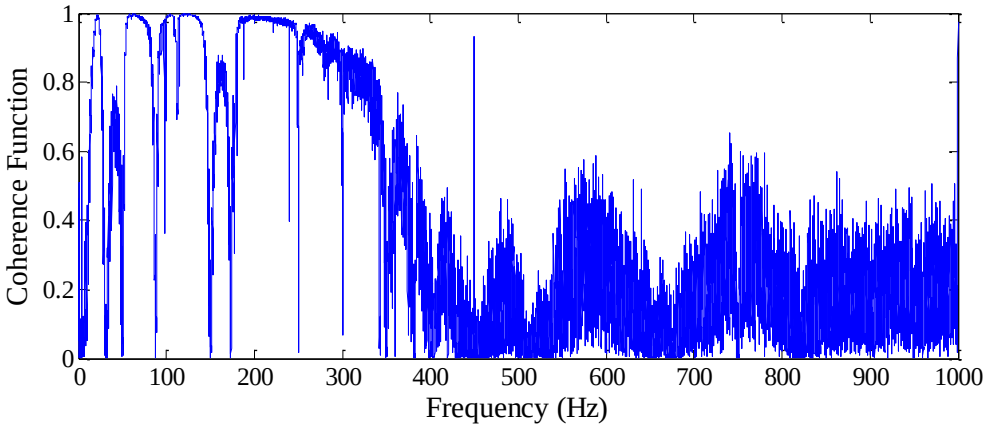

Figure 3.11 Coherence function

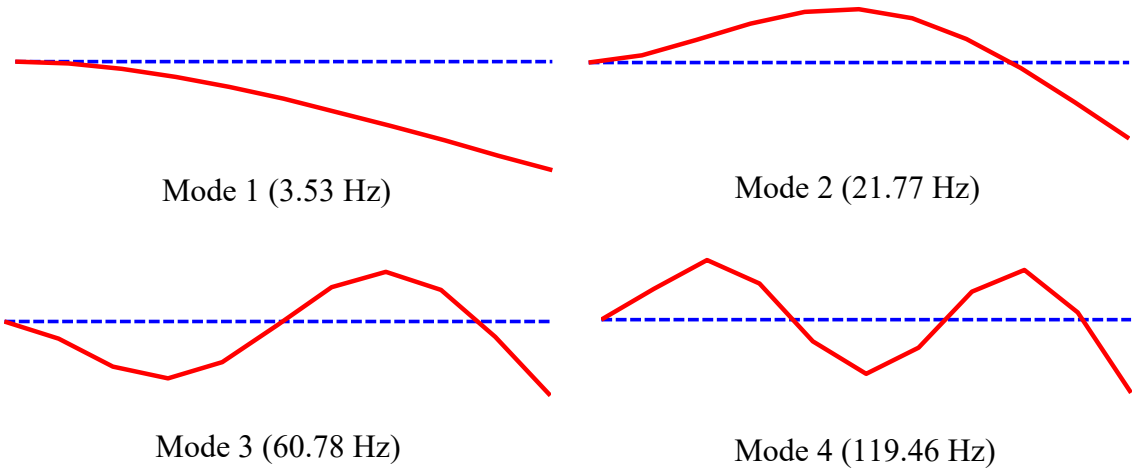

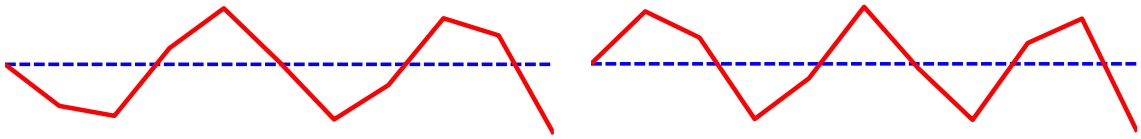

Mode 5 (194.78 Hz) Mode 6 (292.82 Hz)

Figure 3.12 Measured frequencies and mode shapes of the beam strucuture in the undamaged state

Three saw cuts were then sequentially introduced into the beam model (Figure 3.6). The cuts have the same length b = 10 mm but varied depth for simulating different damage severities. Cut 1 at the clamped end was introduced with a depth of d = 10 mm (damage scenario 1, or DS1), representing 40% damage of the cut section. The depth of cut 1 was then increased to d = 15 mm (DS2). Cuts 2 and 3 were successively introduced with depth d = 15 (DS3) and 20 mm (DS4), respectively. The modal testing procedures were repeated for each DS. The frequencies and mode shapes of the damaged states were extracted accordingly (Table 3.4). The natural frequencies experience more significant changes compared with the mode shapes. The maximum averaged change in frequencies is 8.04% with the accumulation of damage, whereas the mode shapes almost remain unchanged, especially for the first four modes.

Table 3.4 Modal data of the beam in the undamaged and damaged states.

Mode	Undamaged	DS1		DS2		DS3		DS4	
	Freq. (Hz)	Freq. (Hz)	MAC (%)	Freq. (Hz)	MAC (%)	Freq. (Hz)	MAC (%)	Freq. (Hz)	MAC (%)
1	3.53	3.49 (−1.24)	99.99	3.38 (−4.41)	99.97	3.33 (−5.91)	99.98	3.36 (−4.91)	99.99
2	21.77	21.39 (−1.72)	99.95	20.85 (−4.26)	99.84	20.29 (−6.81)	99.86	19.76 (−9.22)	99.95
3	60.78	59.46 (−2.16)	99.88	58.93 (−3.04)	99.83	58.38 (−3.95)	99.57	54.37 (−10.55)	99.60
4	119.46	118.31 (−0.96)	99.88	116.01 (−2.88)	99.51	113.35 (−5.12)	99.23	106.31 (−11.01)	99.06
5	194.78	191.98 (−1.44)	99.78	188.74 (−3.10)	99.17	188.46 (−3.25)	98.87	187.17 (−3.91)	99.14
6	292.82	281.56 (−3.84)	98.07	286.76 (−2.07)	94.95	275.08 (−6.06)	98.26	267.45 (−8.66)	97.26
Average (%)		(−1.90)	99.59	(−3.29)	98.88	(−5.18)	99.30	(−8.04)	99.17

Note: Values in parentheses are the frequency change ratios (%) between the damaged and undamaged states.

3.3.3 A Three-storey Frame

The second laboratory example is a three-storey steel frame as shown in Figure 3.13. The bottom supports of the columns were welded on a thick plate, which was fixed on the strong floor in order to model the fixed boundary condition of the frame. The overall height of the frame is 1.5 m and each story is of the same height of 0.5 m. The span of the beam is also 0.5 m. The beams and columns have the same cross section dimension as 75.0×5.0 mm^2. The mass density of the frame is 7.92×10^3 kg/m^3 and the Young's modulus is estimated as 2.0×10^{11} N/m^2.

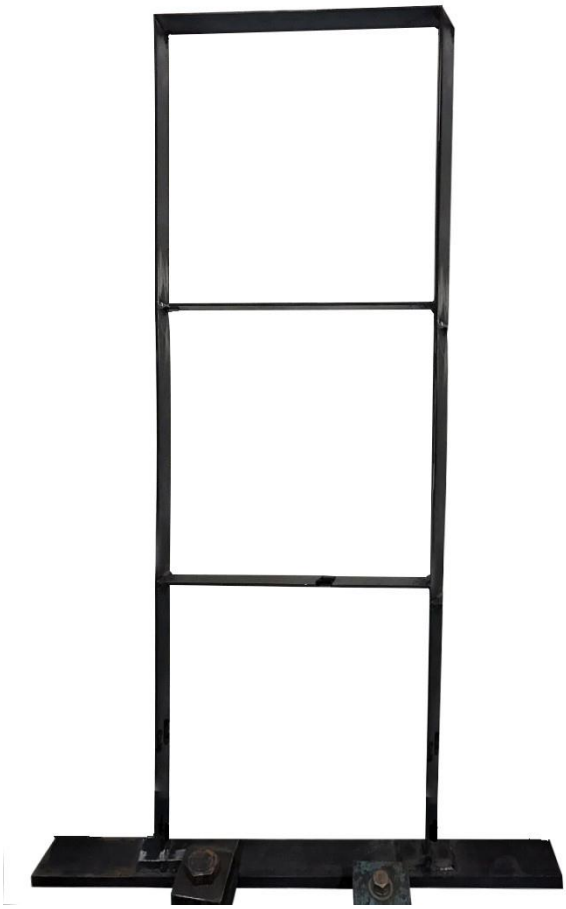

Figure 3.13 Overview of the frame structure

The modal testing was first conducted in the intact state of the frame. The sampling frequency was set as 2000 Hz since the frequency range of interest is about 0~100 Hz. In order to obtain the complete mode shapes of the whole frame, the measurement

points were chosen every 100 mm. Due to the high axial stiffness, the horizontal responses of the points on the beam are identical. Therefore, there were total 39 measurement points as illustrated in Figure 3.14. For the measurement points on the beam and columns, the horizontal and vertical accelerations were measured, respectively. Since there are only nine accelerometers available (Figure 3.15), five sets of experiments were employed with the accelerometers moving along the frame and the hammer remaining unchanged. The measured FRFs of all measurement points were combined together to obtain the complete mode shapes. Additional masses with the same weight as the accelerometers were employed as the dummy sensors as illustrated in Figure 3.15, in order to keep the mass of the model unchanged during the entire testing as the real sensors moved around.

The frame was excited with an instrumented hammer. The direction and location of the excitation point are shown in Figure 3.14. In each set of tests, the structure was impacted eight times and each impact lasted for 30 seconds. After completing the test, the measured input and output time histories were analysed with the DIAMOND software (Figure 3.16 and Figure 3.17). The obtained power spectral density, FRF function, and coherence function are displayed in Figure 3.18~3.20. The first eight frequencies and mode shapes in the range of 0~300 Hz were extracted using the RFP method and are illustrated in Figure 3.21.

The damage was introduced by saw cuts at both sides of the cross section. Two cuts were sequentially introduced to the frame model (Figure 3.14), corresponding to two DSs. Cuts 1 and 2 were located at the column end and the beam/column joint, both are critical locations of the frame structure. The enlarged Cut 1 is shown in Figure 3.22. The saw cuts have the same length b = 20 mm and depth of d = 22.5 mm, leading to the reduction of the moment of inertia of the cut sections by 60%. For each damage case, the aforementioned modal testing was repeated and the measurement points, layout of sensors and added masses, sampling frequency, impact location, impact times, and the length of recording time were exactly the same as those in the undamaged state. The frequencies and mode shapes of damaged states were extracted accordingly. The first eight frequencies and MAC of the frame structure before and after damage are listed in Table 3.5. With the accumulation of damage, the natural frequencies of the structure

decrease, so do the MAC values. In addition, the changes in natural frequency are small (maximum average change of 2.32%), while the changes in the mode shape are more significant with low MAC values.

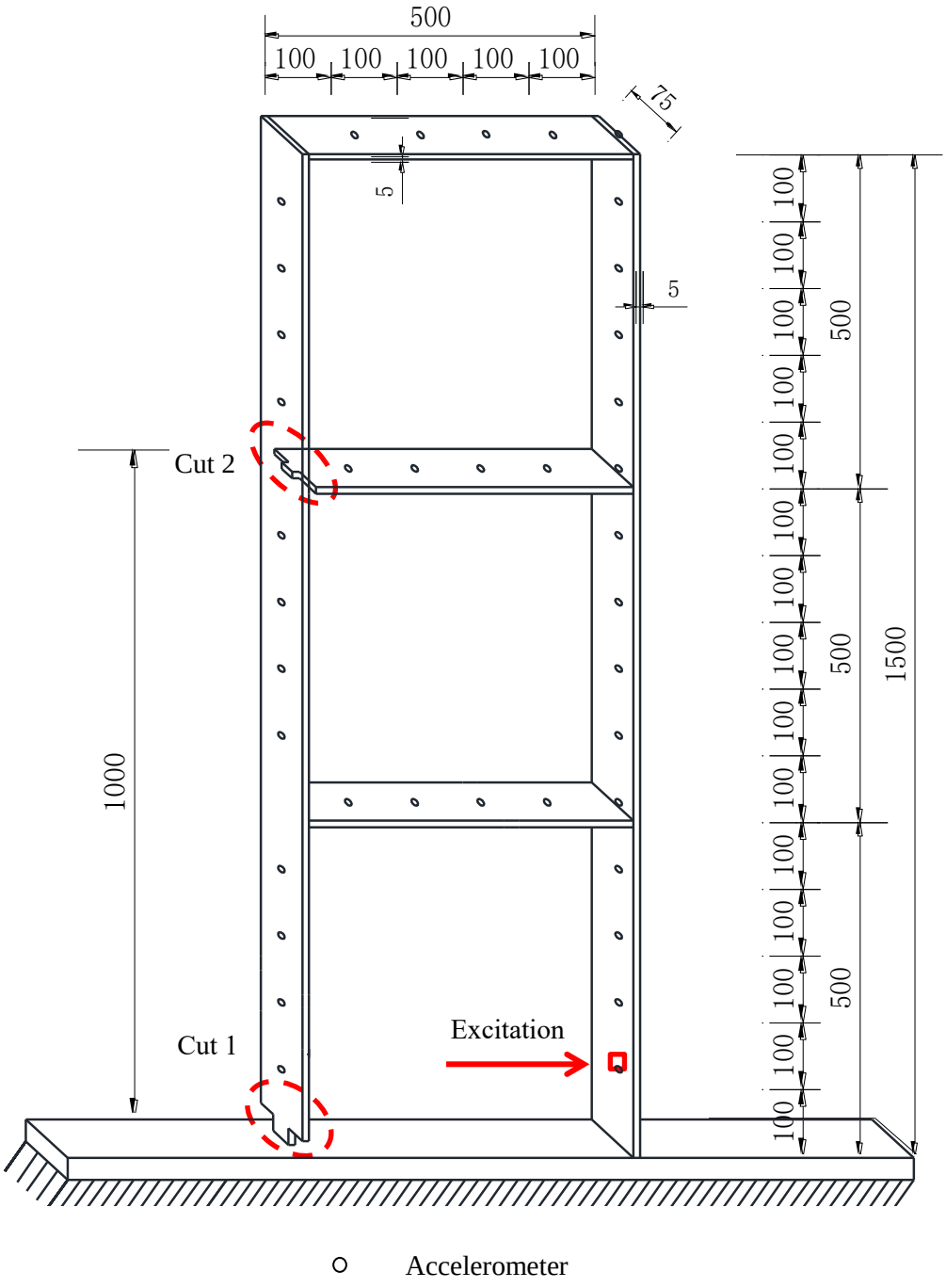

Figure 3.14 Locations of accelerometers and simulated damage (Unit: mm)

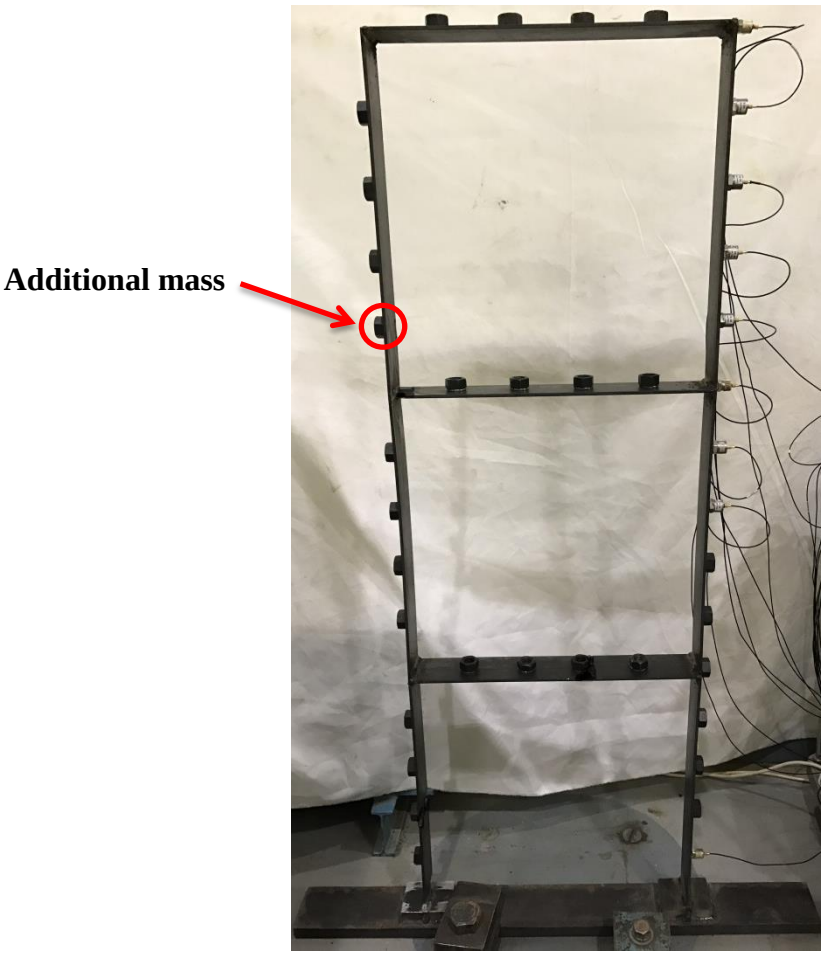

Figure 3.15 Layout of accelerometers and added mass

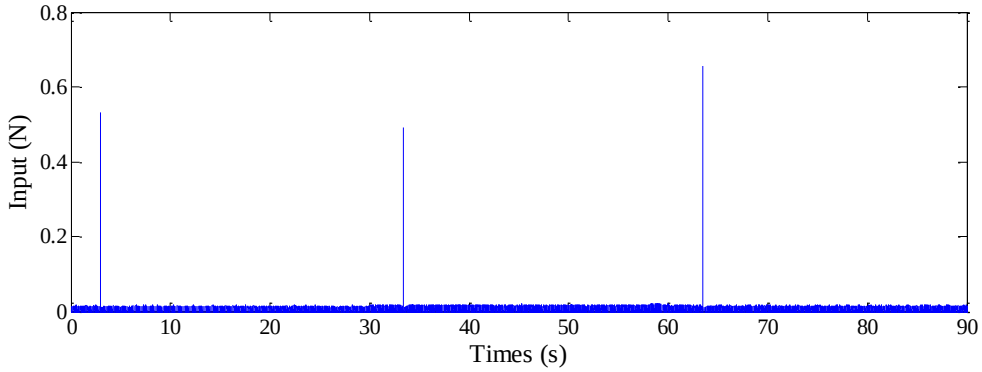

Figure 3.16 Input force time history

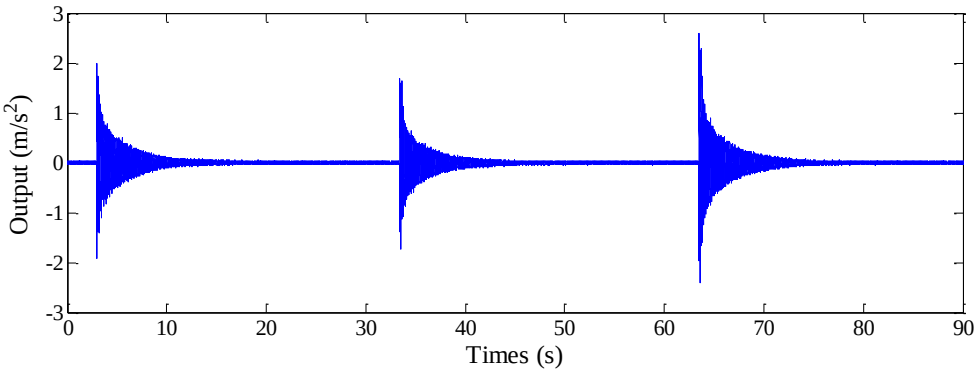

Figure 3.17 Acceleration response time history

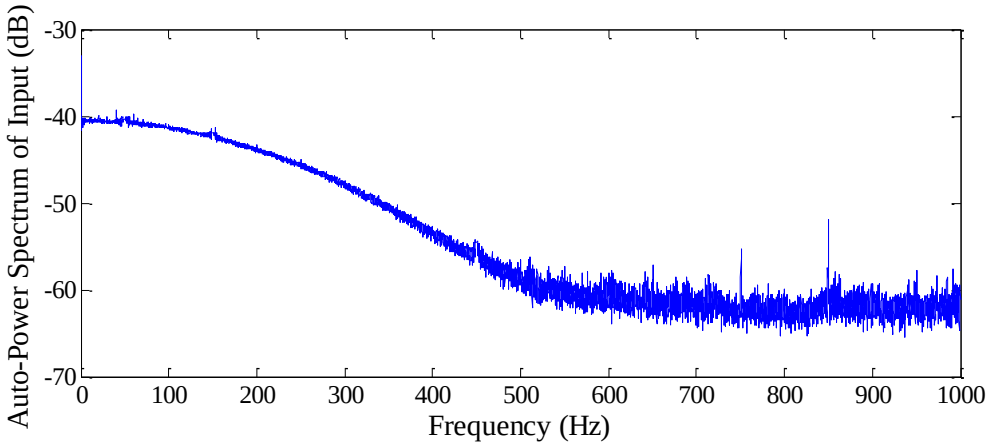

Figure 3.18 Auto-power spectral density of the input force

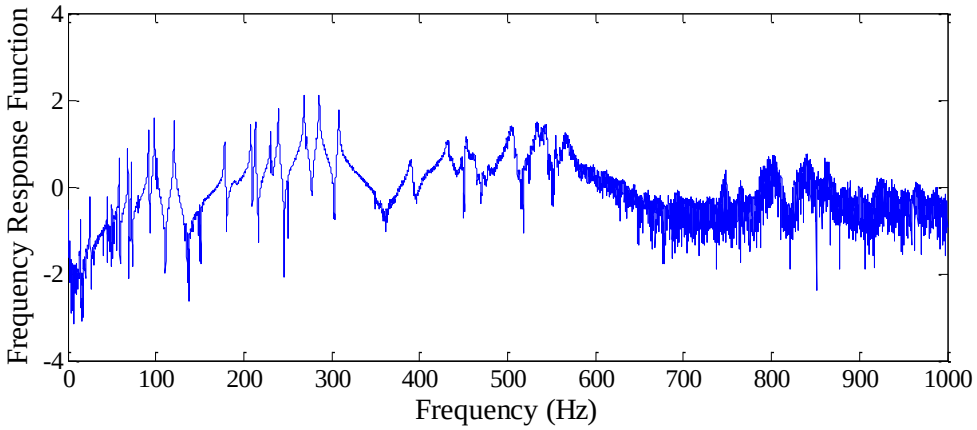

Figure 3.19 Magnitude of FRF

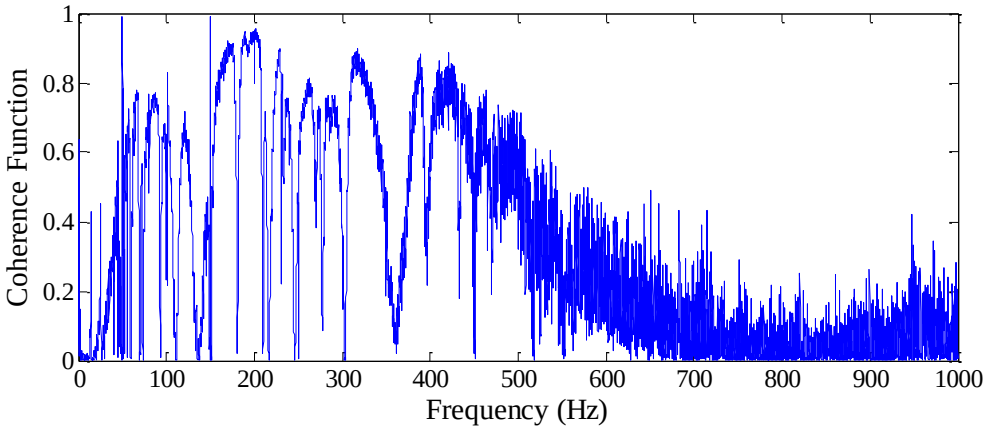

Figure 3.20 Coherence function

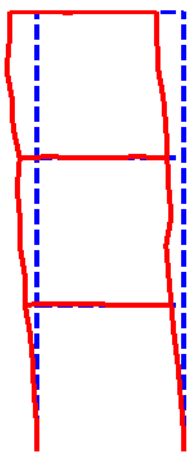

Mode 1 (4.23 Hz)

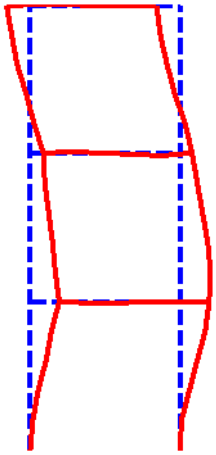

Mode 2 (14.03 Hz)

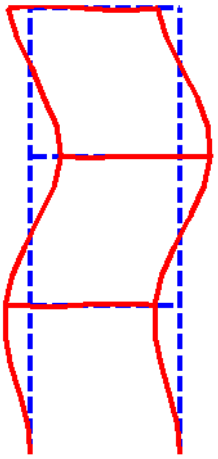

Mode 3 (25.45 Hz)

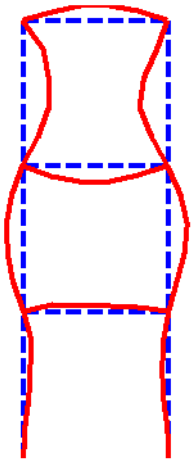

Mode 4 (44.81 Hz)

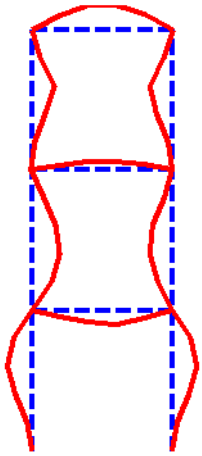

Mode 5 (58.12 Hz)

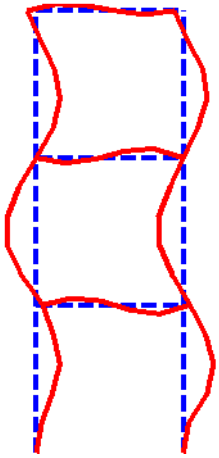

Mode 6 (68.36 Hz)

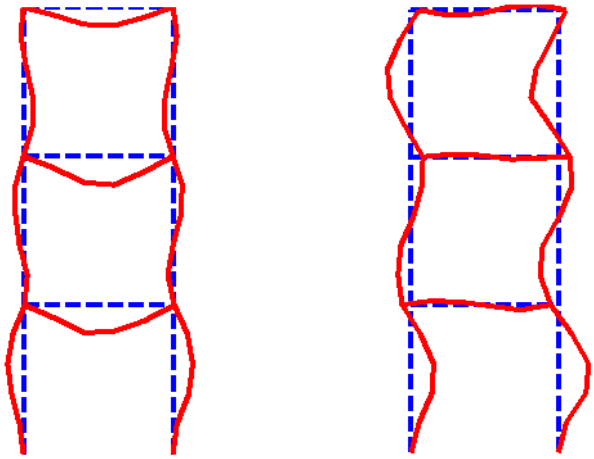

Mode 7 (72.27 Hz) Mode 8 (91.73 Hz)

Figure 3.21 The measured frequencies and mode shapes of the frame structure in the undamaged state

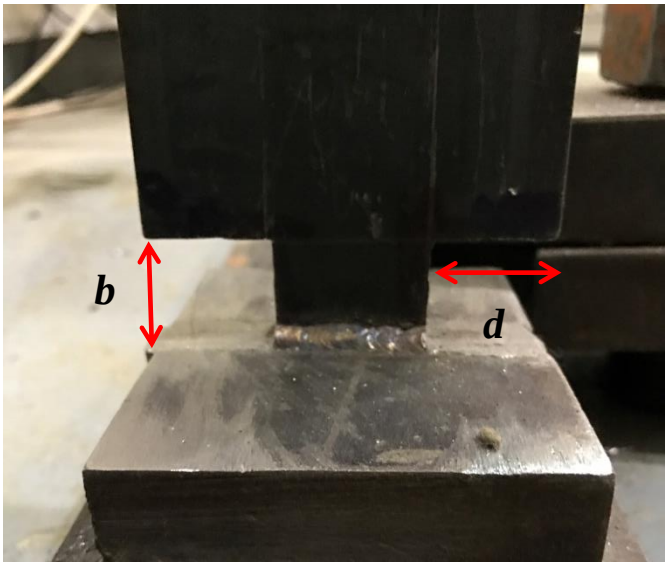

Figure 3.22 Configuration of cut 1

Table 3.5 Modal data of the frame in the undamaged and damaged states.

Mode	Undamaged	DS1		DS2	
no.	Freq. (Hz)	Freq. (Hz)	MAC (%)	Freq. (Hz)	MAC (%)
1	4.23	4.13 (−2.31)	92.02	4.08 (−3.53)	95.78
2	14.03	13.75 (−1.96)	99.02	13.45 (−4.11)	97.49
3	25.45	25.14 (−1.19)	98.87	25.13 (−1.23)	99.01
4	44.81	44.70 (−0.23)	94.74	44.69 (−0.27)	97.59
5	58.12	57.39 (−1.24)	92.45	57.28 (−1.44)	91.46
6	68.36	67.34 (−1.49)	93.01	66.11 (−3.29)	88.14
7	72.27	72.06 (−0.28)	96.30	71.42 (−1.18)	85.80
8	91.73	89.14 (−2.83)	86.79	88.51 (−3.52)	76.38
Average		(−1.44)	94.15	(−2.32)	91.46

Note: Values in parentheses are the frequency change ratios (%) between the damaged and undamaged states.

3.3.4 A Six-bay Frame

The third experimental example is a 3D frame as shown in Figure 3.23. The frame consists of six bays with a total length of 3.0 m. Three end nodes of the structure are cast into a mass concrete block, which is fixed on the strong floor using four steel bolts to model the fixed boundary condition. The frame structure consists of 45 bars and 20 nodes in total (Figure 3.24). The bars are alloy steel tubes and the dimensions and material properties are listed in Table 3.6. All bars are connected by Meroform ball nodes through M12 bolts (Figure 3.25), which are fastened using a torque wrench. The weights of the M12 bolt and the Meroform ball node are 74 g and 234 g, respectively.

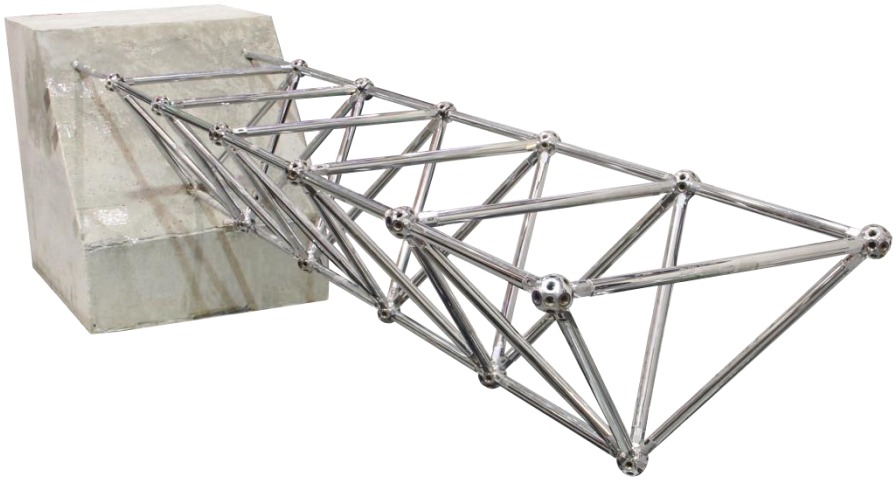

Figure 3.23 Overview of the frame structure

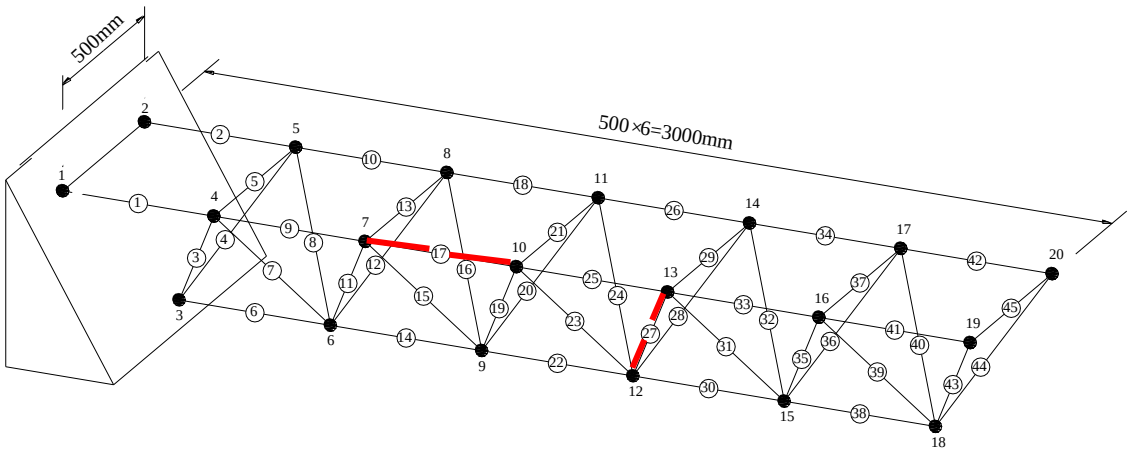

Figure 3.24 Configuration of the frame structure

Table 3.6 Bars used in the frame model.

Length	500 mm
Outer diameter (D)	22 mm
Inner diameter (d)	21 mm
Young's modulus (E)	2.10×10^{11} N/m^2
Mass density (m/V)	7850 kg/m^3

A vibration test was first conducted on the intact structure. The frame was excited by the instrumented hammer and the acceleration responses were measured by the accelerometers. As shown in Figure 3.25, the accelerometers were mounted on the Meroform ball node through a magnetic base. Since the axial deformation is negligible, the accelerations in the lateral and vertical directions of each node (excluding the supports) were measured, resulting in 34 DOFs available in the mode shapes of the frame.

Figure 3.25 Accelerometer at the Meroform ball node

Since the frequency range of interest is from 0 to 100 Hz, the sampling frequency was set as 2000 Hz. Each test lasted for 60 seconds. DIAMOND software was used for processing the excitation and time history responses (Figure 3.26 and Figure 3.27). The power spectral density, FRF function, and coherence function for one measurement set are displayed in Figure 3.28~3.30. The first six frequencies in the range of 0~100 Hz and the associated mode shapes were extracted using the RFP method (Figure 3.31). Mode Nos. 1, 2, and 4 are all torsion modes in the lateral direction, while mode Nos. 5 and 6 are bending modes in the lateral direction, and mode No. 3 is the bending mode in the vertical direction.

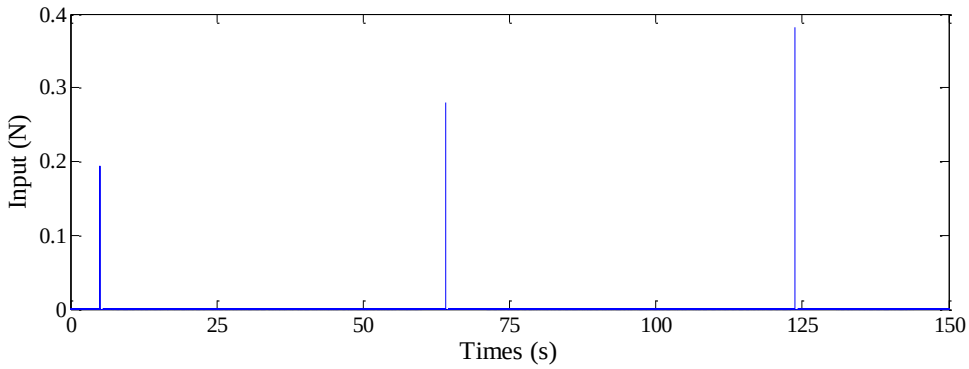

Figure 3.26 Input force time history

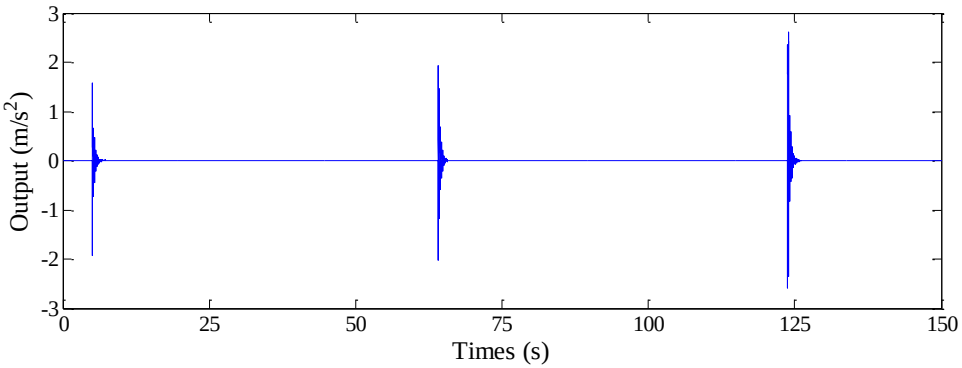

Figure 3.27 Acceleration response time history

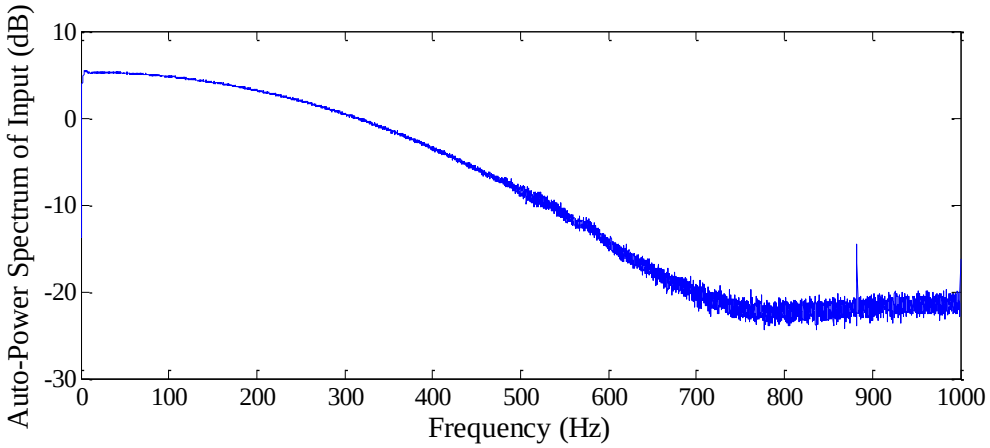

Figure 3.28 Auto-power spectral density of the input force

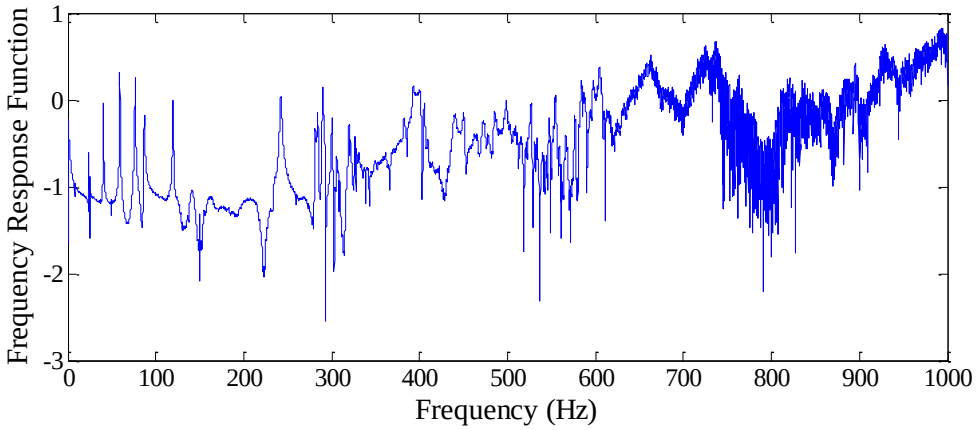

Figure 3.29 Magnitude of FRF

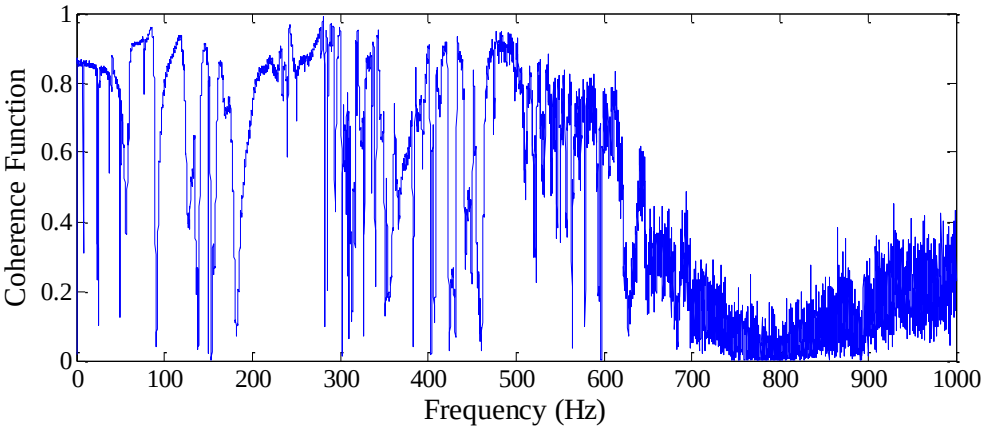

Figure 3.30 Coherence function

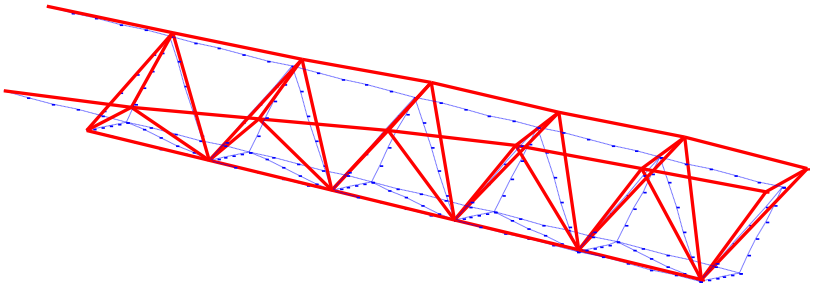

Mode 1 (7.73 Hz)

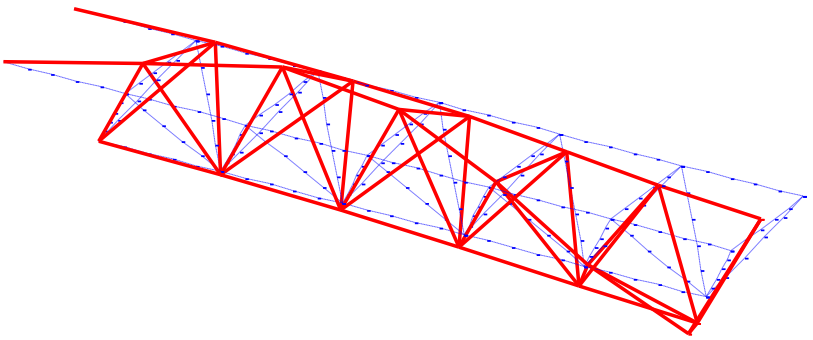

Mode 2 (23.98 Hz)

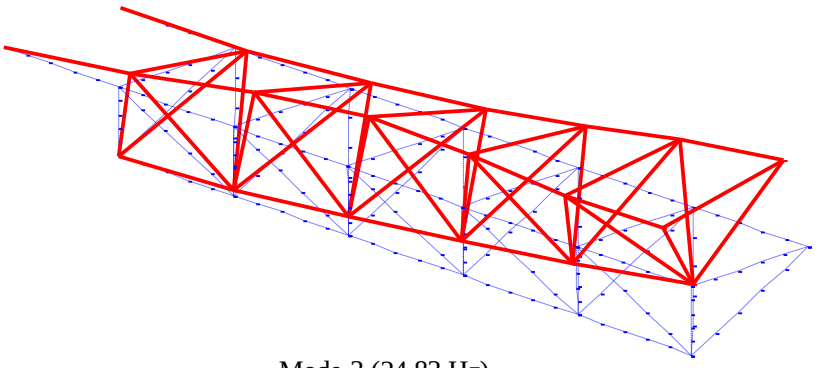

Mode 3 (24.83 Hz)

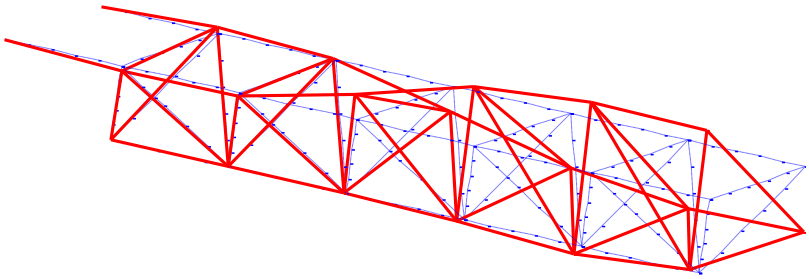

Mode 4 (37.43 Hz)

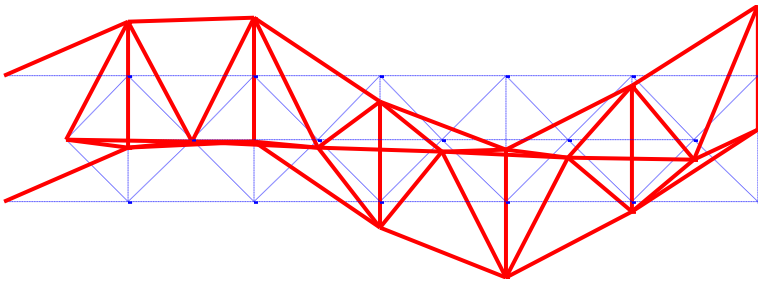

Mode 5 (40.92 Hz)

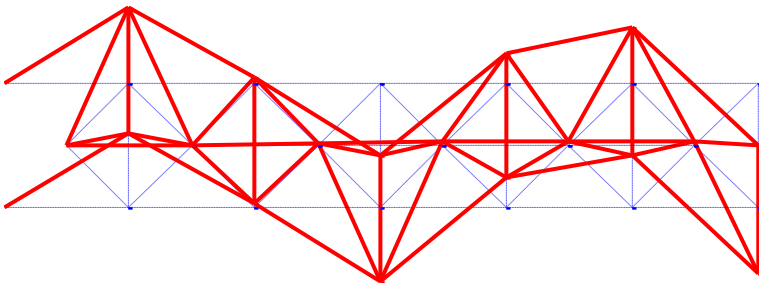

Mode 6 (59.97 Hz)

Figure 3.31 Measured frequencies and mode shapes of the three-dimensional frame in the undamaged state

For steel structures, the joints, e.g., welds or bolts, are the most critical parts for the overall safety (Mehrjoo *et al*., 2008). The failure of most steel structures is caused by the damage of joints. Therefore, the safety of joints is essential to steel structures (An *et al*., 2013). In this regard, four DSs are simulated including damage in bars and joints of the frame model, as listed in Table 3.7. In DS1, Bar No.17 is damaged by replacing the original tube with one made of thinner thickness. After the replacement, all the connection bolts were checked and fastened to the original torsional moment (i.e., 30 Nm) to ensure the structural connections unchanged before and after damage was introduced. In DS2, a joint damage was simulated by loosening the bolt connecting Bar No.27 and Node No.13. Two more severe damage cases, DS3 and DS4, were subsequently introduced.

Table 3.7 Four DSs for the frame structure.

Scenario	Description
DS1	Bar No.17 is damaged by replacing the original tube with a damaged one
DS2	Bar No.27 is damaged by loosening the bolt near Node 13
DS3	Bar No.27 is damaged by loosening the bolts at two ends
DS4	DS1+DS3

For each DS, the modal testing was similarly conducted and the frequencies and mode shapes of the damaged states were extracted accordingly as listed in Table 3.8. It can be seen that the changes in natural frequencies are very small especially for DS1 and DS2, while the changes in the mode shapes are more significant with low MAC values.

Table 3.8 Modal data of the frame in the undamaged and damaged states.

Mode	Undamaged	DS1		DS2		DS3		DS4	
	Freq. (Hz)	Freq. (Hz)	MAC (%)	Freq. (Hz)	MAC (%)	Freq. (Hz)	MAC (%)	Freq. (Hz)	MAC (%)
1	7.73	7.70 (−0.30)	91.51	7.71 (−0.22)	98.23	7.68 (−0.67)	81.30	7.66 (−0.81)	92.30
2	23.98	23.93 (−0.21)	99.74	23.93 (−0.23)	99.62	23.79 (−0.80)	58.72	23.87 (−0.45)	88.30
3	24.83	24.69 (−0.56)	99.44	24.69 (−0.56)	98.81	24.06 (−3.12)	80.19	24.25 (−2.34)	83.34
4	37.43	36.96 (−1.27)	89.96	37.28 (−0.42)	80.65	36.93 (−1.34)	81.73	35.66 (−4.73)	81.06
5	40.92	40.71 (−0.53)	97.64	40.83 (−0.24)	99.97	40.56 (−0.88)	84.35	40.45 (−1.16)	98.99
6	59.97	59.65 (−0.53)	97.54	59.86 (−0.18)	98.80	59.10 (−1.45)	82.35	59.20 (−1.27)	96.31
Average		(−0.57)	95.97	(−0.31)	96.01	(−1.38)	78.11	(−1.79)	90.05

Note: Values in parentheses are the frequency change ratios (%) between the damaged and undamaged states.

CHAPTER 4

STRUCTURAL DAMAGE DETECTION BASED ON L_1 REGULARIZATION TECHNIQUE

4.1 Introduction

Conventional vibration-based damage detection methods employ the Tikhonov regularization in model updating to deal with the problems of underdeterminacy and measurement noise. However, the Tikhonov regularization tends to provide over smooth solutions that the identified damage is distributed to many structural elements. This result does not match the sparsity property of the actual damage scenario, in which structural damage typically occurs at a small number of locations only in comparison with the total elements of the entire structure. In this study, an l_1 regularization-based model updating technique is developed by utilizing the sparsity of structural damage.

For all regularization problems, the regularization parameter, which controls the trade-off between data fidelity and solution size, exerts a crucial effect on the solution. However, since the l_1 regularization problem has no closed-form solution, the associated regularization parameter is usually selected by experience. In this regard, two strategies of selecting the regularization parameter for the l_1-regularized damage detection problem have been proposed. The first method utilizes the residual and solution norms of the optimization problem and ensures that they are both small. The other method is based on the discrepancy principle (DP), which requires that the variance of the discrepancy between the calculated and measured responses is close to the variance of the measurement noise.

4.2 Sparse Regularization Technique

For the sparse recovery problem introduced in Section 2.3, the unknown vector $\boldsymbol{\theta}$ could be obtained by minimizing the following least-squares loss function

$$\widehat{\boldsymbol{\theta}} = \arg\min_{\widehat{\boldsymbol{\theta}}} \|\boldsymbol{X\theta} - \boldsymbol{y}\|_2^2 \tag{4.1}$$

Since the regularization technique is effective in coping with the ill-posed and underdetermined problem, a regularization term is introduced to the objective function in order to obtain a unique and reasonable solution

$$\widehat{\boldsymbol{\theta}} = \arg\min_{\widehat{\boldsymbol{\theta}}} \|\boldsymbol{X\theta} - \boldsymbol{y}\|_2^2 + \beta\|\boldsymbol{\theta}\|_p^p \tag{4.2}$$

where β is the regularization parameter. The residual norm $\|\boldsymbol{X\theta} - \boldsymbol{y}\|_2^2$ is the data-fitting term which measures the data fidelity, while $\|\boldsymbol{\theta}\|_p^p$ $(p \geq 0)$ is the regularization term (or solution norm) reflecting the expection of the solution to be found. The value of p is determined by the prior information about $\boldsymbol{\theta}$ corresponding to different regularization techniques. For $p > 0$, the l_p norm is defined as

$$\|\boldsymbol{\theta}\|_p = \left(\sum_{i=1}^{N} |\theta_i|^p\right)^{\frac{1}{p}} \tag{4.3}$$

For $p = 0$, the l_0 norm is obtained as the limit for $p \to 0$

$$\|\boldsymbol{\theta}\|_0 = \lim_{p\to 0} \|\boldsymbol{\theta}\|_p^p = \lim_{p\to 0} \left(\sum_{i=1}^{N} |\theta_i|^p\right) \tag{4.4}$$

That is, the l_0 norm is equal to the number of non-zero entries of the vector. It should be noted that for $0 \leq p < 1$, the resulting function does not define a true norm, since it violates the properties defined for a norm.

When $p = 2$, the corresponding technique is called Tikhonov regularization (or l_2 regularization), which is the most commonly used approach of regularization (Tikhonov, 1963). It is also known as ridge regression in statistics. The objective function takes the following form

$$\widehat{\boldsymbol{\theta}} = \arg\min_{\widehat{\boldsymbol{\theta}}} \ \|\boldsymbol{X\theta} - \boldsymbol{y}\|_2^2 + \beta\|\boldsymbol{\theta}\|_2^2 \tag{4.5}$$

This optimization problem has a closed-form solution as

$$\widehat{\boldsymbol{\theta}} = (\boldsymbol{X}\boldsymbol{X}^T + \beta\boldsymbol{I})^{-1}\boldsymbol{X}^T\boldsymbol{y} \tag{4.6}$$

where $\boldsymbol{I}$ is the identity matrix. The Tikhonov regularization has received widely applications since it has a closed-form solution with low computation complexity. Moreover, as the solution of the optimization problem is continuous with respect to β, there are tractable methods for choosing the regularization parameter. The main drawback of the Tikhonov regularization is that it has limited resolution and cannot recover sharp features of the unknown vector. Consequently, it results in an over smooth solution.

The regularization term $\|\boldsymbol{\theta}\|_p^p$ for different values of p is plotted in Figure 4.1, which shows the individual contribution of each entry of $\boldsymbol{\theta}$ to the l_p norm $\|\boldsymbol{\theta}\|_p^p$. It can be seen that the curve of l_2 norm is convex. For $|\theta| \leq 1$ in our problems, as θ approaches one, the corresponding $\|\theta\|_2^2$ becomes dominant in the objective function. Accordingly, the optimization algorithm will concentrate on the large terms by penalizing them to get smaller such that the overall misfit is reduced (Theodoridis *et al*., 2012). For the Tikhonov regularization, strong features are penalized more severely compared to weak features and thus a smooth solution is provided. It is obvious that the Tikhonov regularization is not applicable to sparse recovery problems. Alternative norms in place of the l_2 norm which have the sparsifying effect are required.

In order to preserve sparsity of the unknown vector, the penalty on strong features should be lowered. As shown in Figure 4.1, the curves of l_p-quasi-norms $(0 < p < 1)$

are nonconvex. The contributions of small values of $\boldsymbol{\theta}$ to the regularization term $\|\boldsymbol{\theta}\|_p^p$ could not be neglected. The components of $\|\boldsymbol{\theta}\|_p^p$ with small values of $\boldsymbol{\theta}$ can still have a say during the optimization process and can be penalized by being pushed to smaller values. Strong features are penalized less severely as compared with the l_2 norm. In particular, the l_0 norm, which counts the number of non-zero elements in the vector, is the extreme case. Only the components of $\|\boldsymbol{\theta}\|_0$ that could considerably minimize the objective function will be kept and the rest will be forced to zero. Therefore, the l_p regularization with $0 \leq p < 1$ has sparsity-preserving property and is suitable for sparse signal recovery (Theodoridis *et al.*, 2012). Unfortrunately, for $0 \leq p < 1$, the corresponding nonconvex optimization problem is NP-hard. Solving this NP-hard problem requires a combinatory search over all possible subsets of $\boldsymbol{\theta}$, and is thus computationally infeasible for large scale problems since the computational complexity is of exponential dependence on the dimension of $\boldsymbol{\theta}$ (Chartrand and Staneva, 2008; Natarajan, 1995). Moreover, the global optimal solution cannot be obtained for the nonconvex optimization problem (Chartrand and Yin, 2008). Due to these limitations, the l_p regularization ($0 \leq p < 1$) has not received widely applications in sparse signal recovery.

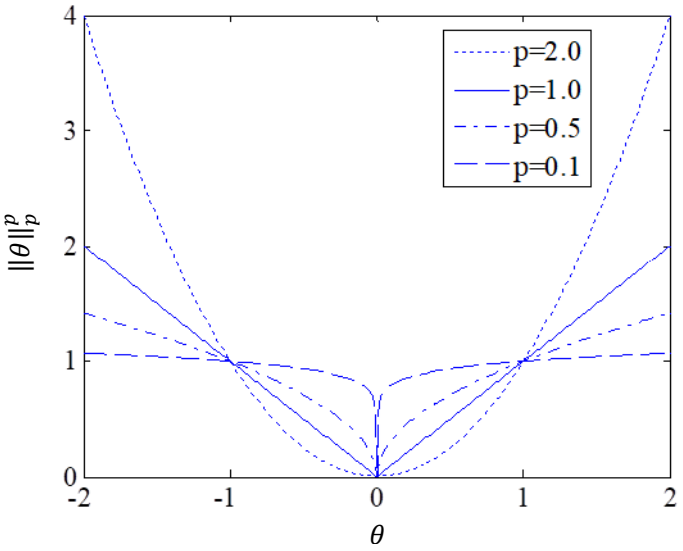

Figure 4.1 $\|\boldsymbol{\theta}\|_{\boldsymbol{p}}^{\boldsymbol{p}}$ for different values of p

For all the true norms ($p \geq 1$), only the l_1 norm retains relatively large values for $|\theta| < 1$ and is the closest to the l_p-quasi-norms (Figure 4.1). It has been proved

mathematically that the l_p regularization techniques with $0 \leq p \leq 1$ all favor sparsity in the solution (Candes *et al*., 2008). Although the l_p regularization ($0 \leq p < 1$) could provide a sparser solution, the l_1 regularization is convex and could be solved effectively via linear programming approaches (Boyd and Vandenberghe, 2004). The l_1 regularization technique has been empolyed to promote sparsity for a long time and attracted considerable interest in the past decades. Some researchers proposed that, under certain conditions, the l_1 regularization is equivalent to the l_0 regularization with high probability (Candès and Tao, 2006; Donoho, 2006b). The l_1 regularization is formulated as follows

$$\widehat{\boldsymbol{\theta}} = \arg\min_{\widehat{\boldsymbol{\theta}}} \ \|\boldsymbol{X\theta} - \boldsymbol{y}\|_2^2 + \beta\|\boldsymbol{\theta}\|_1 \tag{4.7}$$

Although the objective function in Equation (4.7) is convex, it is not differentiable and thus does not have a closed-form solution (Boyd and Vandenberghe, 2004).

4.3 Damage Detection using l_1-regularized Model Updating

Civil structures are generally large in size and contain a large number of components. However, the number of available vibration measurements is limited resulting in an underdetermined problem in mathematics. To this end, most previous studies employ super-elements in numerical modelling and model updating. For example, in the study by Hao and Xia (2002), several saw cuts each with 25 mm long were introduced to a portal frame to simulate damage. Euler-Bernoulli beam elements each with 100 mm long were used in the FE model and damage was represented by the stiffness reduction of the damaged elements. As the elements are significantly longer than the cuts, a cut of 80% section reduction causes a small stiffness reduction in the corresponding element and there has been no quantitative relation between the cut size and the element stiffness reduction. Consequently, the simulated damage cannot be quantified.

Another difficulty in structural damage detection is that the problem is essentially an inverse problem and is typically ill-posed. Therefore, measurement noise will be amplified and leads to inaccurate damage identification. In this regard, most vibration-based damage detection methods employ the Tikhonov regularization (or l_2

regularization) to deal with this problem (Ahmadian *et al*., 1998; Weber *et al*., 2009; Li and Law, 2010). As introduced above, the Tikhonov regularization tends to force all non-zero coefficients in the solution. Consequently, damage identification results are distributed to many structural elements, most of which are falsely identified as damage (Zhou *et al*., 2015; Zhang and Xu, 2016; Hou *et al*., 2018).

In practice, structural damage usually occurs in a few sections or members only especially at the early stage. For example, structural early damage tends to appear in some column ends or the mid-span of beams where the maximum stresses are located. For steel structures, fatigue damage usually occurs at a few fatigue-critical members only. The small number of damage locations can be treated as sparsity as compared with the total elements of the entire structure. Structural damage sparsity is an important prior information that can be utilized for more accurate damage identification. The minimum-rank approach of directly model updating is the earlier study exploiting the concept of sparsity for structural damage detection. Since structural damage is sparse in the spatial domain, the perturbation matrices of the structural properties tend to be of small rank. Kaouk and Zimmerman (1994) proposed the minimum rank perturbation theory to solve the optimal matrix update problem. The modal force error was expressed by the perturbations to the mass, damping, and stiffness matrices, and eigenvectors based on the structural motion function. A non-zero entry in the modal force error was interpreted as the indication of the location of damage. Doebling (1996) presented the minimum-rank elemental update method for structural damage detection and model refinement. The proposed method computed a minimum-rank solution for the perturbations of the elemental stiffness parameters instead of the global stiffness matrix, while constraining the connectivity of the global stiffness matrix. It was found that the best identification result was obtained when the number of modes used was equal to the expected rank of the elemental stiffness perturbation vector.

In FE model updating based structural damage identification, the stiffness matrix in the undamaged state can be expressed in the following form

$$\boldsymbol{K} = \sum_{i=1}^{n} \alpha_i \boldsymbol{K}^i \tag{4.8}$$

where $\boldsymbol{K}^i$ is the *i*th element stiffness matrix and α_i is the element stiffness parameter, and *n* is the number of elements in the FE model. Under the assumption that only the element stiffness is reduced when damage occurs, the structural stiffness matrix in the damaged state takes the following form

$$\boldsymbol{K}_d = \sum_{i=1}^{n} \tilde{\alpha}_i \, \boldsymbol{K}^i \tag{4.9}$$

where $\tilde{\alpha}_i$ is the element stiffness parameter in the damaged state.

The stiffness reduction factor (SRF) is then defined as (Xia *et al*., 2008; Zhou *et al*., 2015)

$$\theta_i = \frac{\tilde{\alpha}_i - \alpha_i}{\alpha_i} \tag{4.10}$$

The SRF is chosen as the damage parameter and the values of SRF indicate both damage location and damage severity. $\theta_i = 0$ indicates that the *i*th element is intact; while $\theta_i = -1$ means the element is completely damaged. If only a small number of elements are damaged, $\boldsymbol{\theta}$ is a sparse vector with several non-zero items at the damaged locations but with many zeros at others. Damage identification, which aims to induce the sparse damage index $\boldsymbol{\theta}$, becomes a sparse recovery problem. In this regard, the following l_1 regularization instead of the Tikhonov regularization is introduced to the model updating objective function to not only stabilize the ill-posed problem, but also enforce sparsity in the solution.

$$\widehat{\boldsymbol{\theta}} = \arg\min_{\tilde{\boldsymbol{\theta}}} \; \|\boldsymbol{R}^A(\boldsymbol{\theta}) - \boldsymbol{R}^E\|_2^2 + \beta\|\boldsymbol{\theta}\|_1 \tag{4.11}$$

As reviewed in Section 2.3, the vibration-based damage detection methods utilizing the sparsity of structural damage either use natural frequency only or time-history acceleration responses or numerical data. Using the time-domain data for damage identification is not efficient as the calculation of structural responses is time-

consuming. Frequencies are usually not sensitive to local damage and the small frequency changes caused by structural damage tend to be masked by noise in the measurement data. In general, mode shapes could provide spatial information and are thus more sensitive to local damage. Therefore, this study utilizes both natural frequencies and mode shapes in model updating for damage detection. Based on Equation (4.11), the optimization problem is rewritten as

$$\widehat{\boldsymbol{\theta}} = \arg\min_{\widehat{\boldsymbol{\theta}}} \left(\frac{1}{m}\sum_{i=1}^{m}\left[\frac{\lambda_i^A(\boldsymbol{\theta}) - \lambda_i^E}{\lambda_i^E}\right]^2 + \frac{1}{m \times np}\sum_{i=1}^{m}\sum_{j=1}^{np}\left[\phi_{ji}^A(\boldsymbol{\theta}) - \phi_{ji}^E\right]^2 + \frac{\beta}{n}\|\boldsymbol{\theta}\|_1 \right) \tag{4.12}$$

where λ_i and $\boldsymbol{\phi}_{ji}$ are the *i*th eigenvalue and corresponding mode shape at *j*th point, respectively, *np* is the number of measurement points, and subscripts "*A*" and "*E*" represent the items from the analytical model and experiment, respectively. Here the eigenvalue residual, eigenvector residual, and the regularization term are divided by the length of the vectors (i.e., *m*, *m*×*np*, and *n*, respectively) to make these three parts comparable. This optimization problem can be solved using the active set or conjugate gradient algorithms (Body, 2004).

Since mode shapes are dimensionless and may differ by a constant, direct comparison of two mode shape vectors with different scales may cause the results completely incorrect. In this connection, the modes shapes calculated from the FE model should be adjusted such that they are in the same direction and same scale as the measured mode shapes, through multiplying the modal scale factor (MSF) defined as follows (Allemang, 2003)

$$MSF\left(\boldsymbol{\phi}_i^{A0}, \boldsymbol{\phi}_i^E\right) = \frac{\left(\boldsymbol{\phi}_i^{A0}\right)^T \boldsymbol{\phi}_i^E}{\left(\boldsymbol{\phi}_i^{A0}\right)^T \boldsymbol{\phi}_i^{A0}} \tag{4.13}$$

$$\boldsymbol{\phi}_i^A = \boldsymbol{\phi}_i^{A0} \times MSF \tag{4.14}$$

where $\boldsymbol{\phi}_i^{A0}$ is the *i*th calculated mode shape before adjustment.

4.4 Selection Strategies for the Regularization Parameter

In regularization methods, the regularization parameter plays a critical role by trading off the size and fitness of the regularized solution (Hansen, 2001). In general, the regularization parameter β is not known *a priori* and problem dependent. A well-balanced regularization parameter can effectively deal with the ill-posedness of the inverse problem and yield a meaningful and stable solution. A number of methods have been developed to determine the optimal regularization parameter for inverse problems in mathematics. These methods include DP (Phillips, 1962; Morozov, 1966, 2012), ordinary and generalized cross validations (GCV) (Golub *et al*., 1979), universal rules (Mallat, 1999), and min–max rules (Johnstone, 1994). The l_2 regularization has the closed-form solution. As such, tractable methods have been developed (Bauer and Lukas, 2011), such as the widely used L-curve criterion (Hansen, 1992). However, the selection criterion of the regularization parameter for the l_1 regularization problem is very limited since it has no closed-form solution.

In SHM and structural damage detection, an appropriate regularization parameter for the l_1-regularized problem is problem-dependent and typically selected by experience. Mascarenas *et al*. (2013) set the regularization parameter as unit heuristically. Yang and Nagarajaiah (2015) reported the insensitivity of the solution to the regularization parameter and set it as 0.01 in CS-based modal identification. Another study (Yang and Nagarajaiah, 2014a) calculated the regularization parameter using $\beta = 1/\sqrt{N}$ (where N is the number of the time history sampling points corresponding to the dimension of the unknown vector). Zhang and Xu (2016) chose the regularization parameter by using the reweighted l_1 regularization technique. Yao *et al*. (2011) showed that the plot of the residual term versus the regularization term on the linear scale resembled an “L” shape; afterward, they selected the regularization parameter corresponding to the corner of the L curve.

In this study, two strategies are developed for selecting the regularization parameter for the l_1-regularized damage detecetion problem.

4.4.1 Parameter Selection using Residual and Solution Norms

The regularization parameter controls the trade-off between data fidelity and solution sparsity. The 2-norm of the residue $\|\boldsymbol{R}(\boldsymbol{\theta}) - \boldsymbol{R}^E\|_2^2$ evaluates the data fidelity, and the 1-norm $\|\boldsymbol{\theta}\|_1$ measures the sparsity of the solution. Therefore, the residual and solution norms are closely associated with the regularization parameter.

For a small regularization parameter, the optimization algorithm will concentrate on the residual norm $\|\boldsymbol{R}(\boldsymbol{\theta}) - \boldsymbol{R}^E\|_2^2$ in order to reduce the overall misfit effectively. Consequently, the analytical modal parameters are very close to the measured values, leading to an overfitting solution. On the contrary, for a large regularization parameter, the regularization term $\beta\|\boldsymbol{\theta}\|_1$ becomes dominant in the objective function and thus be penalized more severely during the optimization process. Consequently, the residual norm increases, and the result losses data fidelity. Moreover, if β exceeds a threshold β_{max}, a zero solution ($\theta = 0$) is obtained (Koh *et al*., 2007). Therefore, an appropriate regularization parameter β should be between the two extremes and keep these two norms small at the same time in order to obtain a stable and reasonable solution.

In Tikhonov regularization, the L-curve criterion utilized a parametric plot of the solution norm versus the residual norm on the log-log scale to find the optimal regularization parameter (Hansen, 1992). Taking Figure 4.2 for an example, it is a generic L-curve for the Tikhonov regularization and each marked point corresponds to a particular regularization parameter. The corner of the curve is a good choice of the regularization parameter, which results in a small solution norm as well as a small residual norm at the same time. However, this L-shaped curve is not guaranteed for the l_1-regularized problem. For the standard linear optimization problem in Equation (4.2), the shape of the trade-off curve depends on the distribution of singular values of the forward operator $\boldsymbol{X}$ (Malioutov *et al*., 2005). Moreover, since l_1 regularization does not have a closed-form solution, the curvature of the "L-curve" cannot be expressed explicitly. Therefore, it is difficult to locate the corner of the "L-curve" to identify an optimal regularization parameter as that in the Tikhonov regularization. In addition, although the L-curve criterion has been proved to give a reasonable and good parameter choice for many problems, the corner sometimes does not indicate the optimal

regularization parameter. Au (2007) presented a numerical example and constructed the L-curve, in which λ represents the regularization parameter. It had been found that the corner did not give the optimal solution as shown in Figure 4.3 and the presented problem had the best fit elsewhere. Further, he showed that the solutions corresponding to the regularization parameters near the corner all closed to the true solution with adequate accuracy. In this regard, the L-curve of the solution norm versus the residual norm will be used as a preliminary guide for selection of the regularization parameter in this study. Rather than one single value, an appropriate range of the regularization parameter will be determined.

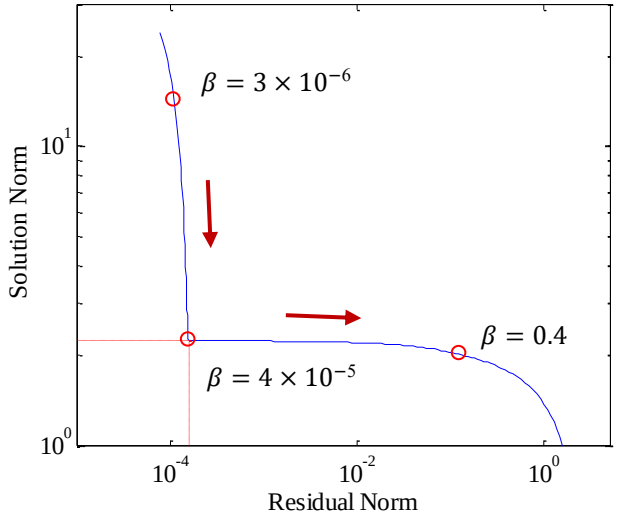

Figure 4.2 The L-curve for a Tikhonov regularization problem

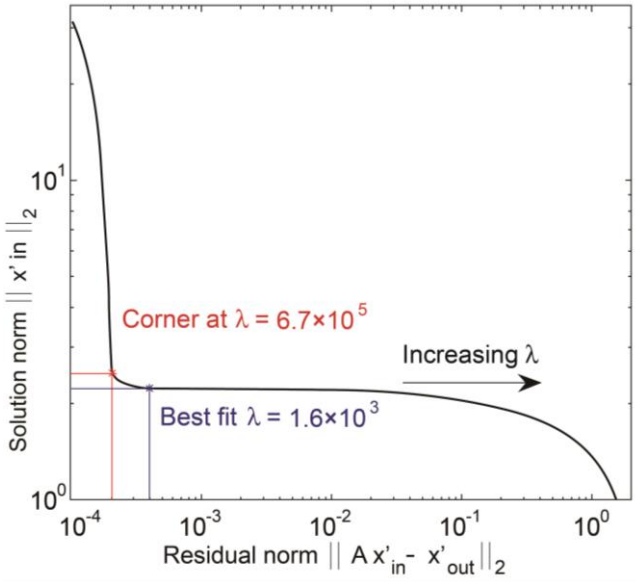

Figure 4.3 L-curve for the Hilbert operator (Ref. Au (2007))

The regularization path is the set of solutions for all values of the regularization parameter (Mairal and Yu, 2012). Previous studies have shown that for the l_1 regularization problem in Equation (4.7), the regularization path is piecewise linear, with a finite number of linear segments (Osborne *et al*., 2000; Efron *et al*., 2004; Rosset and Zhu, 2007). In order to explicitly illustrate the regularization path for l_1 regularization, a simple example is introduced, where $\boldsymbol{X} \in R^{1000\times5}$ is constructed from an orthogonal polynomial basis, $\boldsymbol{\theta} = (1,\ 0,\ 1,\ 0,\ 0)^T$ with two non-zero entries, and $\boldsymbol{\varepsilon}$ is the Gaussian random noise with a zero mean and standard deviation of 30%. Figure 4.4 shows the regularization paths of each entry of $\boldsymbol{\theta}$ ($\theta_i,\ i = 1\sim5$) with respect to the regularization parameter β. The vertical dash lines correspond to the steps along the regularization paths. θ_i approach zero with the increase of β, in the order of $i =$ 4, 2, 5, 1, 3. For any given β, only a subset of the variables have nonzero values. For example, at $\beta = 0.35$, only θ_1, θ_3, and θ_5 remain and are used to construct the predictions of the measurements. The vertical solid line corresponds to the solution that gives the best recovery accuracy as only θ_1 and θ_3 are actually nonzero.

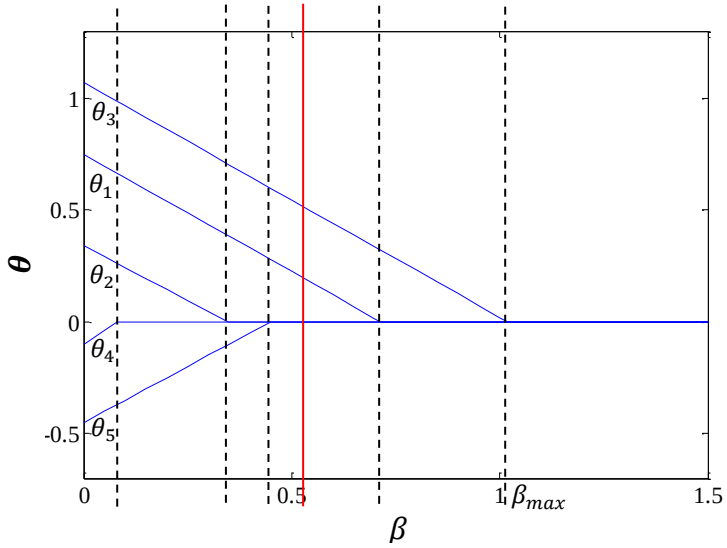

Figure 4.4 Regularization paths of the l_1 regularization problem (Ref. Rosset and Zhu, (2007))

The piecewise linear property of the regularization path has only been proved for linear l_1-regularized problems. Although the present l_1-regularized model updating prolem in Equation (4.11) is nonlinear, it is intuitive that with the increase of β, the undesirable

non-zero variables are forced to zero sequentially, while the actual non-zero variables likely remain. Inspired by this piecewise linear property, in this study, the curves of the residual and solution norms versus the regularization parameter are utilized to determine the appropriate regularization parameter. For a given damage detection problem, the corresponding objective function is first solved over a range of β. The associated residual and solution norms are calculated and plotted versus the regularization parameter. The solution norm decreases, whereas the residual norm increases with an increasing regularization parameter. The optimal regularization parameter should keep these two norms small at the same time. There are breakpoints (also known as kinks in statistics) exist on the curves corresponding to the steps along the regularization paths. The first inflection point with the following step is thus determined as the appropriate range of the regularization parameter. The procedures and results will be illustrated in Section 4.5.

4.4.2 Parameter Selection based on DP

The second strategy is based on the DP used in the l_2 counterpart. The DP has gained wide applications in machine learning and statistics areas for l_2 regularization problems. Lukas (1995) applied the DP for choosing the regularization parameter in a discrete and probabilistic setting and also investigated the asymptotic properties of the estimated regularization parameter. Hämarik and Raus (2006) developed the DP for parameter selection of the Tikhonov regularization with a given error bound of data. Dong *et al.* (2018) utilized the DP to choose the regularization parameter for current distribution reconstruction and compared its performance with the L-curve, the GCV, and the quasi-optimality (QO) criteria. It showed that: 1) the L-curve criterion performed much worse than DP, GCV, and QO; 2) GCV demands enormous computational effort and is not as stable as other parameter selectors; and 3) QO is not applicable to iterative and nonlinear regularization problems. Therefore, when the statistics of the noise could be estimated, the DP is a prime choice since the rationale behind is clear and only the residuals are required to be computed.

Considering the standard l_1-regularized problem in Equation (4.7), the unknown desired solution is denoted by $\widehat{\boldsymbol{\theta}} \in R^N$, which satisfies $\boldsymbol{X}\widehat{\boldsymbol{\theta}} = \boldsymbol{y} - \boldsymbol{\varepsilon}$. Hence,

$$\left\|\boldsymbol{X}\widehat{\boldsymbol{\theta}} - \boldsymbol{y}\right\| = \|\boldsymbol{\varepsilon}\| \tag{4.15}$$

The DP aims to find a regularization parameter $\beta \geq 0$, such that the corresponding solution $\boldsymbol{\theta}_\beta$ satisfies the following equation

$$\left\|\boldsymbol{X}\boldsymbol{\theta}_\beta - \boldsymbol{y}\right\| = \|\boldsymbol{\varepsilon}\| \tag{4.16}$$

Forcing $\boldsymbol{y}_\beta\left(= \boldsymbol{X}\boldsymbol{\theta}_\beta\right)$ exactly the same as $\boldsymbol{y}$ is insensible because $\boldsymbol{y}$ contains error. The reproduced $\boldsymbol{y}_\beta$ should approximate $\boldsymbol{y}$ within the expected value of the error $\boldsymbol{\varepsilon}$ (Phillips, 1962; Morozov, 1966, 2012).

For the vibration-based damage detection problem, the perturbation $\boldsymbol{\varepsilon}$ is primarily attributed to the measurement noise of the modal data. According to the DP, the residual of the modal parameter calculated from a proper regularization parameter should match some statistical characteristics of the noise. The DP could be relaxed as follows considering the existence of uncertainties

$$\left|\left\|\boldsymbol{R}_\beta(\boldsymbol{\theta}) - \boldsymbol{R}^E\right\| - \|\boldsymbol{\varepsilon}\|\right| \leq Tol \tag{4.17}$$

where $\boldsymbol{R}_\beta(\boldsymbol{\theta})$ is the analytical modal parameter calculated from the identified damage state for a particular β.

In this study, the DP is revised to be suitable to the l_1-regularized problem. In practice, the experimentally measured modal data are contaminated by measurement noise, which is generally assumed as a stochastic process (Philips *et al*., 2009; Wu and Law, 2004; Tondreau *et al*., 2011), as shown in the following equation

$$\boldsymbol{R}^E = (1 + \boldsymbol{\varepsilon})\boldsymbol{R} \tag{4.18}$$

where $\boldsymbol{R}$ is the true modal parameter without noise, $\boldsymbol{\varepsilon}\sim N(0,\ \delta^{-1}\boldsymbol{I})$ following the Gaussian distribution, and δ denotes the noise level. The relative discrepancy between the calculated modal data and the measured ones is expressed by the following equation

$$\boldsymbol{D} = \frac{\boldsymbol{R}^E - \boldsymbol{R}_\beta(\boldsymbol{\theta})}{\boldsymbol{R}_\beta(\boldsymbol{\theta})} = \boldsymbol{\varepsilon} \tag{4.19}$$

Therefore, the selection criterion of the regularization parameter ensures that the modal parameter in the identified damage state corresponding to β satisfies the following

$$Var(\boldsymbol{D}) = E\left[\left\|\frac{\boldsymbol{R}^E - \boldsymbol{R}_\beta(\boldsymbol{\theta})}{\boldsymbol{R}_\beta(\boldsymbol{\theta})}\right\|_2^2\right] = E[\ \|\boldsymbol{\varepsilon}\|_2^2] = \delta^2 \tag{4.20}$$

The measurement noise should be estimated in advance by using prior information or through measurements. The implementation process will be explained in detail and demonstrated using the following experimental examples.

4.4.3 A Summary of the Regularization Parameter Selection

For a given damage detection problem, the corresponding objective function is first solved for different β values ranging from 0 to $i \cdot \Delta\beta$ $(i = 0,1,\cdots,n)$, with an increment of $\Delta\beta$. Each β results in one set of damage index $\boldsymbol{\theta}$. The residual norm $\left\|\boldsymbol{R}_\beta(\boldsymbol{\theta}) - \boldsymbol{R}^E\right\|_2^2$ and solution norm $\|\boldsymbol{\theta}\|_1$ are then calculated. Since the regularization parameter may differ by orders for different structures, the calculation range and step size $\Delta\beta$ should be set accordingly.

For the first proposed method, the residual and solution norms versus the regularization parameter are plotted separately to determine the appropriate regularization parameter of which both norm values are small at the same time. If the noise information is available, the DP-based strategy can be utilized. The L-curve of the solution norm versus the residual norm is first used to identify a preliminary range of the regularization parameter. Then, the DP is applied within this possible range to select the appropriate regularization parameter. Finally, the overlapping part of the two selected

ranges is determined as the appropriate range of the regularization parameter. Actually, according to the available data, the two proposed selection strategies can be used individually.

4.5 Case Studies

Two experimental examples described in Chapter 3, i.e., a cantilever beam and a three-storey frame, are used here to demonstrate the effectiveness of the proposed regularization parameter selection and the l_1-regularized damage detection method. A numerical planar truss is employed to investigate the robustness of the proposed method to measurement noise. The effect of the mode number on the damage detection results is also investigated. The advantage of the present l_1 regularization over the traditional l_2 regularization method in damage detection is demonstrated.

4.5.1 The Cantilever Beam

As the l_1 regularization technique is able to maintain the sparsity of the solution using a smaller number of measurements, the structure can be modelled using a relatively large number of elements that enables the local damage to be directly quantified. The beam is modeled using 100 Euler–Bernoulli beam elements (10 mm long). The length of one element is identical to the length of each cut; as such, the damage severity of each cut is equal to the reduction in the moment of inertia of the cross section and is quantified by SRF. The actual damage locations and severities of the four DSs are listed in Table 4.1.

Among the total 100 elements of the beam model, only 1 to 3 damaged elements have non-zero SRF values. Therefore, the SRF vector ($\boldsymbol{\theta}$) is very sparse. The first six frequencies and mode shapes at 10 points are utilized for damage detection, resulting in 66 measurement data in total. The identification is an underdetermined problem because 100 unknown SRF values have to be identified. In order to reduce the influence of modelling uncertainties of the initial FE model, the measured modal data in the undamaged state is first used to update the initial FE model (Xia and Hao, 2003). No regularization is introduced in this step. The updated model represents a more accurate

reference model in the undamaged state as its modal properties agree with the measured ones. This reference FE model will be used for damage detection.

Table 4.1 Damage locations and severities for the four damage scenarios.

Scenario	Element no.	Damage severity (SRF)
DS1	1	−40%
DS2	1	−60%
DS3	1	−60%
	50	−60%
DS4	1	−60%
	50	−60%
	75	−80%

4.5.1.1 Damage scenario DS1

For DS1, the objective function, i.e., Equation (4.12), is solved for different β values ranging from 0 to 1.0, with an increment of $\Delta\beta = 0.005$. The residual and solution norms versus β are plotted in Figure 4.5. Be noted that these two norms correspond to the terms in Equation (4.12) after normalization. With increasing β, the solution norm drops quickly first, then decreases slowly, and suddenly drops to zero when β reaches the maximal regularization parameter $\beta_{\max} = 0.485$. The residual norm rises rapidly at the beginning and increases gradually from $\beta = 0.025$. The residual and solution norms change slowly as β is between 0.06 and 0.485. The regularization parameter in this range achieves a fair balance in keeping both norms small. Therefore, $\beta = 0.06 \sim 0.485$ is determined as the appropriate range.

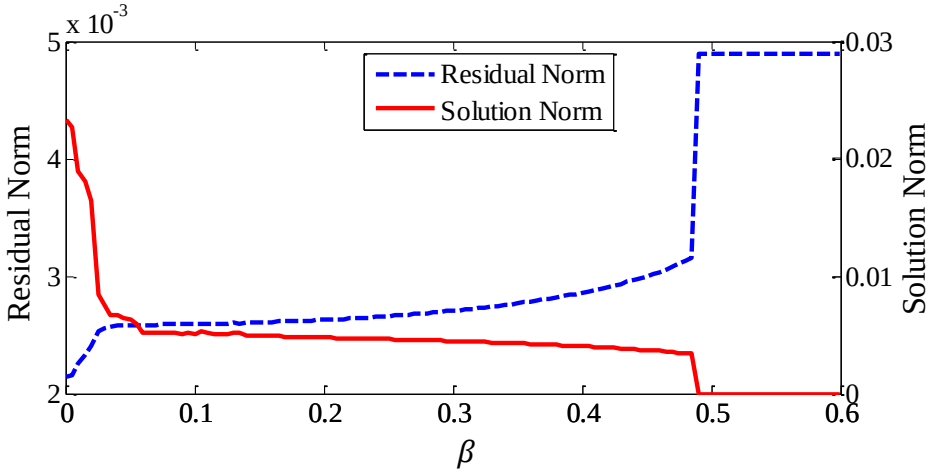

Figure 4.5 Residual and solution norms for different values of $\boldsymbol{\beta}$ in DS1

The DP is also applied. First, a possible range of the proper regularization parameter is determined based on the plot of the solution norm versus the residual norm on the linear scale. The variance of the discrepancy between the calculated and measured modal data is then calculated over this possible range.

In the present study, natural frequencies are assumed to contain 1% noise as suggested by previous studies (Philips, 2009; Weng *et al*., 2012; Mottershead and Friswell, 1993; Friswell and Penny, 1997), that is, the standard deviation of noise $\delta = 0.01$. For each regularization parameter β and the corresponding calculated $\boldsymbol{\theta}$, the discrepancy of natural frequencies can be calculated as

$$\boldsymbol{D} = \frac{\boldsymbol{f}^E - \boldsymbol{f}_\beta(\boldsymbol{\theta})}{\boldsymbol{f}_\beta(\boldsymbol{\theta})} \tag{4.21}$$

where $\boldsymbol{f}^E$ is the measured natural frequency vector, and $\boldsymbol{f}_\beta(\boldsymbol{\theta})$ is the calculated natural frequencies of the damaged structure corresponding to β. According to Equation (4.20), the regularization parameter is selected such that the variance of the discrepancy $Var\big(\boldsymbol{D}(\beta)\big)$ is closest to the estimated $\delta^2 = 1\times10^{-4}$.

The solution norm versus the residual norm for DS1 is plotted in Figure 4.6 (a). The enlarged diagram with β within the range of 0.025–0.485 is shown in Figure 4.6 (b). Although this curve has some resemblance to "L", it bunches up at some points. Therefore, it is difficult to identify the optimal regularization parameter by locating the "corner", as that in the l_2-regularized problems. Instead, a possible range of β, which is around the corner of the L-shaped curve, can be determined. For DS1, the possible range of the regularization parameter is approximately 0.025–0.485.

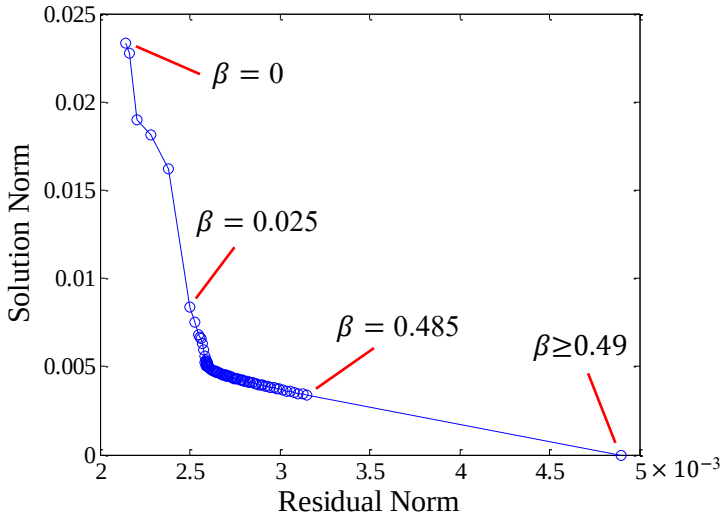

(a) β between 0 and 1

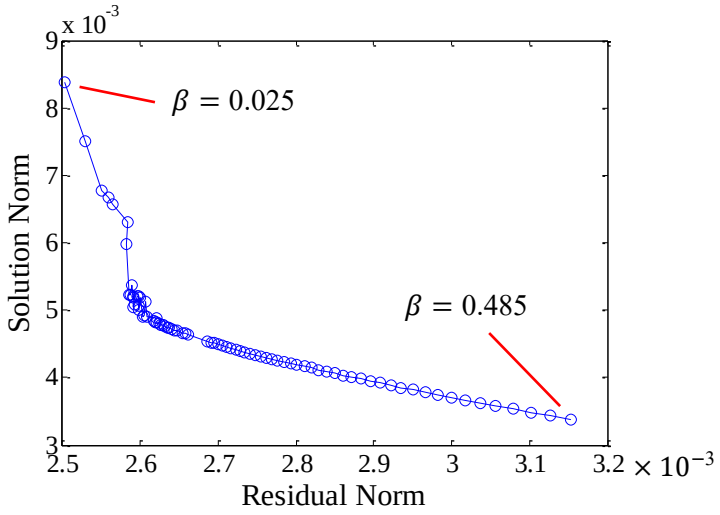

(b) β between 0.025 and 0.485

Figure 4.6 Solution norm versus residual norm for $\boldsymbol{\beta} \in [0, 1]$ (DS1)

Figure 4.7 shows the $Var(\boldsymbol{D}(\beta))$ for different values of β within the range of 0.025–0.485. The variances in the range are all larger than the estimated value and vary slightly. Therefore, $\beta = 0.025$~0.485 is determined as the appropriate range of the regularization parameter because the variances in this range are all close to 1×10^{-4}. The feasible ranges determined by the two proposed strategies are almost the same.

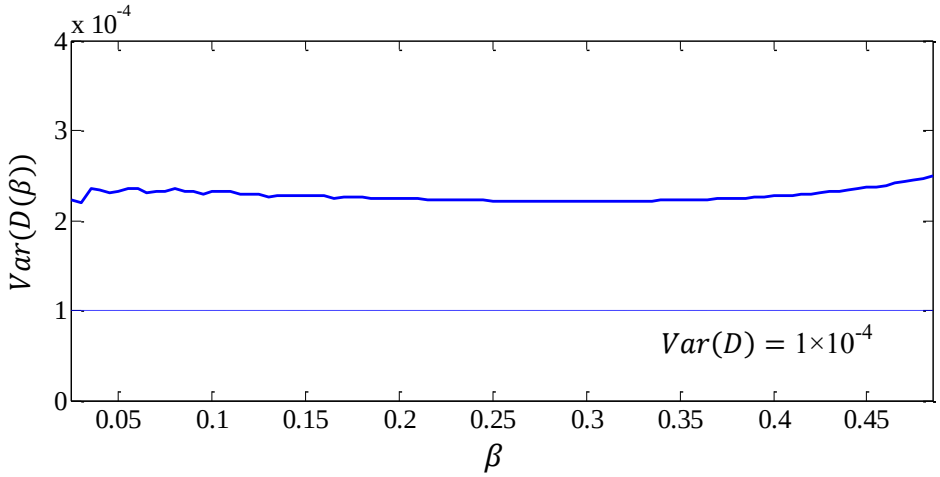

Figure 4.7 $\boldsymbol{Var(D(\beta))}$ as $\boldsymbol{\beta} \in [0.025, 0.485]$ (DS1)

The damage identification results of SRFs are displayed in Figure 4.8 for different values of β. For $\beta = 0.01$, although the true damage at element 1 can be detected, the identified SRFs are distributed among a number of elements. When the regularization parameter is within 0.025–0.485, the damage identification results are accurate. At $\beta = 0.025$, although several elements are falsely identified as damaged, the identified SRFs are very small and can be neglected. For other three regularization parameters, the identified damage severities are all close to the true value (SRF_1= –0.4), and no false identification occurs. When $\beta > 0.485$, the solution becomes zero, and no damage can be detected. The plot is then not shown here.

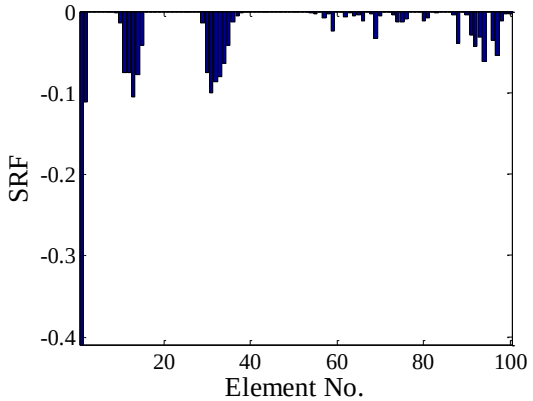

(a) $\beta = 0.01$

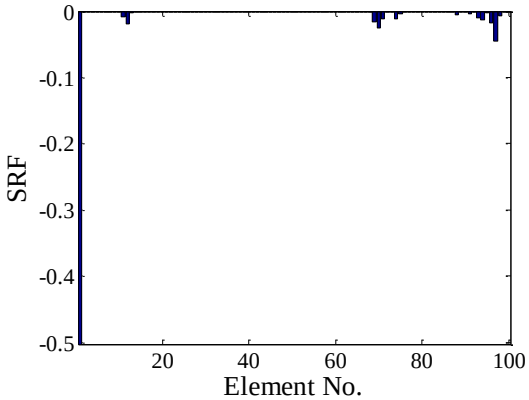

(b) $\beta = 0.025$

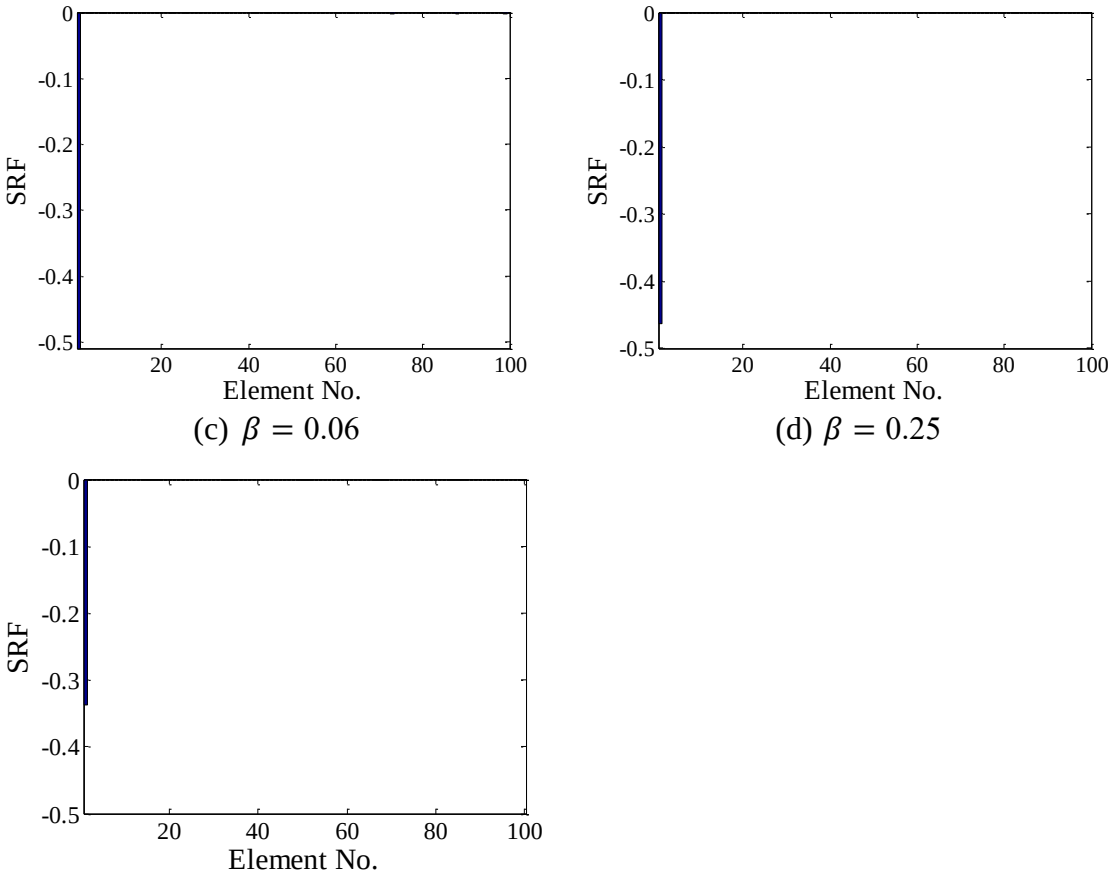

(c) $\beta = 0.06$ (d) $\beta = 0.25$

(e) $\beta = 0.485$

Figure 4.8 Damage identification results for DS1

4.5.1.2 Damage scenario DS2

For DS2, the objective function is similarly solved for different β values ranging from 0 to 1.0 with an increment $\Delta\beta = 0.005$. The curves of the residual and solution norms versus β are shown in Figure 4.9. At $\beta \geq 0.085$, the residual and solution norms are almost unchanged with increasing β. Therefore, the appropriate range of the regularization parameter is determined as $\beta = 0.085$~0.95, which keeps the two norms small at the same time.

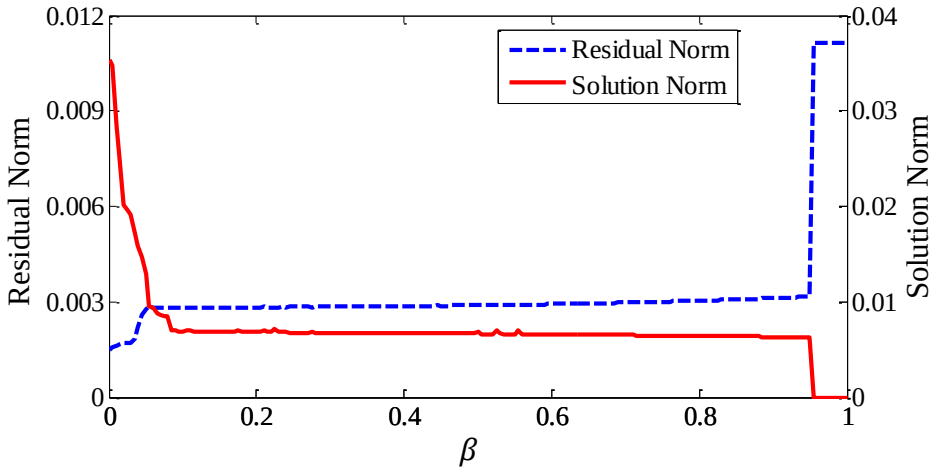

Figure 4.9 Residual and solution norms for different values of $\boldsymbol{\beta}$ in DS2

The solution norm versus the residual norm is shown in Figure 4.10. The suitable β is first estimated as 0.055–0.95. $Var(\boldsymbol{D}(\beta))$ in the range are displayed in Figure 4.11. The variances vary slightly with increasing β and are all lower than the estimated value. Therefore, $\beta = 0.055$~0.95 is selected. This range is slightly wider than that determined using the previous strategy. The damage identification results for different values of β in the range are shown in Figure 4.12. In all cases, the damage location and severity (SRF_1= –0.6) are identified accurately. When β is out of the range, the damage identification results are incorrect and not shown here for brevity.

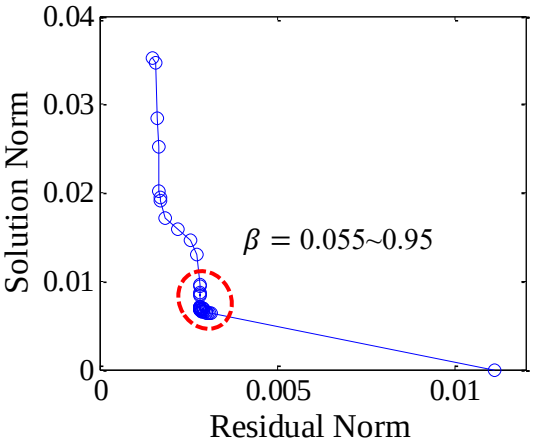

Figure 4.10 Solution norm versus residual norm as $\beta \in [0, 1]$

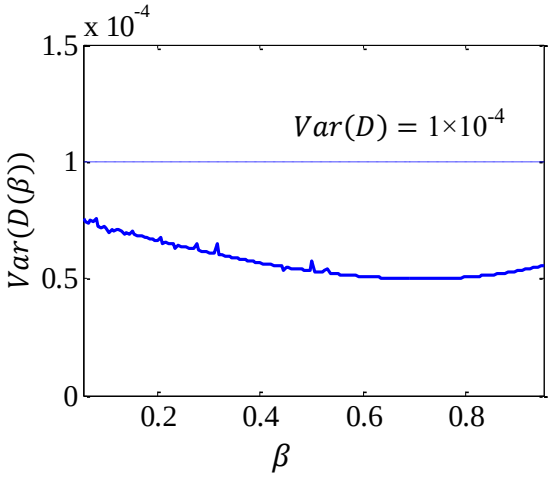

Figure 4.11 $Var(\boldsymbol{D}(\beta))$ as $\beta \in [0.055, 0.95]$ (DS2)

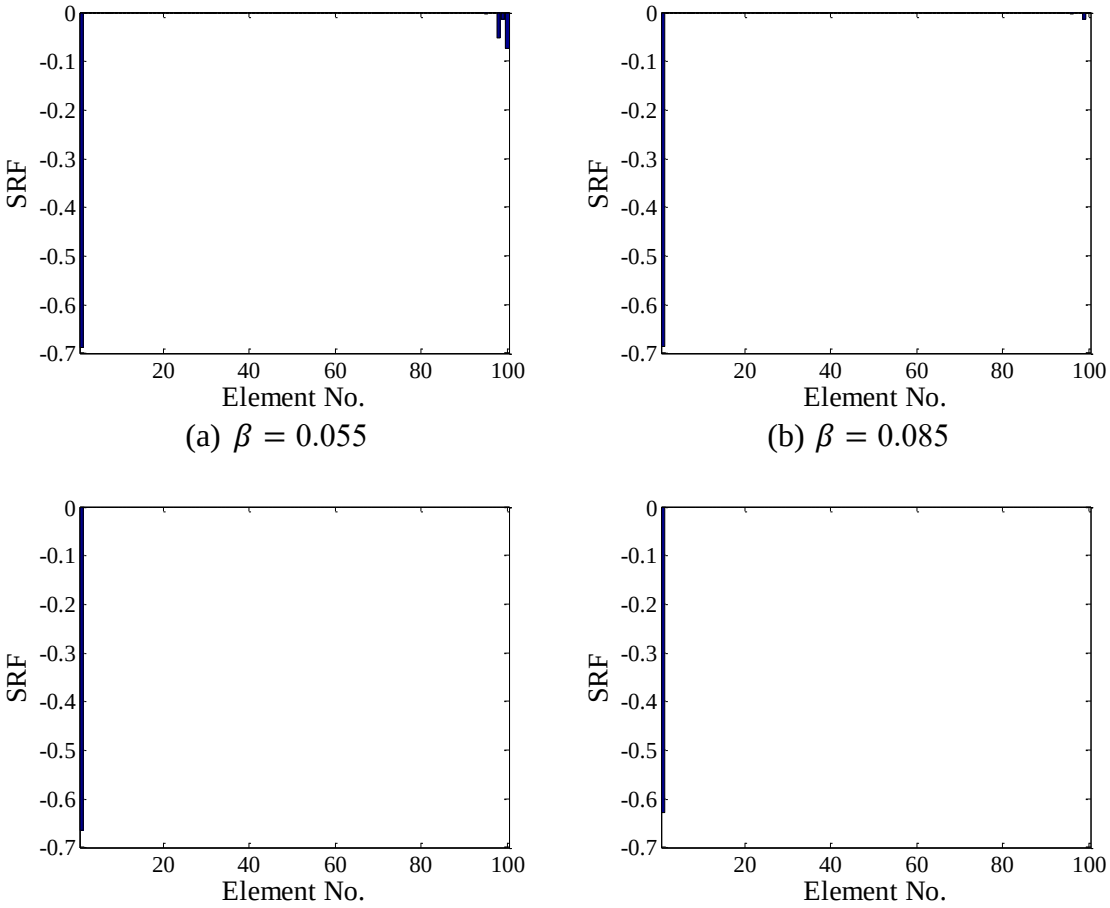

(a) $\beta = 0.055$ (b) $\beta = 0.085$

(c) $\beta = 0.49$ (d) $\beta = 0.95$

Figure 4.12 Damage identification results for DS2

4.5.1.3 Damage scenario DS3

For DS3, the objective function is solved for β ranging from 0 to 1.4 with $\Delta\beta = 0.005$. The residual and solution norms versus β are displayed in Figure 4.13, which exhibit a step-like pattern. There are two steps along the curves corresponding to two non-zero items in the SRF vector. Through numerical study, it has been found that the number of steps equals to the number of damaged elements, i.e., the number of non-zero items in the damage index vector.

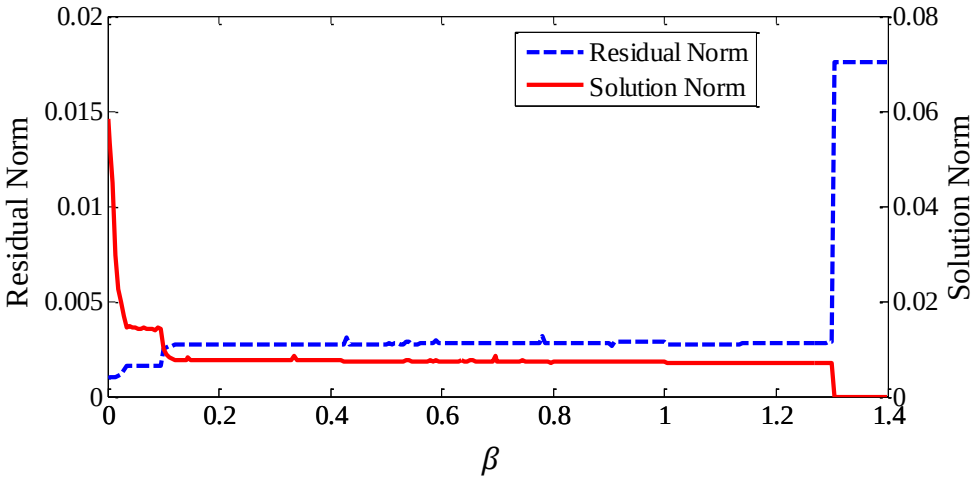

Figure 4.13 Residual and solution norms for different values of $\boldsymbol{\beta}$ in DS3

It can be seen that the solution norm drops quickly first, that is, the undesirable non-zero variables are forced to zero. When β is within 0.035–0.095, the residual and solution norms are almost unchanged with increasing β. At $\beta > 0.095$, the solution norm decreases suddenly, whereas the residual norm increases. With the increase of β, the residual and solution norms are nearly constant until the maximal regularization parameter is reached. As introduced previously, the actual two non-zero variables are less likely to be eliminated and thus the curves of the residual and solution norms have two steps. Therefore, the appropriate range of the regularization parameter is determined as $\beta = 0.035$~0.095. It is usually the case that the sparsity of the solution increases with increasing regularization parameter, leading to loss of data fidelity. The two non-zero variables are forced to be zero sequentially by increasing the regularization parameter. When β is within 0.1–1.295, only one actual non-zero item remains, leading to the false damage identification result. This appropriate range is smaller than those of the previous two DSs, indicating that the inverse problem corresponding to DS3 is more sensitive to the regularization parameter.

The solution norm versus the residual norm for DS3 is shown in Figure 4.14. The suitable range of the regularization parameter is estimated as 0.035~1.30. $Var(\boldsymbol{D}(\beta))$ for different β values within the range are displayed in Figure 4.15, exhibiting a step-like pattern. The variances for $\beta \in [0.035, 0.095]$ are very close to the estimated value (i.e., 1×10^{-4}), whereas a big and abrupt increase occurs at $\beta = 0.10$. Therefore,

0.035~0.095 is determined as the suitable range of the regularization parameter, consistent with the result obtained using the previously discussed method.

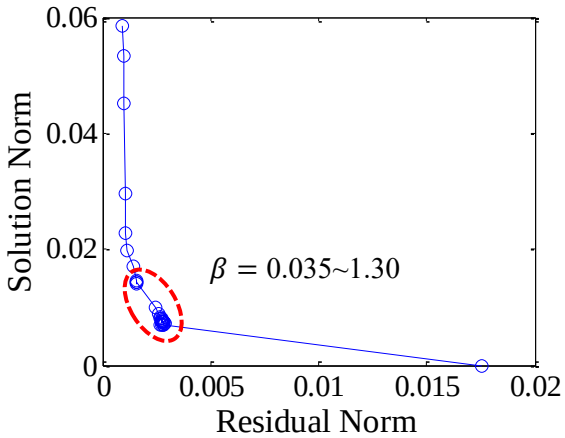

Figure 4.14 Solution norm versus residual norm as $\beta \in [0, 1]$

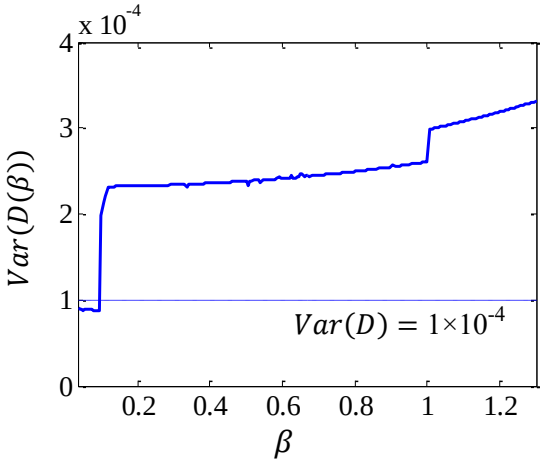

Figure 4.15 $Var(\boldsymbol{D}(\beta))$ as $\beta \in [0.035, 1.30]$ (DS3)

The damage identification results are displayed in Figure 4.16. For $\beta = 0.035$ and $\beta = 0.095$, both damaged elements can be located and quantified correctly. When $\beta = 0.10$, the damaged elements can be detected, but the severity of the damage at the mid-span is incorrect. For $\beta = 0.80$, the damage at the mid-span of the beam cannot be identified.

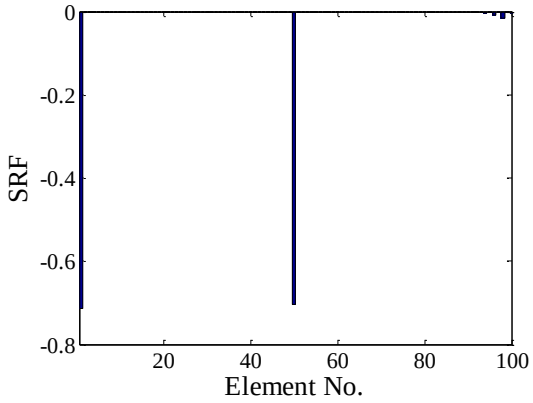

(a) $\beta = 0.035$

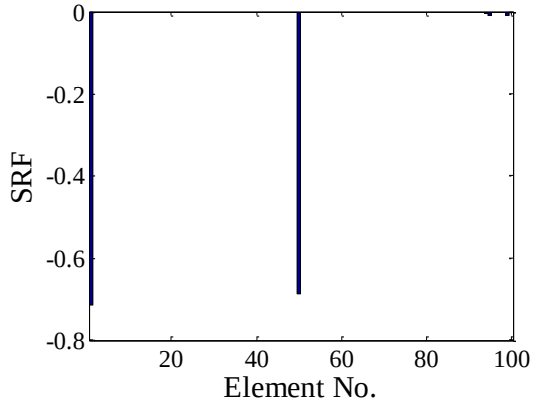

(b) $\beta = 0.095$

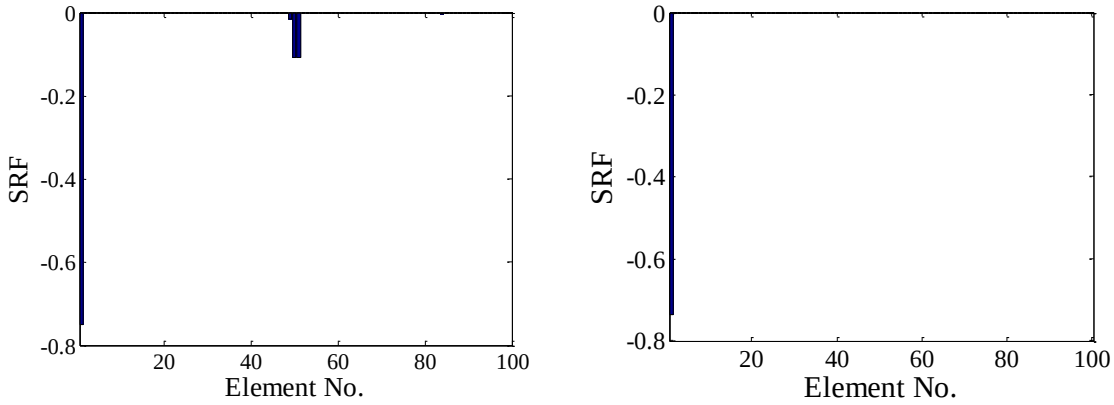

(c) $\beta = 0.10$ (d) $\beta = 0.80$

Figure 4.16 Damage identification results for DS3

4.5.1.4 Damage scenario DS4

For DS4, the objective function is solved for different β values ranging from 0 to 2.2 with the increment $\Delta\beta = 0.005$. The plots of residual and solution norms versus $\beta \in [0, 0.4]$ are shown in Figure 4.17. The appropriate range of the regularization parameter is determined as $\beta = 0.095$~0.145, which keeps both the residual and solution norms small at the same time.

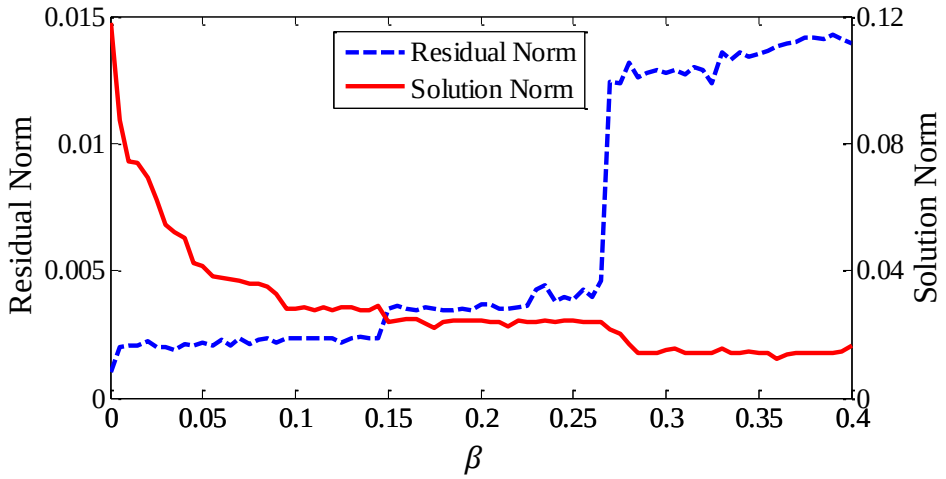

Figure 4.17 Residual and solution norms for different values of $\boldsymbol{\beta}$ in DS4

The solution norm versus the residual norm is shown in Figure 4.18. The suitable range of the regularization parameter for DS4 is estimated as 0.095–0.30. $Var(\boldsymbol{D}(\beta))$ for different values of β in the possible range are displayed in Figure 4.19. The corresponding variances are all close to the estimated value as $\beta < 0.15$. Thus, the

appropriate range of the regularization parameter is $\beta = 0.095$~0.145, consistent with the result of previous strategy.

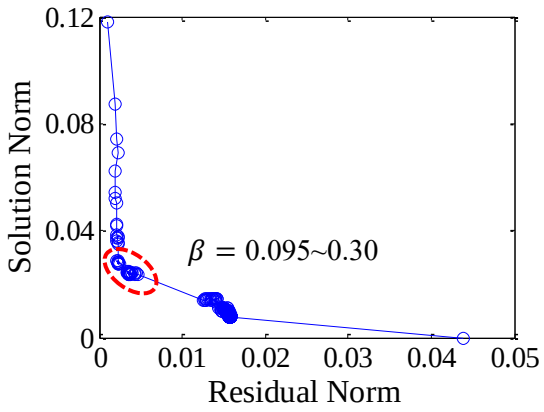

Figure 4.18 Solution norm versus residual norm as $\beta \in [0, 2.2]$

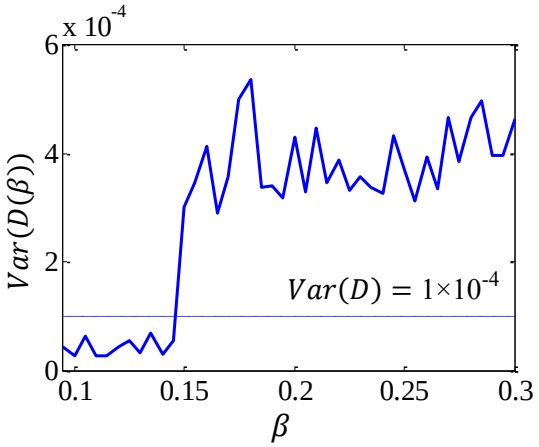

Figure 4.19 $Var(\boldsymbol{D}(\beta))$ as $\beta \in [0.095, 0.30]$ (DS4)

The damage identification results for different values of β are shown in Figure 4.20. At $\beta = 0.03$, the identification result is not sparse, and a considerable number of undamaged elements are falsely identified as damaged. For $\beta = 0.095$ and $\beta = 0.145$, the damaged elements (nos. 1, 50, and 75) are located and quantified accurately. At $\beta = 0.18$, the damage in the mid-span (no. 50) cannot be detected.

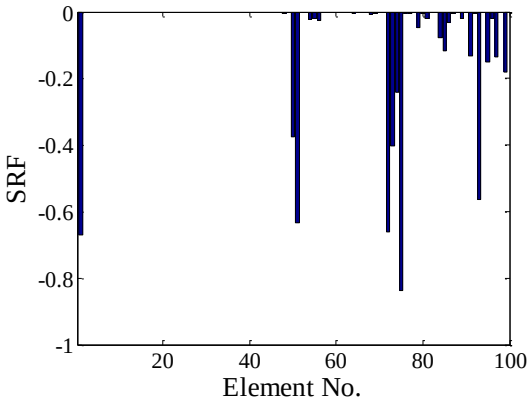

(a) $\beta = 0.03$

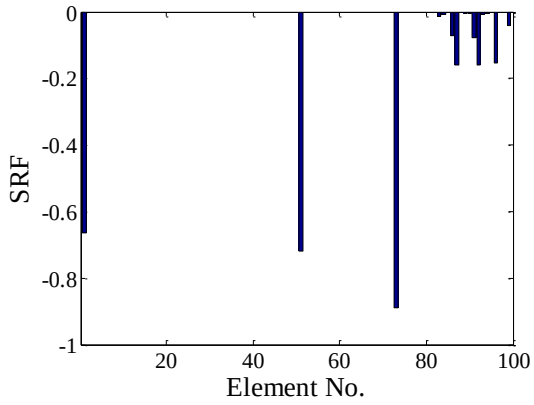

(b) $\beta = 0.095$

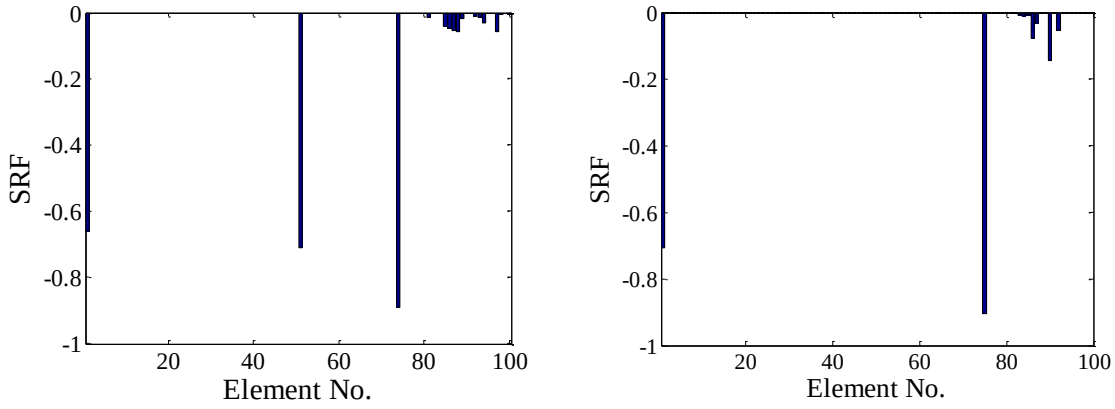

(c) $\beta = 0.145$ (d) $\beta = 0.18$

Figure 4.20 Damage identification results for DS4

The experimental results show that multiple damage scenarios are more difficult to be identified accurately, as compared with the single damage scenario. The feasible ranges of the regularization parameter for DS3 and DS4 with multiple damage are narrower than those of the two single damage cases DS1 and DS2. Therefore, the damage identification accuracy for multiple damage scenarios is more sensitive to the regularization parameter.

4.5.2 The Three-storey Frame

In the FE analysis, the frame is modelled with 225 elements, and each are 20 mm long, which is identical to that of the cuts. Cuts 1 and 2 are located at elements 1 and 176, respectively. Therefore, SRF(1) = –60% in DS1, and SRF(1) = SRF(176) = –60% in DS2. The actual SRF vector has at most two non-zero items, which is extremely sparse compared to the total 225 elements. Lumped masses are added at the corresponding node to represent the masses of the accelerometers. With consideration of the modeling uncertainties, the FE model is first updated using the modal data measured from the undamaged state.

The appropriate ranges of the regularization parameter are determined using the two proposed strategies. For DS1, the appropriate range of the regularization parameter is $\beta = 0.06$~0.93. The damage identification results for different values of β are shown in Figure 4.21. At $\beta = 0.02$, the actual damaged element (no. 1) can not be detected,

whereas a number of elements are falsely identified as damaged. For $\beta = 0.35$, the damaged element can be located and quantified correctly.

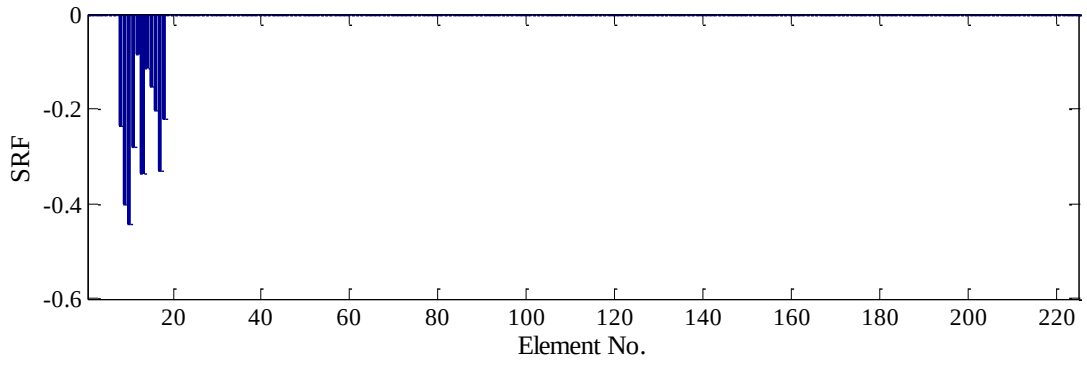

(a) $\beta = 0.02$

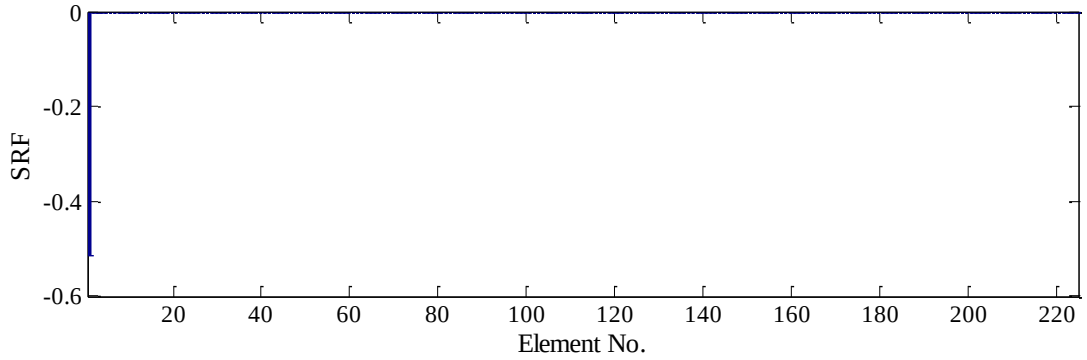

(b) $\beta = 0.35$

Figure 4.21 Damage identification results for DS1

For DS2, $\beta = 0.12$~0.35 is determined as the feasible range of the regularization parameter. The damage identification results for different values of β are shown in Figure 4.22. Accurate damage identification results can be obtained using the regularization parameter within 0.12–0.35. The damaged elements can be correctly detected, and no false identification occurs. At $\beta = 0.60$, which is out of the feasible range, only damage at the column end (element 1) is identified, and the other damage at element 176 is not detected.

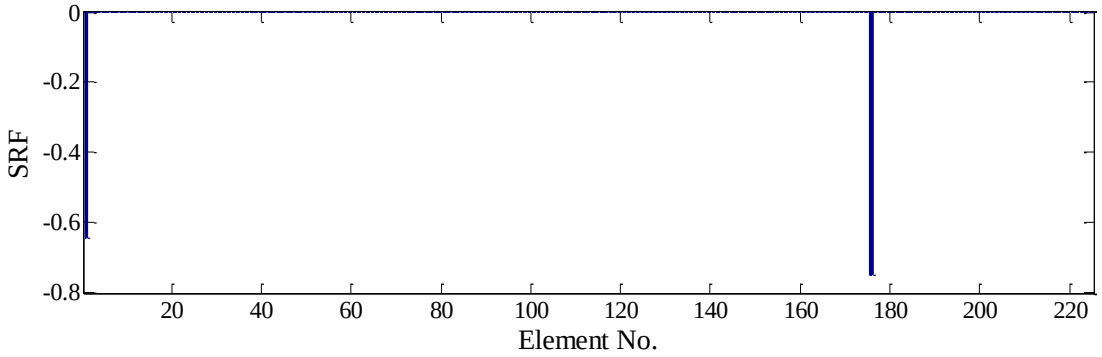

(a) $\beta = 0.20$

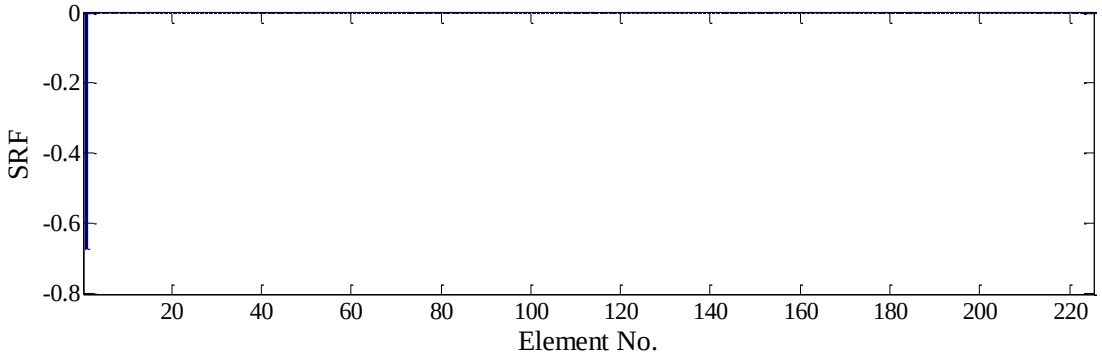

(b) $\beta = 0.60$

Figure 4.22 Damage identification results for DS2

In the example, all eight frequencies and mode shapes at all 39 measurement points are used for damage detection. To investigate the effect of the number of modes on the damage detection result, the first three natural frequencies and mode shapes are also used for DS2. In the case, there are 120 measurement data and 225 unknown SRF values to be identified. Using the proposed l_1 regularization technique, the damage identification results are shown in Figure 4.23. The two damaged elements are still identified with good accuracy and no false identification occurs.

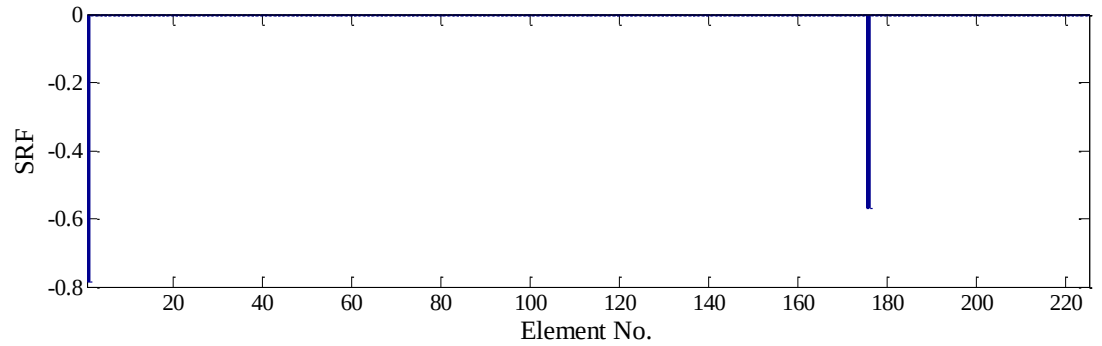

Figure 4.23 Damage identification results for DS2 using three frequencies and mode shapes

The l_2 regularization technique is also employed here to identify damage for comparison. The following objective function corresponding to Equation (4.12) is minimized for damage identification

$$\widehat{\boldsymbol{\theta}} = \arg\min_{\widehat{\boldsymbol{\theta}}} \left(\frac{1}{m} \sum_{i=1}^{m} \left[\frac{\lambda_i^A(\boldsymbol{\theta}) - \lambda_i^E}{\lambda_i^E} \right]^2 + \frac{1}{m \times np} \sum_{i=1}^{m} \sum_{j=1}^{np} \left[\phi_{ji}^A(\boldsymbol{\theta}) - \phi_{ji}^E \right]^2 + \frac{\beta}{n} \|\boldsymbol{\theta}\|_2^2 \right) \tag{4.22}$$

The only difference between Equation (4.12) and Equation (4.22) is that the 2-norm is used as the solution norm in Equation (4.22). The regularization parameter β is determined by the L-curve criterion used for the Tikhonov regularization (Hansen, 1992), which is calculated as 0.0301 and 0.0292 for the present two damage scenarios. The corresponding damage identification results are displayed in Figure 4.25. In both cases, the identification results are not sparse and a considerable number of undamaged elements are falsely identified as damaged. The actual damaged element no. 1 cannot be detected for DS2. Although the damaged element 176 is detected roughly, the damage severity differs much from the true value (80% reduction). The above comparison demonstrates that the l_1 regularization-based damage detection technique is able to identify sparse damaged elements, whereas the l_2 regularization cannot.

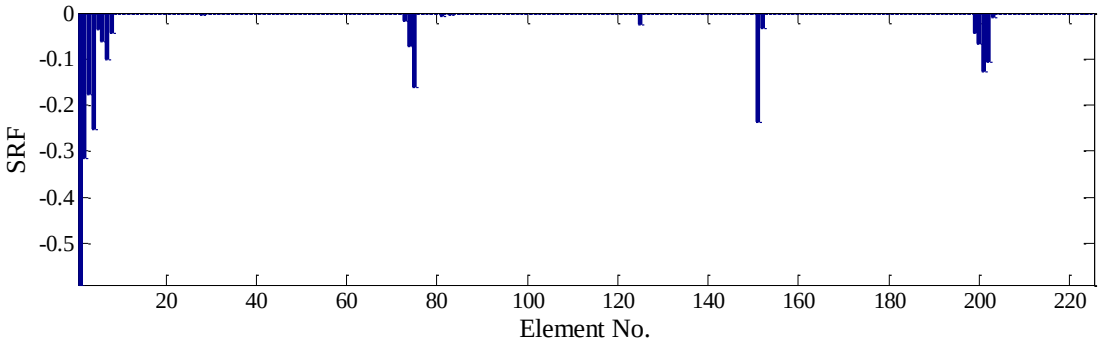

(a) DS1 ($\beta = 0.0301$)

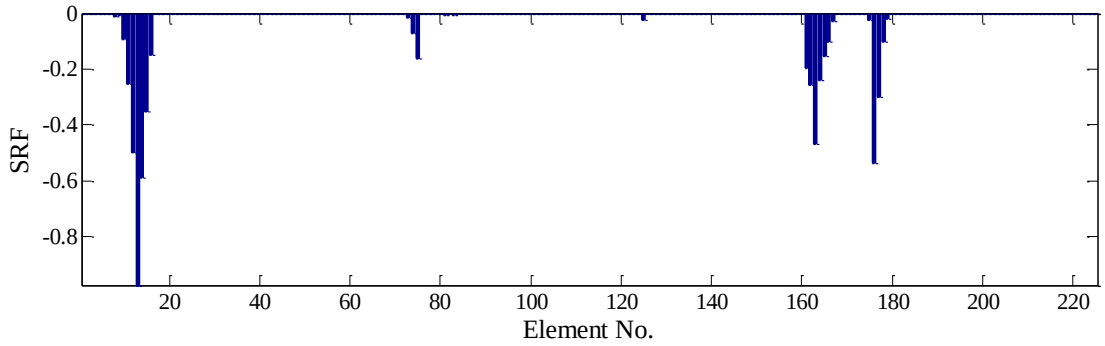

(b) DS2 ($\beta = 0.0292$)

Figure 4.24 Damage identification results for two damage scenarios with the l_2 regularization technique

4.5.3 The Planar Truss

The planar truss has no experimental data. Therefore, random noise with the normal distribution is added to the numerical modal parameters as shown in Equation (4.18) to consider the measurement noise effect. Previous studies (Mottershead and Friswell, 1993; Friswell and Penny, 1997) have suggested that natural frequencies may contain 1% noise and mode shapes may contain 8%−10% noise in practical ambient vibration tests. Therefore, two different levels of noise as listed in Table 4.2 are introduced into the frequencies and mode shapes of the damaged structure using Equation (4.18). The natural frequencies and MAC of the undamaged and damaged structures are compared in Table 4.3. It is noted that a few natural frequencies in the damaged states are higher than the undamaged ones due to the random noise.

Table 4.2 Noise levels for the frequency and mode shape.

Noise level	Frequency	Mode shape
1	1%	10%
2	2%	20%

Table 4.3 Frequencies and MAC of the truss in the undamaged and damaged states.

Mode	Undamaged	Damaged					
		No noise		Noise level 1		Noise level 2	
	Freq. (Hz)	Freq. (Hz)	MAC (%)	Freq. (Hz)	MAC (%)	Freq. (Hz)	MAC (%)
1	36.92	34.50 (–6.55)	99.79	34.37 (–6.91)	99.79	33.89 (–8.20)	99.78
2	77.11	76.00 (–1.44)	99.80	76.04 (–1.39)	99.80	75.51 (–2.07)	99.80
3	135.59	135.52 (–0.06)	99.98	136.67 (+0.80)	99.98	133.39 (–1.63)	99.98
4	226.36	217.90 (–3.74)	98.58	221.95 (–1.95)	98.56	216.31 (–4.44)	98.56
5	253.52	252.95 (–0.22)	99.42	250.23 (–1.30)	99.39	253.55 (+0.01)	99.38
6	364.15	361.33 (–0.77)	87.06	361.21 (–0.81)	86.95	362.59 (–0.43)	86.93
Average		–2.13	97.43	–1.92	97.41	–2.79	97.41

Note: Values in parentheses are the frequency change ratios (%) between the damaged and undamaged states.

The damage identification results are shown in Figure 4.26. The regularization parameter is selected within the specified range determined using the the residual and solution norms. First the modal data without any noise are used for damage detection. The damage location and severity can be identified accurately and no false identification occurs. For noise level 1, the damage location is determined correctly and the identified SRF is very close to the true value. In the case of noise level 2, the damage location can be accurately located with the damage severity slightly larger than the true value (50% reduction). The numerical results show that the developed l_1 regularization-based damage detection technique has good robustness to noise and works well even under a high noise level.

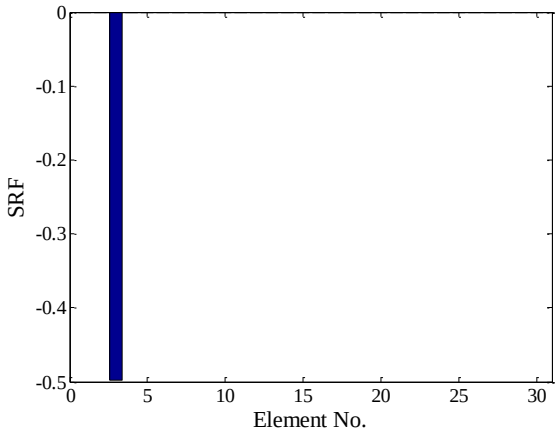

(a) Noise-free ($\beta = 0.005$)

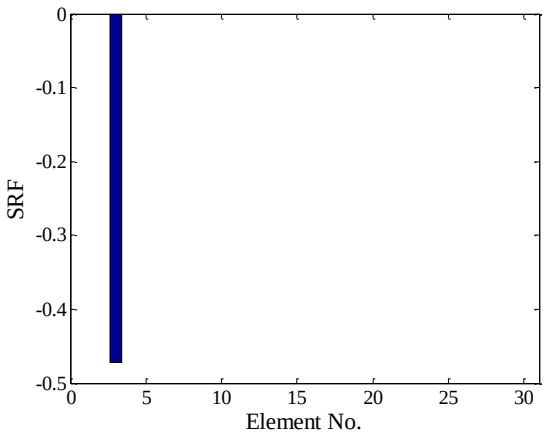

(b) Noise level 1 ($\beta = 0.003$)

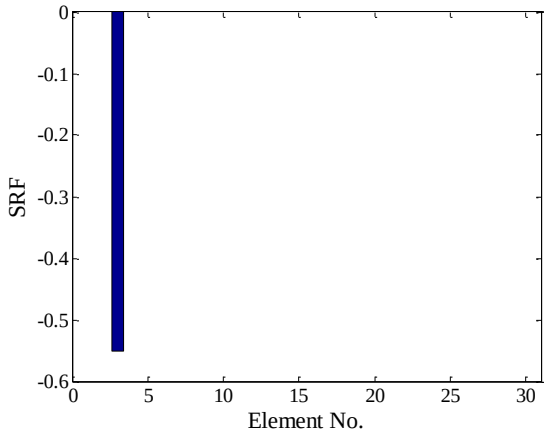

(c) Noise level 2 ($\beta = 0.145$)

Figure 4.25 Damage identification results of the planar truss

4.6 Summary

A sparse damage detection technique using the natural frequencies and mode shapes is developed in this chapter. Through exploiting the sparse property of the structural damage, the l_1 regularization technique is employed to identify the sparse damage among a large number of potential elements. The proposed method enables the local damage being directly quantified through using fine elements in the FE modelling. The advantages of combining frequency changes and mode shape changes are that frequencies can be measured conveniently and accurately and mode shapes could provide spatial information of structures and are sensitive to local damage.

Two strategies for selecting the regularization parameter for the l_1-regularized damage detection problem are proposed. Following the similar idea of the L-curve criterion for l_2 regularization, the first selection method utilizes the residual and solution norms to determine the appropriate range of the regularization parameter. The other selection criterion is developed based on the DP such that the variance of the discrepancy between the calculated and measured modal data is close to the variance of the measurement noise.

Both numerical and experimental examples verify that the proposed sparse damage detection method can successfully identify single and multiple damage, even there are a large number of unknowns. It is advantageous over the traditional l_2 regularization

technique. The examples also demonstrate that the proposed method is robust to noise even under the severe noise situation. An appropriate range of the regularization parameter can be determined using the two proposed techniques and the results are consistent. Accurate damage identification results can be obtained when the regularization parameter is selected within the specified range even for multiple damage scenarios. When the regularization parameter is out of the range, true damage may not be detected, or undamaged elements may be falsely identified as damaged. The suitable range depends on the structure and damage scenario. A wider range indicates that the damage detection problem is insensitive to the regularization parameter.

CHAPTER 5

GENETIC ALGORITHM BASED OPTIMAL SENSOR PLACEMENT FOR L_1-REGULARIZED DAMAGE DETECTION

5.1 Introduction

In the previous chapter, sparse recovery theory has been applied to damage detection by utilizing the sparsity feature of structural damage. The theory requires that the columns of the sensing matrix suffice certain independence criteria. In l_1-regularized damage detection, the sensitivity matrix serves as the sensing matrix and is directly related to sensor locations. In this regard, an OSP technique is proposed such that the resulting sensitivity matrix is of the maximum independence in the columns or is of the least mutual coherence. Given a total number of sensors, the selection of sensor locations is a combinatorial problem. A GA is thus used to solve this optimization problem, in which the mutual coherence of the sensitivity matrix is minimized.

5.2 Sensing Matrix for L_1-regularized Damage Detection

In sparse recovery problems, recovery accuracy largely depends on the number of measurements and their degree of independence. Considering the standard sparse recovery problem in Equation (4.7), the linear operator $\boldsymbol{X}$ is referred to as the sensing matrix which projects the unknown vector into a low-dimensional measurement vector. Through operating on the unknown vector $\boldsymbol{\theta}$, the sensing matrix $\boldsymbol{X}$ stores the information about $\boldsymbol{\theta}$ in the measurement $\boldsymbol{y}$. Therefore, the performance of sparse recovery strongly relies on the properties of the sensing matrix. The measurements should retain as much information as possible to recover the unknown vector accurately using few measurements. To this end, the sensing matrix should be constructed with the

columns as independently as possible to ensure the stable and exact recovery of the sparse vector (Theodoridis *et al*., 2014).

For an accurate sparse recovery, the sensing matrix should satisfy some certain criteria, such as spark (Gorodnitsky and Rao, 1997; Donoho and Elad, 2003), restricted isometry property (RIP) (Candès and Tao, 2005) and mutual coherence (Mallat and Zhang, 1993; Elad, 2007). These conditions measure the independence of the columns of the sensing matrix and are closely related to each another. The spark of a given matrix is the smallest number of its linearly dependent columns (Theodoridis, *et al*., 2014). The spark can only be obtained through a combinatorial search over all possible combinations of the columns of the matrix and thus is not convenient for implementation. The RIP was firstly proposed by Candès and Tao (2005). They define the *S*-restricted isometry constant δ_S to be the smallest number such that the sensing matrix $\boldsymbol{X}$ in Equation (4.7) obeys

$$(1-\delta_S)\|\boldsymbol{\theta}\|_2^2 \leq \|\boldsymbol{X}\boldsymbol{\theta}\|_2^2 \leq (1+\delta_S)\|\boldsymbol{\theta}\|_2^2 \tag{5.1}$$

for all *S*-sparse vectors $\boldsymbol{\theta}$. The sensing matrix $\boldsymbol{X}$ satisfyies the RIP of order *S*. δ_S measures how close all linear combinations of *S* columns of $\boldsymbol{X}$ behave like an orthonormal system, and $\delta_S = 0$ for the orthonormal matrix. The RIP is related to the condition number of the sensing matrix. Better conditioned $\boldsymbol{X}$ is, more accurate for sparse recovery (Candès and Tao, 2005). Computing the restricted isometry constant δ_S is strongly NP-hard and even difficult to approximate (Tillmann and Pfetsch, 2014; Natarajan and Wu, 2014). Therefore, the corresponding property is difficult to evaluate. Finally, the mutual coherence of the sensing matrix $\boldsymbol{X} \in R^{M\times N}$ is defined as (Mallat and Zhang, 1993)

$$\mu(\boldsymbol{X}) = \max \frac{\left|\boldsymbol{x}_i^T \boldsymbol{x}_j\right|}{\|\boldsymbol{x}_i\| \cdot \left\|\boldsymbol{x}_j\right\|}, \quad i,j = 1,\dots,N \tag{5.2}$$

where $\boldsymbol{x}_i$ $(i = 1,\dots,N)$ is the *i*th column of $\boldsymbol{X}$. $\mu(\boldsymbol{X}) \in [0,1]$ measures the maximum linear dependency of the columns of matrix $\boldsymbol{X}$. Since the spark and RIP constant are

difficult to compute, mutual coherence can be obtained easier and is thus used as the measure of the independence of the sensing matrix in this study.

Comparing Equation (2.9) in sensitivity-based model updating with Equation (4.7) for the standard sparse recovery problem, the sensitivity matrix acts as the sensing matrix in l_1-regularized damage detection. Since natural frequencies and mode shapes are utilized in the model updating, the sensitivity matrix consists of the corresponding two parts as

$$\mathbf{S} = \begin{bmatrix} \mathbf{S}_{\boldsymbol{\lambda}} \\ \mathbf{S}_{\boldsymbol{\phi}} \end{bmatrix} \tag{5.3}$$

$\mathbf{S}_{\boldsymbol{\lambda}}$ is the eigenvalue sensitivity matrix and can be expressed as

$$\mathbf{S}_{\boldsymbol{\lambda}} = \left[\mathbf{S}_{\lambda_1}, \mathbf{S}_{\lambda_2}, \cdots, \mathbf{S}_{\lambda_m}\right]^T \tag{5.4}$$

$$\mathbf{S}_{\lambda_i} = \frac{\partial \lambda_i}{\partial \boldsymbol{\theta}} = \left\{\frac{\partial \lambda_i}{\partial \theta_1}, \frac{\partial \lambda_i}{\partial \theta_2}, \cdots, \frac{\partial \lambda_i}{\partial \theta_n}\right\} \tag{5.5}$$

The eigenvector sensitivity matrix $\mathbf{S}_{\boldsymbol{\phi}}$ can be expressed as

$$\mathbf{S}_{\boldsymbol{\phi}} = \left[\mathbf{S}_{\boldsymbol{\phi}_1}, \mathbf{S}_{\boldsymbol{\phi}_2}, \cdots, \mathbf{S}_{\boldsymbol{\phi}_m}\right]^T \tag{5.6}$$

$$\mathbf{S}_{\boldsymbol{\phi}_i} = \frac{\partial \boldsymbol{\phi}_i}{\partial \boldsymbol{\theta}} = \begin{bmatrix} \frac{\partial \phi_{1,i}}{\partial \theta_1} & \frac{\partial \phi_{1,i}}{\partial \theta_2} & \cdots & \frac{\partial \phi_{1,i}}{\partial \theta_n} \\ \frac{\partial \phi_{2,i}}{\partial \theta_1} & \frac{\partial \phi_{2,i}}{\partial \theta_2} & \cdots & \frac{\partial \phi_{2,i}}{\partial \theta_n} \\ \vdots & \vdots & \ddots & \vdots \\ \frac{\partial \phi_{np,i}}{\partial \theta_1} & \frac{\partial \phi_{np,i}}{\partial \theta_2} & \cdots & \frac{\partial \phi_{np,i}}{\partial \theta_n} \end{bmatrix} \tag{5.7}$$

where $\phi_{j,i}$ is the *i*th mode shape at *j*th point. When point *j* is measured, the mode shape at the point $\phi_{j,i}$ will be included in the model updating. Therefore, the sensitivity matrix $\mathbf{S}$ is directly related to the mode shapes in the measured points or sensor locations.

Sensor placement exerts an influence on mode shapes only, not on natural frequencies. Therefore, this study aims to determine an OSP so that the mutual coherence of the

sensitivity matrix of the mode shapes, i.e. $\mu(\mathbf{S}_\phi)$, is minimized. Once the OSP is determined, or the measurement points are selected, the mode shape sensitivity that corresponds to the points will be included in the sensitivity matrix $\mathbf{S}_\phi$. The obtained optimal sensor locations and associated sensitivity matrix are then used in the l_1-regularized damage detection. The sensing matrix is calculated from the analytical model, and it is thus independent on the damage states.

5.3 Sensor Location Optimization using GA

In practice, the number of available sensors is always limited due to the economy and technology considerations in practice. As aforementioned, different sensor locations result in different sensitivity matrices and consequently may affect the accuracy of sparse damage identification. Therefore, given a total number of sensors, sensor locations should be carefully selected or optimized, which is referred to as OSP.

A number of OSP techniques have been developed in recent years (Kammer, 1991; Kirkegaard and Brincker, 1994; Papadimitriou, 2004; Chang and Pakzad, 2014; Heo *et al*., 1997; Meo and Zumpano, 2005; Yi *et al*., 2015). Hemez and Farhat (1994) extended the effective independence concept and proposed the OSP technique for damage detection according to the strain energy distribution of the structure. Zhou *et al.* (2013) introduced a new sensor placement index in terms of the ratio of two parameters, namely, the contribution of the measurement points to the Fisher information matrix (Shi *et al*., 2000a), and the damage sensitivity to the measurement noise (Xia and Hao, 2000).

OSP is basically a combinatorial problem. For example, we need to identify n_p distinct locations from all possible candidates. For the combinatorial problem, the global optimum is difficult to obtain using conventional techniques. With the development of computational intelligence, intelligence algorithms have been widely used for damage detection and SHM (Casciati, 2008; Casciati and Elia, 2017). Among them, GAs have been widely used and proved to be effective in solving combinatorial optimization problems (Goldberg, 1989). Yao *et al*. (1993) perhaps was the first to use a GA to optimize sensor placement for modal identification, in which the determinant of the

Fisher information matrix was selected as the fitness function. Worden and Burrows (2001) applied a GA to determine the sensor distribution for fault diagnosis. Liu *et al.* (2008) introduced an improved GA to find the OSP for spatial lattice structures, in which MSE and MAC were taken as the fitness functions.

In this study, a binary-coded GA is used to explore the OSP that results in the minimum mutual coherence of $\mathbf{S}_{\phi}$. Inspired by the Darwinian principle of natural selection, GA was firstly introduced by Holland (1975). A detailed description of GAs can be found in Holland (1975) and Goldberg (1989).

GA is a global optimization method that starts with an initial population of randomly generated chromosomes. Each chromosome refers to a candidate solution, and the component of a chromosome is called gene, which is an integer of 0 or 1.

Considering the sensor placement problem, n_p sensors are to be placed amongst l candidate locations. One sensor placement scheme is represented by one chromosome. Therefore, each chromosome consists of l genes that are set to 1 if a sensor is placed at the corresponding location or 0 otherwise. The total number of 1 in the chromosome is equal to n_p, the number of sensors. For example, the chromosome 1001000010 represents that three sensors are placed at points 1, 4 and 9, amongst 10 candidates.

Reproduction, crossover and mutation are three important genetic operators to produce a new offspring generation. The reproduction is conducted according to the fitness of the individual chromosome which is evaluated by an objective function. The chromosome with a high fitness has a high probability to be selected as the parent chromosome.

Once the parent chromosomes have been selected, they are paired up randomly for mating, which is referred to as crossover. A crossover point along the chromosome pair is randomly assigned, then the substrings after the selected point are swapped to form two offspring. This process ensures that the features of two parent chromosomes are transferred to the next generation. A crossover probability p_c is applied to all parent chromosomes. p_c is generally close to 1 such that most parents will exchange their genes.

The operations of reproduction and crossover may reduce the population diversity, and thus the chromosomes tend to become significantly similar over several generations. Therefore, perturbations are introduced into the population to protect against the premature convergence to a non-optimal solution. Mutation serves the function by replacing a gene in a chromosome at a randomly selected location with a probability p_{m}. The mutation probability is usually a small value.

The processes of reproduction, crossover and mutation will repeat for many generations until a preset convergence criterion is satisfied. In the present OSP problem, the number of sensors is fixed. If the number of genes 1 in a chromosome is not n_p, then a forced mutation operator is introduced by replacing the number of genes 1 with 0 or the other way round. The forced mutation operator will not influence the GA convergence. Population size, p_{c} and p_{m}, affect the GA performance and should be tuned in advance. The GA procedure is briefly shown in Figure 5.1.

A GA generally tends to maximize fitness, and the present OSP aims to minimize mutual coherence; hence, the minimization problem should be converted into a maximization problem. The concerned mutual coherence ranges between 0 and 1. The objective function is thus defined as

$$J = 1 - \mu\left(\mathbf{S}_{\phi}\right) \tag{5.8}$$

The fitness function operates on the encoded genes that measure the performance of a specific sensor configuration. A sensor configuration with a smaller mutual coherence has a higher fitness, then has a higher probability to survive. The OSP corresponds to the minimum mutual coherence, thereby containing the most information about structural parameters and leading to the most accurate and reliable damage identification results.

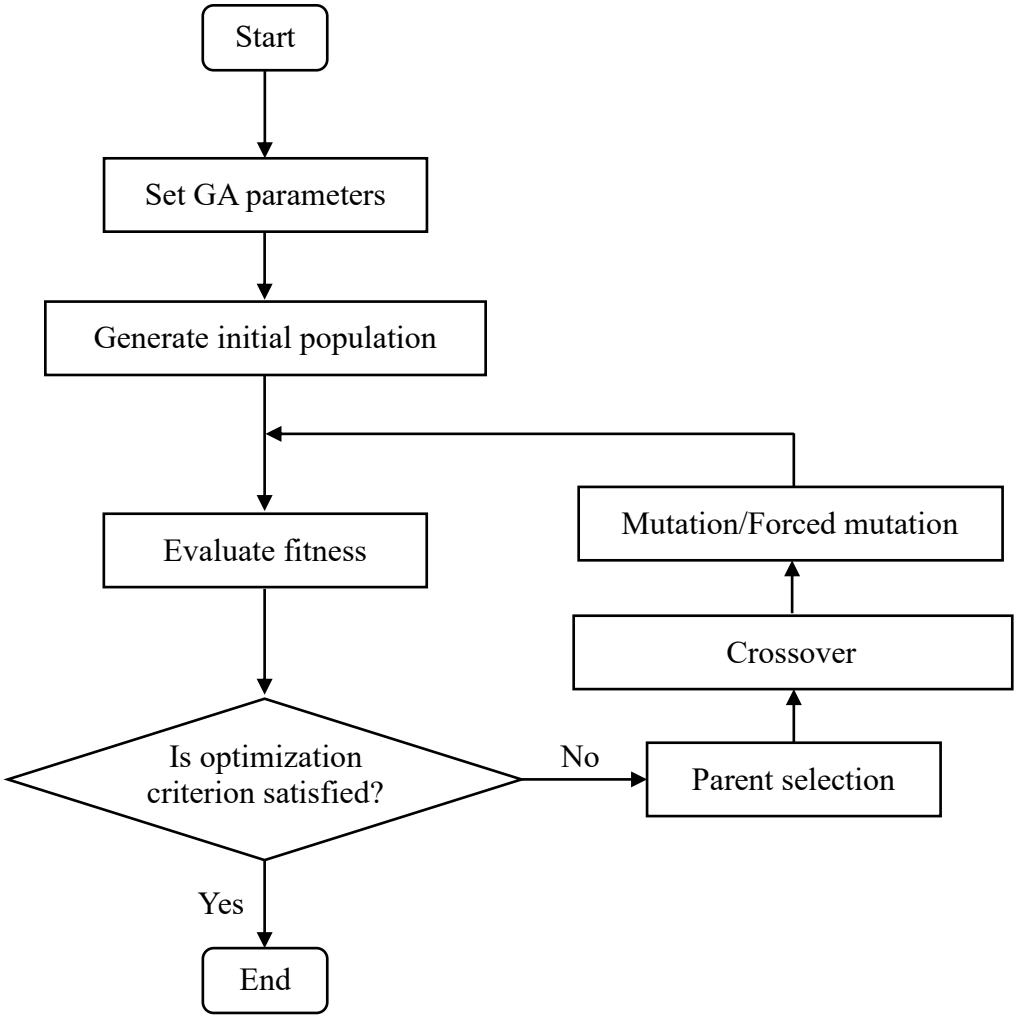

Figure 5.1 Flow chart of the GA

5.4 Case Studies

The experimental cantilever beam and the three-storey frame described in Chapter 3 are utilized to verify the effectiveness and reliability of the proposed sensor placement technique.

5.4.1 The Cantilever Beam

5.4.1.1 OSP using GA

The FE model and the SRFs for DS1 to DS4 of the cantilever beam are the same as introduced in Section 4.5.1. Although 10 sensors have been placed on the beam (i.e.

Nos. 1–10 in Figure 5.2), we select 5 points out of 10 to demonstrate the proposed OSP technique. Equation (5.8) is then maximized, and the maximum fitness corresponds to OSP. In the binary-coded GA, the population size is set to 100. The probabilities of crossover and mutation, i.e. p_c and p_m, are 0.85 and 0.1, respectively. The number of generations is 100.

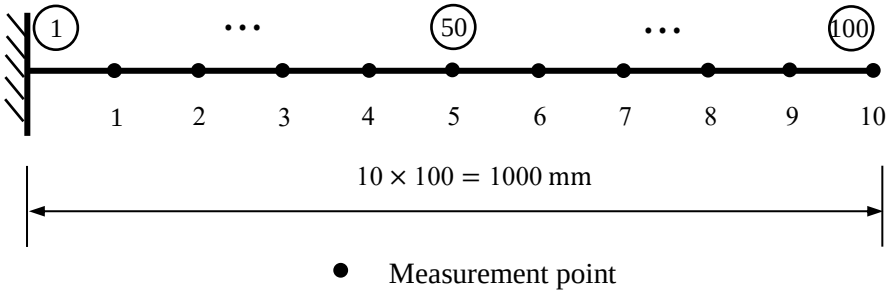

Figure 5.2 FE model and measurement configuration of the beam structure

The initial population in GA is randomly generated and may affect the converged results. Therefore, the presented GA runs 10 times to investigate the convergence and repeatability of the proposed sensor placement technique. The results show that the obtained sensor locations in 10 operations are identical, i.e. points 4, 6, 8, 9 and 10, as shown in Figure 5.3. The selected sensor locations are close to the free end of the cantilever beam. Be noted that the OSP is obtained from the undamaged FE model, thus independent of the damage condition. The numbers of generations upon convergence during the 10 runs are listed in Table 5.1. All runs converge within 10 generations, thus indicating the fast convergence of the present technique.

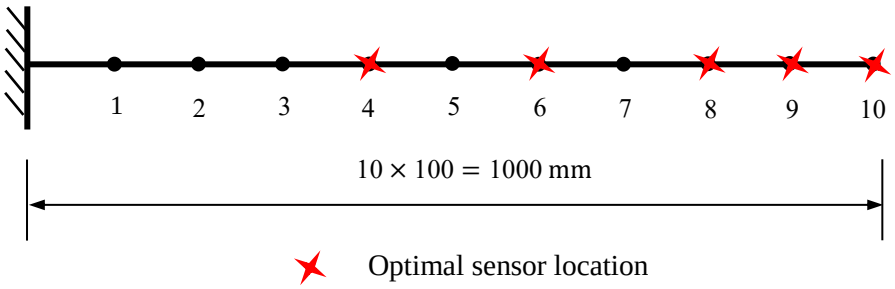

Figure 5.3 OSP of the beam structure

Table 5.1 Convergence of different initial populations.

Run no.	1	2	3	4	5	6	7	8	9	10
No. of generations upon convergence	9	8	7	8	6	8	8	8	9	5

The maximal and averaged fitness with respect to the generation history during one operation are shown in Figure 5.4. Both increase with the generation number. The maximum value tends to a constant rapidly, and the averaged fitness reaches the maximum after nine generations.

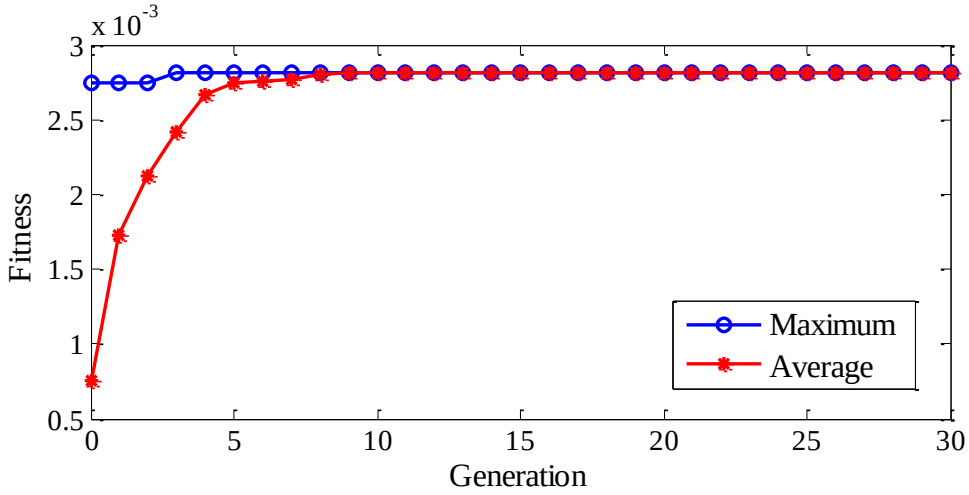

Figure 5.4 History of convergence for the OSP of the beam

5.4.1.2 Damage detection results

Damage detection is conducted using the selected sensor subset to demonstrate the effectiveness of the proposed OSP technique. The appropriate regularization parameter is determined utilizing the first strategy proposed in the previous chapter. The parameter which keeps both residual and solution norms small is determined as an appropriate regularization parameter.

The damage identification results of the four DSs are shown in Figure 5.5 together with the corresponding regularization parameters. The actual damage locations are detected successfully for all DSs. For DS1 and DS2, the identified damage severities are slightly larger than the true values, i.e. 40% and 60% reduction, respectively. For DS3, the

damage at the mid-span is quantified accurately, but the severity of the damaged element no. 1 is still larger than the true value. For DS4, the damaged elements (nos. 1, 50 and 75) are quantified with good accuracy. Although several elements are falsely identified as damaged, their SRF values are very small (less than 5%) and the errors can be ignored. Therefore, all DSs are correctly identified using the mode shapes that correspond to the proposed OSP. The present damage identification results are similar to those using 10 sensors as displayed in Section 4.5.1.

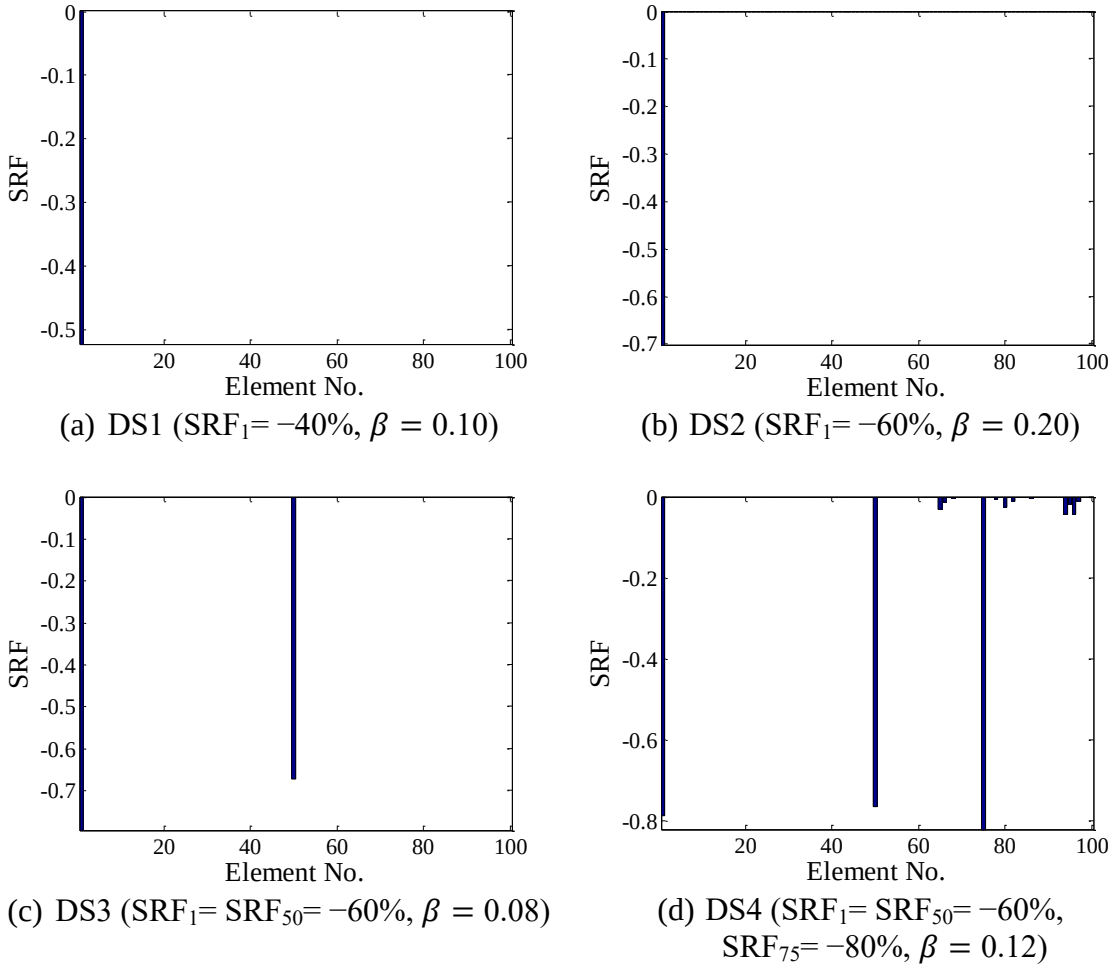

(a) DS1 ($SRF_1 = -40\%$, $\beta = 0.10$) (b) DS2 ($SRF_1 = -60\%$, $\beta = 0.20$)

(c) DS3 ($SRF_1 = SRF_{50} = -60\%$, $\beta = 0.08$) (d) DS4 ($SRF_1 = SRF_{50} = -60\%$, $SRF_{75} = -80\%$, $\beta = 0.12$)

Figure 5.5 Damage identification results for four DSs of the beam

5.4.2 The Three-storey Frame

5.4.2.1 OSP using GA

The proposed sensor placement technique is similarly applied to determine the sensor locations for the frame. The population size is set to 200. The crossover and mutation probabilities, i.e. p_c and p_m, are set to 0.85 and 0.1, respectively. The number of generations is 150.

As introduced previously, the frame has 39 candidate locations in total as shown in Figure 5.6. Two measurement selection schemes are studied to investigate the effect of the number of sensors. Scheme 1 has 20 points, and Scheme 2 has 15 points. Using the proposed algorithm, the selected measurement points for the two schemes are shown in Figure 5.7. Although the two different measurement schemes are determined independently, the selected sensor locations in Scheme 2 are from those of Scheme 1. Since the frame is symmetric, the selected sensor locations are almost symmetric. For both selection schemes, the selected points are all close to the free end as observed for the previous cantilever beam. Moreover, it can be seen that the beam-column joints are selected which are critical locations of the frame structure. For comparison, Scheme 3 has 15 points that are uniformly distributed on the beams and columns. This scheme represents a conventional sensor placement without optimization.

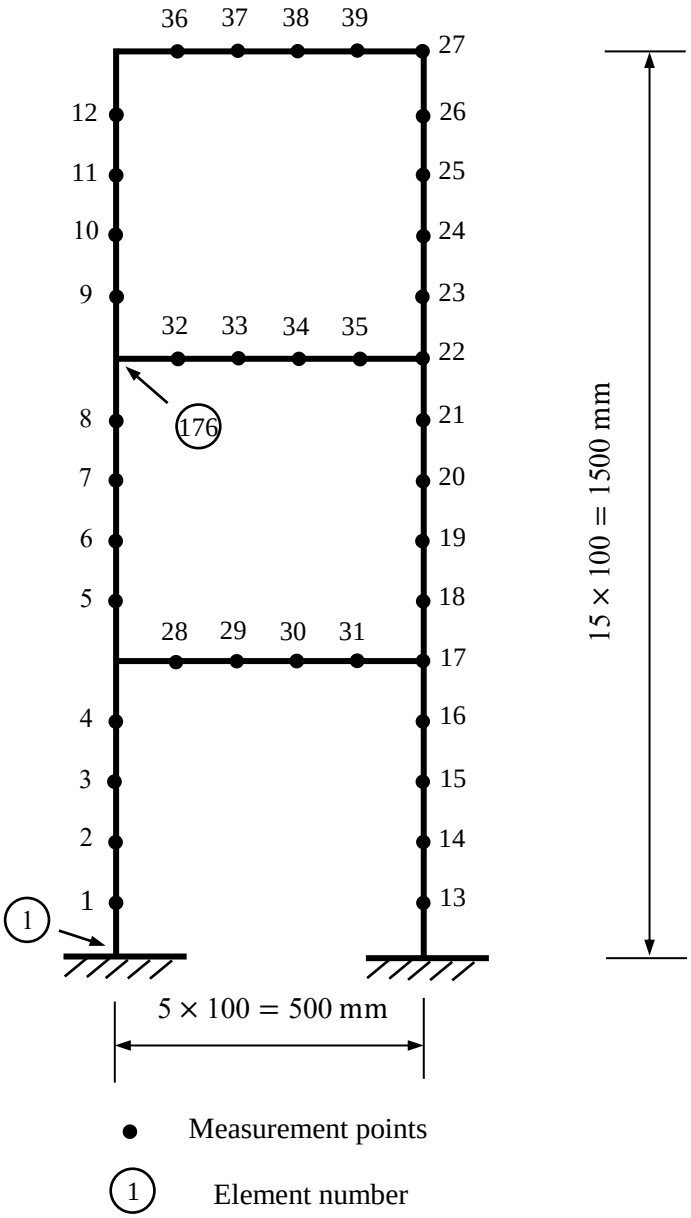

Figure 5.6 FE model and measurement configuration of the frame

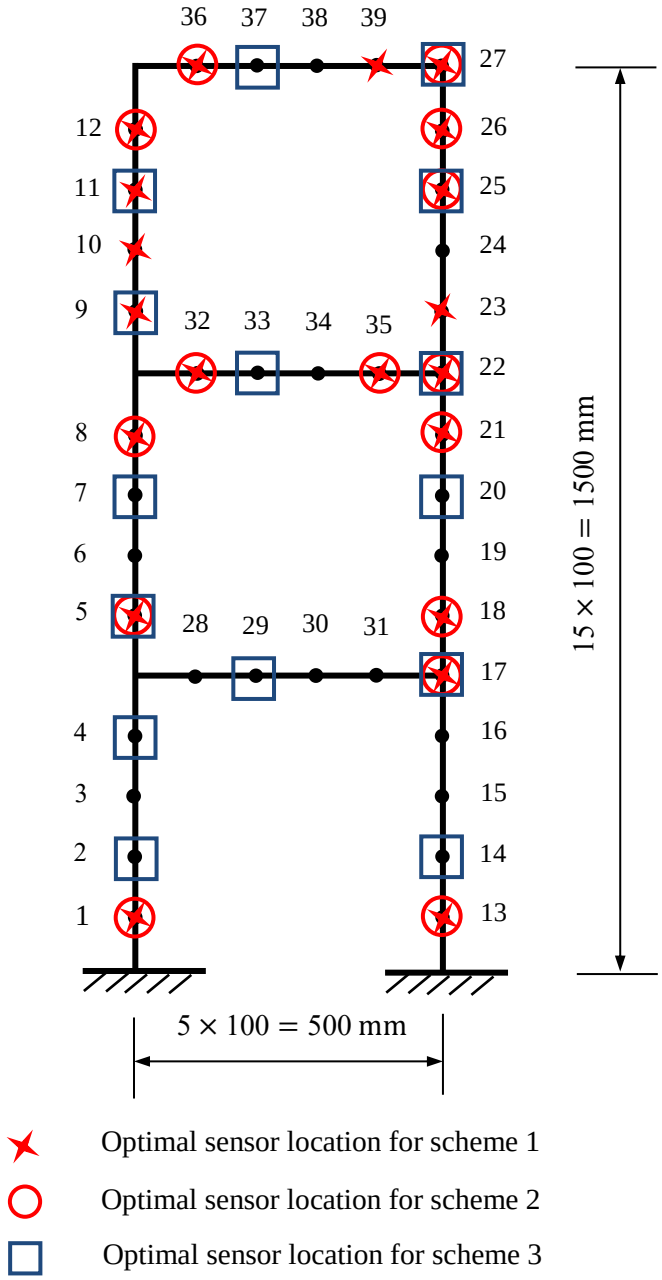

Figure 5.7 OSP of the frame

The fitness convergence curves for the two OSP schemes are shown in Figure 5.8. The maximum and average fitness values steadily tend to a constant with the increase in the generation number. When 20 points are required (Scheme 1), the average fitness reaches the maximum fitness value in 52 generations. When 15 points are selected (Scheme 2), it converges in 62 generations.

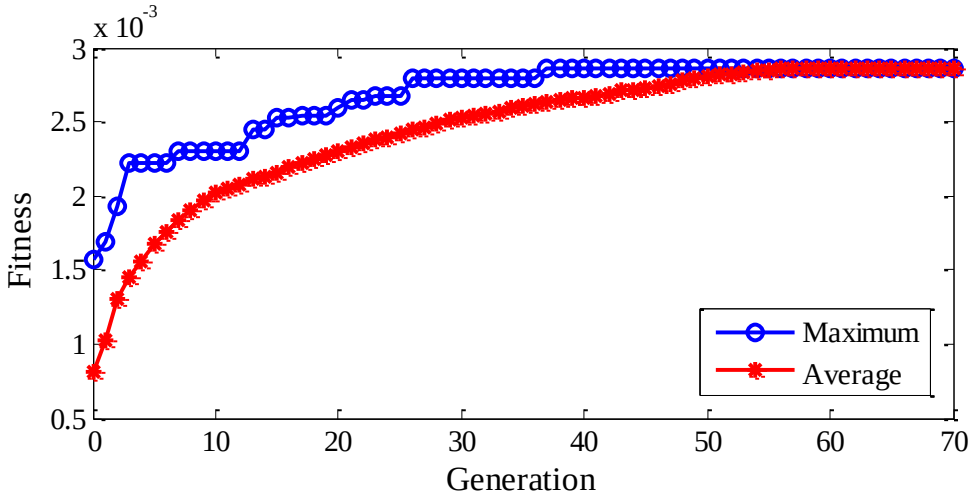

(a) Scheme 1: 20 measurement points

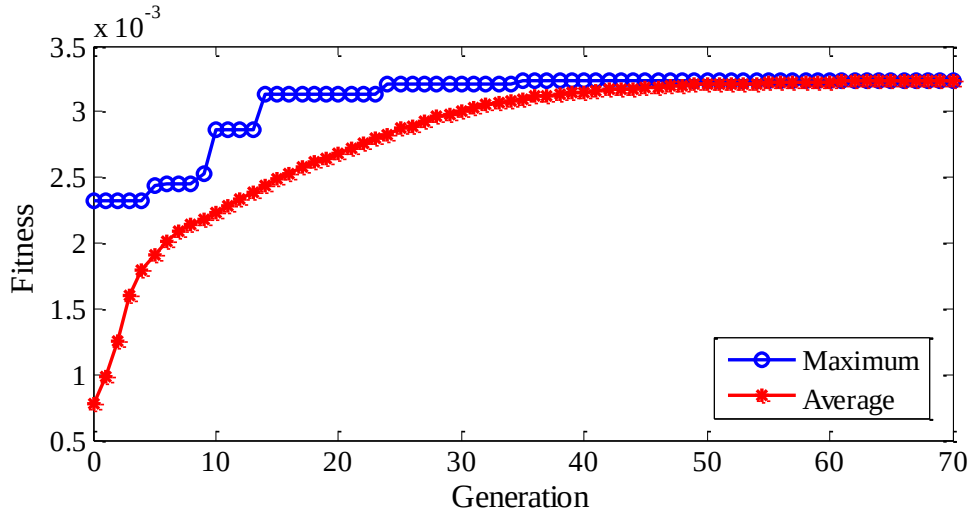

(b) Scheme 2: 15 measurement points

Figure 5.8 History of convergence for the OSP of the frame

In Schemes 1 and 2, the proposed GA is run for 10 times with different initial populations. The number of generations upon convergence is listed in Table 5.2. In the case of 20 measurement points, all 10 runs converge within 63 generations. In the other case of 15 measurement points, all 10 runs converge in 92 generations. The number of generations required for convergence in this structure is much more than that of the cantilever beam because the population size and chromosome length of the present example are larger than the beam. In both structures, 10 runs result in the same OSP. This result shows that the proposed GA based on mutual coherence is robust, and the obtained OSP is reliable.

Table 5.2 Convergence for different numbers of measurement points.

Run no.	Number of generations	
	Scheme 1 (20 measurement points)	Scheme 2 (15 measurement points)
1	58	62
2	42	63
3	45	84
4	63	68
5	62	63
6	56	92
7	63	64
8	57	80
9	50	60
10	63	70

5.4.2.2 Damage detection results

Damage detection of the frame is conducted using the measured frequencies and mode shapes that correspond to the selected sensor locations. For measurement Schemes 1 and 2, 168 and 128 measurement data are, respectively, available. The residual and solution norms are utilized to determine the appropriate regularization parameter.

The damage identification results of the three schemes for two DSs are shown in Figure 5.9. For DS1, the damage location and severity can be identified accurately using all three schemes. For DS2, two damaged elements (nos. 1 and 176) are located accurately, and no false identification occurs when Schemes 1 and 2 are used, although the identified damage severity has a small error. The numbers of measurement points for Schemes 2 and 3 are identical. However, the damage identification results for DS2 are different. For Scheme 3, the damaged element no. 1 is detected successfully, but the element no. 166 is not. These results show that sensor placement exerts a significant effect on damage detection accuracy and that damage can be accurately identified on the basis of the proposed OSP technique.

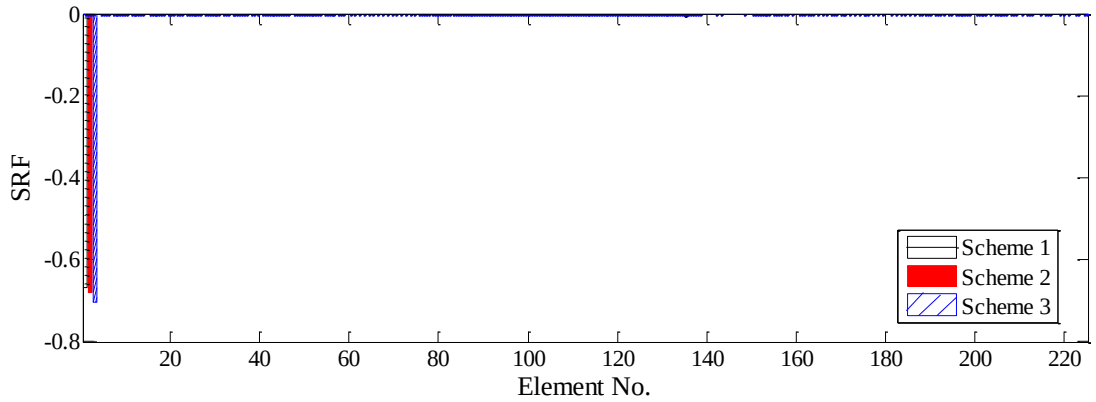

(a) DS1 ($SRF_1 = -60\%$)

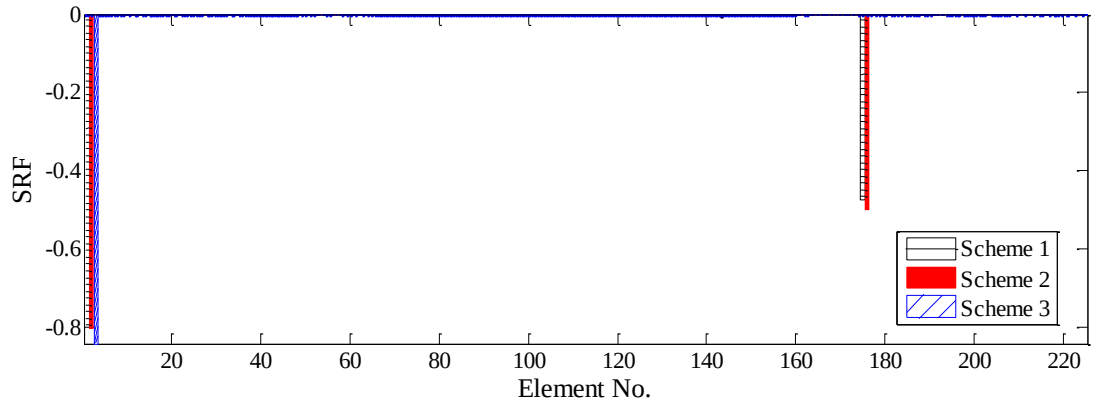

(b) DS2 ($SRF_1 = SRF_{176} = -60\%$)

Figure 5.9 Damage identification results of the frame using different measurement points

5.5 Summary

Sensor locations play an important role in damage identification, and selection of sensor locations is a combinatorial problem. A GA-based sensor placement technique is proposed in this chapter for minimizing the mutual coherence of the sensitivity matrix in the l_1-regularized damage detection. The present technique works on the sensitivity matrix in the undamaged state and thus does not need the prior knowledge of damage location and severity. Therefore, it is applicable to damage detection of real structures.

Although GAs usually depend on the initial population, the experimental studies demonstrate that the present GA offers consistent OSP results using different initial populations. Two examples also show that satisfactory damage detection results are

obtained using the modal data based on the optimal sensor configuration. Moreover, the l_1 regularization technique is effective in identifying sparse damage accurately.

CHAPTER 6

STRUCTURAL DAMAGE DETECTION BASED ON ITERATIVELY REWEIGHTED L_1 REGULARIZATION ALGORITHM

6.1 Introduction

In Chapter 4, an l_1 regularization-based damage detection method is developed to exploit the sparsity condition of structural damage. However, in practice, the solution obtained by the l_1 regularization technique is typically suboptimal. The l_0 regularization technique outperforms the l_1 regularization in various aspects for sparse recovery, whereas the associated nonconvex optimization problem is NP-hard and computationally infeasible. In this chapter, a damage detection method based on the IRLR algorithm is proposed. An iterative procedure is employed such that the nonconvex optimization problem of the l_0 regularization can be efficiently solved through transforming it into a series of weighted l_1 regularization problems.

6.2 L_1 and L_0 Regularization for Sparse Recovery

As metioned previously, the l_0 norm is an appropriate numerical measure of sparsity which counts the non-zero components of the vector. As a matter of fact, the l_0 regularization is the earliest regularization technique for sparse recovery which yields the sparsest solution (Taylor *et al*., 1979; Chartrand and Staneva, 2008; Xu *et al*., 2010). Previous studies show that the l_0 regularization technique outperforms the l_1 regularization in various aspects (Chartrand, 2007; Chartrand and Yin, 2008; Foucart and Lai, 2009; Saab and Yilmaz, 2010). For example, the former is more robust to noise than the latter (Chartrand and Staneva, 2008; Chen and Gu, 2015), whereas requires fewer measurements for exact recovery (Chartrand and Staneva, 2008; Chartrand, 2007).

Some researchers proposed that, under certain conditions, the l_1 regularization is equivalent to the l_0 regularization with high probability (Candès and Tao, 2006; Donoho, 2006b). However, the conditions, that guarantee the equivalence between l_0 and l_1 regularizations, are usually too strong to be satisfied in practical applications. For example, the sensing matrix in l_1 regularization should suffice certain independence criteria (Candès and Tao, 2005; Candès et al, 2006). For the present structural damage detection problem, the sensitivity matrix **S** serves as the sensing matrix. It is generally ill-conditioned because the columns are almost linearly dependent. Once the independence criteria are not satisfied, the solution is suboptimal (Zuo et al., 2013; Zhang, 2010). Both theoretical analysis and numerical experiments have shown that using the l_0 regularization often results in sparser solutions with smaller reconstruction error than using the l_1 regularization (Chartrand and Staneva, 2008; Xu *et al*., 2010; Chartrand, 2007; Cetin and Karl, 2001). Nevertheless, the l_0 regularization technique has not received widely applications due to its computational complexity as introduced in Section 4.2.

6.3 Damage Detection using IRLR Algorithm

In this chapter, a one-step FE model updating method is used, in which the measured modal parameters before and after damage are compared directly (Wu *et al*., 2018; Hao and Xia, 2002). Unlike the two-step model updating approach used in Chapter 4, the one-step technique will update the initial FE model such that the changes in the calculated modal parameters due to structural damage are close to the changes in the measured counterparts. The damage parameters $\boldsymbol{\theta}$ can be calculated by solving the below optimization problem instead

$$\widehat{\boldsymbol{\theta}} = \arg\min_{\boldsymbol{\theta}} \ \|\Delta \boldsymbol{R}^A(\boldsymbol{\theta}) - \Delta \boldsymbol{R}^E\|_2^2 \tag{6.1}$$

As introduced previously, the l_0 regularization technique is ideal to recover the sparse damage by adding an l_0 regularization term in the objective function as

$$\widehat{\boldsymbol{\theta}} = \arg\min_{\widehat{\boldsymbol{\theta}}} \ \|\Delta \boldsymbol{R}^A(\boldsymbol{\theta}) - \Delta \boldsymbol{R}^E\|_2^2 + \beta\|\boldsymbol{\theta}\|_0 \tag{6.2}$$

As aforementioned, the l_0 norm is nonconvex and discontinuous. Consequently, the optimization problem in Equation (6.2) is NP-hard and is generally impossible to be solved (Chartrand and Staneva, 2008; Zuo *et al*., 2013; Natarajan, 1995).

In order to achieve a balance between the recovery performance and the computational complexity, the IRLR algorithm is proposed as an effective alternative to the l_0 regularization technique (Candès *et al*., 2008). Rather than directly solving the nonconvex l_0 regularization problem, the IRLR algorithm proposed a weighted l_1 regularization as

$$\widehat{\boldsymbol{\theta}} = \arg\min_{\widehat{\boldsymbol{\theta}}} \ \|\Delta \boldsymbol{R}^A(\boldsymbol{\theta}) - \Delta \boldsymbol{R}^E\|_2^2 + \beta \sum_{i=1}^{n} w_i|\theta_i| \tag{6.3}$$

where w_i is the weight corresponding to the damage parameter θ_i and is constructed as

$$w_i = \frac{1}{|\theta_i|} \tag{6.4}$$

Since the weight is inversely proportional to the solution magnitude, the weighted l_1 minimization in Equation (6.3) is equivalent to the l_0 regularization.

As the true damage parameters θ_i are unknown in advance, the appropriate weights cannot be obtained directly. In this regard, an iterative procedure is proposed. In each iteration, the damage parameter θ_i in the previous run is used to estimate w_i as Equation (6.4). Equation (6.3) is then minimized to obtain a new damage parameter θ_i. The IRLR algorithm for structural damage detection is implemented as follows:

1. Initialize the weights $w_i^{(0)} = 1 \ \ (i = 1, 2, \ldots, n)$.
2. At the *k*th iteration $(k \geq 1)$

   Solve the weighted l_1 minimization problem

$$\widehat{\boldsymbol{\theta}}^{(k)} = \arg\min_{\widehat{\boldsymbol{\theta}}} \|\Delta \boldsymbol{R}^{A}(\boldsymbol{\theta}) - \Delta \boldsymbol{R}^{E}\|_2^2 + \beta \sum_{i=1}^{n} w_i^{(k-1)} |\theta_i| \tag{6.5}$$

Update the weights

$$w_i^{(k)} = \frac{1}{\left|\theta_i^{(k)}\right| + \zeta} \tag{6.6}$$

3. Repeat Step 2 for the (k+1)th iteration until the convergence criterion $\left\|\widehat{\boldsymbol{\theta}}^{(k)} - \widehat{\boldsymbol{\theta}}^{(k-1)}\right\|_2 / \left\|\widehat{\boldsymbol{\theta}}^{(k)}\right\|_2 \leq Tol$ is met or when k reaches a preset maximum iteration number $k_{\max}$.

The parameter $\zeta > 0$ is introduced in Equation (6.6) to provide stability and to ensure that the zero-valued items in $\boldsymbol{\theta}^{(k)}$ do not rigorously prohibit a nonzero estimate at the next step. Numerical results show that the IRLR algorithm is robust to the choice of ε (Candès *et al*., 2008). When both natural frequencies and mode shapes are utilized for damage detection, Equation (6.5) can be further rewritten as

$$\begin{aligned}\widehat{\boldsymbol{\theta}}^{(k)} = arg\min_{\widehat{\boldsymbol{\theta}}} \Bigg\{ & \frac{1}{m} \sum_{i=1}^{m} \left(\left[\frac{\lambda_i^A(\boldsymbol{\theta}) - \lambda_i^0}{\lambda_i^0} \right] - \left[\frac{\lambda_i^D - \lambda_i^U}{\lambda_i^U} \right] \right)^2 \\ & + \frac{1}{m \times np} \sum_{i=1}^{m} \sum_{j=1}^{np} \left(\left[\phi_{ji}^A(\boldsymbol{\theta}) - \phi_{ji}^0 \right] - \left[\phi_{ji}^D - \phi_{ji}^U \right] \right)^2 \\ & + \frac{\beta}{n} \sum_{i=1}^{n} w_i^{(k-1)} |\theta_i| \Bigg\}\end{aligned} \tag{6.7}$$

In each iteration, Step 2 solves an l_1 regularization problem, to which the existing algorithms can be effectively applied. During the iterative process, many weights w_i approach infinity, enforcing the corresponding damage parameters θ_i approaches zero. Consequently the sparsity of damage is ensured. The experimental example presented in the next section shows that the IRLR algorithm converges in a few steps.

6.4 Case Study

The 3D frame described in Chapter 3 is used here to demonstrate the effectiveness of the proposed method. Each bar of the frame is divided into 5 Euler-Bernoulli beam elements, resulting in a total of 225 elements in the FE model, each with 100 mm long. As shown in Table 6.1, the modal data of the FE model agree well with the experimental data.

Table 6.1 Modal data of the experimental model and initial FE model.

Mode No.	Experiment Freq. (Hz)	FE model Freq. (Hz)	Frequency difference (%)	MAC (%)
1	7.73	7.78	0.65	99.84
2	23.98	24.13	0.63	88.05
3	24.83	24.45	–1.53	93.55
4	37.43	37.03	–1.07	97.13
5	40.92	40.73	–0.46	98.59
6	59.97	60.58	1.02	98.72
	Average		0.89	95.98

The damaged Bar Nos.17 and 27 correspond to elements 81~85 and elements 131~135 in the FE model, respectively. The joint damage can be equivalently regarded as the change in the stiffness of the bar connecting the joint. The damaged elements for the four DSs are given in Table 6.2. The four DSs have at most seven damaged elements, which is extremely sparse compared to the total 225 elements. Given the first six frequencies and six mode shapes at 34 DOFs are utilized for damage detection, there are 210 measurement data. Therefore, the damage identification is an underdetermined problem. The parameter ζ used in the IRLR algorithm is suggested to be smaller than the expected nonzero magnitudes of the unknown vector (Candès *et al*., 2008). In this regard, the parameter ζ is set as 0.001. Moreover, numerical and experimental studies showed that the improvement of the accuracy of sparse recovery mainly benefits from the first few reweighting iterations. Therefore, the maximum iteration number and the convergence tolerance are set as $k_{max} = 10$ and $Tol = 0.001$, respectively. The regularization parameter β used in Equation (6.7) is determined from the residual and solution norms.

Table 6.2 Four DSs of the frame structure.

Scenario	DS1	DS2	DS3	DS4
Damaged elements No. in FE model	81~85	135	131 and 135	81~85, 131, and 135

The damage identification results for four DSs are shown in Figure 6.1 together with the corresponding regularization parameters. For DS1, the damaged elements (Nos.81~85) are detected correctly and no false identification occurs. For DS2, the joint damage at element 135 is correctly located with a considerable SRF. For DS3, damage at two ends of Bar No.27 (elements 131 and 135) are identified accurately with almost the same severities. For DS4, both damage of a bar and damage at the joints are located. In DS2~DS4, several intact elements are falsely identified with damage. Their SRFs are very small (less than 0.1), and the locations (elements 121 and 125 on Bar No.25) are very close to the true damage (Bar No.27). Therefore, the identification error is negligible.

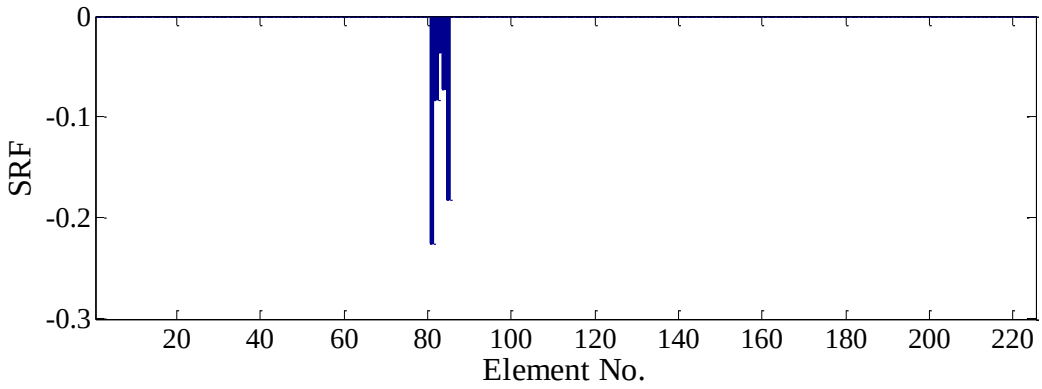

(a) DS1 ($\beta = 0.015$)

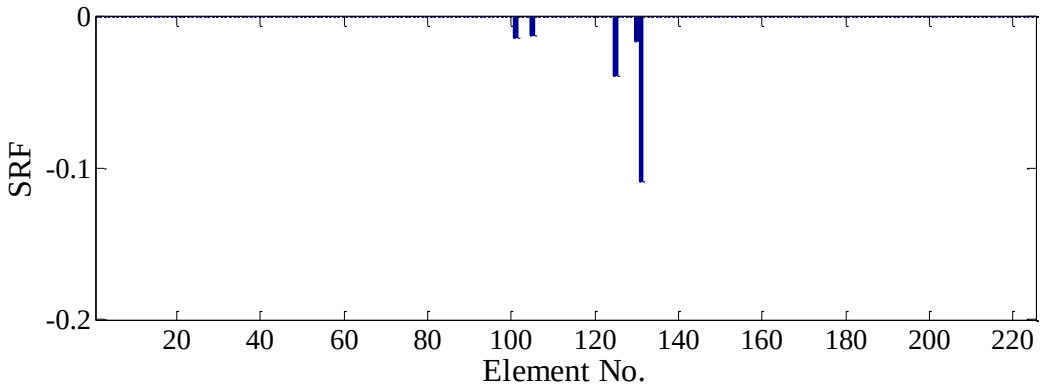

(b) DS2 ($\beta = 0.03$)

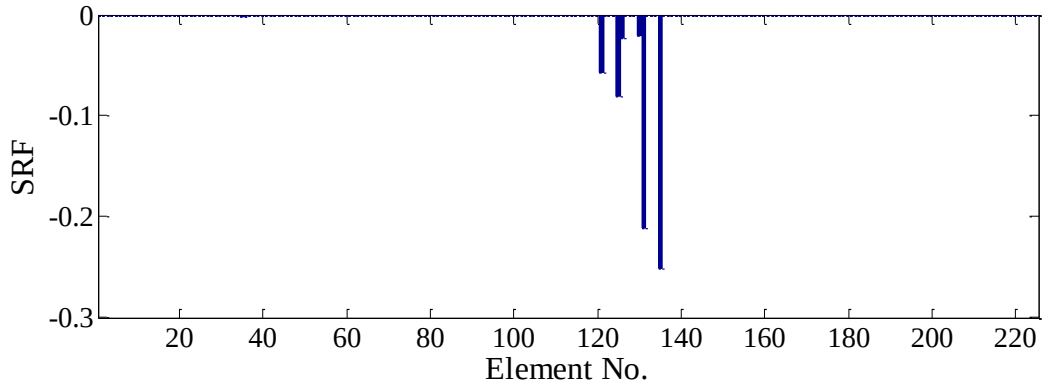

(c) DS3 ($\beta = 0.035$)

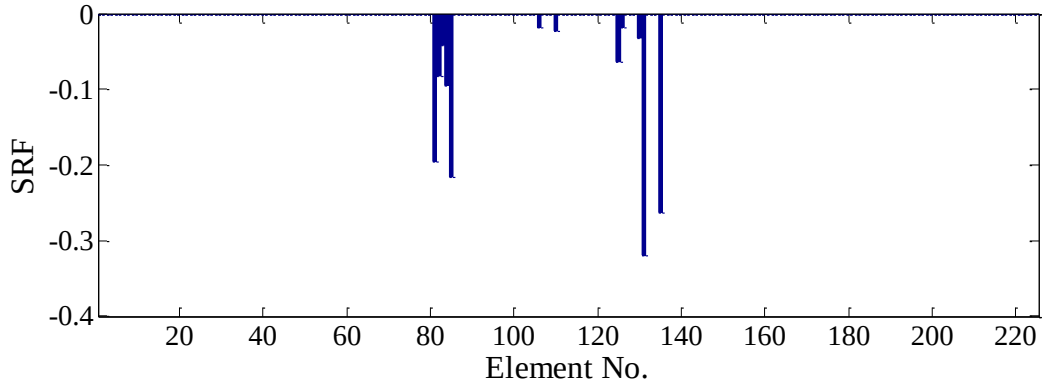

(d) DS4 ($\beta = 0.01$)

Figure 6.1 Damage identification results of the frame with the IRLR algorithm

For comparison purpose, the l_1 regularization technique without reweighting is also applied for damage identification, which aims to minimize the following objective function

$$\widehat{\boldsymbol{\theta}}^{(k)} = arg\min_{\hat{\boldsymbol{\theta}}} \left\{ \frac{1}{m}\sum_{i=1}^{m}\left(\left[\frac{\lambda_i^A(\boldsymbol{\theta})-\lambda_i^0}{\lambda_i^0}\right]-\left[\frac{\lambda_i^D-\lambda_i^U}{\lambda_i^U}\right]\right)^2 + \frac{1}{m\times np}\sum_{i=1}^{m}\sum_{j=1}^{np}\left(\left[\phi_{ji}^A(\boldsymbol{\theta})-\phi_{ji}^0\right]-\left[\phi_{ji}^D-\phi_{ji}^U\right]\right)^2 + \frac{\beta}{n}\sum_{i=1}^{n}|\theta_i| \right\} \tag{6.8}$$

The damage identification results of the four DSs are displayed in Figure 6.2. The SRF of DS1 is almost the same as that using the IRLR algorithm. For DSs 2–4, the SRF results are not sparse enough and quite a number of undamaged elements are falsely identified as damaged. The actual damaged elements cannot be well identified as their severities do not differ much from those of the falsely identified elements. The above

comparison demonstrates that the present damage detection method based on the IRLR algorithm is able to provide sparser and more accurate damage identification results than the l_1 regularization-based approach.

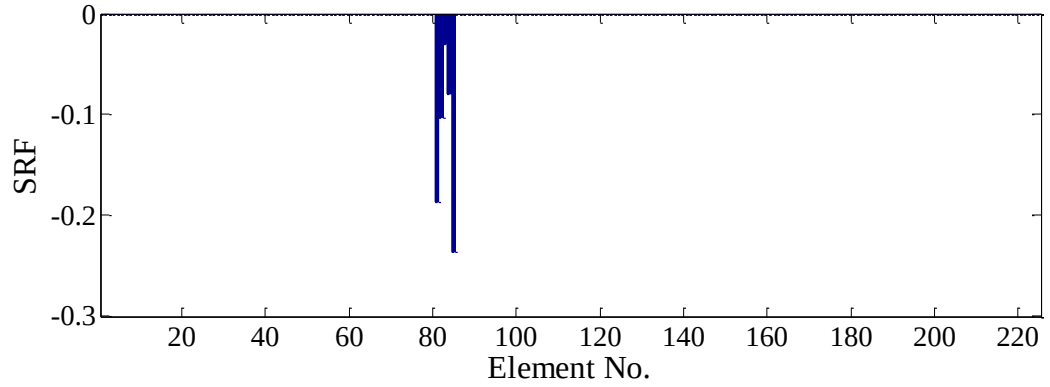

(a) DS1 ($\beta = 0.01$)

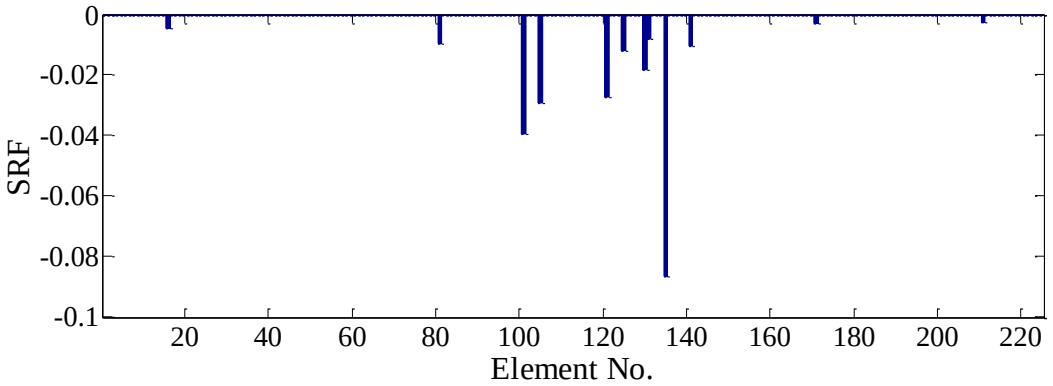

(b) DS2 ($\beta = 0.01$)

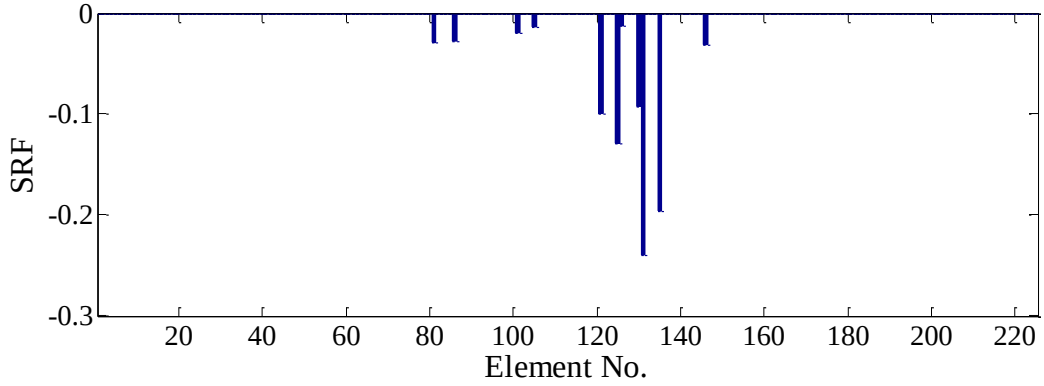

(c) DS3 ($\beta = 0.03$)

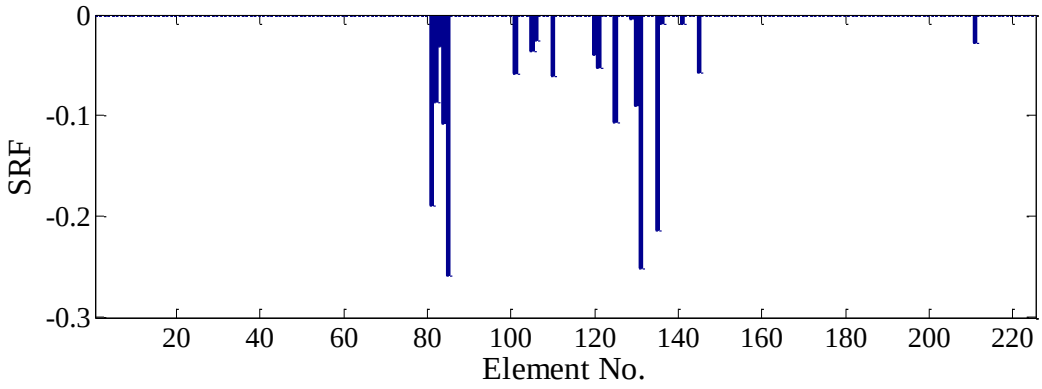

(d) DS4 ($\beta = 0.005$)

Figure 6.2 Damage identification results of the frame with the l_1 regularization technique

6.5 Summary

A sparse damage detection method is proposed in this chapter based on the IRLR algorithm. The sparse property of the structural damage has been exploited through an iterative procedure, which is equivalent to the l_0 regularization technique. Rather than directly solving the nonconvex l_0 regularization problem, the IRLR algorithm consists of a series of weighted l_1 minimization problem, which can be solved using the existing algorithms.

The experimental example shows that the proposed IRLR method is effective in identifying the sparse damage among a large number of potential elements, even when the changes of the modal parameters are very small. It is advantageous over the l_1 regularization technique and results in the sparser damage identification results with higher accuracy.

CHAPTER 7

SPARSE BAYESIAN LEARNING FOR STRUCTURAL DAMAGE DETECTION USING EXPECTATION–MAXIMIZATION TECHNIQUE

7.1 Introduction

Structural damage sparsity is an important prior information in practice. Previous chapters have demonstrated that exploiting this prior information results in accurate damage identification using the developed l_1 and l_0 regularization techniques. In this chapter, the sparsity of structural damage will be exploited from a Bayesian perspective.

Bayesian methods provide an efficient way to deal with the ill-posed and underdetermined problem by specifying probability distributions over uncertain parameters, which is equivalent to introducing a regularization term to the optimization problem (Williams, 1995). SBL is effective in promoting sparsity in the inferred predictors and has been rapidly developed recently in the context of regression and classification (Tipping, 2001; Wipf *et al*., 2003; Bishop, 2006). For linear regression problems, the latent variables and associated hyper-parameters are iteratively obtained using type-II maximization likelihood (Bishop, 2006). During the process, most hyper-parameters tend to approach infinity, and thus the corresponding latent variables approach zero, resulting in a sparse regression model. However, this method is ineffective in structural damage detection using modal parameters, which have a nonlinear relation with structural damage. Consequently, the analytical solution of the type-II maximization likelihood is unavailable.

Rather than directly tackling this nonlinear problem, Huang and Beck (2015) and Huang *et al.* (2017a) proposed an iterative procedure, which involves a series of coupled linear regression problems. A hierarchical SBL approach combined with Laplace's asymptotic

approximation was used to infer the stiffness reductions on the basis of experimentally identified modal parameters. However, all uncertain hyper-parameters of the sophisticated hierarchical Bayesian model should be estimated, which is a nontrivial task. Huang *et al.* (2017b) converted the nonlinear function of structural stiffness parameters into a series of coupled linear-in-the-parameter problems. Two Gibbs sampling algorithms representing a special case of the MCMC simulation were proposed to provide a full treatment of the posterior PDFs of uncertain parameters for damage assessment. However, the computational efficiency of posterior sampling for the MCMC methods remains a major concern. Mustafa *et al.* (2015) utilized linear optimization to identify the posterior statistics of the model parameters for model updating and damage detection, instead of solving the challenging nonlinear optimization problem.

In this chapter, an iterative EM technique is employed to tackle the nonlinear problem, without performing the asymptotic approximation or stochastic simulation. During the iteration, structural damage and hyper-parameters are updated through an expectation and maximization processes alternatively. Two sampling methods are utilized during the expectation procedure. Upon convergence, some hyper-parameters approach infinity and the associated damage variables become zero, resulting in the sparsity of damage.

7.2 Structural Model Class

The structural model class, $\mathcal{M}$, is based on a set of linear structural models, where each model has a known mass matrix **M** and an uncertain stiffness matrix **K** parameterized by the stiffness parameters α_i. The *r*th structural eigenvalue and the corresponding mode shape are governed by the following eigenvalue equation

$$(\mathbf{K} - \lambda_r \mathbf{M})\boldsymbol{\phi}_r = \mathbf{0} \tag{7.1}$$

Suppose that N_m modes of vibration have been identified from modal testing so that the identified eigenvalues and mode shapes can be expressed as

$$\boldsymbol{\lambda}^E = \{\lambda_1^E, \lambda_2^E, \cdots, \lambda_{N_m}^E\} \tag{7.2}$$

$$\boldsymbol{\Phi}^E = \left[\boldsymbol{\phi}_1^E, \boldsymbol{\phi}_2^E, \cdots, \boldsymbol{\phi}_{N_m}^E\right] \tag{7.3}$$

where $\boldsymbol{\phi}_r^E \in R^{N_p}$ denotes the identified mode shape of the *r*th mode at N_p measurement points. A set of modal data is expressed as

$$\boldsymbol{\mathcal{D}} = [\boldsymbol{\lambda}^E, \boldsymbol{\Phi}^E] \tag{7.4}$$

7.3 Bayesian Probabilistic Framework

Bayes' theorem is used to develop a PDF for the damage parameters $\boldsymbol{\theta}$, conditional on the measured modal data $\boldsymbol{\mathcal{D}}$ and chosen class of models $\mathcal{M}$ (Vanik *et al*., 2000)

$$p(\boldsymbol{\theta}|\boldsymbol{\mathcal{D}}, \mathcal{M}) = c^{-1} p(\boldsymbol{\mathcal{D}}|\boldsymbol{\theta}, \mathcal{M}) p(\boldsymbol{\theta}|\mathcal{M}) \tag{7.5}$$

where $p(\boldsymbol{\theta}|\boldsymbol{\mathcal{D}}, \mathcal{M})$ is the posterior PDF of the damage parameters given the modal data $\boldsymbol{\mathcal{D}}$ and model class $\mathcal{M}$; $c = p(\boldsymbol{\mathcal{D}}|\,\mathcal{M})$ is a normalizing constant referred to as evidence or marginal likelihood which does not affect the shape of the posterior distribution; $p(\boldsymbol{\mathcal{D}}|\boldsymbol{\theta}, \mathcal{M})$ is the likelihood function for the damage parameters $\boldsymbol{\theta}$; and $p(\boldsymbol{\theta}|\mathcal{M})$ is the prior PDF of the damage parameters. The evidence can be used to estimate the hyper-parameters, as described later.

In Bayeisan inference, the computation of the posterior probability of unknown parameters is usually intractable and the approximation tools are required. For example, the high-dimensional integral of the posterior PDF cannot be computed analytically. Based on the topology of the likelihood function $p(\boldsymbol{\mathcal{D}}|\boldsymbol{\theta}, \mathcal{M})$ and data $\boldsymbol{\mathcal{D}}$, three categories for a model class have been defined, i.e., globally identifiable, locally identifiable, and unidentifiable, corresponding to unique, multiple but isolated, and a continuum of maximum likelihood estimate (Huang *et al*., 2018).

If the model class is globally identifiable according to the available data $\boldsymbol{\mathcal{D}}$, Laplace's approximation method can be used to approximate the integral in the evidence $p(\boldsymbol{\mathcal{D}}|\,\mathcal{M})$ (Beck and Katafygiotis, 1998; Beck, 2010). However, Laplace's approximation has several limitations, one of which is that the accuracy of the

approximation depends on the dimension of the parameter vector (Onar, 2014). If the measurements are considerably fewer than the model parameters, then the corresponding Bayesian updating results may be inaccurate. For the unidentifiable and locally identifiable problems, simulation-based techniques, such as MCMC samplers, can be used to compute the posterior statistics of unknown parameters (Metropolis *et al.*, 1953; Ching and Chen, 2007; Cheung and Beck, 2010; Lam *et al.*, 2018; Nichols *et al.*, 2010). However, the MCMC algorithm has high computational cost, especially for models with numerous parameters to be inferred. Moreover, evaluating convergence and accuracy for the MCMC methods is difficult, even when conducted empirically.

7.4 Sparse Bayesian Modelling

7.4.1 Likelihood Functions for Damage Parameters

In this section, a sparse Bayesian model is developed which automatically promotes sparsity in the inferred damage parameters θ. To simplify the notation, the dependence of the PDF on $\mathcal{M}$ is dropped hereafter.

According to the axioms of probability, the PDF of the modal data $p(\boldsymbol{\mathcal{D}}|\boldsymbol{\theta})$ in Equation (7.5) can be expressed as (Vanik and Beck, 2000)

$$p(\boldsymbol{\mathcal{D}}|\boldsymbol{\theta}) = \prod_{r=1}^{N_m} p(\lambda_r^E|\boldsymbol{\theta}) p(\boldsymbol{\phi}_r^E|\boldsymbol{\theta}) \tag{7.6}$$

To construct the prior distribution, the measurement error is introduced to the measured eigenvalues and mode shapes as

$$\lambda_r(\boldsymbol{\theta}) = \lambda_r^E(1 + \nu_r) \tag{7.7}$$

$$\boldsymbol{\phi}_r(\boldsymbol{\theta}) = \boldsymbol{\phi}_r^E + \boldsymbol{e}_r \tag{7.8}$$

where ν_r and $\boldsymbol{e}_r$ are measurement errors of frequencies and mode shapes, respectively, and are treated as independent Gaussian variables as (Ching and Beck, 2004; Jaynes, 2003).

$$\nu_r \sim N(0, \eta^{-1}) \tag{7.9}$$

$$\boldsymbol{e}_r \sim N(0,\ \gamma^{-1}\boldsymbol{I}) \tag{7.10}$$

where hyper-parameters η and γ reflect the precision of the identified eigenvalues $\boldsymbol{\lambda}^E$ and mode shapes $\boldsymbol{\Phi}^E$, respectively. In this chapter, the precision, which is equal to the reciprocal of the variance of the variables, is used instead of the variance for convenience. The resulting likelihood function of $\boldsymbol{\theta}$ based on the measured eigenvalues $\boldsymbol{\lambda}^E$ is

$$p(\boldsymbol{\lambda}^E|\boldsymbol{\theta},\eta) = \left(\frac{\eta}{2\pi}\right)^{\frac{N_m}{2}} exp\left\{-\frac{\eta}{2}\sum_{r=1}^{N_m}\left[\frac{\lambda_r(\boldsymbol{\theta}) - \lambda_r^E}{\lambda_r^E}\right]^2\right\} \tag{7.11}$$

and the likelihood function of $\boldsymbol{\theta}$ based on the measured mode shapes $\boldsymbol{\Phi}^E$ is

$$p(\boldsymbol{\Phi}^E|\boldsymbol{\theta},\gamma) = \left(\frac{\gamma}{2\pi}\right)^{\frac{N_p \cdot N_m}{2}} exp\left\{-\frac{\gamma}{2}\sum_{r=1}^{N_m}\|\boldsymbol{\phi}_r^E - \boldsymbol{\phi}_r(\boldsymbol{\theta})\|_2^2\right\} \tag{7.12}$$

7.4.2 Prior Distribution for Damage Parameters

As introduced previously, the prior PDF of the damage parameters is chosen to provide regularization for the ill-posed inverse damage detection problem. SBL proposes to use the ARD prior to incorporating a preference for sparser parameters (Tipping, 2001; Huang *et al*., 2017; Mackay, 1992; Huang *et al*., 2018). Accordingly, the ARD prior is adopted in this chapter to promote sparsity in the damage parameters. The damage parameters $\boldsymbol{\theta}$ are assumed to be Gaussian with zero mean and covariance matrix $\boldsymbol{A} = diag(\rho_1^{-1}, \cdots, \rho_n^{-1})$, such that

$$p(\boldsymbol{\theta}|\boldsymbol{\rho}) = \prod_{i=1}^{n} p(\theta_i|\rho_i) = \left(\frac{1}{2\pi}\right)^{\frac{n}{2}} \prod_{i=1}^{n}\left[\rho_i^{\frac{1}{2}}\, exp\left\{-\frac{1}{2}\rho_i\theta_i^2\right\}\right] \tag{7.13}$$

where the individual hyper-parameter ρ_i represents the precision of the associated damage parameter θ_i.

7.4.3 Posterior Distribution for Damage Parameters

From Equation (7.5), the posterior PDF of the damage parameters $\boldsymbol{\theta}$ is expressed as

$$\begin{aligned} p(\boldsymbol{\theta}|\boldsymbol{\lambda}^E, \boldsymbol{\Phi}^E, \boldsymbol{\rho}, \eta, \gamma) &= c^{-1} p(\boldsymbol{\lambda}^E|\boldsymbol{\theta}, \eta) p(\boldsymbol{\Phi}^E|\boldsymbol{\theta}, \gamma) p(\boldsymbol{\theta}|\boldsymbol{\rho}) \\ &= c^{-1} \left(\frac{\eta}{2\pi}\right)^{\frac{N_m}{2}} \left(\frac{\gamma}{2\pi}\right)^{\frac{N_p \cdot N_m}{2}} \left(\frac{1}{2\pi}\right)^{\frac{n}{2}} \left(\prod_{i=1}^{n} \rho_i^{\frac{1}{2}}\right) exp\left\{-\frac{\eta}{2}\sum_{r=1}^{N_m}\left[\frac{\lambda_r(\boldsymbol{\theta}) - \lambda_r^E}{\lambda_r^E}\right]^2\right. \\ &\left. -\frac{\gamma}{2}\sum_{r=1}^{N_m}\|\boldsymbol{\phi}_r^E - \boldsymbol{\phi}_r(\boldsymbol{\theta})\|_2^2 - \frac{1}{2}\sum_{i=1}^{n}(\rho_i \theta_i^2)\right\} \end{aligned} \quad (7.14)$$

with the distributions on the right-hand side as defined by Equations (7.11), (7.12), and (7.13), respectively. This posterior probability distribution will be used to quantify the plausibility of all possible values of the damage parameters.

7.5 Bayesian Inference Using EM Algorithm

The posterior PDF of the damage parameters, as defined in Equation (7.14), depends on the estimates of the hyper-parameters $\boldsymbol{\xi} = \{\boldsymbol{\rho}, \eta, \gamma\}$, which can be obtained by maximizing the evidence $p(\boldsymbol{\lambda}^E, \boldsymbol{\Phi}^E|\boldsymbol{\xi})$, known in the statistics literature as type-II maximization likelihood (Bishop, 2006). As introduced previously, the evidence is the normalizing term that appears in the denominator in Bayes' theorem. According to the Total Probability Theorem, the evidence is obtained by integrating over the damage parameters as

$$p(\boldsymbol{\lambda}^E, \boldsymbol{\Phi}^E|\boldsymbol{\xi}) = \int p(\boldsymbol{\theta}, \boldsymbol{\lambda}^E, \boldsymbol{\Phi}^E|\boldsymbol{\rho}, \eta, \gamma) d\boldsymbol{\theta} = \int p(\boldsymbol{\lambda}^E|\boldsymbol{\theta}, \eta) p(\boldsymbol{\Phi}^E|\boldsymbol{\theta}, \gamma) p(\boldsymbol{\theta}|\boldsymbol{\rho}) d\boldsymbol{\theta} \quad (7.15)$$

However, the computation of the integral in Equation (7.15) is intractable, as the frequencies and mode shapes are in nonlinear relations with $\boldsymbol{\theta}$.

In this study, the EM algorithm is proposed to maximize the natural log evidence $\ln p(\boldsymbol{\lambda}^E, \boldsymbol{\Phi}^E|\boldsymbol{\xi})$ instead. The EM algorithm enables parameter estimation in probabilistic models, where the model depends on unobserved latent variables. It alternates between performing an expectation (E) step and a maximization (M) step. $\boldsymbol{\theta}$ is regarded as a latent variable and $\{\boldsymbol{\theta}, \boldsymbol{\lambda}^E, \boldsymbol{\Phi}^E\}$ is referred to as the complete data set. The complete-data natural log likelihood function is expressed as

$$\begin{aligned}\ln p\,(\boldsymbol{\theta}, \boldsymbol{\lambda}^E, \boldsymbol{\Phi}^E|\boldsymbol{\xi}) &= \ln p(\boldsymbol{\lambda}^E|\boldsymbol{\theta}, \eta) + \ln p(\boldsymbol{\Phi}^E|\boldsymbol{\theta}, \gamma) + \ln p(\boldsymbol{\theta}|\boldsymbol{\rho}) \\ &= \frac{N_m}{2}\ln\left(\frac{\eta}{2\pi}\right) - \frac{\eta}{2}\sum_{r=1}^{N_m}\left[\frac{\lambda_r^E - \lambda_r(\boldsymbol{\theta})}{\lambda_r^E}\right]^2 + \frac{N_0 \cdot N_m}{2}\ln\left(\frac{\gamma}{2\pi}\right) \\ &- \frac{\gamma}{2}\sum_{r=1}^{N_m}\|\boldsymbol{\phi}_r^E - \boldsymbol{\phi}_r(\boldsymbol{\theta})\|_2^2 + \frac{n}{2}\ln\left(\frac{1}{2\pi}\right) + \frac{1}{2}\sum_{i=1}^{n}\ln\rho_i - \frac{1}{2}\sum_{i=1}^{n}(\rho_i\theta_i^2)\end{aligned} \tag{7.16}$$

Given the difficulty of direct maximization of $\ln p(\boldsymbol{\lambda}^E, \boldsymbol{\Phi}^E|\boldsymbol{\xi})$ with respect to $\boldsymbol{\xi}$, the EM algorithm proposes to maximize the expectation of the complete-data $E\{\ln p\,(\boldsymbol{\theta}, \boldsymbol{\lambda}^E, \boldsymbol{\Phi}^E|\boldsymbol{\xi})\}$ instead (Bishop, 2006; Dempster *et al*., 1977), such that

$$\begin{aligned}E\{\ln p\,(\boldsymbol{\theta}, \boldsymbol{\lambda}^E, \boldsymbol{\Phi}^E|\boldsymbol{\xi})\} &= \frac{N_m}{2}\ln\left(\frac{\eta}{2\pi}\right) - \frac{\eta}{2}E\left\{\sum_{r=1}^{N_m}\left[\frac{\lambda_r^E - \lambda_r(\boldsymbol{\theta})}{\lambda_r^E}\right]^2\right\} \\ &+ \frac{N_p \cdot N_m}{2}\ln\left(\frac{\gamma}{2\pi}\right) - \frac{\gamma}{2}E\left\{\sum_{r=1}^{N_m}\|\boldsymbol{\phi}_r^E - \boldsymbol{\phi}_r(\boldsymbol{\theta})\|_2^2\right\} + \frac{n}{2}\ln\left(\frac{1}{2\pi}\right) \\ &+ \frac{1}{2}\sum_{i=1}^{n}\ln\rho_i - \frac{1}{2}\sum_{i=1}^{n}\rho_i E(\theta_i^2)\end{aligned} \tag{7.17}$$

In practice, the complete data set is not available and the latent variable $\boldsymbol{\theta}$ is given by the posterior distribution $p(\boldsymbol{\theta}|\boldsymbol{\lambda}^E, \boldsymbol{\Phi}^E, \boldsymbol{\xi})$. In the E step, given the current value of the hyper-parameter $\boldsymbol{\xi}^{\text{old}}$, the posterior distribution of $\boldsymbol{\theta}$ given by $p\left(\boldsymbol{\theta}\middle|\boldsymbol{\lambda}^E, \boldsymbol{\Phi}^E, \boldsymbol{\xi}^{\text{old}}\right)$ is used to determine the expectation of the complete-data $E\{\ln p\,(\boldsymbol{\theta}, \boldsymbol{\lambda}^E, \boldsymbol{\Phi}^E|\boldsymbol{\xi})\}$. In the subsequent M step, the new estimate $\boldsymbol{\xi}^{\text{new}}$ is obtained by maximizing the expectation

with respect to $\boldsymbol{\xi}$. By differentiating Equation (7.17) with respect to $\boldsymbol{\rho}$, η, and γ, and then setting these derivatives to zero, we obtain

$$\frac{\partial E\{\ln p\,(\boldsymbol{\theta}, \boldsymbol{\xi}|\boldsymbol{\lambda}^E, \boldsymbol{\Phi}^E)\}}{\partial \rho_i} = \frac{1}{2\rho_i} - \frac{1}{2}E(\theta_i^2) = 0 \tag{7.18}$$

$$\frac{\partial E\{\ln p\,(\boldsymbol{\theta}, \boldsymbol{\xi}|\boldsymbol{\lambda}^E, \boldsymbol{\Phi}^E)\}}{\partial \eta} = \frac{N_m}{2}\frac{1}{\eta} - \frac{1}{2}\,E\left\{\sum_{r=1}^{N_m}\left[\frac{\lambda_r^E - \lambda_r(\boldsymbol{\theta})}{\lambda_r^E}\right]^2\right\} = 0 \tag{7.19}$$

$$\frac{\partial E\{\ln p\,(\boldsymbol{\theta}, \boldsymbol{\xi}|\boldsymbol{\lambda}^E, \boldsymbol{\Phi}^E)\}}{\partial \gamma} = \frac{N_p \cdot N_m}{2}\frac{1}{\gamma} - \frac{1}{2}E\left\{\sum_{r=1}^{N_m}\|\boldsymbol{\phi}_r^E - \boldsymbol{\phi}_r(\boldsymbol{\theta})\|_2^2\right\} = 0 \tag{7.20}$$

The hyper-parameters are then solved as

$$\rho_i = \frac{1}{E(\theta_i^2)} \tag{7.21}$$

$$\eta = \frac{N_m}{E\left\{\sum_{r=1}^{N_m}\left[\frac{\lambda_r^E - \lambda_r(\boldsymbol{\theta})}{\lambda_r^E}\right]^2\right\}} \tag{7.22}$$

$$\gamma = \frac{N_p \cdot N_m}{E\left\{\sum_{r=1}^{N_m}\|\boldsymbol{\phi}_r^E - \boldsymbol{\phi}_r(\boldsymbol{\theta})\|^2\right\}} \tag{7.23}$$

$E\{\cdot\}$ denotes an expectation with respect to the posterior distribution of $\boldsymbol{\theta}$ using the current estimates of the hyper-parameters $\boldsymbol{\xi}^{\text{old}}$.

7.5.1 Posterior Sampling

Posterior sampling is conducted to approximate the expectations in Equations (7.21), (7.22), and (7.23). We first approximate the conditional posterior PDF $p(\boldsymbol{\theta}|\boldsymbol{\lambda}^E, \boldsymbol{\Phi}^E, \boldsymbol{\rho}, \eta, \gamma)$ of stiffness parameter $\boldsymbol{\theta}$ in Equation (7.14) by a multivariate Gaussian distribution using Laplace's method of asymptotic approximation (Beck and Katafygiotis, 1998). This is based on the assumption that the modal data $\boldsymbol{\mathcal{D}} = [\boldsymbol{\lambda}^E, \boldsymbol{\Phi}^E]$ available is sufficient to constrain the updated parameter $\boldsymbol{\theta}$ to give a globally identifiable model class. The mean of the Gaussian distribution is the MAP estimate $\widehat{\boldsymbol{\theta}}$,

which is calculated by maximizing $\ln p\left(\boldsymbol{\theta}|\boldsymbol{\lambda}^E, \boldsymbol{\Phi}^E, \boldsymbol{\xi}\right)$, or equivalently minimizing the following objective function

$$J(\boldsymbol{\theta}) = \eta \sum_{r=1}^{N_m} \left[\frac{\lambda_r^E - \lambda_r(\boldsymbol{\theta})}{\lambda_r^E}\right]^2 + \gamma \sum_{r=1}^{N_m} \sum_{j=1}^{N_p} \left[\phi_{jr}^E - \phi_{jr}(\boldsymbol{\theta})\right]^2 + \sum_{i=1}^{n} (\rho_i \theta_i^2) \tag{7.24}$$

The covariance matrix $\boldsymbol{\Sigma}_{\boldsymbol{\theta}}$ of the approximated Gaussian distribution is equal to the inverse of the Hessian matrix $\mathcal{H}\left(\widehat{\boldsymbol{\theta}}\right)$ calculated at $\widehat{\boldsymbol{\theta}}$, where the ($i$, j) component of the Hessian matrix $\mathcal{H}\left(\widehat{\boldsymbol{\theta}}\right)$ is given by

$$\mathcal{H}_{i,j}\left(\widehat{\boldsymbol{\theta}}\right) = \left.\frac{\partial^2 J(\boldsymbol{\theta})}{\partial \boldsymbol{\theta}_i \partial \boldsymbol{\theta}_j}\right|_{\boldsymbol{\theta}=\widehat{\boldsymbol{\theta}}} \tag{7.25}$$

Since the dimension of $\boldsymbol{\theta}$ is large, the obtained covariance matrix is not positive semi-definiteness. In this regard, we calculate the variance for each damage parameter θ_i independently (Vanik and Beck, 2000). Then we generate samples from the posterior PDF $p(\boldsymbol{\theta}|\boldsymbol{\lambda}^E, \boldsymbol{\Phi}^E, \boldsymbol{\rho}, \eta, \gamma)$ and the probabilistic information encapsulated in $p(\boldsymbol{\theta}|\boldsymbol{\lambda}^E, \boldsymbol{\Phi}^E, \boldsymbol{\rho}, \eta, \gamma)$ is characterized by the posterior samples $\boldsymbol{\theta}^{(k)}, k = 1, \ldots, K$. The expectations in (7.21), (7.22) and (7.23) are finally approximated by (7.26), (7.27) and (7.28), respectively

$$E(\theta_i^2) = \int \theta_i^2 p(\theta_i|\boldsymbol{\lambda}^E, \boldsymbol{\Phi}^E, \boldsymbol{\rho}, \eta, \gamma) d\theta_i \approx \frac{1}{K} \sum\nolimits_{k=1}^{K} \left((\theta_i)^{(k)}\right)^2 \tag{7.26}$$

$$\begin{aligned} E\left\{\sum_{r=1}^{N_m} \left[\frac{\lambda_r^E - \lambda_r(\boldsymbol{\theta})}{\lambda_r^E}\right]^2\right\} &= \int \sum_{r=1}^{N_m} \left[\frac{\lambda_r^E - \lambda_r(\boldsymbol{\theta})}{\lambda_r^E}\right]^2 p(\theta_i|\boldsymbol{\lambda}^E, \boldsymbol{\Phi}^E, \boldsymbol{\rho}, \eta, \gamma) d\boldsymbol{\theta} \\ &\approx \frac{1}{K} \sum\nolimits_{k=1}^{K} \sum_{r=1}^{N_m} \left[\frac{\lambda_r^E - \lambda_r\left(\boldsymbol{\theta}^{(k)}\right)}{\lambda_r^E}\right]^2 \end{aligned} \tag{7.27}$$

$$E\left\{\sum_{r=1}^{N_m}\|\boldsymbol{\phi}_r^E-\boldsymbol{\phi}_r(\boldsymbol{\theta})\|^2\right\}=\int\sum_{r=1}^{N_m}\|\boldsymbol{\phi}_r^E-\boldsymbol{\phi}_r(\boldsymbol{\theta})\|^2\,p(\theta_i|\boldsymbol{\lambda}^E,\boldsymbol{\Phi}^E,\boldsymbol{\rho},\eta,\gamma)d\boldsymbol{\theta}$$
$$\approx\frac{1}{K}\sum_{r=1}^{N_m}\left\|\boldsymbol{\phi}_r^E-\boldsymbol{\phi}_r\left(\boldsymbol{\theta}^{(k)}\right)\right\|^2 \tag{7.28}$$

7.5.2 Likelihood Sampling

Considering the complexity of the posterior PDF $p(\boldsymbol{\theta}|\boldsymbol{\lambda}^E,\boldsymbol{\Phi}^E,\boldsymbol{\rho},\eta,\gamma)$, which might not be Gaussian, another sampling method is proposed based on the likelihood function of $\boldsymbol{\theta}$. N_s sets of modal data $\boldsymbol{\mathcal{D}}_j=[\boldsymbol{\lambda}^{E_j},\boldsymbol{\Phi}^{E_j}]$ $(j=1,2,\dots,N_s)$, are generated according to the measured modal data following Gaussian distribution, that is, Equations (7.9) and (7.10). The mean of the Gaussian distribution is equal to the measured modal data with assigned variance. For each data set, given the current estimates of the hyper-parameters $\boldsymbol{\xi}$, the MAP estimate $\widehat{\boldsymbol{\theta}}$ is calculated by minimizing the objective function in Equation (7.24). The expectation is then performed with respect to the MAP values of $\boldsymbol{\theta}$ as

$$E(\theta_i^2)=E\left(\hat{\theta}_i^2\right) \tag{7.29}$$

$$E\left\{\sum_{r=1}^{N_m}\left[\frac{\lambda_r^E-\lambda_r(\boldsymbol{\theta})}{\lambda_r^E}\right]^2\right\}=E\left\{\sum_{r=1}^{N_m}\left[\frac{\lambda_r^E-\lambda_r\left(\widehat{\boldsymbol{\theta}}\right)}{\lambda_r^E}\right]^2\right\} \tag{7.30}$$

$$E\left\{\sum_{r=1}^{N_m}\|\boldsymbol{\phi}_r^E-\boldsymbol{\phi}_r(\boldsymbol{\theta})\|^2\right\}=E\left\{\sum_{r=1}^{N_m}\left\|\boldsymbol{\phi}_r^E-\boldsymbol{\phi}_r\left(\widehat{\boldsymbol{\theta}}\right)\right\|^2\right\} \tag{7.31}$$

7.5.3 Summary

Each iteration uses estimates of $\boldsymbol{\xi}$ to determine the posterior distribution of the latent variable $\boldsymbol{\theta}$. The current distribution of $\boldsymbol{\theta}$ is in turn utilized to improve the estimates of $\boldsymbol{\xi}$. The proposed EM algorithm is implemented as follows:

1. Initialize the hyper-parameters $\boldsymbol{\xi}^{(0)}$ and latent variable $\boldsymbol{\theta}^{(0)}$.
2. At the *i*th iteration,

   E step: Compute the MAP estimates of $\widehat{\boldsymbol{\theta}}^{(i)}$ through minimizing $J(\boldsymbol{\theta})$ in Equation (7.24) given hyper-parameters $\boldsymbol{\xi}^{(i-1)}$; Calculate the expectations in Equations

(7.21)~(7.23) using (7.26)~(7.28) for the posterior sampling or (7.29)~(7.31) for the likelihood sampling;

M step: Through maximization of $E\{\ln p\,(\boldsymbol{\theta}, \boldsymbol{\lambda}^E, \boldsymbol{\Phi}^E|\boldsymbol{\xi})\}$ with respect to $\boldsymbol{\rho}$, η, and γ, update the hyper-parameters to $\boldsymbol{\xi}^{(i)}$ according to Equations (7.21), (7.22), and (7.23), given $\widehat{\boldsymbol{\theta}}^{(i)}$.

3. Repeat Step 2 for the (i+1)th iteration until the following convergence criterion is met:

$$\left\|\widehat{\boldsymbol{\theta}}^{(i)} - \widehat{\boldsymbol{\theta}}^{(i-1)}\right\|_2 / \left\|\widehat{\boldsymbol{\theta}}^{(i)}\right\|_2 \leq Tol$$

It is noted that the posterior sampling is conducted after E step once $\widehat{\boldsymbol{\theta}}^{(i)}$ is obtained at each iteration step, whereas the likelihood sampling is conducted at the initialization stage only.

7.6 Case Studies

A numerical and an experimental cantilever beams described in Chapter 3 are employed to demonstrate the effectiveness of the proposed EM-based SBL method.

7.6.1 The Numerical Cantilever Beam

In this numerical example, the natural frequencies only are used for damage detection. Therefore, the objective function in Equation (7.24) is simplified as

$$J_1(\boldsymbol{\theta}) = \eta \sum_{r=1}^{N_m} \left[\frac{\lambda_r^E - \lambda_r(\boldsymbol{\theta})}{\lambda_r^E}\right]^2 + \sum_{i=1}^{n} (\rho_i \theta_i^2) \tag{7.32}$$

To implement the EM process, the hyper-parameters $\boldsymbol{\rho}$ and η should be initialized by setting them to the precision of the uncertainties. The uncertainty level of the damage parameters is assumed as 10% of the exact damage parameter. Therefore, the initial value $\rho_i^{(0)} = 1/(10\%)^2 = 100$ ($i = 1, 2, \ldots, 45$). In practical vibration tests, natural frequencies may typically contain 1% noise (Xia and Hao, 2003; Adewuyi *et al.*, 2009; Mottershead and Friswell, 1993; Hou *et al.*, 2018). Consequently, $\eta^{(0)} = 1/(1\%)^2 = 1 \times 10^4$. The ratio of ρ_i to η is analogous to the regularization parameter used in the

IRLS algorithm, which is $\rho_i^{(0)} / \eta^{(0)} = 0.01$ in the current example. The initial damage parameters $\boldsymbol{\theta}^{(0)}$ are set at their nominal values $\boldsymbol{\theta}^{(0)} = \{0, \ldots, 0\}^T$, indicating that no damage is present.

With the minimization of Equation (7.32), the MAP values of the damage parameters are then obtained. Using the posterior sampling, 5000 samples of $\boldsymbol{\theta}^{(k)}$ are generated and then the hyper-parameters are calculated through Equations (7.21)~(7.23) and (7.26)~(7.28). With the proposed iterative EM, the MAP values of $\boldsymbol{\theta}$ in each iteration are updated and shown in Figure 7.1. In the first iteration, a number of elements have non-zero SRFs. After one more iteration, the identified damage parameters tend to approach the actual values and the process converges after three iterations only.

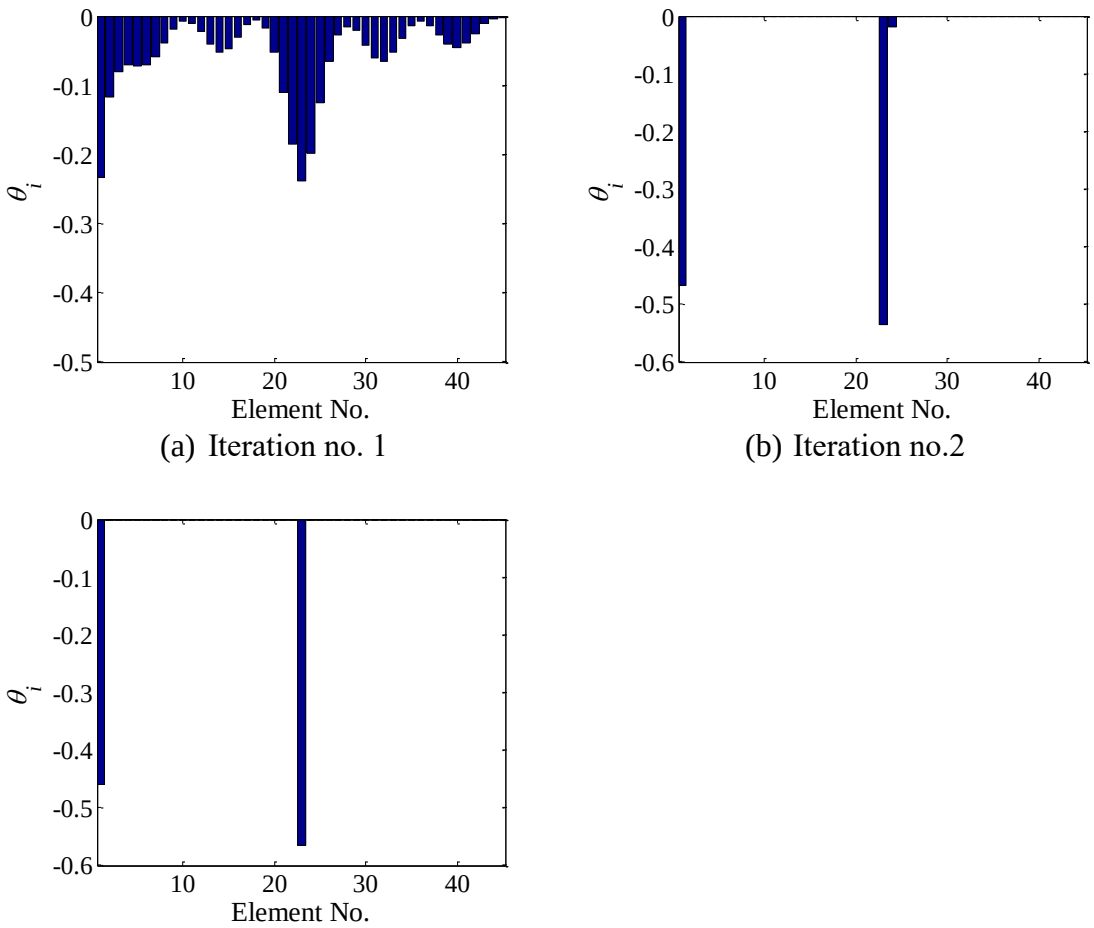

(a) Iteration no. 1

(b) Iteration no.2

(c) Iteration no.3

Figure 7.1 Damage identification results during the iterative process using posterior sampling

The likelihood sampling is then also applied, in which 50 sets of natural frequencies are generated (i.e., N_s=50) with Gaussian distribution having a zero mean and 1% standard deviations of the true values. Within EM, each set of sampled natural frequencies results in one set of MAP values of the damage parameters, from which the expectations are calculated according to Equations (7.29)~(7.31). The mean of the MAP values of $\boldsymbol{\theta}$ in each iteration are shown in Figure 7.2. Similar to the above results, the damage parameters converge after four iterations only and the actual damaged elements are correctly located and quantified. Although the likelihood sampling approach takes one more iteration, the identified damage parameters are more accurate than those of the posterior sampling.

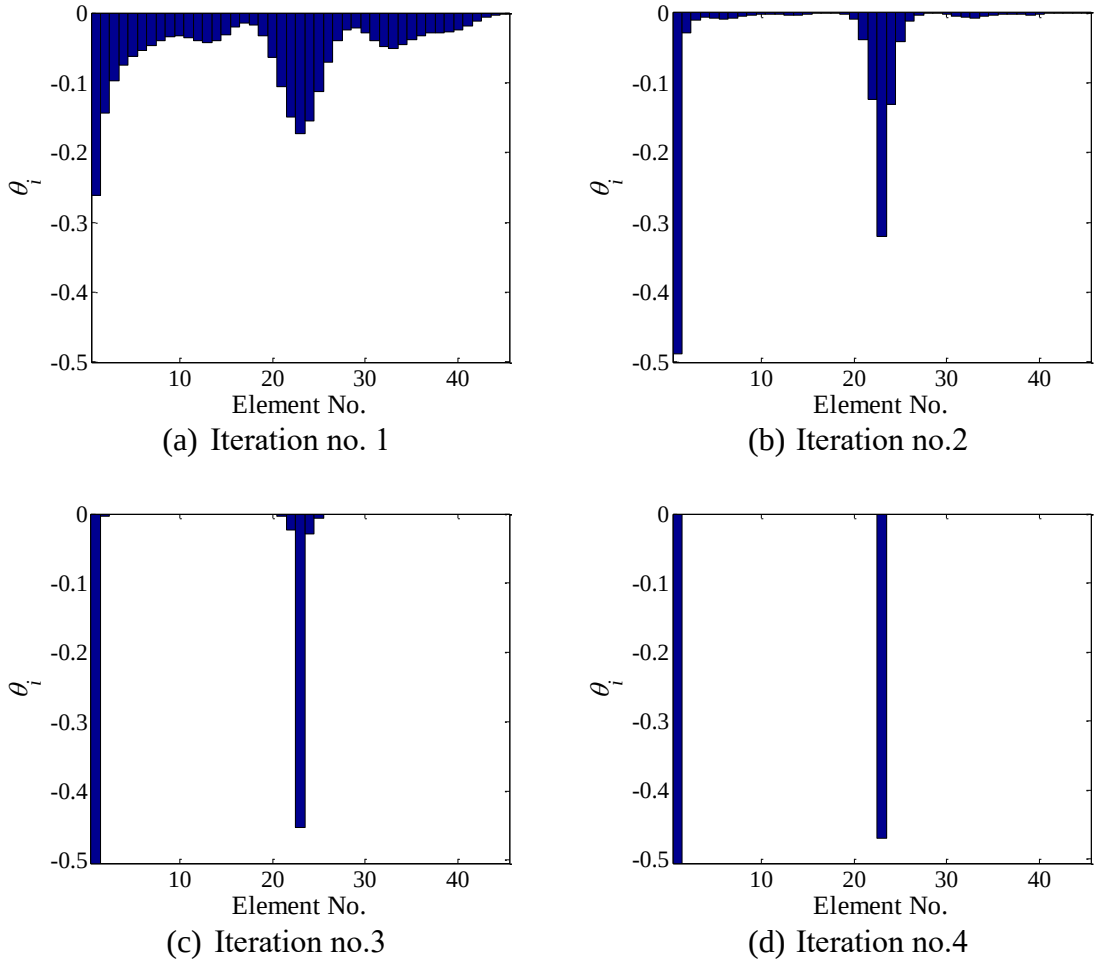

Figure 7.2 Damage identification results during the iterative process using likelihood sampling

During the iteration, the hyper-parameters also change continuously. η and a few representative ρ_i are shown in Figure 7.3 for the two sampling methods. As the iteration proceeds, the hyper-parameters associated with the damaged elements, i.e., ρ_1 and ρ_{23}, decrease quickly and converge after only a few iterations. For the undamaged Element 45, the corresponding hyper-parameter ρ_{45} increases rapidly to a sizeable number (a logarithmic coordinate is used). The variation of η is not significant during the process.

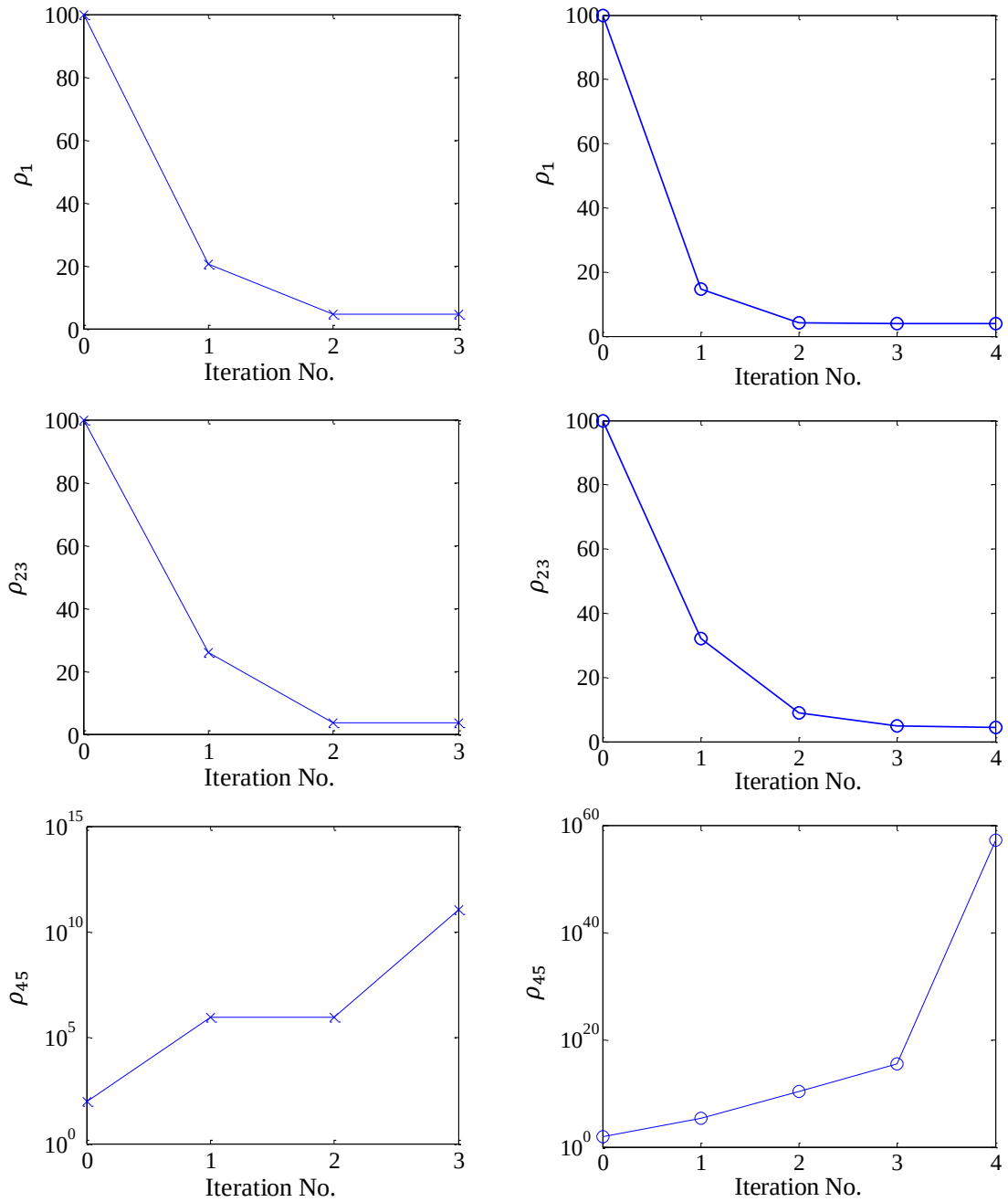

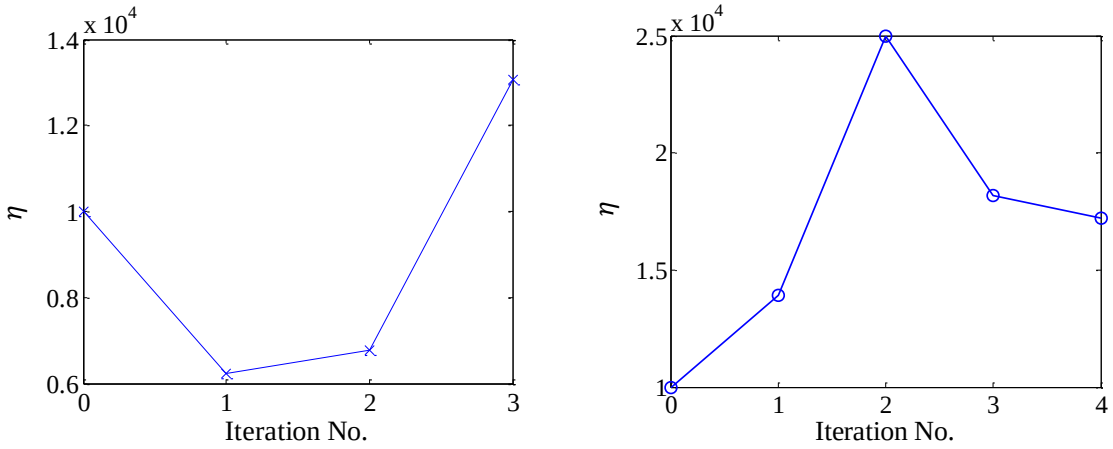

(a) Posterior sampling (b) Likelihood sampling

Figure 7.3 Variation of hyper-parameters during the iterative process

To investigate the effect of noise on damage detection accuracy, a different level of Gaussian noise of the frequencies is introduced, namely, Noise Level 2 has a zero mean and 2% standard deviation of the exact natural frequencies. In this regard, the initial estimate of the hyper-parameter η becomes $1/(2\%)^2 = 2.5 \times 10^3$. Therefore, the equivalent regularization parameters is 0.04, with the initial $\rho_i^{(0)} = 100 \quad (i = 1, 2, \dots, 45)$ remaining unchanged.

Using the same EM procedure, the identified MAP values of the damage parameters are shown in Figures 7.4 and 7.5 using two sampling methods. The convergence occurs in three and four iterations, respectively. In the case of the posterior sampling, the true damage at Element 1 is detected correctly, whereas Element 23 at the mid-span cannot. Using the likelihood sampling, both damaged elements are located accurately and the identified SRFs are close to their actual values.

The above numerical results show that the proposed EM algorithm is effective in locating and quantifying structural damage. For the posterior sampling, the convergence rate is faster; while the damage identification results obtained are not accurate as compared with the likelihood sampling, especially at the higher noise level. Previous studies indicated that the main disadvantage of the EM algorithm is its slow convergence in some cases (Ching and Beck, 2004; Dempster *et al.*, 1977). However, the proposed EM algorithm for damage detection has fast convergence. All converge within four iterations for the two noise levels.

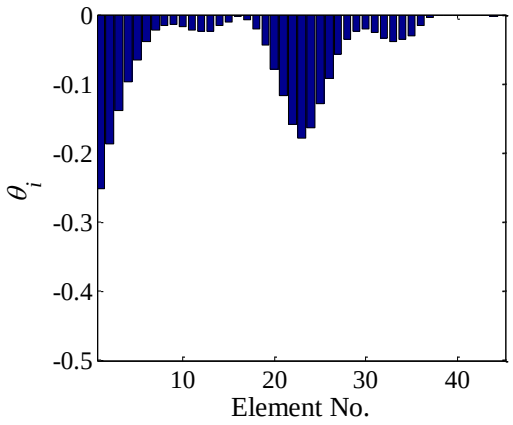

(a) Iteration no. 1

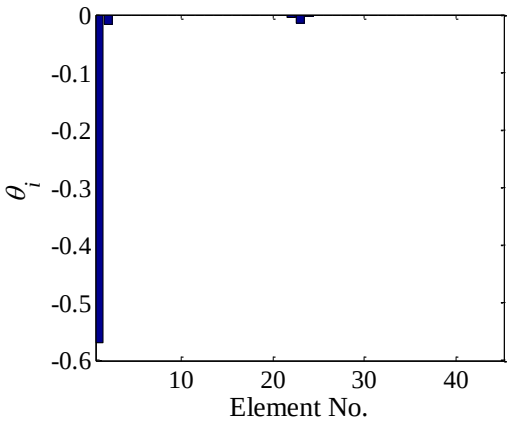

(b) Iteration no.2

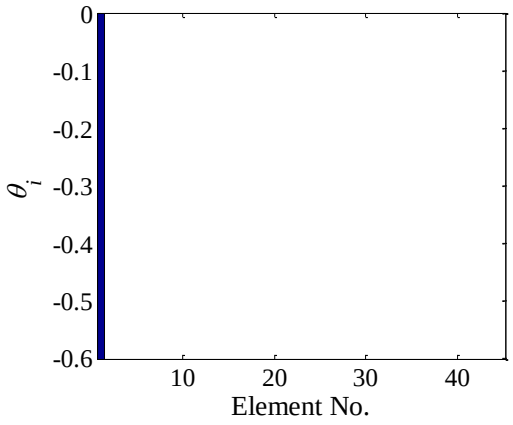

(c) Iteration no.3

Figure 7.4 Damage identification results for Noise level 2 using posterior sampling

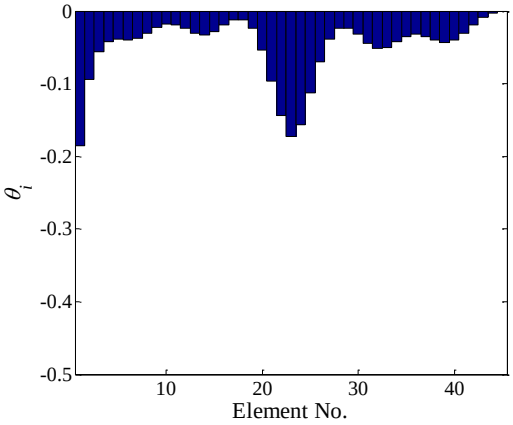

(a) Iteration no.1

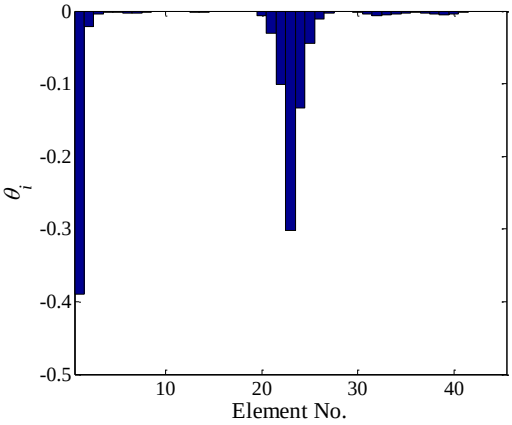

(b) Iteration no.2

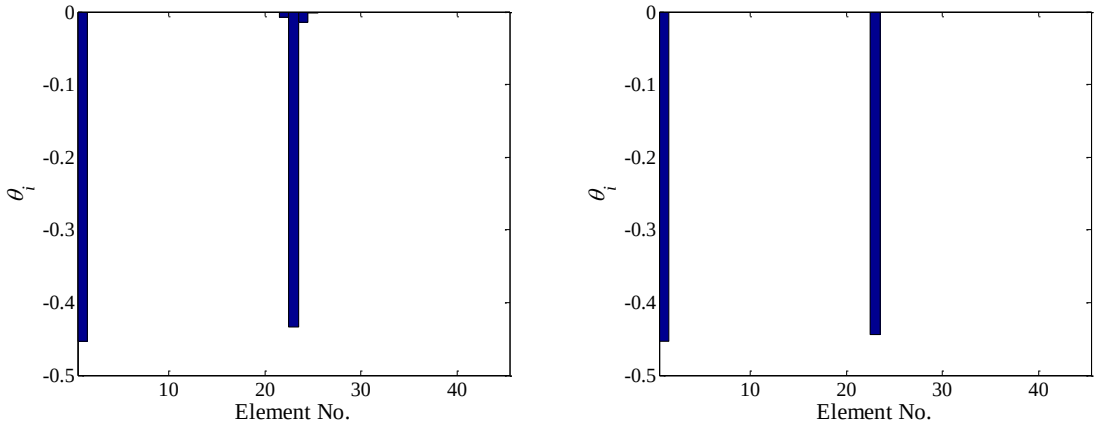

(c) Iteration no.3 (d) Iteration no.4

Figure 7.5 Damage identification results for Noise level 2 using likelihood sampling

7.6.2 The Experimental Cantilever Beam

The proposed EM technique is then applied to the experimental beam studied in Section 4.5.1, which is divided into 100 Euler–Bernoulli beam elements, each 10 mm long. The damage locations and severities quantified by SRF for the four DSs are introduced in Table 4.1.

In the experimental beam, only one set of measured modal data are available. In the likelihood sampling, 50 sets of modal data $\boldsymbol{\mathcal{D}}_j = [\boldsymbol{\lambda}^{E_j}, \boldsymbol{\Phi}^{E_j}]$ $(j = 1, 2, \dots, 50)$ are generated as λ_r^E

$$\lambda_r^{E_j} \sim N(\lambda_r^E, (0.01\lambda_r^E)^2) \tag{7.33}$$

$$\boldsymbol{\phi}_r^{E_j} \sim N(\boldsymbol{\phi}_r^E, (0.05)^2 \boldsymbol{I}) \tag{7.34}$$

where the uncertainty levels of 1% and 5% are adopted for natural frequencies and mode shapes, respectively, as natural frequencies are generally measured more accurately than mode shapes. The hyper-parameters are thus initialized as $\eta^{(0)} = 1 \times 10^4$, $\gamma^{(0)} = 400$ and $\rho_i^{(0)} = 100$ $(i = 1,2, \dots,100)$.

First, only the natural frequencies are utilized for damage detection. Following the iterative procedures summarized in Section 7.5.3, the most plausible values of the

damage parameters can be obtained using the two proposed sampling methods. To quantify the damage identification accuracy, the identification error τ is defined as

$$\tau = \sqrt{\frac{\left\|\hat{\boldsymbol{\theta}} - \overline{\boldsymbol{\theta}}\right\|_2^2}{n}} \tag{7.35}$$

where $\overline{\boldsymbol{\theta}}$ denotes the actual damage parameters (i.e., SRF) in the experiment. The damage identification results of the four DSs using the likelihood sampling are shown in Figure 7.6. For DS1 and DS2, the actual damage is located and quantified with good accuracy. For DS3, the two damaged elements are located successfully, while the severity of the damage at the mid-span is smaller than the true value, i.e., with 60% reduction. For DS4, the actual damage locations are detected successfully with some errors in the identified severities. However, when using the posterior sampling, the results are not accurate, for example, only the damaged Element 1 can be detected for DS3. The results are not shown here for brevity.

When both the natural frequencies and mode shapes are used, the optimal damage parameters are calculated by minimizing the objective function in Equation (7.30) iteratively. The damage identification results using the likelihood sampling are shown in Figure 7.7. For the single damage scenarios, i.e., DS1 and DS2, the damage identification results are almost the same as those using frequencies only. For DS3, the identified damage severity of the damage at the mid-span becomes closer to the actual value and the error reduces to 4.12%. For DS4, the identification error reduces to 2.27%. Therefore the damage identification accuracy is improved significantly by incorporating the mode shape data. For all DSs using different kinds of modal parameters, the results converge within five iterations. Again the results using the posterior sampling are not accurate.

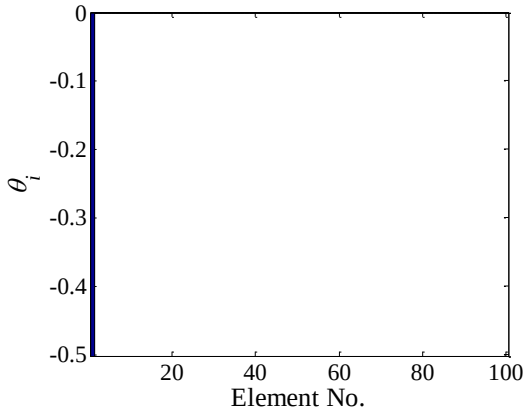

(a) DS1 ($\bar{\theta}_1 = -0.4, \tau = 1.00\%$)

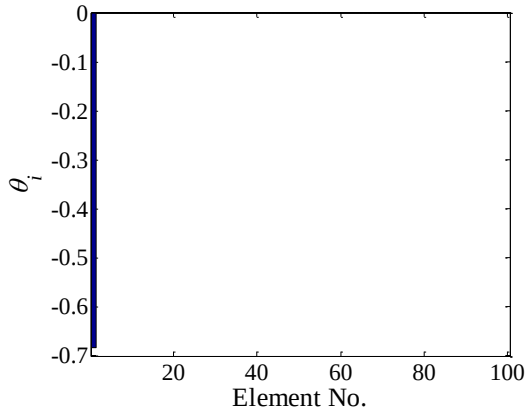

(b) DS2 ($\bar{\theta}_1 = -0.6, \tau = 0.83\%$)

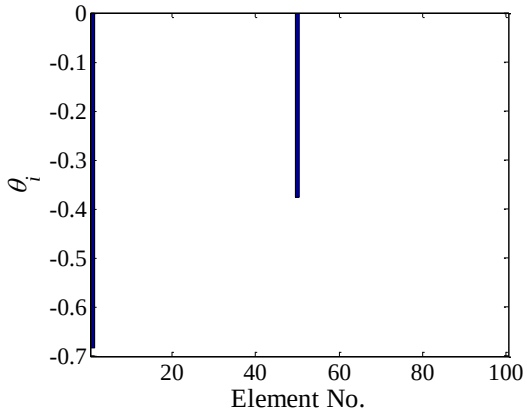

(c) DS3 ($\bar{\theta}_1 = \bar{\theta}_{50} = -0.6, \tau = 2.36\%$)

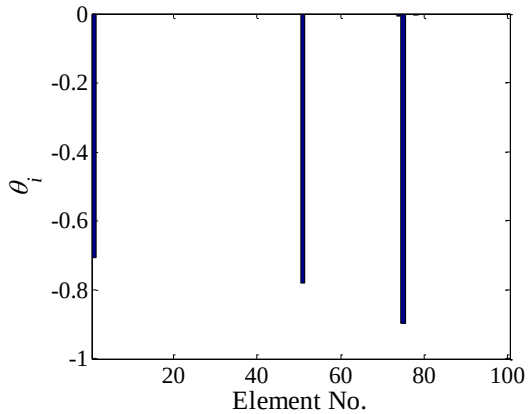

(d) DS4 ($\bar{\theta}_1 = \bar{\theta}_{50} = -0.6, \bar{\theta}_{75} = -0.8, \tau = 2.36\%$)

Figure 7.6 Damage identification results for four DSs using frequencies only

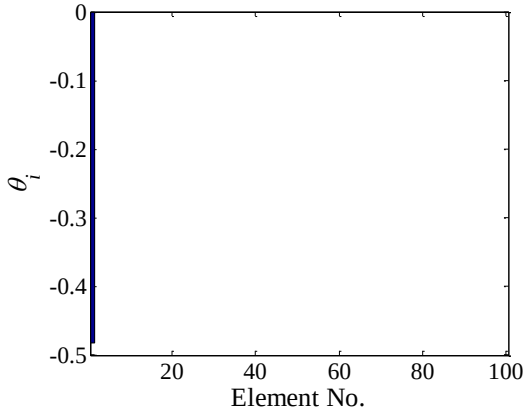

(a) DS1 ($\bar{\theta}_1 = -0.4, \tau = 0.83\%$)

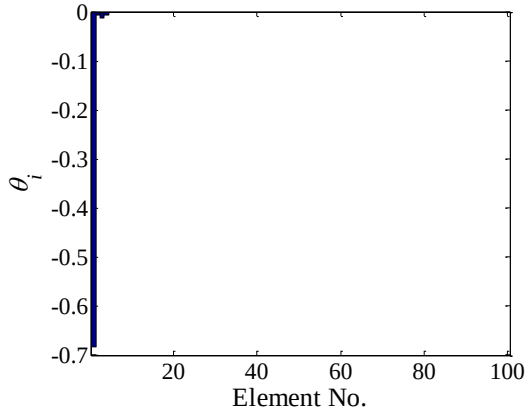

(b) DS2 ($\bar{\theta}_1 = -0.6, \tau = 0.80\%$)

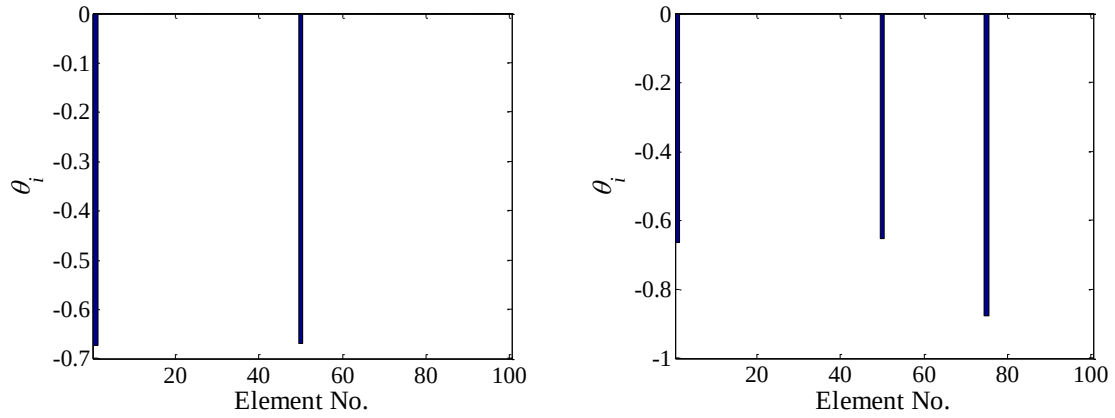

(c) DS3 ($\bar{\theta}_1 = \bar{\theta}_{50} = -0.6, \tau = 1.03\%$) (d) DS4 ($\bar{\theta}_1 = \bar{\theta}_{50} = -0.6, \bar{\theta}_{75} = -0.8, \tau = 1.06\%$)

Figure 7.7 Damage identification results for for four DSs using frequencies and mode shapes

The main advantages of the EM algorithm are its simplicity and ease of implementation. Moreover, the EM algorithm is proven to be stable and robust (Couvreur, 1996). In this study, the integral of the nonlinear inverse problem is avoided through an iterative procedure. The MAP values of the damage parameters are determined adaptively, and the sparsity of the damage parameters is secured automatically. As examples show, during the iterative process, many hyper-parameters α_i approach infinity, and the corresponding θ_i approaches zero.

7.7 Comparison of SBL with the Deterministic Regularization Approaches

The SBL has some similarities with the sparse recovery theory that uses the regularization technique. In Equation (7.24), the first two terms are equivalent to the data-fitting terms with different weights and the third term to the regularization term with ρ as the regularization parameter in sparse recovery. In this study, each damage parameter θ_i is assigned with an individual hyper-parameter ρ_i, indicating that each damage parameter has a unique regularization parameter. A large ρ_i carries a significant weight in the corresponding θ_i and thus enforces it to be close to zero during the optimization, thereby achieving the sparse solution to θ. From Equation (7.21), the regularization parameter is at the similar level of $1/\theta^2$. Therefore, Equation (7.24) is equivalent to the iteratively reweighted least squares (IRLS) (Daubechies *et al*., 2010;

Chartrand and Yin, 2008; Chartrand and Staneva, 2008; Adewuyi *et al*., 2009), which is equivalent to the l_0 regularization.

If all damage parameters $\boldsymbol{\theta}$ are assumed to have a uniform Gaussian prior distribution, the hyper-parameter $\boldsymbol{\rho}$ becomes a single value. The resulting objective function (Equation [7.24]) is equivalent to the l_2 regularization, which may cause the identified damage distributed to many structural elements and fail to obtain the sparse solution. The following prior has been shown to encourage sparsity in the solution (Wipf and Rao, 2004)

$$p(\boldsymbol{\theta}) \sim exp\left(-\sum_{i=1}^{n}|\theta_i|^p\right) \tag{7.36}$$

where $p \in [0, 1]$. If a Laplace prior (i.e., $p = 1$) is applied to the damage parameters, then the corresponding objective function is equivalent to the l_1 regularization, or Basis Pursuit (Babacan *et al*., 2010). When $p \in [0, 1)$, the objective function with l_p-norm regulzatization corresponds to the FOCal Underdetermined System Solver (FOCUSS) algorithm (Gorodnitsky and Rao, 1997).

The l_1 regularization problem could be solved effectively via linear programming approaches, which gurantee convergence to the global minimum (Boyd and Vandenberghe, 2004). However, the obtained global minimum does not necessarily coincide with the maximally sparse solution, which is referred to as structural error (Wipf and Rao, 2004). On the contrary, the objective function employed by FOCUSS with l_p-norm $(0 \leq p < 1)$ has many local minima. For $0 \leq p < p'$, the global minimum will be achieved at the sparsest soluton, i.e., minimum l_0-norm solution, where p' can be arbitrarily small (Wipf and Rao, 2004; Leahy and Jeffs, 1991). Therefore, the FOCUSS algorithms suffer from convergence errors instead, that usually converge to suboptimal local minima. The SBL retains the desirable property of the l_0 regularization, of which the global minimum is obtained at the sparsest solution. Moreover, it has been proved that the SBL has no structural error and fewer convergence errors than FOCUSS. Therefore, the SBL is more likely to converge to the optimal sparest solution. For both

the SBL and FOCUSS algorithms, the local minima have been demonstrated to be achieved at sparse solutions.

Sparse recovery theory using the regularization techniques disregards the relative uncertainties between different variables, and requires estimation of the regularization parameter. However, in SBL, the hyper-parameters possess a clear physical meaning that represents the precision of the uncertainties. The hyper-parameters are updated automatically, thereby avoiding the tricky selection of the regularization parameter in sparse recovery theory. Therefore, the SBL technique is more general and more flexible relative to sparse recovery theory.

7.8 Summary

An SBL method has been proposed in this chapter for probabilistic structural damage detection using modal parameters. The sparsity of structural damage has been exploited as important prior information from the Bayesian perspective. The integral of the nonlinear eigenvalue equation is avoided through an iterative procedure based on the EM algorithm. Moreover, two sampling methods have been proposed and compared to approximate the evidence. Without employing a complicated Bayesian model with asymptotic approximation or utilizing stochastic simulation, this proposed method is concise and easy to implement.

Numerical and experimental examples demonstrate that the proposed method is effective in identifying single and multiple damage elements, even when the measurement data are much fewer than the damage parameters. The damage identification results also show that the likelihood sampling is more robust to noise and accurate than the posterior sampling. The convergence using the EM for damage detection is very rapid. Moreover, the damage identification accuracy has been improved by incorporating mode shape data, especially for multiple damage scenarios.

Compared with the regularization-based sparse recovery theory, the EM-based SBL is more general as more hyper-parameters are used and own clear physical meaning.

Moreover, the hyper-parameters can be updated automatically, thereby avoiding the selection of the regularization parameter in the sparse recovery.

CHAPTER 8

CONCLUSIONS AND FUTURE RESEARCH

8.1 Conclusions

Sparse damage detection methods based on sparse recovery and SBL were developed in this study. First, the l_1 and l_0 regularization techniques have been developed and applied to detect sparse damage. Second, the sparsity of structural damage is exploited from the Bayesian perspective through specifying a sparsity inducing prior. Two numerical examples and three experimental structures are utilized to investigate the effectiveness and reliability of the proposed damage detection methods. The results and findings are summarized as follows.

1. The l_1-regularized damage detection method is able to locate and quantify single and multiple damage correctly using only a few vibration measurements. Moreover, it is robust to noise even under the severe noise situation. The l_1-regularized model updating technique outperforms the traditional l_2 regularization technique that the damage detection results match the sparse damage scenario in practice;
2. An appropriate range of the regularization parameter, rather than one single value, can be determined using the two proposed strategies and the results are consistent. When any one regularization parameter in this range is selected, damage can be accurately identified even for multiple damage scenarios. This range also indicates the sensitivity degree of the damage identification problem to the regularization parameter;
3. A sensor placement technique is developed based on the GA. It is independent on the damage states and satisfactory damage identification results can be obtained using the modal data based on the determined optimal sensor configuration. The results are more accurately than using the modal data based on empirically selected sensor locations;

4. The proposed IRLR algorithm is equivalent to the l_0 regularization technique. This method is advantageous over the l_1 regularization technique that the sparser damage identification results with higher accuracy are obtained;
5. An SBL method has been proposed using the EM technique for probabilistic structural damage detection. The method can accurately locate and quantify the sparse damage, even when the measurement data are much fewer than the damage parameters. Compared with the regularization-based methods, the EM-based SBL is easy to implement while contains clear physical meaning and avoids the selection of the regularization parameter.

As the sparsity is exploited in the proposed regularization and SBL techniques, the sparse damage can be identified accurately among a large number of candidate elements. Therefore, the structure of interest can be modelled using fine elements, which allows local damage be detected with a small number of vibration measurements. This is a big breakthrough of the global vibration-based methods.

8.2 Future Research

Although improvements have been made compared with the conventional damage detection methods, there are still a number of issues remain and require further research in order to apply the methods to practical full-scale structures.

1. The present study does not consider the uncertainties associated with the environmental variations. Damage detection analysis under different environmental conditions is a significant challenge and merits further study. Moreover, a new damage index should be developed which is sensitive to damage but not sensitive to environmental changes;
2. Successful sparse recovery depends on several factors, namely, number and severity of damage, number of measurements, number of total elements, and level of measurement uncertainty. Moreover, the measures of sparsity and the problem indeterminacy may affect the recovery accuracy significantly. Therefore, parametric study is highly worthwhile in the future to investigate the effect of these

parameters on damage detection. The success probability of damage detection can then be determined;

3. For structural damage detection, it is typically assumed that the structure behaves linearly before and after damage. However, in practice, the structure usually exhibits nonlinear behaviours due to geometrical nonlinearity, material nonlinearity, and constraint and contact nonlinearity. The structural nonlinearity, which has been ignored in this study, requires further study;
4. For large-scale structures, the FE model usually contains thousands of elements and damage is thus sparser compared with the structures in laboratories. Moreover, the problem indeterminacy increases which is defined as the ratio of the number of measurements to the number of total updating parameters. Therefore, the present sparse damage detection methods should be further studied and extended in order to be applied to practical large-scale structures.

APPENDIX A

EXPECTATION–MAXIMIZATION ALGORITHM

The EM algorithm is a general probabilistic technique for finding maximum likelihood or MAP estimates based on unobserved latent variable models (Bishop, 2006). Our goal in this study is to estimate the hyper-parameters $\boldsymbol{\xi} = \{\boldsymbol{\rho}, \eta, \gamma\}$ based on the observed modal data $\boldsymbol{\mathcal{D}} = [\boldsymbol{\lambda}^E, \boldsymbol{\Phi}^E]$ by treating the stiffness parameter $\boldsymbol{\theta}$ as the latent variable using the EM algorithm.

Since it is difficult to evaluate the evidence (marginal likelihood) function $p(\boldsymbol{\lambda}^E, \boldsymbol{\Phi}^E|\boldsymbol{\xi})$ analytically, direct maximization of $p(\boldsymbol{\lambda}^E, \boldsymbol{\Phi}^E|\boldsymbol{\xi})$ with respect to $\boldsymbol{\xi} = \{\boldsymbol{\rho}, \eta, \gamma\}$ is blocked. In this regard, a distribution $q(\boldsymbol{\theta})$ defined over the latent variable $\boldsymbol{\theta}$ is introduced which can be any non-negative PDF of $\boldsymbol{\theta}$ with unity integral. According to the product rule of probability

$$\ln p(\boldsymbol{\lambda}^E, \boldsymbol{\Phi}^E|\boldsymbol{\xi}) + \ln p(\boldsymbol{\theta}|\boldsymbol{\lambda}^E, \boldsymbol{\Phi}^E, \boldsymbol{\xi}) = \ln p(\boldsymbol{\theta}, \boldsymbol{\lambda}^E, \boldsymbol{\Phi}^E|\boldsymbol{\xi}) \tag{A.1}$$

Therefore, for any choice of $q(\boldsymbol{\theta})$, the following decomposition holds

$$\begin{aligned} \ln p(\boldsymbol{\lambda}^E, \boldsymbol{\Phi}^E|\boldsymbol{\xi}) &= \int q(\boldsymbol{\theta}) \ln p(\boldsymbol{\lambda}^E, \boldsymbol{\Phi}^E|\boldsymbol{\xi})\, d\boldsymbol{\theta} \\ &= \int q(\boldsymbol{\theta}) \ln \left\{ \frac{p(\boldsymbol{\theta}, \boldsymbol{\lambda}^E, \boldsymbol{\Phi}^E|\boldsymbol{\xi})}{p(\boldsymbol{\theta}|\boldsymbol{\lambda}^E, \boldsymbol{\Phi}^E, \boldsymbol{\xi})} \right\} d\boldsymbol{\theta} \\ &= \mathcal{L}(q, \boldsymbol{\xi}) + \mathrm{KL}(q \parallel p) \end{aligned} \tag{A.2}$$

where we have defined

$$\mathcal{L}(q, \boldsymbol{\xi}) = \int q(\boldsymbol{\theta}) \ln \left\{ \frac{p(\boldsymbol{\theta}, \boldsymbol{\lambda}^E, \boldsymbol{\Phi}^E|\boldsymbol{\xi})}{q(\boldsymbol{\theta})} \right\} d\boldsymbol{\theta} \tag{A.3}$$

$$\mathrm{KL}(q \parallel p) = -\int q(\boldsymbol{\theta}) \ln \left\{ \frac{p(\boldsymbol{\theta}|\boldsymbol{\lambda}^E, \boldsymbol{\Phi}^E, \boldsymbol{\xi})}{q(\boldsymbol{\theta})} \right\} d\boldsymbol{\theta} \tag{A.4}$$

As shown in Equations (A.3) and (A.4), $\mathcal{L}(q, \boldsymbol{\xi})$ depends on the distribution $q(\boldsymbol{\theta})$ and $\boldsymbol{\xi}$, and $\mathrm{KL}(q \parallel p)$ is the Kullback-Leibler divergence between $q(\boldsymbol{\theta})$ and the posterior distribution $p(\boldsymbol{\theta}|\boldsymbol{\lambda}^E, \boldsymbol{\Phi}^E, \boldsymbol{\xi})$ (Kullback and Leibler, 1951). The Kullback-Leibler divergence $\mathrm{KL}(q \parallel p) \geq 0$, with $\mathrm{KL}(q \parallel p) = 0$ if and only if $q(\boldsymbol{\theta}) = p(\boldsymbol{\theta}|\boldsymbol{\lambda}^E, \boldsymbol{\Phi}^E, \boldsymbol{\xi})$ (Kullback and Leibler, 1951; Kullback, 1968). Therefore, $\mathcal{L}(q, \boldsymbol{\xi}) \leq \ln p(\boldsymbol{\lambda}^E, \boldsymbol{\Phi}^E|\boldsymbol{\xi})$ is a lower bound of $\ln p(\boldsymbol{\lambda}^E, \boldsymbol{\Phi}^E|\boldsymbol{\xi})$.

The EM algorithm is a two-stage iterative optimization technique. Given the current values of the hyper-parameters $\boldsymbol{\xi}^{\mathrm{old}}$, the lower bound $\mathcal{L}(q, \boldsymbol{\xi})$ is maximized when $q(\boldsymbol{\theta})$ is equal to the posterior distribution $p\left(\boldsymbol{\theta}\middle|\boldsymbol{\lambda}^E, \boldsymbol{\Phi}^E, \boldsymbol{\xi}^{\mathrm{old}}\right)$. In this case, the lower bound $\mathcal{L}(q, \boldsymbol{\xi})$ equals to the log evidence $\ln p(\boldsymbol{\lambda}^E, \boldsymbol{\Phi}^E|\boldsymbol{\xi})$. Substituting $q(\boldsymbol{\theta}) = p\left(\boldsymbol{\theta}\middle|\boldsymbol{\lambda}^E, \boldsymbol{\Phi}^E, \boldsymbol{\xi}^{\mathrm{old}}\right)$ into Equation (A.3), the lower bound $\mathcal{L}(q, \boldsymbol{\xi})$ takes the form

$$\begin{aligned} \mathcal{L}(q, \boldsymbol{\xi}) = & \int p\left(\boldsymbol{\theta}\middle|\boldsymbol{\lambda}^E, \boldsymbol{\Phi}^E, \boldsymbol{\xi}^{\mathrm{old}}\right) \ln p(\boldsymbol{\theta}, \boldsymbol{\lambda}^E, \boldsymbol{\Phi}^E|\boldsymbol{\xi})\, d\boldsymbol{\theta} - \\ & \int p\left(\boldsymbol{\theta}\middle|\boldsymbol{\lambda}^E, \boldsymbol{\Phi}^E, \boldsymbol{\xi}^{\mathrm{old}}\right) \ln p\left(\boldsymbol{\theta}\middle|\boldsymbol{\lambda}^E, \boldsymbol{\Phi}^E, \boldsymbol{\xi}^{\mathrm{old}}\right) d\boldsymbol{\theta} = E\{\ln p\,(\boldsymbol{\theta}, \boldsymbol{\lambda}^E, \boldsymbol{\Phi}^E|\boldsymbol{\xi})\} + \mathrm{const} \end{aligned} \tag{A.5}$$

where the constant term is the negative entropy of the q distribution and is independent of $\boldsymbol{\theta}$. Subsequently, the distribution $q(\boldsymbol{\theta}) = p\left(\boldsymbol{\theta}\middle|\boldsymbol{\lambda}^E, \boldsymbol{\Phi}^E, \boldsymbol{\xi}^{\mathrm{old}}\right)$ is incorporated and the lower bound $\mathcal{L}(q, \boldsymbol{\xi})$ is maximized with respect to $\boldsymbol{\xi}$ to give rise to $\boldsymbol{\xi}^{\mathrm{new}}$. As shown in Equation (A.5), maximization of $\mathcal{L}(q, \boldsymbol{\xi})$ is equivalent to maximize the expectation of the complete-data log likelihood $\mathcal{Q}\left(\boldsymbol{\xi},\ \boldsymbol{\xi}^{\mathrm{old}}\right) = E\{\ln p\,(\boldsymbol{\theta}, \boldsymbol{\lambda}^E, \boldsymbol{\Phi}^E|\boldsymbol{\xi})\}$ with respect to the distribution $q(\boldsymbol{\theta}) = p\left(\boldsymbol{\theta}\middle|\boldsymbol{\lambda}^E, \boldsymbol{\Phi}^E, \boldsymbol{\xi}^{\mathrm{old}}\right)$.

In summary, the EM algorithm seeks to find the maximum of the evidence function $p(\boldsymbol{\lambda}^E, \boldsymbol{\Phi}^E|\boldsymbol{\xi})$ by iteratively applying two steps. In the E step, the current value of the hyper-parameters $\boldsymbol{\xi}^{\mathrm{old}}$ is utilized to determine the posterior distribution of $\boldsymbol{\theta}$ given by $p\left(\boldsymbol{\theta}\middle|\boldsymbol{\lambda}^E, \boldsymbol{\Phi}^E, \boldsymbol{\xi}^{\mathrm{old}}\right)$. This posterior distribution is then used to estimate the expectation $\mathcal{Q}\left(\boldsymbol{\xi},\ \boldsymbol{\xi}^{\mathrm{old}}\right) = E\{\ln p\,(\boldsymbol{\theta}, \boldsymbol{\lambda}^E, \boldsymbol{\Phi}^E|\boldsymbol{\xi})\}$. In the M step, the new parameter estimate $\boldsymbol{\xi}^{\mathrm{new}}$ is determined by maximizing the function

$$\boldsymbol{\xi}^{\text{new}} = arg\max_{\boldsymbol{\xi}} \mathcal{Q}\left(\boldsymbol{\xi}, \boldsymbol{\xi}^{\text{old}}\right) \tag{A.6}$$

The EM algorithm is initialized by choosing the starting values for $\boldsymbol{\xi}$, then the E step and M step are performed successively until satisfactory convergence is achieved. The convergence of the EM algorithm has been proved that $\ln p(\boldsymbol{\lambda}^E, \boldsymbol{\Phi}^E|\boldsymbol{\xi})$ always increases during the iterations and such that the estimated values approach the most probable values of $\boldsymbol{\xi}$ monotonically (Moon, 1996; Wu, 1983; Boyles, 1983).

REFERENCES

Abdo MB, Hori M. A numerical study of structural damage detection using changes in the rotation of mode shapes. *Journal of Sound and Vibration* 2002; **251**(2):227–239.

Adams R, Cawley P, Pye C, Stone B. A vibration technique for non-destructively assessing the integrity of structures. *Journal of Mechanical Engineering Science* 1978; **20**(2):93–100.

Adewuyi AP, Wu Z, Serker NHMK. Assessment of vibration-based damage identification methods using displacement and distributed strain measurements. *Structural Health Monitoring* 2009; **8**(6):443–461.

Ahmadian H, Mottershead J, Friswell M. Regularisation methods for finite element model updating. *Mechanical Systems and Signal Processing* 1998; **12**(1):47–64.

Allemang RJ. The modal assurance criterion–twenty years of use and abuse. *Sound and Vibration* 2003; **37**(8):14–23.

Allemang RJ, Brown DL. A correlation coefficient for modal vector analysis. In: *Proceedings of the 1st International Modal Analysis Conference*, Orlando, Florida, 8–10 November 1982, pp. 110–116.

Alvandi A, Cremona C. Assessment of vibration-based damage identification techniques. *Journal of Sound and Vibration* 2006; **292**(1):179–202.

Au JK. *An ab initio approach to the inverse problem-based design of photonic bandgap devices*. PhD Dissertation, Engineering and Applied Science, California Institute of Technology, California, United States, 2007.

Babacan S, Molina R, Katsaggelos A. Bayesian compressive sensing using Laplace priors. *IEEE Transactions on Image Processing* 2010; **19**(1):53–63.

Bakhary N, Hao H, Deeks AJ. Damage detection using artificial neural network with consideration of uncertainties. *Engineering Structures* 2007; **29**(11):2806–2815.

Bakhary N, Hao H, Deeks AJ. Structure damage detection using neural network with multi-stage substructuring. *Advances in Structural Engineering* 2010; **13**(1):95–110.

Bao Y, Beck JL, Li H. Compressive sampling for accelerometer signals in structural health monitoring. *Structural Health Monitoring* 2011; **10**(3):235–246.

Bao Y, Li H, Chen Z, Zhang F, Guo A. Sparse l_1 optimizatio-based identification approach for the distribution of moving heavy vehicle loads on cable-stayed bridges. *Structural Control and Health Monitoring* 2016; **23**(1):144–155.

Bao Y, Li H, Ou J. Emerging data technology in structural health monitoring: compressive sensing technology. *Journal of Civil Structural Health Monitoring* 2014; **2**(4):77–90.

Bao Y, Li H, Sun X, Yu Y, Ou J. A data loss recovery approach for wireless sensor networks using a compressive sampling technique. *Structural Health Monitoring* 2013; **12**(1):78–95.

Baraniuk RG. More is less: signal processing and the data deluge. *Science* 2011; **331**(6018):717–719.

Bauer F, Lukas MA. Comparingparameter choice methods for regularization of ill-posed problems. *Mathematics and Computers in Simulation* 2011; **81**(9):1795–1841.

Bayissa WL, Haritos N, Thelandersson S. Vibration-based structural damage identification using wavelet transform. *Mechanical Systems and Signal Processing* 2008; **22**(5):1194–1215.

Beck JL. Bayesian system identification based on probability logic. *Structural Control and Health Monitoring* 2010; **17**(7):825–847.

Beck JL, Au SK. Bayesian updating of structural models and reliability using Markov Chain Monte Carlo simulation. *Journal of Engineering Mechanics* 2002; **128**(4):380–391.

Beck JL, Katafygiotis LS. Updating models and their uncertainties. I: Bayesian statistical framework. *Journal of Engineering Mechanics* 1998; **124**(4):455–461.

Bishop CM. *Pattern Recognition and Machine Learning*. Berlin: Springer, 2006.

Boyd S, Vandenberghe L. *Convex optimization*. New York: Cambridge University Press, 2004.

Boyles RA. On the convergence of the EM algorithm. *Journal of the Royal Statistical Society* 1983; **45**(1):47–50.

Brownjohn JMW. *Non-destructive testing using measurements of structural damping*. BSc Dissertation, Department of Mechanical Engineering, University of Bristol, Bristol, UK, 1979.

Cai TT, Wang L. Orthogonal matching pursuit for sparse signal recovery with noise. *IEEE Transactions on Information Theory* 2011; **57**(7):4680–4688.

Candès EJ, Romberg J, Tao T. Robust uncertainty principles: exact signal reconstruction from highly incomplete frequency information. *IEEE Transactions on Information Theory* 2006; **52**(2):489–509.

Candès EJ, Tao T. Decoding by linear programming. *IEEE Transactions on Information Theory* 2005; **51**(12):4203–4215.

Candès EJ, Tao T. Near optimal signal recovery from random projections: universal encoding strategies? *IEEE Transactions on Information Theory* 2006; **52**(12):5406–5425.

Candès EJ, Wakin M, Boyd S. Enhancing sparsity by reweighted l_1 minimization. *Journal of Fourier Analysis and Applications* 2008; **14**(5):877–905.

Carden EP, Fanning P. Vibration based condition monitoring: a review. *Structural Health Monitoring* 2004; **3**(4):355–377.

Carlin BP, Polson NG. Inference for nonconjugate Bayesian models using the Gibbs sampler. *The Canadian Journal of Statistics* 1991; **19**(4):399–405.

Carvalho C, Polson N, Scott J. The horseshoe estimator for sparse signals. *Biometrika* 2010; **97**(2):465–480.

Casciati S. Stiffness identification and damage localization via differential evolution algorithms. *Structural Control and Health Monitoring* 2008; **15**(3):436–449.

Casciati S. Statistical approach to a SHM benchmark problem. *Smart Structures and Systems* 2010; **6**(1):17–27.

Casciati S, Elia L. Damage localization in a cable-stayed bridge via bio-inspired metaheuristic tools. *Structural Control and Health Monitoring* 2017; **24**(5):e1922.

Castello D, Stutz L, Rochinha F. A structural defect identification approach based on a continuum damage model. *Computers and Structures* 2002; **80**(5):417–436.

Castillo I, Schmidt-Hieber J, van der Vaart A. Bayesian linear regression with sparse priors. *The Annals of Statistics* 2015; **43**(5):1986–2018.

Cawley P. Long range inspection of structures using low frequency ultrasound. In: *Proceedings of the Structural Damage Assessment Using Advanced Signal Processing Procedures*, University of Sheffield, UK, 30 June–2 July 1997, pp. 1–17.

Cetin M, Karl WC. Feature-enhanced synthetic aperture radar image formation based on nonquadratic regularization. *IEEE Transactions on Image Processing* 2001; **10**(4):623–631.

Chandrashekhar M, Ganguli R. Damage assessment of structures with uncertainty by using mode-shape curvatures and fuzzy logic. *Journal of Sound and Vibration* 2009; **326**(3):939–957.

Chang K, Shen Z, Lee G. Modal analysis technique for bridge damage detection. In: *Proceedings of the Symposium of Structural Engineering Natural Hazards and Mitigation*, Irvine, California, United States, 19–21 April 1993, pp. 1083–1088.

Chang M, Pakzad SN. Optimal sensor placement for structural modal identification. *Journal of Bridge Engineering* 2014; **19**(6):1–10.

Chartrand R. Exact reconstruction of sparse signals via nonconvex minimizaion. *IEEE Signal Processing Letters* 2007; **14**(10):707–710.

Chartrand R, Staneva V. Restricted isometry properties and nonconvex compressive sensing. *Inverse Problems* 2008; **24**(3):1–14.

Chartrand R, Yin W. Iteratively reweighted algorithms for compressive sensing. In: *Proceedings of IEEE International Conference on Acoustics, Speech and Signal Processing*, Las Vegas, Nevada, USA, 31 March–4 April 2008, pp. 3869–3872.

Chen L, Gu Y. Local and global optimality of l_p minimization for sparse recovery. In: *Proceedings of IEEE International Conference on Acoustics, Speech and Signal Processing*, South Brisbane, Queensland, Australia, 19–24 April 2015, pp. 3596–3600.

Chen S, Donoho D, Saunders M. Atomic decomposition by basis pursuit. *SIAM Journal on Scientific Computing* 1998; **20**(1):33–61.

Cheung SH, Beck JL. Calculation of the posterior probability for Bayesian model class assessment and averaging from posterior samples based on dynamic system data. *Computer-Aided Civil and Infrastructure Engineering* 2010; **25**(5):304–321.

Ching J, Beck JL. Bayesian analysis of the phase II IASC–ASCE structural health monitoring experimental benchmark data. J*ournal of Engineering Mechanics* 2004; **130**(10):1233–44.

Ching J, Chen YC. Transitional Markov Chain Monte Carlo method for Bayesian model updating, model class selection and model averaging. *Journal of Engineering Mechanics* 2007; **133**(7):816–832.

Ching J, Phoon KK, Beck JL, Huang Y. Identifiability of geotechnical site-specific trend functions. *ASCE-ASME Journal of Risk and Uncertainty in Engineering Systems, Part A: Civil Engineering* 2017; **3**(4):04017021.

Claerbout JF, Muir F. Robust modeling with erratic data. *Geophysics* 1973; **38**(5):826–844.

Cornwell P, Doebling SW, Farrar CR. Application of the strain energy damage detection method to plate-like structures. *Journal of Sound and Vibration* 1999; **224**(2):359–374.

Couvreur C. The EM algorithm: A guided tour. In: *Proceedings of the 2nd IEEE European Workshop on Computer-Intensive Methods in Control and Signal Processing*, Prague, Czech Republic, 28–30 August 1996, pp. 209–222.

Crespo P, Ruotolo R, Surace C. Non-linear modeling of a cracked beam. In: *Proceedings of the 14th International Modal Analysis Conference*, Dearborn, Michigan, 12–15 February 1996, pp. 1017–1022.

Das S, Saha P, Patro SK. Vibration-based damage detection techniques used for health monitoring of structures: A review. *Journal of Civil Structural Health Monitoring* 2016; **6**(3):477–507.

Daubechies I, DeVore R, Fornasier M, GÜNTÜRK CS. Iteratively reweighted least squares minimization for sparse recovery. *Communications on Pure and Applied Mathematics* 2010; **63**(1):1–38.

Davis G, Mallat S, Zhang Z. Adaptive time-frequency decompositions with matching pursuits. In: *Proceedings of the IEEE-SP International Symposium on Time-Frequency and Time-Scale Analysis*, Victoria, BC, Canada, 4–6 October 1992, pp. 7–10.

Doebling SW. Minimum-rank optimal update of elemental stiffness parameters for structural damage identification. *AIAA Journal* 1996; **34**(12):2615–2621.

Doebling SW, Farrar CR, Prime MB, Shevitz DW. Damage identification and health monitoring of structural and mechanical systems from changes in their vibration characteristics: a literature review, *Los Alamos National Laboratory Report*, 1996.

Dong J, Zhang G, Zhang Z, Geng Y, Wang J. Inverse problem solution and regularization parameter selection for current distribution reconstruction in switching arcs by inverting magnetic fields. *Mathematical Problems in Engineering* 2018; 2018e:7452863.

Donoho DL. Compressed sensing. *IEEE Transactions on Information Theory* 2006a; **52**(4):1289–1306.

Donoho DL. For most large underdetermined systems of linear equations the minimal l_1-norm solution is also the sparsest solution. *Communications on Pure and Applied Mathematics* 2006b; **59**(7):907–934.

Donoho DL, Elad M. Optimally sparse representation in general (nonorthogonal) dictionaries via l_1 minimization. *Proceedings of the National Academy Sciences of the United States of America* 2003; **100**(5):2197–2202.

Donoho DL, Logan BF. Signal recovery and the large sieve. *SIAM Journal on Applied Mathematics* 1992; **52**(2):577–591.

Donoho DL, Stark PB. Uncertainty principles and signal recovery. *SIAM Journal on Applied Mathematics* 1989; **49**(3):906–931.

Efron B, Hastie T, Johnson I, Tibshirani R. Least angle regression. *The Annals of Statistics* 2004; **32**(2):407–499.

Elad M. Optimized projections for compressed sensing. *IEEE Transactions on Signal Processing* 2007; **55**(12):5695–5702.

Engl HW, Hanke M, Neubauer A. *Regularization of inverse problems*. Dordrecht, Netherlands: Kluwer Academic Publishers, 1996.

Eraky A, Saad A, Anwar AM, Abdo A. Damage detection of plate-like structures based on residual force vector. *HBRC Journal* 2016; **12**(3):255–262.

Fan XY, Li J, Hao H, Ma SL. Identification of minor structural damage based on electromechanical impedance sensitivity and sparse regularization. *Journal of Aerospace Engineering* 2018; **31**(5):04018061.

Fanning PJ, Carden EP. Experimentally validated added mass identification algorithm based on frequency response functions. *Journal of Engineering Mechanics* 2004; **130**(9):1045–1051.

Farrar CR, Doebling SW. *Damage detection and evaluation II. Modal Analysis and Testing*. Dordrecht, Netherlands: Kluwer Academic Publishers, 1999.

Farrar CR, Doebling SW, Nix DA. Vibration–based structural damage identification. *Philosophical Transactions of the Royal Society of London Series A-Mathematical, Physical and Engineering Sciences* 2001; **359**(1778):131–149.

Farrar CR, Jauregui DA. Comparative study of damage identification algorithms applied to a bridge: II. Numerical study. *Smart Materials and Structures* 1998; **7**(5):704–719.

Faul AC, Tipping ME. Analysis of sparse Bayesian learning. In: *Proceedings of Advances in Neural Information Processing Systems (NIPS 14)*, Vancouver, British Columbia, Canada, 1 September 2002, pp. 383–389.

Foucart S, Lai M. Sparsest solutions of underdetermined linear systems via l_q-minimization for $0 < q \leqslant 1$. *Applied and Computational Harmonic Analysis* 2009; **26**(3):395–407.

Friswell M, Mottershead JE. *Finite element model updating in structural dynamics*. Dordrecht, Netherlands: Kluwer Academic Publishers, 1995.

Friswell M, Penny JE. The practical limits of damage detection and location using vibration data. In: *Proceedings of the 11th VPI and SU Symposium on Structural Dynamics and Control*, Blacksburg, Virginia, 12–14 May 1997, pp. 31–40.

Fritzen CP, Jennewein D, Kiefer T. Damage detection based on model updating methods. *Mechanical Systems and Signal Processing* 1998; **12**(1):163–186.

Frýba L, Pirner M. Load tests and modal analysis of bridges. *Engineering Structures* 2001; **23**(1):102–109.

Gelman A, Carlin JB, Stern HS, Rubin DB. *Bayesian Data Analysis*. Boca Raton, Florida: CRC Press, 2003.

Goldberg DE. *Genetic algorithms in search, machine learning and optimisation*. New York: Addison Wesley, 1989.

Golub GH, Heath M, Wahba G. Generalized cross–validation as a method for choosing a good ridge parameter. *Technometrics* 1979; **21**(2):215–223.

Gorodnitsky IF, Rao BD. Sparse signal reconstruction from limited data using FOCUSS: A reweighted minimum norm algorithm. *IEEE Transactions on Signal Processing* 1997; **45**(3):600–616.

Griffin J, Brown P. Inference with normal-gamma prior distributions in regression problems. *Bayesian Analysis* 2010; **5**(1):171–88.

Guan H, Karbhari VM. Improved damage detection method based on element modal strain damage index using sparse measurement. *Journal of Sound and Vibration* 2008; **309**(3):465–494.

Hadjileontiadis L, Douka E. Crack detection in plates using fractal dimension. *Engineering Structures* 2007; **29**(7):1612–1625.

Hadjileontiadis L, Douka E, Trochidis A. Fractal dimension analysis for crack identification in beam structures. *Mechanical Systems and Signal Processing* 2005; **19**(3):659–674.

Hämarik U, Raus T. On the choice of the regularization parameter in ill-posed problems with approximately given noise level of data. *Journal of Inverse and Ill-posed Problems* 2006; **14**(3):251–266.

Hans CM. Bayesian lasso regression. *Biometrika* 2009; **96**(4):835–45.

Hansen PC. Analysis of discrete ill-posed problems by means of the L-curve. *SIAM Review* 1992; **34**(4):561–580.

Hansen PC. The L-curve and its use in the numerical treatment of inverse problems. In: *Computational Inverse Problems in Electrocardiology*, WIT Press, Southampton, UK, pp. 119–142, 2001.

Hao H, Xia Y. Vibration-based damage detection of structures by genetic algorithm. *Journal of Computing in Civil Engineering* 2002; **16**(3):222–229.

Hearn G, Testa RB. Modal analysis for damage detection in structures. *Journal of Structural Engineering* 1991; **117**(10):3042–3063.

Hemez FM, Farhat C. An energy based optimum sensor placement criterion and its application to structural damage detection. In: *Proceedings of 12th International Modal Analysis Conference (IMAC)*, Honolulu, Hawaii, 31 January–3 February 1994, pp. 1568–1575.

Heo G, Wang ML, Satpathi D. Optimal transducer placement for health monitoring of long span bridge. *Soil Dynamics and Earthquake Engineering* 1997; **16**:495–502.

Hernandez EM. Identification of isolated structural damage from incomplete spectrum information using l_1-norm minimization. *Mechanical Systems and Signal Processing* 2014; **46**(1):59–69.

Holland JH. *Adaption in natural and artificial systems*. Ann Arbor: University of Michigan Press, 1975.

Hou RR, Xia Y, Zhou XQ. Structural damage detection based on l_1 regularization using natural frequencies and mode shapes. *Structural Control and Health Monitoring* 2018; **25**(3):e2107.

Hou Z, Noori M, Amand RS. Wavelet-based approach for structural damage detection. *Journal of Engineering Mechanics* 2000; **126**(7):677–683.

Hua XG, Ni YQ, Chen ZQ, Ko JM. An improved perturbation method for stochastic finite element model updating. *International Journal for Numerical Method in Engineering* 2008; **73**(3):1845–1864.

Huang Y, Beck JL. Hierarchical sparse Bayesian learning for structural health monitoring with incomplete modal data. *International Journal for Uncertainty Quantification* 2015; **5**(2):139–69.

Huang Y, Beck JL. Full Gibbs sampling procedure for Bayesian system identification incorporating sparse Bayesian learning with automatic relevance determination. *Computer-Aided Civil and Infrastructure Engineering* 2018; **33**(9):712–730.

Huang Y, Beck JL, Li H. Hierarchical sparse Bayesian learning for structural damage detection: Theory, computation and application. *Structural Safety* 2017a; **64**:37–53.

Huang Y, Beck JL, Li H. Bayesian system identification based on hierarchical sparse Bayesian learning and Gibbs sampling with application to structural damage assessment. *Computer Methods in Applied Mechanics and Engineering* 2017b; **318**:382–411.

Huang Y, Beck JL, Li H. Multi-task sparse Bayesian learning with applications in Structural Health Monitoring. *Computer-Aided Civil and Infrastructure Engineering* 2018a; DOI: 10.1111/mice.12408.

Huang Y, Beck JL, Wu S, Li H. Robust Bayesian compressive sensing for signals in structural health monitoring. *Computer-Aided Civil and Infrastructure Engineering* 2014; **29**(3):160–179.

Huang Y, Li H, Wu S, Yang YC. Fractal dimension based damage identification incorporating multi-task sparse Bayesian learning. *Smart Materials and Structures* 2018b; **27**:075020.

Huang Y, Shao C, Wu B, Beck JL, Li H. State-of-the-art review on Bayesian inference in structural system identification and damage assessment. *Advances in Structural Engineering* 2018; DOI: 10.1177/1369433218811540.

Isakov V. *Inverse Problems for Partial Differential Equations*. New York: Springer, 2006.

Jaishi B, Ren WX. Damage detection by finite element model updating using modal flexibility residual. *Journal of Sound and Vibration* 2006; **290**(1):369–387.

Jaynes ET. *Probability theory: The logic of science*. Cambridge, UK: Cambridge University Press, 2003.

Ji S, Xue Y, Carin L. Bayesian compressive sensing. *IEEE Transactions on Signal Processing* 2008; **56**(6):2346–2356.

Jiang X, Mahadevan S. Bayesian wavelet methodology for structural damage detection. *Structural Control and Health Monitoring* 2008; **15**(7):974–991.

Johnson EA, Lam HF, Katafygiotis LS, Beck JL. A benchmark problem for structural health monitoring and damage detection. In: *Proceedings of the 14th Engineering Mechanics Conference*, Austin, Texas, May 2000, ASCE.

Johnson EA, Lam HF, Katafygiotis LS, Beck JL. Phase 1 IASC–ASCE structural health monitoring benchmark problem using simulated data. *Journal of Engineering Mechanics* 2004; **130**(1):3–15.

Johnstone IM. On minimax estimation of a sparse normal mean vector. *The Annals of Statistics* 1994; **22**(1):271–289.

Kammer DC. Sensor placement for on-orbit modal identification and correlation of large space structures. *Journal of Guidance, Control Dynamics* 1991; **14**(2):251–259.

Kaouk M, Zimmerman DC. Structural damage assessment using a generalized minimum rank perturbation theory. *AIAA Journal* 1994; **32**(4):836–842.

Katafygiotis LS, Beck JL. Updating models and their uncertainties. II: Model Identifiability. *Journal of Engineering Mechanics* 1998; **124**(4):463–467.

Kim JT, Stubbs N. Model-uncertainty impact and damage-detection accuracy in plate girder. *Journal of Structural Engineering* 1995; **121**(10):1409–1417.

Kim JT, Stubbs N. Improved damage identification method based on modal information. *Journal of Sound and Vibration* 2002; **252**(2):223–238.

Kim JT, Stubbs N. Crack detection in beam-type structures using frequency data. *Journal of Sound and Vibration* 2003; **259**(1):145–160.

Kirkegaard PH, Brincker R. On the optimal locations of sensors for parametric identification of linear structural systems. *Mechanical Systems and Signal Processing* 1994; **8**(6):639–647.

Koh K, Kim SJ, Boyd S. An interior-point method for large-scale l_1-regularized logistic regression. *Journal of Machine Learning Research* 2007; **8**(7):1519–1555.

Kosmatka JB, Ricles JM. Damage detection in structures by modal vibration characterization. *Journal of Structural Engineering* 1999; **125**(12):1384–1392.

Kullback S. *Information Theory and Statistics*. Mineola, NY: Dover Publications, 1968.

Kullback S, Leibler RA. On information and sufficiency. *Annals of Mathematical Statistics* 1951; **22**(1):79–86.

Lam HF, Yang JH, Au SK. Markov chain Monte Carlo-based Bayesian method for structural model updating and damage detection. *Structural Control Health Monitoring* 2018; **25**:e2140.

Leahy RM, Jeffs BD. On the design of maximally sparse beamforming arrays. *IEEE Transactions on Antennas and Propagation* 1991; **39**(8):1178–1187.

Lee JJ, Lee JW, Yi JH, Yun CB, Jung HY. Neural networks-based damage detection for bridges considering errors in baseline finite element models. *Journal of Sound and Vibration* 2005; **280**(3):555–578.

Lee U, Shin J. A frequency response function-based structural damage identification method. *Computers and Structures* 2002; **80**(2):117–132.

Li HL, Deng XY, Dai HL. Structural damage detection using the combination method of EMD and wavelet analysis. *Mechanical Systems and Signal Processing* 2007; **21**(1):298–306.

Li X, Law S. Adaptive Tikhonov regularization for damage detection based on nonlinear model updating. *Mechanical Systems and Signal Processing* 2010; **24**(6):1646–1664.

Lieven N, Ewins D. Spatial correlation of mode shapes, the coordinate modal assurance criterion (COMAC). In: *Proceedings of the 6th International Modal Analysis Conference*, Orlando, Florida, USA, 1–4 February 1988, pp. 690–695.

Liew K, Wang Q. Application of wavelet theory for crack identification in structures. *Journal of Engineering Mechanics* 1998; **124**(2):152–157.

Lin J, Nassar M, Evans BL. Impulsive noise mitigation in powerline communications using sparse Bayesian learning. *IEEE Journal on Selected Areas of Communications* 2013; **31**(7):1172–1183.

Liu PL. Identification and damage detection of trusses using modal data. *Journal of Structural Engineering* 1995; **121**(4):599–608.

Liu W, Gao WC, Sun YI, Xu MJ. Optimal sensor placement for spatial lattice structure based on genetic algorithms. *Journal of Sound and Vibration* 2008; **317**:175–189.

Lu CJ, Hsu YT. Vibration analysis of an inhomogeneous string for damage detection by wavelet transform. *International Journal of Mechanical Sciences* 2002; **44**(4):745–754.

Lukas MA. On the discrepancy principle and generalised maximum likelihood for regularisation. *Bulletin of the Australian Mathematical Society* 1995; **52**(3):399–424.

Mackay DJC. *Bayesian methods for adaptive models*. PhD Dissertation, Computation and Neural Systems, California Institute of Technology, California, United States, 1992.

Maia N, Silva J, Almas E, Sampaio R. Damage detection in structures: from mode shape to frequency response function methods. *Mechanical Systems and Signal Processing* 2003; **17**(3):489–498.

Mairal J, Yu B. Complexity analysis of the Lasso regularization path. In: *Proceedings of the International Conference on Machine Learning (ICML)*, Edinburgh, Scotland, UK, 27 June–3 July 2012, pp 353–360.

Malioutov D, Çetin M, Willsky AS. A sparse signal reconstruction perspective for source localization with sensor arrays. *IEEE Transactions on Signal Processing* 2005; **53**(8):3010–3022.

Mallat S. *A wavelet tour of signal processing*. San Diego, USA: Academic press, 1999.

Mallat S, Zhang Z. Matching pursuits with time-frequency dictionaries. *IEEE Transactions on Signal Processing* 1993; **41**:3397–3415.

Mannan M, Richardson MH. Detection and location of structural cracks using FRF measurements. In: *Proceedings of the 8th International Modal Analysis Conference*, Orlando, Florida, 29 January–1 February 1990, pp. 652–657.

Mascarenas D, Cattaneo A, Theiler J, Farrar C. Compressed sensing techniques for detecting damage in structures. *Structural Health Monitoring* 2013; **12**(4):325–38.

Meo M, Zumpano G. On the optimal sensor placement techniques for a bridge structure. *Engineering Structures* 2005; **27**(10):1488–1497.

Metropolis N, Rosenbluth AW, Rosenbluth MN, Teller AH, Teller E. Equation of state calculations by fast computing machines. *Journal of Chemical Physics* 1953; **21**(6):1087–1092.

Montazer M, Seyedpoor S. A new flexibility based damage index for damage detection of truss structures. *Shock and Vibration* 2014; **2014**:460692.

Moon TK. The expectation–maximization algorithm. *IEEE Signal Processing Magazine* 1996; **13**(6):47–60.

Morassi A. Identification of a crack in a rod based on changes in a pair of natural frequencies. *Journal of Sound and Vibration* 2001; **242**(4):577–596.

Morozov VA. On the solution of functional equations by the method of regularization. *Soviet Mathematics Doklady* 1966; **167**(3):510–512.

Morozov VA. *Methods for solving incorrectly posed problems*. New York: Springer, 2012.

Mottershead J, Friswell M. Model updating in structural dynamics: a survey. *Journal of Sound and Vibration* 1993; **167**(2):347–375.

Mu HQ, Yuen KV. Novel sparse Bayesian learning and its application to ground motion pattern recognition. *Journal of Computing in Civil Engineering* 2017; **31**(5):1943–5487.

Mustafa S, Debnath N, Dutta A. Bayesian probabilistic approach for model updating and damage detection for a large truss bridge. *International Journal of Steel Structures* 2015; **15**(2):473–485.

Natarajan A, Wu Y. Computational complexity of certifying restricted isometry property. In: *Leibniz International Proceedings in Informatics*, Wadern, Germany, 2014, pp. 371–380.

Natarajan BK. Sparse approximate solutions to linear systems. *SIAM Journal on Computation* 1995; **24**(2):227–234.

Ndambi JM, Vantomme J, Harri K. Damage assessment in reinforced concrete beams using eigenfrequencies and mode shape derivatives. *Engineering Structures* 2002; **24**(4):501–515.

Nelson RB. Simplified calculation of eigenvector derivatives. *AIAA Journal* 1976; **14**(9):1201–1205.

Nichols JM, Link WA, Murphy KD, Olson CC. A Bayesian approach to identifying structural nonlinearity using free-decay response: application to damage detection in composites. *Journal of Sound and Vibration* 2010; **329**(15):2995–3007.

Nuno K. *Damage detection of a steel truss bridge using frequency response function curvature method*. Stockholm: KTH Royal Institute of Technology, 2013; **2**:3–8.

Onar A. Laplace approximations in Bayesian lifetime analysis. Wiley StatsRef: *Statistics Reference Online*, 2014.

Osborne MR, Presnell B, Turlach BA. A new approach to variable selection in least squares problems. *IMA Journal of Numerical Analysis*, 2000; **20**:389–404.

Pandey A, Biswas M, Samman M. Damage detection from changes in curvature mode shapes. *Journal of Sound and Vibration* 1991; **145**(2):321–332.

Pandey A, Biswas M. Damage detection in structures using changes in flexibility. *Journal of Sound and Vibration* 1994; **169**(1):3–17.

Papadimitriou C. Optimal sensor placement methodology for parametric identification of structural systems. *Journal of Sound and Vibration* 2004; **278**:923–947.

Peterson S, McLean D, Symans M, Pollock D, Cofer W, Emerson R, Fridley KJ. Application of dynamic system identification to timber beams. II. *Journal of Structural Engineering* 2001; **127**(4):426–432.

Phillips DL. A technique for the numerical solution of certain integral equations of the first kind. *Journal of Association for Computing Machinery* 1962; **9**(1):84–97.

Pradeep K, Rao BN, Srinivasan S, Balasubramaniamd K. Modal strain energy change ratio for damage identification in honeycomb sandwich structures. *Canadian Journal of Basic and Applied Sciences* 2014; **2**(1):10–24.

Qiao P, Lu K, Lestari W, Wang J. Curvature mode shape-based damage detection in composite laminated plates. *Composite Structures* 2007; **80**(3):409–428.

Ratcliffe CP. Damage detection using a modified Laplacian operator on mode shape data. *Journal of Sound and Vibration* 1997; **204**(3):505–517.

Ratcliffe CP, Bagaria WJ. Vibration technique for locating delamination in a composite beam. *AIAA Journal* 1998; **36**(6):1074–1077.

Reddy DM, Swarnamani S. Application of the FRF curvature energy damage detection method to plate like structures. *World Journal of Modelling and Simulation* 2012; **8**(2):147–153.

Rosset S, Zhu J. Piecewise linear regularized solution paths. *Advances in Neural Information Processing Systems* 2004; **35**(3):1012–1030.

Roveri N, Carcaterra A. Damage detection in structures under traveling loads by Hilbert-Huang transform. *Mechanical Systems and Signal Processing* 2012; **28**:128–144.

Rucka M. Damage detection in beams using wavelet transform on higher vibration modes. *Journal of Theoretical and Applied Mechanics* 2011; **49**(2):399–417.

Rytter A. *Vibration Based Inspection of Civil Engineering Structures*. PhD Dissertation, Department of Building Technology and Structural Engineering, Aalborg University, Denmark, 1993.

Saab R, Yilmaz Ö. Sparse recovery by non-convex op-timization – instance optimality. *Applied and Computational Harmonic Analysis* 2010; **29**(1):30–48.

Sahin M, Shenoi R. Quantification and localisation of damage in beam-like structures by using artificial neural networks with experimental validation. *Engineering Structures* 2003; **25**(14):1785–1802.

Salane H, Baldwin Jr J. Identification of modal properties of bridges. *Journal of Structural Engineering* 1990; **116**(7):2008–2021.

Salawu OS. Detection of structural damage through changes in frequency: a review. *Engineering Structures* 1997; **19**(9):718–723.

Salawu OS, Williams C. Bridge assessment using forced-vibration testing. *Journal of Structural Engineering* 1995; **121**(2):161–173.

Sampaio R, Maia N, Silva J. Damage detection using the frequency-response-function curvature method. *Journal of Sound and Vibration* 1999; **226**(5):1029–1042.

Sawyer JP, Rao SS. Structural damage detection and identification using fuzzy logic. *AIAA Journal* 2000; **38**(12):2328–2335.

Shah SP, Popovics JS, Subramaniam KV, Aldea CM. New directions in concrete health monitoring technology. *Journal of Engineering Mechanics* 2000; **126**(7):754–760.

Shi Z, Law S, Zhang L. Optimum sensor placement for structural damage detection. *Journal of Engineering Mechanics* 2000a; **126**(11):1173–1179.

Shi Z, Law S, Zhang L. Damage localization by directly using incomplete mode shapes. *Journal of Engineering Mechanics* 2000b; **126**(6):656–660.

Shi Z, Law S, Zhang L. Improved damage quantification from elemental modal strain energy change. *Journal of Engineering Mechanics* 2002; **128**(5):521–529.

Shih HW, Thambiratnam DP, Chan TH. Vibration based structural damage detection in flexural members using multi-criteria approach. *Journal of Sound and Vibration* 2009; **323**(3):645–661.

Sohn H, Farrar CR, Hemez FM, Shunk DD, Stinemates DW, Nadler BR, Czarnecki JJ. A review of structural health monitoring literature: 1996–2001, *Los Alamos National Laboratory Report*, 2003.

Sohn H, Law K. A Bayesian probabilistic approach for structure damage detection. *Earthquake Engineering and Structural Dynamics* 1997; **26**(12):1259–1281.

Sohn H, Law K. Bayesian probabilistic damage detection of a reinforced-concrete bridge column. *Earthquake Engineering and Structural Dynamics* 2000; **29**(8):1131–1152.

Song H, Zhong L, Han B. Structural damage detection by integrating independent component analysis and support vector machines. *International Journal of Systems Science* 2005; **37**(13):961–967.

Taylor HL, Banks SC, McCoy JF. Deconvolution with the l_1 norm. *Geophysics* 1979; **44**(1):39–52.

Theodoridis S, Kopsinis Y, Slavakis K. Sparsity-aware learning and compressed sensing: An overview. *Academic Press Library in Signal Processing* 2014; **1**:1271–1377.

Tibshirani R. Regression shrinkage and selection via the lasso. *Journal of the Royal Statistical Society* 1996; **58**(1):267–288.

Tikhonov AN. Solution of Incorrectly Formulated Problems and the Regularization Method. *Soviet Mathematics Doklady* 1963; **4**:1035–1038.

Tillmann AM, Pfetsch ME. The computational complexity of the restricted isometry property, the nullspace property, and related concepts in compressed sensing. *IEEE Transactions on Information Theory* 2014; **60**(2):1248–1259.

Tipping ME. Sparse Bayesian learning and the relevance vector machine. *Journal of Machine Learning Research* 2001; **1**:211–244.

Tipping ME, Faul AC. Fast marginal likelihood maximisation for sparse Bayesian models. In: *Proceedings of the 9th International Workshop on Artificial Intelligence and Statistics*, Key West, Florida, USA, 3–6 January 2003.

Tondreau G, Reynders E, Deraemaeker A. Towards a more realistic modelling of the uncertainty on identified mode shapes due to measurement noise. In: *Proceedings of the 9th International Conference on Damage Assessment of Structures*, Oxford, UK, 11–13 July 2011, **305**:012002.

Van Overschee P, De Moor BL. *Subspace Identification for Linear Systems: Theory, Implementation, Applications*. Dordrecht, Netherlands: Kluwer Academic Publishers, 1996.

Vanik MW, Beck JL, Au SK. Bayesian probabilistic approach to structural health monitoring. *Journal of Engineering Mechanics* 2000; **126**(7):738–745.

Wahab MA, De Roeck G. Damage detection in bridges using modal curvatures: application to a real damage scenario. *Journal of Sound and Vibration* 1999; **226**(2):217–235.

Wang S, Liu F, Zhang M. Modal strain energy based structural damage localization for offshore platform using simulated and measured data. *Journal of Ocean University of China* 2014; **13**(3):397–406.

Wang Y, Hao H. An introduction to compressive sensing and its potential applications in structural engineering. In: *The 11th International Symposium on Structural Engineering*, Guangzhou, China, 18–20 December 2010, pp. 1089–1094.

Wang Y, Zhao T. Statistical interpretation of soil property profiles from sparse data using Bayesian compressive sampling. *Geotechnique* 2017; **67**(6):523–36.

Wang Z, Lin R, Lim M. Structural damage detection using measured FRF data. *Computer Methods in Applied Mechanics and Engineering* 1997; **147**(1):187–197.

Wang ZC, Chen GD. Analytical mode decomposition with Hilbert Transform for modal parameter identification of buildings under ambient vibration. *Engineering Structures* 2014; **59**:173–184.

Weber B, Paultre P, Proulx J. Consistent regularization of nonlinear model updating for damage identification. *Mechanical Systems and Signal Processing* 2009; **23**(6):1965–1985.

Weng S. *A new substructuring method for model updating of large scale structures*. PhD Dissertation, Department of Civil and Structural Engineering, The Hong Kong Polytechnic University, Hong Kong, 2010.

Weng S, Xia Y, Xu YL, Zhu HP. An iterative substructuring approach to the calculation of eigensolution and eigensensitivity. *Journal of Sound and Vibration* 2011; **330**(14):3368–3380.

Weng S, Xia Y, Zhou XQ, Xu YL, Zhu HP. Inverse substructure method for model updating of structures, *Journal of Sound and Vibration* 2012; **331**(25):5449–5468.

Wickramasinghe WR, Thambiratnam DP, Chan TH. Use of modal flexibility method to detect damage in suspended cables and the effects of cable parameters. *Electronic Journal of Structural Engineering* 2015; **14**(1):133–144.

Williams O, Blake A, Cipolla R. Sparse Bayesian learning for efficient visual tracking. *IEEE Transactions on Pattern Analysis and Machine Intelligence* 2005; **27**(8):1292–1304.

Williams PM. Bayesian regularization and pruning using a Laplace prior. *Neural Computation* 1995; **7**(1):117–14.

Wipf DP. Sparse estimation with structured dictionaries. In: *Proceedings* of *the 24th Advances in Neural Information Processing Systems*, Granada, Spain, 12–15 December 2011, pp. 2016–2024.

Wipf DP, Palmer J, Rao B. Perspectives on sparse Bayesian learning. *Advances in Neural Information Processing Systems* 2004; **52**(16):2153–2164.

Wipf DP, Rao BD. Sparse Bayesian learning for basis selection. *IEEE Transactions on Signal Processing* 2004; **52**(8):2153–2164.

Worden K, Burrows AP. Optimal sensor placement for fault detection. *Engineering Structures* 2001; **23**(8):885–901.

Wu C. On the convergence properties of the EM algorithm. *The Annals of Statistics* 1983; **11**(1):95–103.

Wu D, Law S. Damage localization in plate structures from uniform load surface curvature. *Journal of Sound and Vibration* 2004; **276**(1):227–244.

Wu D, Law S. Sensitivity of uniform load surface curvature for damage identification in plate structures. *Journal of Vibration and Acoustics* 2005; **127**(1):84–92.

Xia Y, Hao H. Measurement selection for vibration-based structural damage identification. *Journal of Sound and vibration* 2000; **236**(1):89–104.

Xia Y, Hao H. Statistical damage identification of structures with frequency changes. *Journal of Sound and Vibration* 2003; **263**(4):853–870.

Xia Y, Hao H, Brownjohn JMW, Xia PQ. Damage identification of structures with uncertain frequency and mode shape data. *Earthquake Engineering and Structural Dynamics* 2002; **31**(5):1053–1066.

Xia Y, Hao H, Deeks AJ, Zhu X. Condition assessment of shear connectors in slab-girder bridges via vibration measurements. *Journal of Bridge Engineering* 2008; **13**(1):43–54.

Xia Y, Weng S, Xu YL, Zhu HP. Calculation of eigenvalue and eigenvector derivatives with the improved Kron's substructuring method. *Structural Engineering and Mechanics* 2010; **36**(1):37–55.

Xu W, Cao M, Ostachowicz W, Radzieński M, Xia N. Two-dimensional curvature mode shape method based on wavelets and Teager energy for damage detection in plates. *Journal of Sound and Vibration* 2015; **347**:266–278.

Xu YL, Chen J. Structural damage detection using empirical modes decomposition: Experimental investigation. *Journal of Engineering Mechanics-ASCE* 2004; **130**(11):1279–1288.

Xu YL, Xia Y. *Structural health monitoring of long-span suspension bridges*. London: Spon Press, 2011.

Xu ZB, Zhang H, Wang Y, Chang XY, Liang Y. $L_{1/2}$ regularization. *Science Chin*a 2010; **53**(6):1159–1169.

Yan YJ, Cheng L, Wu ZY, Yam LH. Development in vibration-based structural damage detection technique. *Mechanical Systems and Signal Processing* 2007; **21**(5):2198–2211.

Yang JN, Lei Y, Lin S, Huang N. Hilbert–Huang based approach for structural damage detection. *Journal of Engineering Mechanics* 2004; **130**(1):85–95.

Yang JN, Xia Y, Loh CH. Damage identification of bolt connections in a steel frame. *Journal of Structural Engineering* 2014; **140**(3):04013064.

Yang QW, Li JK. Damage identification by the eigenparameter decomposition of structural flexibility change. *International Journal for Numerical Method in Engineering* 2009; **78**(4):444–459.

Yang QW, Liu J. Structural damage identification based on residual force vector. *Journal of Sound and Vibration* 2007; **305**(1):298–307.

Yang Y, Nagarajaiah S. Output-only modal identification with limited sensors using sparse component analysis. *Journal of Sound and Vibration* 2013; **332**(19):4741–4765.

Yang Y, Nagarajaiah S. Blind denoising of structural vibration responses with outliers via principal component pursuit. *Structural Control and Health Monitoring* 2014a; **21**(6):962–978.

Yang Y, Nagarajaiah S. Structural damage identification via a combination of blind feature extraction and sparse representation classification. *Mechanical Systems and Signal Processing* 2014b; **45**(1):1–23.

Yang Y, Nagarajaiah S. Output-only modal identification by compressed sensing: Non-uniform low-rate random sampling. *Mechanical Systems and Signal Processing* 2015; **56**–**57**:15–34.

Yao G, Chang K, Lee G. Damage diagnosis of steel frames using vibrational signature analysis. *Journal of Engineering Mechanics* 1992; **118**(9):1949–1961.

Yao H, Gerstoft P, Shearer PM, Mecklenbräuker C. Compressive sensing of the Tohoku-Oki Mw 9.0 earthquake: Frequency-dependent rupture modes. *Geophysical Research Letters* 2011; **38**(20):1–5.

Yao L, Sethares WA, Kammer DC. Sensor placement for on-orbit modal identification via a genetic algorithm. *AIAA Journal* 1993; **31**(10):1167–9.

Yi TH, Li HN, Zhang XD. Health monitoring sensor placement optimization for Canton Tower using immune monkey algorithm. *Structural Control and Health Monitoring* 2015; **22**(1):123–138.

Yin T, Jiang QH, Yuen KV. Vibration-based damage detection for structural connections using incomplete modal data by Bayesian approach and model reduction technique. *Engineering Structures* 2017; **132**:260–277.

Yoon M, Heider D, Gillespie J, Ratcliffe C, Cran, R. Local damage detection using the two-dimensional gapped smoothing method. *Journal of Sound and Vibration* 2005; **279**(1):119–139.

Zhang C, Huang JZ, Song GQ, Chen L. Structural damage identification by extended kalman filter with l_1-norm regularization scheme. *Structural Control and Health Monitoring* 2017; **24**(11):e1999.

Zhang C, Xu Y. Comparative studies on damage identification with Tikhonov regularization and sparse regularization. *Structural Control and Health Monitoring* 2016; **23**(3):560–579.

Zhang J, Li P, Wu Z. A new flexibility-based damage index for structural damage detection. *Smart Materials and Structures* 2013; **22**(2):025037.

Zhang Z, Aktan A. Application of modal flexibility and its derivatives in structural identification. *Journal of Research in Nondestructive Evaluation* 1998, **10**(1):43–61.

Zhang Z, Rao BD. Sparse signal recovery with temporally correlated source vectors using sparse Bayesian learning. *IEEE Journal of Selected Topics in Signal Processing* 2011; **5**(5):912–926.

Zhong SC, Oyadiji SO. Crack detection in simply supported beams without baseline modal parameters by stationary wavelet transform. *Mechanical Systems and Signal Processing* 2007; **21**(4):1853–1884.

Zhong SC, Oyadiji SO, Ding K. Response-only method for damage detection of beam-like structures using high accuracy frequencies with auxiliary mass spatial probing. *Journal of Sound and Vibration* 2008; **311**(3):1075–1099.

Zhou XQ, Xia Y, Hao H. Sensor placement for structural damage detection considering the measurement uncertainties. *Advances in Structural Engineering* 2013; **16**(5):899–907.

Zhou XQ, Xia Y, Weng S. L_1 regularization approach to structural damage detection using frequency data. *Structural Health Monitoring* 2015; **14**(6):571–582.

Zhou Z, Wegner LD, Sparling BF. Vibration-based detection of small-scale damage on a bridge deck. *Journal of Structural Engineering* 2007; **133**(9):1257–1267.

Zimmerman DC, Kaouk M. Structural damage detection using a minimum rank update theory. *Journal of Vibration and Acoustics* 1994; **116**(2):222–231.

Zuo WM, Meng DY, Zhang L, Feng XC, Zhang D. A generalized iterated shrinkage algorithm for non-convex sparse coding. In: *Proceedings* of *IEEE International Conference on Computer Vision (ICCV)*, Sydney, Australia, 3–6 December 2013, pp. 217–224.